

Title	Upconverting nanoparticles: pushing theory and technology towards biomedical applications
Authors	Souza Matias, Jean
Publication date	2023
Original Citation	Souza Matias, J. 2023. Upconverting nanoparticles: pushing theory and technology towards biomedical applications. PhD Thesis, University College Cork.
Type of publication	Doctoral thesis
Rights	© 2023, Jean Souza Matias. - <a href="https://creativecommons.org/licenses/by-nc-nd/4.0/">https://creativecommons.org/licenses/by-nc-nd/4.0/</a>
Download date	2025-07-03 21:53:14
Item downloaded from	<a href="https://hdl.handle.net/10468/14979">https://hdl.handle.net/10468/14979</a>

Ollscoil na hÉireann, Corcaigh  
**National University of Ireland, Cork**



**UPCONVERTING NANOPARTICLES:  
PUSHING THEORY AND TECHNOLOGY  
TOWARDS BIOMEDICAL APPLICATIONS**

Thesis presented by  
**Jean Souza Matias**

**ORCID: 0000-0001-6745-016X**

for the degree of  
**Doctor of Philosophy**

**University College Cork**  
**Physics Department**

Head of Department: John McInerney  
Supervisor: Stefan Andersson-Engels  
Co-supervisor: Silvia Melgar  
Research advisor: Katarzina Komolibus

2023

UPCONVERTING NANOPARTICLES: PUSHING THEORY AND TECHNOLOGY TOWARDS  
BIOMEDICAL APPLICATIONS

© 2023 Jean Souza Matias  
All rights reserved

Biophotonics, Tyndall National Institute  
Department of Physics  
University College Cork, UCC  
Ireland

*"Frustra fit per plura quod potest fieri per pauciora."*

"It is futile to do with more things that which can be done with fewer"

The principle of economy - William of Ockham



# ABSTRACT

---

Biophotonics faces a significant challenge in developing non-invasive imaging and interrogation techniques with high spatial resolution and penetration depth for precise diagnosis and treatment. These techniques rely on non-ionising radiation and non-toxic contrast agents possessing excellent photo and chemical stabilities. Among the various non-ionising wavelengths, the near-infrared (NIR) optical window offers the highest tissue penetration due to its minimal scattering and absorption in living tissues. Upconverting nanoparticles (UCNPs) possess the desirable properties of absorbing and emitting NIR light, making them ideal contrast agents for biomedical applications. UCNPs have shown promise in deep tissue imaging, optogenetics, photodynamic therapy, temperature sensing, drug delivery, and super-resolution microscopy. However, the efficiency of upconversion (UC) in UCNPs, as quantified by the quantum yield (QY), remains a significant challenge, particularly at low excitation power densities (PDs) where the non-linearity of upconversion luminescence (UCL) dominates. Furthermore, the lack of commercially available devices and standardised protocols that account for the crucial parameters affecting PD-dependent QY further complicates accurate characterisation of these materials. To address these issues, this thesis presents the design and construction of a comprehensive, broad-band, multi-variable QY characterisation system. This opto-electronically engineered setup enables simultaneous measurement of absorption and luminescence at two selected wavelengths. In addition, the fully automated system incorporates capabilities for characterising excitation beam profiles, scattering, and the emission spectrum of luminescent compounds in aqueous solutions. Accurate characterisation of the excitation beam profile is of particular importance due to its influence on the PD-dependent QY behaviour of UCNPs. Varying beam profiles lead to distinct QY values, necessitating beam profile compensation to derive an intrinsic QY property of the material independent of measurement configuration. However, achieving this compensation requires a comprehensive understanding of the mechanisms governing each UC emission wavelength, which has not yet been extensively studied across a wide range of PDs. Consequently, this thesis also includes a detailed theoretical study based on the rates of populating and depopulating the electronic energy states involved in UC processes. The investigation successfully quantifies the transition points at which the UCL transitions from non-linear behaviour of different orders to linearity. The theoretical model is validated using experimental UCL data acquired from two distinct UCNP compounds at various wavelengths. These combined theoretical and experimental studies are of utmost importance for the accurate characterisation and engineering of optimal UCNPs, representing a crucial advancement in the development of high-resolution, deep-penetration biomedical techniques and devices.



# LIST OF PUBLICATIONS

---

---

This thesis is based in the following research papers, which will be referenced using Roman numerals in the text. The works of Papers **I**, **II**, and **III** have been published, whereas Paper **IV** has recently been submitted for publication.

**I Evaluation of relative beam-profile-compensate quantum yield of upconverting nanoparticles over wide dynamic range of power densities**

J. S. Matias, K. Komolibus, S. Konugolu, and  
S. Andersson-Engels.  
*Nanoscale* **14**, 2230-2237 (2022).

**II Multi-variable compensated quantum yield measurements of upconverting nanoparticles with high dynamic range: a systematic approach**

S. Konugolu, J. S. Matias, K. Komolibus, and  
S. Andersson-Engels.  
*Opt Express*. **30(10)**, 16572-16584 (2022).

**III Generalised analytical model of the transition power densities of the upconversion luminescence and quantum yield**

J. S. Matias, K. Komolibus, S. Konugolu, W. Kho-Kiang and  
S. Andersson-Engels.  
*Nanoscale Advances* **5**, 3279 - 3286 (2022).

**IV Beam-profile compensation for quantum yield characterisation of Yb-Tm codoped upconverting nanoparticles emitting at 474 nm, 650 nm and 804 nm (Submitted for publication)**

J. S. Matias, K. Komolibus, S. Konugolu, W. Kho-Kiang and  
S. Andersson-Engels.  
*Nanoscale* -, (2023).



# LIST OF PATENTS

---

The quantum yield characterisation system developed as part of this research has been awarded a patent.

## **I Optical system and method**

S. Konugolu-Venkata-Sekar, S. Andersson-Engels, J. S. Matias  
and K. Komolibus.

*WIPO WO 2021/084137 A1*, (2021).



# ABBREVIATIONS

---

A	Activator
AI	Analog input
AO	Analog output
APD	Avalanch photodiode
CM	Confocal microscopy
CR	Cross-relaxation
CT	Computed tomography
CUC	Cooperative upconversion
CW	Continuous wave
DAQ	Data acquisition card
eQY	External quantum yield
ESA	Excited-state absorption
ET	Energy transfer
ETU	Energy transfer upconversion
FWHM	Full width at half maximum
GSA	Ground-state absorption
iQY	Internal quantum yield
IR	Infrared
IUPAC	International Union of Pure and Applied Chemistry
Laser	Light amplification by stimulated emission of radiation
$\text{Ln}^{3+}$	Lanthanide ions
MPM	Multi-photon microscopy
MRI	Magnetic resonance imaging
NIR	Near infrared
NP	Nanoparticle
PA	Photon avalanche
PD	Power density
PET	Positron emission tomography
QD	Quantum dot
QY	Quantum yield
RE	Rare earth
S	Sensitiser
SEM	Scanning electron microscope
STEM	Scanning transmission electron microscope
SHG	Second harmonic generation
SNR	Signal-to-noise ratio
SPECT	Single-photon emission computed tomography

SWCNT	Single-walled carbon nanotube
TPA	Two-photon absorption
UC	Upconversion
UCL	Upconversion luminescence
UV	Ultraviolet (Refers to the ultraviolet range of the light spectrum)
UCNP	Upconverting nanoparticle
VIS	Visible (Refers to the visible range of the light spectrum)

# CONTENTS

---

---

<b>Abstract</b>	<b>v</b>
<b>Introduction</b>	<b>1</b>
0.1 Motivation . . . . .	1
0.2 Structure of the thesis . . . . .	3
<b>1 Upconversion</b>	<b>5</b>
1.1 Upconversion Mechanisms . . . . .	5
1.1.1 Excited-state absorption (ESA) . . . . .	6
1.1.2 Energy transfer upconversion (ETU) . . . . .	6
1.1.3 Cooperative upconversion (CUC) . . . . .	7
1.1.4 Other types of UC processes . . . . .	8
1.1.5 Photon avalanche effect (PA) . . . . .	8
1.2 Upconverting nanoparticles (UCNPs) . . . . .	8
1.2.1 Upconversion Quantum Yield (QY) . . . . .	9
<b>2 Time-resolved and steady-states of the population densities of the energy levels involved in ETU processes</b>	<b>11</b>
2.1 ETU2 model proposed by Liu et al. . . . .	11
2.2 ETU processes of higher order . . . . .	13
2.2.1 Population densities of the energy states and the transition PD points . . . . .	13
2.2.2 The photon flux and upconversion luminescence (UCL) . . . . .	14
2.2.3 Internal Quantum Yield (iQY) . . . . .	14
2.2.4 The PD limits . . . . .	14
2.2.5 A detailed comparison with the model proposed by Liu et al. . . . .	16
2.2.6 A numerical example . . . . .	16
2.3 Dynamics . . . . .	17
2.3.1 Numerical approach . . . . .	18
2.4 Summary . . . . .	20
<b>3 A semi-relative quantum yield system</b>	<b>23</b>
3.1 Absolute QY evaluation . . . . .	23
3.2 Relative QY evaluation . . . . .	23
3.3 A semi-relative multi-characterisation setup . . . . .	24
3.3.1 The system . . . . .	25
3.3.2 Alignment of the excitation and luminescence beams . . . . .	31
3.3.3 Calibration . . . . .	32
3.3.4 Measurement protocol . . . . .	39
3.3.5 Analysis protocol . . . . .	41
3.4 Summary . . . . .	43
<b>4 The excitation beam profile-compensation and high dynamic range of PDs</b>	<b>45</b>
4.1 The excitation beam profile compensation . . . . .	46
4.2 Expanding the PD dynamic range of the excitation illumination . . . . .	47
4.3 An example study . . . . .	47
4.4 Detailed comparison of different compensation approaches . . . . .	49
4.5 Summary . . . . .	51
<b>5 A complete QY characterisation of UC emissions in the NIR and VIS ranges incorporating multiple ETU Processes</b>	<b>53</b>
5.1 Methodology . . . . .	53
5.2 Characterisation . . . . .	54
5.2.1 The transition PD points . . . . .	55
5.2.2 The beam profile compensated iQY . . . . .	58
5.3 Summary . . . . .	59
<b>Conclusions and future perspective</b>	<b>61</b>

Comments on the Papers	63
Comments on the Patents	65
Acknowledgements	67
References	69
Appendix	79

## Papers

---

- |     |  |     |
|-----|--|-----|
| I   | Evaluation of relative beam-profile-compensate quantum yield of upconverting nanoparticles over wide dynamic range of power densities                                      | 95  |
| II  | Multi-variable compensated quantum yield measurements of upconverting nanoparticles with high dynamic range: a systematic approach   | 105 |
| III | Generalised analytical model of the transition power densities of the upconversion luminescence and quantum yield  | 121 |
| IV  | Beam-profile compensation for quantum yield characterisation of Yb-Tm codoped upconverting nanoparticles emitting at 474 nm, 650 nm and 804 nm (Submitted for publication) | 131 |

**Patent**

---

I	Optical system and method	143
---	---------------------------	-----

# INTRODUCTION

---

## 0.1 Motivation

The significance of upconverting nanoparticles is rooted in the fundamental requirements of Biophotonics. Biophotonics is a discipline that investigates optical processes occurring naturally or synthetically in bioengineered materials within biological systems. It places particular emphasis on sensing and imaging techniques facilitated by fluorescent markers or contrast agents, which enable drug delivery and the dynamic tracking of living cells or tissues. Biomedical imaging plays a crucial role in non-invasive tissue visualisation and characterisation techniques [1–3], encompassing various applications such as cancer diagnosis [4, 5], surgical margin evaluation, intra-operative guidance [6], retinal disease diagnosis [7], and preclinical imaging of small animals [8, 9]. Bioimaging techniques are defined by their penetration depth and spatial resolution [10], with no single technique fully encompassing both optimal characteristics [2]. Microscopic techniques, including confocal microscopy (CM) and multi-photon microscopy (MPM), offer high spatial resolution but limited penetration depth. On the other hand, macroscopic techniques like magnetic resonance imaging (MRI), positron emission tomography (PET), computed tomography (CT), and single-photon emission computed tomography (SPECT) provide greater penetration depth but lower spatial resolution [2, 3, 10]. Fig. 0.1 compares several imaging modalities in terms of penetration depth and spatial resolution. Furthermore, certain tomographic techniques employ potentially hazardous ionising radiation and require minutes to hours to generate imaging results, limiting their real-time visualisation capabilities [3].

The significance of upconverting nanoparticles (UCNPs) stems from their vital role in the field of Biophotonics. Biomedical applications heavily rely on fluorescence imaging techniques [11], which offer advantages such as low cost, high sensitivity, non-ionising radiation, rapid response within milliseconds, and resolution down to tens of nanometres [11, 12]. However, conventional optical imaging predominantly employs visible (VIS) light, which experiences significant attenuation when interacting with the surface of living tissues due to the high scattering and absorption at VIS wavelengths [3, 11]. In contrast, near-infrared (NIR) fluorescence imaging exhibits a tissue penetration depth of around 1-2 *cm*, which surpasses the capabilities of VIS techniques [11, 13]. An ideal contrast agent for enhancing the resolution and sensitivity of NIR fluorescence imaging should possess both excitation and emission within the NIR optical window (700-1400 *nm*) [14, 15]. While NIR fluorescent organic dyes and conjugated polymers have shown promise, maintaining satisfactory brightness remains challenging due to issues such as photobleaching and low stability when in contact with living tissues [3, 16]. Other materials, such as single-walled carbon nanotubes (SWCNTs) and infrared quantum dots (QDs), have also been explored for NIR fluorescence imaging applications [17, 18]. However, SWCNTs, with their large lengths and needle-like structures, have been reported to cause tissue damage and

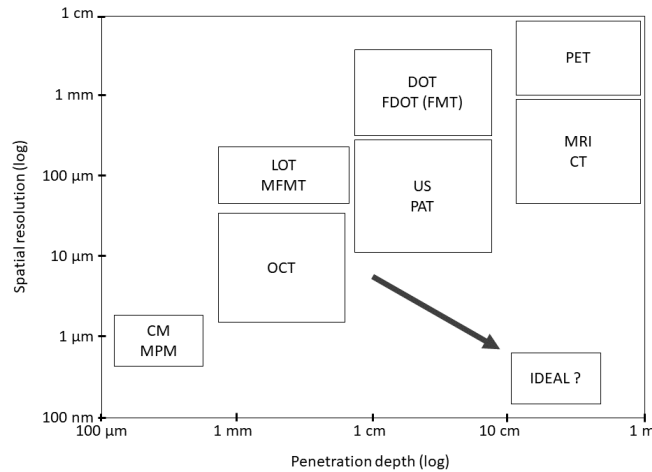


Figure 0.1: A comparison of various bioimaging modalities in terms of their penetration depth and spatial resolution. CM - Confocal microscopy; MPM - multi-photon microscopy; OCT - Optical coherence tomography; LOT - laminar optical tomography; MFMT - Mesoscopic fluorescence molecular tomography; FDOT - Fluorescence diffuse optical tomography; FMT - Fluorescence molecular tomography; PAT - Photoacoustic tomography; SPECT - Single-photon emission computed tomography. The arrow indicates an ideal technique with both high spatial resolution and penetration depth. The image has been adapted from [10].

chronic toxicity [19]. In comparison to these contrast agents, UCNPs have garnered considerable attention as potential optical imaging probes [2, 3, 11, 15, 20–29]. UCNPs exhibit photo and chemical stability, tunable multi-wavelength emissions ranging from ultraviolet (UV) to NIR, including the VIS range [30, 31]. Their well-defined atomic-like electronic transitions result in sharper emission lines ( $\sim 10\text{-}20\text{ nm}$  full width at half maximum) compared to QDs ( $\sim 25\text{-}40\text{ nm}$ ) and dyes, which can span over  $100\text{ nm}$  [3]. Furthermore, studies on different surface modifications have demonstrated that UCNPs can exhibit high biostability, low dissolution, and low toxicity in aqueous environments such as living tissues [32]. Refer to Tab. 0.1 for a comparison of the characteristics of UCNPs, dyes, and QDs. These appealing characteristics make UCNPs not only promising for *in vivo* and *in vitro* biomedical imaging applications [33], but also suitable for various biophotonic fields such as optogenetics [34], diffuse optical tomography [35], biosensors [27], photodynamic therapy [26], temperature sensing [36, 37], solar energy [38, 39], photocatalysis [40], and super-resolution microscopy [41–44]. In fact, *in vivo* applications of UCNPs are still in their early stages, although recent advances in super-resolution microscopy utilizing UCNPs with giant non-linearity have marked a breakthrough in the field [25]. Researchers have achieved spatial resolutions of approximately  $70\text{ nm}$ , well below the previously reported lower limit of  $250\text{ nm}$  [45], enabling detailed visualisation of subcellular structures [43]. Fig. 0.2 illustrates some of the vast applications of UCNPs.

Despite their considerable potential, the upconversion efficiency, also known as quantum yield (QY), is diminished as the size of the particles decreases [46]. Consequently, to attain a discernible luminescence signal, UCNPs necessitate high excitation power densities (PDs), which are constrained in biological applications [47]. Nevertheless, the PD required for UCNPs imaging is significantly lower than that needed for multiphoton microscopy, as photons are absorbed sequentially in the up-

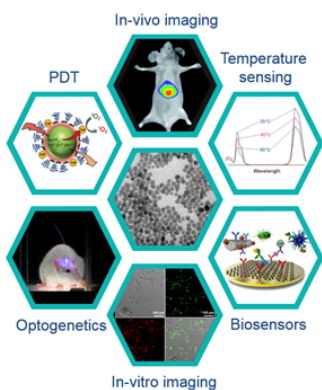


Figure 0.2: Illustrative depiction of select applications demonstrating the utility of UCNPs.

Table 0.1: Advantages of employing UCNPs in biomedical applications compared to dyes and QDs. UCNPs offer numerous advantageous features, although their inherent limitation of a relatively low QY presents a critical challenge.

	QDs	Dyes	UCNPs
Non-toxic	✗	✓	✓
No autofluorescence	✗	✗	✓
Penetration depth	✓	✗	✓
Photo-stability	✓	✗	✓
Chemical-stability	✓	✓	✓
Narrow emission line	✗	✗	✓
Functionalisation	✗	✓	✓
Quantum Yield	✓	✓	✗

conversion (UC) process [48]. Furthermore, unlike fluorescence, the UC efficiency is PD-dependent and diminishes markedly at low excitation intensities due to the non-linear nature of upconversion luminescence (UCL) in relation to the excitation PD [1]. Accurately evaluating the UC efficiency presents challenges in both experimental methodology and analysis [1, 49, 50]. Nonetheless, a thorough examination of this property is a critical prerequisite for engineering optimal UCNPs for biomedical applications. Therefore, this study focuses on investigating the UC and QY of UCNPs, exploring their non-linear PD dependence from both theoretical and experimental perspectives.

## 0.2 Structure of the thesis

The present thesis consists of an investigation into the UC processes and QY in UCNPs. It involves the development of a theoretical model for UC QY and the establishment of an in-lab QY setup for comprehensive UCNP characterisation. The QY system and analytical model were successfully used to study both NIR and VIS emitting UCNPs. The following five chapters provide a summary of the conducted research:

**Chap. 1 – Upconversion** provides an overview of UCNPs and their UC mechanisms. This chapter presents a summary of the historical background, tracing the evolution of UC discovery from theoretical to experimental perspectives. A comparison of the various mechanisms responsible for the UC phenomenon is presented, with particular emphasis on the energy transfer upconversion (ETU) process, known for its high efficiency. Additionally, the chapter explores the characteristics of typical UCNPs, including how different structures and compositions influence their emission spectrum and QY.

**Chap. 2 – Time-resolved and steady-states of the population densities of the energy levels involved in ETU processes** presents an extensive investigation of the ETU processes involved in the emission lines of UCNPs. This study focuses on elucidating the non-linear characteristics of UCL and QY. A rigorous analytical model is developed and employed in numerical simulations to analyse the dynamics of population densities and their steady state. The model encompasses ETU processes of arbitrary order, enabling the explanation of UC in UCNPs with multi-wavelength emissions. Furthermore, the chapter defines and quantifies transition points where the non-linear power of UC emission is altered, facilitating a comparison between the distinctive behaviours of UCNPs and their bulk upconverting crystal counterparts at the microscopic level.

A concise summary of these findings is presented in Paper **III**.

**Chap. 3 – A semi-relative quantum yield system** provides a comprehensive background overview of different experimental methods used for evaluating the QY of UCNPs. The chapter also offers a detailed description of the QY system developed in the laboratory. It is based on the research presented in Paper **II** and Patent **I**. Instead of simply presenting the contents of previously published papers and patents, this chapter focuses on the subsequent improvements made to the system. It explores technical aspects, measurement techniques, and analysis protocols employed in QY evaluation.

**Chap. 4 – The excitation beam profile-compensation and high dynamic range of PDs** examines the impact of beam-profile on the UCL and QY. The chapter introduces a beam-profile compensation technique for assessing the intrinsic efficiency of UC, known as internal QY. This compensation method utilises the developed model discussed in Chap. 2, which encompasses ETU processes, including higher-order processes such as ETU2, ETU3, ETU4, etc. An application of the study focusing on the ETU2 process is presented in Paper **I**.

**Chap. 5 – A complete QY characterisation of UC emissions in the NIR and VIS ranges incorporating multiple ETU Processes** concludes the thesis by providing a complete characterisation of a multi-wavelength emitting UCNP spanning the VIS to NIR range. This investigation includes the analysis of ETU transitions of different orders. The study demonstrates the successful application of the in-lab QY system, as described in Chap. 3, for the thorough characterisation of UCNPs. Additionally, the study effectively employs the analytical model presented in Chap. 2 to determine the transition points of UCL and calculate the beam-profile compensated internal QY for ETU2 and ETU3 processes. The findings of this final study are consolidated in Paper **IV**.

---



---

# UPCONVERSION

---



---

In contrast to fluorescence, UC follows a different scheme in terms of energy conservation. Fluorescent emitters adhere to the Stokes principle, which states that the excitation photons possess higher energy than the emitted photons. The energy deficit is readily understood as losses incurred during electronic transitions within the process. However, UC entails emitted light with higher energy than the absorbed light, constituting an anti-Stokes process. Anti-Stokes emissions were recognized prior to the 1960s as a result of thermal fluctuations on the order of a few  $kT$ <sup>1</sup> above the excited states. In contrast, UC emissions can exceed excitation energies by a factor of 100 times  $kT$ . Despite its seemingly contradictory nature, UC is a valid process, and the energy surplus can be explained by the involvement of excited states in multi-photon absorptions before a single photon is emitted [48].

## 1.1 Upconversion Mechanisms

The first reported process of UC<sup>2</sup>, called Excited-state absorption (ESA), was proposed by Bloembergen in 1959 while investigating a sensor known as quantum counters. However, this process exhibited very weak emissions. In 1966, Auzel observed visible green emissions while studying Yb<sup>3+</sup>-Er<sup>3+</sup>-codoped glasses excited by NIR light. This led to the demonstration that energy transfer (ET) processes<sup>3</sup> could occur between the excited states of rare earth (RE) ions Auzel. Subsequent experiments were conducted on crystalline structures to enhance the efficiency of this phenomenon. As a result, blue emissions were achieved in Yb<sup>3+</sup>-Tm<sup>3+</sup>-codoped systems. The NIR and blue emissions were attributed to UC processes involving the absorption of two and three photons, respectively.

In addition to the previously mentioned mechanisms, another significant contribution to the understanding of UC came from Ovsyankin and Feofilov in 1966. Independently, Ovsyankin and Feofilov proposed a third mechanism involving cooperative processes between two ions while investigating quantum counters using ion pairs such as Yb<sup>3+</sup>-Tm<sup>3+</sup>, Yb<sup>3+</sup>-Er<sup>3+</sup>, and Yb<sup>3+</sup>-Ho<sup>3+</sup> [54]. Currently, there exist multiple known mechanisms contributing to UC, either in isolation or in combination. The

---

<sup>1</sup>Unit of energy equivalent to  $4.11 \times 10^{-21}$  J. Also written as  $k_B T$ , it is the product of the Boltzmann constant,  $k$ , and temperature,  $T$ .

<sup>2</sup>In its initial stage, the term UC was not yet defined and the process was commonly named as anti-Stokes fluorescence [51].

<sup>3</sup>At that time the process had different names: summation of photons, infrared-to-visible conversion, cooperative luminescence, anti-Stokes fluorescence by ET, quantum counting through ET, or APTE (for Addition de Photons par Transfert d'Energie) named by Auzel, which later was referred as energy transfer upconversion (ETU) to describe one of the mechanisms responsible for the UC process [48, 51].

subsequent sub-sections will provide detailed explanations of these principal processes.

### 1.1.1 Excited-state absorption (ESA)

In 1959, Bloembergen proposed the concept of detecting and quantifying infrared (IR) radiation using RE ions incorporated into a solid matrix [52]. The underlying principle of this process involved using a photon source to elevate electrons from the ions' ground state to an excited state, which had been previously populated by IR photons<sup>4</sup>. However, due to the weak UC emissions observed in early experimental demonstrations, the practical realization of this proposition required the development of laser technology. Fig. 1.1 illustrates the ESA process, wherein electrons undergo ground state absorption (GSA), followed by excited-state absorption (ESA), resulting in the pumping of electrons to higher energy states. Ultimately, the electronic radiative decay from the higher energy state to the ground state emits a single photon with a shorter wavelength, indicative of UC.

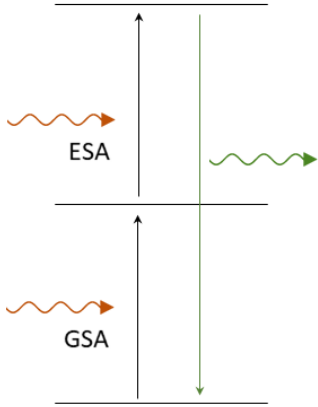


Figure 1.1: UC due to the ESA process. Electrons, pumped to a higher energy level through GSA and ESA, subsequently decay to the ground state, emitting a shorter-wavelength upconverted photon.

### 1.1.2 Energy transfer upconversion (ETU)

The process of ETU occurs when the absorption and emission events involve different ions within a host matrix. In this process, one ion, known as the sensitizer (S), absorbs a photon through GSA, exciting an electron to an excited state. Upon returning to the ground state, the electron releases energy either in the form of a photon (radiative process) or a phonon (non-radiative process). As this energy propagates through the matrix, it encounters an activator (A) ion. The ET from the sensitizer to the activator promotes one of the activator's electrons to an excited state. In 1966, Auzel demonstrated that the ET process was not limited to interactions between an excited state and the ground state (referred to as ETU1 process). It could also occur between excited states, resulting in more efficient upconverted emissions compared to the ESA process [53]. When the final excited state involved in the process is the second excited state, and two photons are absorbed, the process is referred to as ETU2. Similarly, for higher energy levels and the involvement of more photons, higher-order energy transfer processes are named ETU3, ETU4, and so on. Fig. 1.2 presents a schematic diagram illustrating the UC process through ETU, involving an energy transfer to the ground state (ETU1) and to an excited state (ETU2).

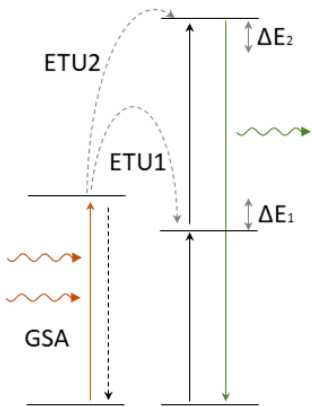


Figure 1.2: UC through the ETU process. The sensitizer absorbs excitation photons and transfers their energy to the activator through phonons in the host matrix lattice. Subsequent ETs pump the activator's electrons to higher energy levels, followed by direct decay to the ground state, emitting a shorter-wavelength upconverted photon. The energy mismatches ( $\Delta E$ ) are associated with UC facilitated by multiple phonons.

Radiative transfers occur in resonant systems, where the energy difference between the absorption levels of the sensitizer and the corresponding levels involved in energy transfer in the activator is nearly identical. In such cases, the emission spectrum of the sensitizer changes with the activator's concentration, while the lifetime of the sensitizer remains constant as the photons are emitted regardless. Conversely, in non-radiative transfers, the lifetime of the sensitizer is highly dependent on both the activator's concentration and the emission intensity. However, the shape of the emission spectrum remains independent [48]. Non-radiative processes can also occur through non-resonant mechanisms, aided by multi-phonons, which account for the energy mismatch observed in Figure Fig. 1.2. A special example of non-radiative transfer is cross-relaxation (CR), where both ions involved are identical, resulting in the population of an intermediate electronic level. Cross-relaxation is significant as it can lead to self-quenching of UC when the concentration of identical ions surpasses a critical level. In such cases, the closely spaced identical ions enable this process to occur [48].

<sup>4</sup>This two-step process is also referred to as two-step absorption.

The interaction between the ions was initially investigated by Förster in 1948, where he considered the Coulomb interactions of Van der Waals type and specifically examined dipole-dipole interactions. Förster's theoretical treatment of these interactions was based on quantum mechanics formalism [55]. Subsequently, Dexter proposed an extension of this theory to include multipole interactions a few years later in 1953 [56]. This development led to the formulation of the energy transfer probability  $p_{SA}$  between a sensitizer and an activator at a distance  $R$ , which is given by Eq. (1.1) in Auzel's work [51].

$$p_{SA} = \frac{(R_0/R)^s}{\tau_S}, \quad (1.1)$$

where  $R_0$  is the critical distance for which excitation transfer and spontaneous deactivation of the sensitizer are equally probable,  $\tau_S$  represents the sensitizer lifetime and  $s$  is a positive integer, such as:

$$s = \begin{cases} 6, & \text{for dipole-dipole interactions} \\ 8, & \text{for dipole-quadrupole interactions} \\ 10, & \text{for quadrupole-quadrupole interactions.} \end{cases}$$

In a macroscopic system composed of a large number of assembled ions, a rigorous analysis of the UC process requires the application of rate equations derived from statistical mechanics. These rate equations account for the population of particles in various energy states [57]. In such systems, ET can occur between ions of the same type (sensitizer-sensitizer or activator-activator) or between different types (sensitizer-activator). When ET takes place between ions of the same type, the energy can propagate through the matrix in a stepwise manner over long distances before UC occurs. This phenomenon, known as energy migration or energy diffusion, is influenced by the concentration of the ions involved. By strategically placing sensitizers and activators in different layers, it is possible to engineer more efficient materials and prevent concentration-induced UC quenching [58]. However, it is important to note that high dopant concentrations can lead to undesired processes such as back ET from activator to sensitizer or deleterious ET between activators [51].

### 1.1.3 Cooperative upconversion (CUC)

In cooperative upconversion (CUC), multiple impurity centres participate in either sensitization or luminescence processes. In cooperative sensitization, two excited ions transfer their accumulated energy to another ion, which subsequently reaches an excited state and relaxes back to the ground state, emitting the upconverted light. This process is illustrated in Fig. 1.3. On the other hand, cooperative luminescence involves the emission of a single upconverted photon resulting from the interaction between two excited ions. The first observation of cooperative luminescence was made by Nakazawa and Shionoya during the study of  $\text{Yb}^{3+}$  emission in  $\text{YbPO}_4$  crystalline powder [59]. The energy diagram in Fig. 1.4 provides an illustration of this process.

Cooperative processes are generally less efficient compared to ETU processes. The efficiency of cooperative sensitization is approximately  $10^{-6}$ , while cooperative luminescence has an efficiency of around  $10^{-8}$  [48].

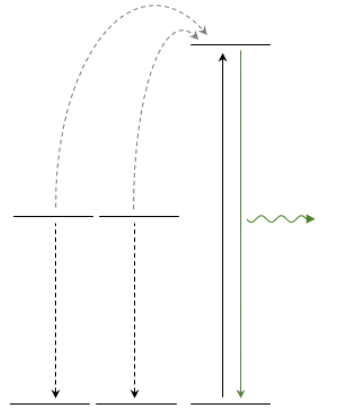


Figure 1.3: Cooperative sensitization. In this process, two excited ions collaborate to transfer their accumulated energy to another ion, exciting it to a higher excited state. Subsequently, the ion relaxes back to the ground state, emitting an upconverted photon.

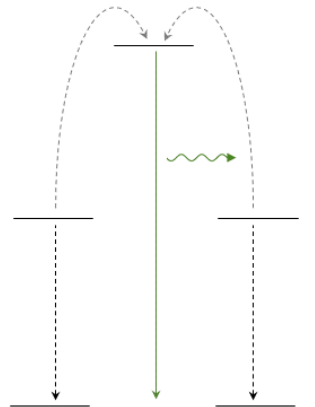


Figure 1.4: Cooperative luminescence. It occurs when two excited ions interact with each other, resulting in the emission of a single upconverted photon.

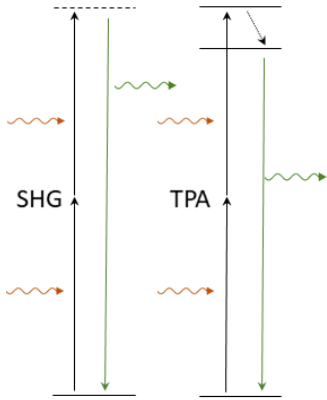


Figure 1.5: SHG on the left, and TPA on the right. In SHG, the electrons are excited to a virtual energy state, whereas in the TPA mechanism, the excitation occurs to an existing state.

Table 1.1: Order of magnitude of efficiency for the main UC mechanisms [48].

Mechanisms	Efficiency
ETU	$\sim 10^{-3}$
ESA	$\sim 10^{-5}$
Coop. Sens.	$\sim 10^{-6}$
Coop. Lum.	$\sim 10^{-8}$
SHG	$\sim 10^{-11}$
TPA	$\sim 10^{-13}$

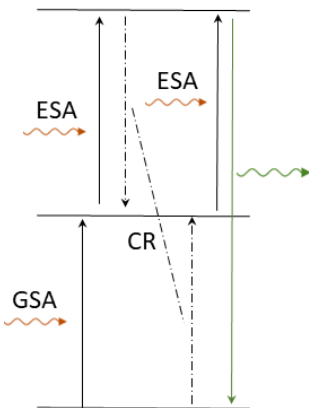


Figure 1.6: PA effect occurs subsequent to resonant ESA and weak GSA, triggering a CR process. During CR, electrons in the second higher excited state relax to an intermediate state, exciting electrons from the ground state to the excited state where the ESA occurs.

### 1.1.4 Other types of UC processes

Other types of less efficient UC processes have also been identified, including second harmonic generation (SHG)<sup>5</sup>, and the two-photon absorption (TPA)<sup>6</sup>, shown in Fig. 1.5. In SHG, the electrons in the ground state are excited to a virtual energy state, and the emitted light has exactly twice the energy of the pumping light. This process does not involve absorption. On the other hand, TPA involves the absorption of two photons, which excite the electrons to a real metastable state. From there, the electrons can relax either to the ground state or to another intermediate state. A summary of the approximate efficiency magnitudes for the different UC processes described in this section is presented in Tab. 1.1.

### 1.1.5 Photon avalanche effect (PA)

Another notable phenomenon associated with UC is the photon avalanche (PA) effect, which was first observed by Chivian et al. in 1979 during their investigation of ESA in  $\text{LaCl}_3$  and  $\text{LaBa}_3$  crystals doped with  $\text{Pr}^{3+}$  [63]. The researchers noticed a significant increase in the emission intensity<sup>7</sup> of Pr ions, accompanied by a decrease in transmission, when the crystals were subjected to laser radiation slightly above a critical intensity [48, 63]. The observed phenomenon was attributed to a CR process that led to an enhanced population of an excited state. As a result, the electrons were capable of absorbing photons from the laser pump and being excited to a higher state, which subsequently emitted the upconverted light. A simplified schematic diagram illustrating the PA effect is shown in Fig. 1.6. The specific mechanism responsible for the initial excitation to the second excited state depicted in the figure was not determined in the original publication of this discovery.

The PA effect introduces a significant non-linearity to UC processes and offers a promising avenue for enhancing energy transfer mechanisms, particularly ESA, thereby leading to improved UC efficiency. In recent developments, the PA effect has been identified as a remarkable feature in the field of imaging techniques, contributing to the advancement of resolution capabilities. Lee et al.'s work demonstrated the potential of the PA effect in achieving an impressive resolution of approximately  $70 \text{ nm}$ , surpassing the resolution limits of previously reported super-resolution systems [25, 43, 45].

## 1.2 Upconverting nanoparticles (UCNPs)

Lanthanide UCNPs exhibit unique non-linear optical properties. They possess a rich  $4f$  electronic configuration within the lanthanide ions ( $\text{Ln}^{3+}$ ), allowing for multi-wavelength emissions ranging from UV to NIR [3]. The well-defined and tunable nature of the  $4f$  electronic transitions in lanthanide UCNPs is a consequence of the shielding provided by the  $5s$  and  $5p$  orbitals. These orbitals effectively protect the  $4f$  transitions from photobleaching, making them resilient to the surrounding environment. In free  $\text{RE}^{3+}$  ions, electric dipole transitions between the  $4f$  states are forbidden. However, when embedded in a solid matrix, the crystal

<sup>5</sup>The SHG was first demonstrated by Franken et al. after the invention of lasers, since the process requires high intensity coherent light [60].

<sup>6</sup>The same occurred for the TPA, which was originally predicted by Göppert-Mayer in 1931, but only experimentally observed 30 years later with the laser invention [62].

<sup>7</sup>In their original study, the authors did not observe upconversion (UC); instead, they observed fluorescence emission originating from an excited state transitioning to another intermediate excited state.

field slightly breaks the degeneracy of the energy levels, enabling  $4f-4f$  transitions to occur [64].

To facilitate upconversion processes, the lanthanide ions must be separated by a certain distance, and in the case of ETU, the energy transfer occurs through phonons in the lattice. Therefore, the host matrix plays a crucial role in maintaining the ideal separation distance between the ions. UCNPs are not simple miniaturizations of their bulk counterparts; their properties are strongly influenced by the surface-to-volume ratio. In bulk crystals, dopant ions can occupy random lattice sites, resulting in a homogeneous system where surface elements have minimal influence. However, in crystalline nanoparticles, dopants are not randomly distributed, and surface ions exert a proportional influence compared to the embedded ions within the lattice [46]. During the synthesis of UCNPs in solution, factors such as the concentration and ionic radii of the reagents, as well as the growing particle size, influence the distribution of ions on the particle surface and in the solution. This leads to a varying density of UCNPs along their radial coordinate [46]. This asymmetry creates a non-homogeneous crystal field, known to influence the emission probability in lanthanides and impart the UCNPs with their unique luminescence properties. However, the surface effect also has a negative impact on UCL, reducing its efficiency as the particle size decreases. This phenomenon is known as surface quenching effect. To mitigate this effect, a common technique is to add an inert shell without RE elements involved in upconversion. Currently, the most efficient UCNPs for UC at approximately  $975\text{ nm}$  excitation are core-shell sodium fluoride particles with hexagonal symmetry. These particles are codoped with Yb as a sensitizer and Tm, Er, or Ho as activators, represented as  $\beta\text{-NaYF}_4\text{:Yb,X@NaYF}_4$ , where  $X = \text{Er, Tm, or Ho}$ . The inert shell typically has the same composition as the host matrix [65]. Fig. 1.7 shows a cuvette containing UCNPs being irradiated by NIR beam and emitting upconverted light in the blue and NIR wavelengths.

### 1.2.1 Upconversion Quantum Yield (QY)

One of the most important parameters in assessing the performance of UCNP compounds is their QY, which quantifies their efficiency in converting low-energy light to higher-energy light. However, evaluating QY presents challenges both in terms of experimental methodologies and data processing and analysis. Unlike fluorescence, the QY of UCNPs is highly dependent on the PD due to the involvement of multiphoton absorption in the upconversion process. This non-linear PD dependence necessitates considering the distortions caused by the excitation beam profile during QY evaluation [1, 49, 66, 67].

Furthermore, at low power densities, the non-linearity of upconversion becomes more prominent, resulting in a significant reduction in QY. The relatively weak upconversion signal requires sensitive and accurate devices that are not readily available commercially. Some research groups have calculated QY through absolute measurements using integrating spheres to collect the upconverted emission from the sample in all directions [68–71]. Others have evaluated QY relative to a fluorescent reference with a known QY [35, 49, 72, 73]. Additionally, the lack of standardized protocols has led to variations in QY terminologies and definitions. For instance, the external QY (eQY) is defined as the ratio of emitted photons to incident photons on the sample. In contrast, the internal QY (iQY) considers the number of absorbed photons instead of incident photons, as shown in Eq. (1.2) [74],



Figure 1.7: A cuvette containing water-dispersed UCNPs doped with Yb and Tm. The sample is irradiated by a NIR laser beam, resulting in a visible blue upconverted emission. Although not visible to the naked eye, the purple hue surrounding the blue emission line represents the NIR emission and scattered light captured by a smartphone camera.

$$\eta_{m \rightarrow j} = \frac{n_{m \rightarrow j}}{n_a}, \quad (1.2)$$

where,  $\eta_{m \rightarrow j}$  represents the iQY for electronic transitions from an energy state  $m$  to a lower state  $j$ ,  $n_{m \rightarrow j}$  is the number of photons emitted through this radiative transition, and  $n_a$  is the number of photons absorbed by the sample.

---

# TIME-RESOLVED AND STEADY-STATES OF THE POPULATION DENSITIES OF THE ENERGY LEVELS INVOLVED IN ETU PROCESSES

---

The ETU process is currently recognized as the most efficient among UC processes. Although, there has been limited theoretical investigation into the PD dependence of UC QY. In 2005, Suyver et al. initially calculated the PD dependence<sup>1</sup> of the population density of energy states involved in UC through energy transfer between a sensitizer and an activator [75]. Building upon this work, Liu et al. extended the concept in 2013 by using rate equations to calculate the PD-dependent iQY for a two-photon UC process. They quantified, for the first time, the PD transition point where the UCL of an ETU2 process transitions from quadratic dependence to linear [1].

This chapter focuses on studying the PD dependence of iQY for a general ETU $_j$  process involving the absorption of  $j$  photons. The transition points that define the shifts between regimes with different orders of non-linearity in the UCL and QY will be introduced. Analytical solutions for the steady states and dynamics of the process are investigated by applying a simplified rate-equations model.

## 2.1 ETU2 model proposed by Liu et al.

It is widely recognized that the UCL intensity,  $L$  [ $W/cm^2$ ], exhibits a non-linear dependence on the PD,  $\rho$  [ $W/cm^2$ ]. This dependence varies from an order  $j$  [-] (*i.e.*,  $\rho^j$ ) at low excitation levels to an order of 1 (*i.e.*,  $\rho$ ) at high excitation PDs for an ETU $_j$  process, where  $j$  photons are involved in the absorption [76]. As a consequence, the iQY,  $\eta$  [-], exhibits a PD dependence order ranging from  $j - 1$  to 0, as the iQY is defined as the ratio of emitted photons to absorbed photons, with absorption being linearly proportional to PDs [71]. Eqs. (2.1) and (2.2) represent the PD dependence of UCL and iQY, respectively, at low excitation PD limits,

$$L_j \propto \rho^j, \quad (2.1)$$

$$\eta_j \propto \rho^{j-1}. \quad (2.2)$$

---

<sup>1</sup>In their paper, entitled "Anomalous power dependence of sensitized upconversion luminescence", Suyver et al. refer to the effect as *power dependence* instead of PD dependence.

The PD dependence of the iQY arises from the interplay between two main competing mechanisms responsible for the depopulation of the excited states in the activators: the ET process and linear decay [1, 75]. Liu et al.'s model is derived from rate equations and considers a system consisting of two ions, with the first ion having two levels (ground state  $|a\rangle$  and excited state  $|b\rangle$ ) for the sensitizer, and the second ion having three levels (ground state  $|0\rangle$  and two excited states  $|1\rangle$  and  $|2\rangle$ ) for the activator, as depicted in Fig. 2.1.

The rate equations describing this model are presented in Eqs. (2.3),

$$\begin{aligned}\dot{N}_b &= \alpha\rho N_a - N_b R_b, \\ \dot{N}_1 &= W_0 N_0 N_b - W_1 N_1 N_b - N_1 R_1, \\ \dot{N}_2 &= W_1 N_1 N_b - N_2 R_2,\end{aligned}\quad (2.3)$$

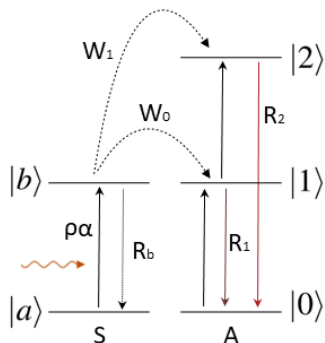


Figure 2.1: Simplified energy level diagram illustrating a two-ion system with a coupled two- and three-level configuration. The absorption process takes place in the S ions, where electrons are excited from the state  $|a\rangle$  to  $|b\rangle$  upon irradiation with a power density  $\rho$ . The parameter  $\alpha$  denotes the S absorption cross-section, which represents the probability of photon absorption. ET occurs at rates  $W_0$  and  $W_1$  to the ground state  $|0\rangle$  and excited state  $|1\rangle$ , respectively. The decay rates from the excited states to the ground states are indicated by the  $R$  constants.

where  $N$  [ $cm^{-3}$ ] represents the population density of the energy states, which are denoted by indices such as  $a, b, 0, 1$ . The dot notation,  $\dot{N}$  [ $cm^{-3}s^{-1}$ ] signifies the rate of change of the population density.  $\alpha$  [ $cm^2J^{-1}$ ] corresponds to the sensitizer's cross-sectional area, given by the ratio of the absorption cross section,  $\sigma$  [ $cm^2$ ], to the product of Planck's constant,  $h$  [ $J_s$ ], and the resonant frequency,  $\nu$  [ $Hz$ ], associated with associated with the energy difference between states  $|a\rangle$  and  $|b\rangle$ , as shown in Eq. (2.4). The constant  $W$  [ $s^{-1}$ ] represent the energy transfer rates for an electronic transition from an energy state corresponding to its index to another state immediately above it. The constant  $R$  [ $s^{-1}$ ] is the linear decay rate from the energy state corresponding to its index to ground state, accounting for both radiative and non-radiative processes,

$$\alpha = \frac{\sigma}{h\nu}. \quad (2.4)$$

Consequently, PD-dependent iQY is determined by solving the rate equations to obtain the steady states<sup>2</sup>. The equation representing the PD dependence of the iQY is given by Eq. (2.5),

$$\eta_2 = \eta_s \frac{\rho}{\rho + \rho_b}, \quad (2.5)$$

where  $\rho_b$  [ $W/cm^2$ ] represents the PD balancing point at which the iQY is exactly half of the its maximum saturation value given by the constant  $\eta_s$  [–] at high PDs, given by Eq. (2.6),

$$\eta_s = \frac{W_0 N_0 R_2^{rad}}{R_b R_2}, \quad (2.6)$$

where the symbol  $R_2^{rad}$  [ $s^{-1}$ ] represents the radiative decay rate from the state  $|2\rangle$  to the ground state  $|0\rangle$ . The constant  $\rho_b$  also defines the transition point of the transition from non-linear to linear regimes of UCL, and is given by Eq. (2.7),

$$\rho_b = \frac{R_1 R_b}{W_1 \alpha N_a}. \quad (2.7)$$

This simplified model is applicable to UCNPs that exhibit single-wavelength emission in an ETU2 process. It does not take into consideration energy transfers to higher energy levels beyond the state  $|2\rangle$ . Liu et al. also made the approximation that the population density  $N_a$  remains constant at low excitation PDs, specifically when  $\rho \ll R_b/\alpha^3$ .

<sup>2</sup>The steady state is reached when the population densities of the energy states have reached equilibrium, indicated by  $\dot{N} = 0$ .

<sup>3</sup>In the case of Yb as a sensitizer with a typical absorption cross-section of  $\sigma \approx 10^{-20}$ , and considering a range of values for  $R_b$  reported in the literature [77, 78], the condition for low power densities is satisfied when  $\rho \ll 5000 W/cm^2$ .

Additionally, the depopulation of  $N_b$  due to ET is considered negligible compared to the spontaneous emission rate.

## 2.2 ETU processes of higher order

In higher order ETU processes, the contribution of  $W_2$  cannot be neglected, while still satisfying the conditions described by Eqs. (2.1) and (2.2) for PD dependence. As a result, a general model can be developed to describe a system with an arbitrary number of excited energy levels,  $m$ , for the activator. Each excited level  $|j\rangle$  is exclusively populated through electronic transitions from the energy level immediately below it,  $|j-1\rangle$ , via ET. Depopulation of each excited level can occur through either linear decay to the ground state of the activator,  $|0\rangle$ , or through an electronic transition to the next excited state,  $|j+1\rangle$ , facilitated by an ET process. Fig. 2.2 depicts a simplified energy level diagram illustrating this process for the  $j^{\text{th}}$  excited energy state.

The set rate equations that describes this general model is given by Eqs. (2.8),

$$\begin{aligned}
 N_S &= N_a + N_b, \\
 \dot{N}_b &= \alpha\rho N_a - N_b R_b, \\
 N_A &= \sum_{i=0}^m N_i, \\
 &\vdots \\
 \dot{N}_j &= W_{j-1} N_{j-1} N_b - W_j N_j N_b - N_j R_j, \\
 &\vdots
 \end{aligned} \tag{2.8}$$

where  $j \in \{1, 2, \dots, m\}$ .

### 2.2.1 Population densities of the energy states and the transition PD points

At the steady state, the population densities of the excited states are given by Eqs. (2.9) and (2.10),

$$N_b = \frac{\alpha\rho N_S}{R_b + \alpha\rho}, \tag{2.9}$$

$$N_j = \frac{W_{j-1} N_{j-1} N_b}{W_j N_b + R_j}. \tag{2.10}$$

The solution provided in Eq. (2.10) is applicable to any excited state below the state  $|j\rangle$ . Therefore, the general solution, as given in Eq. (2.11), is obtained by replacing the solution for the population density of the state  $|b\rangle$  and recursively substituting the solutions for the lower states into Eq. (2.10),

$$N_j = \frac{W_0 N_0 \rho^j}{W_j} \prod_{i=1}^j \frac{1}{\rho + \rho'_i}, \tag{2.11}$$

where  $\rho'_i$  [ $W/cm^2$ ] represents the transition PD point given by Eq. (2.12),

$$\rho'_i = \frac{R_i(R_b + \alpha\rho)}{W_i \alpha N_S}. \tag{2.12}$$

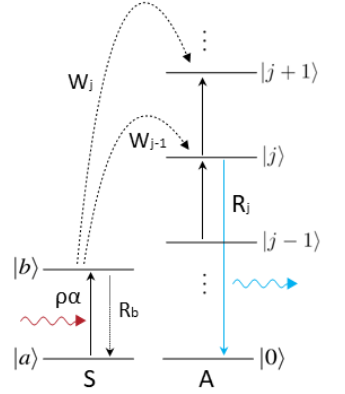


Figure 2.2: Simplified energy level diagram illustrating a system consisting of two ions with a coupled two-level and  $m$ -level structure. In this system, an arbitrary excited state  $|j\rangle$  is populated through ET from the sensitizer, which pumps electrons from the  $|j-1\rangle$  state. The  $|j\rangle$  state is depopulated through ET, exciting electrons to the next excited state  $|j+1\rangle$ , and through a linear decay process that leads to the ground state  $|0\rangle$ .

The constant  $\rho'_i$  is PD dependent, however, for the limit where  $\rho \ll R_b/\alpha$ , which is valid for most applications,  $\rho'_i$  converges to the constant  $\rho_i$ , Eq. (2.13),

$$\rho_i = \frac{R_i R_b}{W_i \alpha N_S}. \quad (2.13)$$

The transition PD point quantifies the threshold where the UCL exhibits a transition between different orders of non-linearity. Currently, subjective terms such as "low PDs" and "high PDs" are used to differentiate between the non-linear and linear regimes [1, 21, 49, 79]. However, this approach is inaccurate because different samples and emission wavelengths undergo transitions at different points. Moreover, higher order ETU processes (*e.g.*, ETU3, ETU4) have multiple transition points, which are not accounted for in subjective descriptions.

### 2.2.2 The photon flux and upconversion luminescence (UCL)

When electrons undergo radiative decay from the state  $|j\rangle$ , photons are emitted. The resulting photon flux, denoted as  $\phi_j$  [ $cm^{-3}s^{-1}$ ], is directly proportional to the population density of the state  $|j\rangle$  by a constant factor  $R_j^{rad}$ . This constant factor represents the radiative decay rate from the respective energy state, as shown in Eq. (2.14),

$$\phi_j = \phi_{j_o} \rho^j \prod_{i=1}^j \frac{1}{\rho + \rho'_i}, \quad (2.14)$$

where  $\phi_{j_o}$  [ $cm^{-3}s^{-1}$ ] represents the saturation photon flux, defined by the Eq. (2.15),

$$\phi_{j_o} = \frac{W_0 N_0 R_j^{rad}}{W_j}. \quad (2.15)$$

Similarly, the UCL,  $L_j$  [ $W/cm^3$ ], can be obtained by multiplying the photon flux by the energy of each photon, as described in Eq. (2.16),

$$L_j = \phi_j h \nu_j, \quad (2.16)$$

where the constant  $\nu_j$  [ $Hz$ ] represents the frequency of the emitted photons.

### 2.2.3 Internal Quantum Yield (iQY)

The UC iQY is calculated by dividing the emission photon flux by the absorption photon flux, as defined in Eq. (1.2). The absorption photon flux can be expressed as the product of  $\alpha$ ,  $N_a$ , and  $\rho$ . Therefore, the iQY for the energy state  $|j\rangle$  is determined by Eq. (4.5),

$$\eta_j = \frac{\phi_{j_o}}{\alpha N_a} \rho^{j-1} \prod_{i=1}^j \frac{1}{\rho + \rho'_i}. \quad (2.17)$$

### 2.2.4 The PD limits

The slope of the UCL versus the PD plot, represented in a double logarithmic scale, is a crucial parameter to evaluate as it relates to the number of absorbed photons during the ETU process. The measurement of the slope, denoted as  $\kappa$  [-], at low power densities provides the order of the ETU process. The expression for obtaining  $\kappa$  is given by Eq. (2.19),

$$\kappa_j = \frac{d}{d \ln(\rho)} \ln(L_j). \quad (2.18)$$

Thus, by solving the Eq. (2.18), the expression for  $\kappa$  as given in Eq. (2.19) is obtained,

$$\kappa_j = j - \sum_{i=1}^j \frac{\rho(1 + \varphi_i)}{\rho(1 + \varphi_i) + \rho_i}, \quad (2.19)$$

where  $\varphi_i$  is represented by Eq. (2.20),

$$\varphi_i = \frac{R_i}{W_i N_S}. \quad (2.20)$$

### Low PD limit

Applying the limit to the UCL as the excitation PD tends to 0, i.e.,  $\rho \rightarrow 0$ , or equivalently  $\rho \ll \rho_i$ , the slope  $\kappa_j$  tends to the index  $j$  of the excited energy state. In terms of UCL, the result of the low PD limit is given by Eq. (2.21), which is consistent with experimental observations [1, 67, 75, 76] and confirmed in Paper I.

$$\lim_{\rho \rightarrow 0} L_j \propto \rho^j. \quad (2.21)$$

As a consequence, applying the limit to the iQY gives a result of order  $j - 1$ , as shown in Eq. (2.22),

$$\lim_{\rho \rightarrow 0} \eta_j \propto \rho^{j-1}. \quad (2.22)$$

### High PD limits

At high PD limits, where  $\rho \rightarrow \infty$  or at least  $\rho \gg \rho_i$  for all transition points  $\rho_i$ , the slope  $\kappa_j$  tends to 0, indicating that the UCL reaches a saturation point, as shown in Eq. (2.23),

$$\lim_{\rho \rightarrow \infty} L_j \propto L_s, \quad (2.23)$$

where, the constant  $L_s$  [ $W/cm^3$ ] characterises the luminescence saturation. The saturation is a consequence of the the equilibrium between the population and depopulation mechanisms of the energy level, which depend on the population density of the sensitizer's excited state  $|b\rangle$ . Consequently, the iQY tends to 0 at this limit. Experimental measurements of Er-Yb codoped micro particles have observed this saturation at excitation PDs above  $30 W/cm^2$ [80]. However, anomalous power dependence has been observed in other upconverting systems, where the UCL does not exhibit saturation even at PDs on the order of  $10^3 W/cm^2$  Paper I,  $10^4 W/cm^2$ [75], and  $10^5 W/cm^2$ [67]. These experimental results indicate that the minimum slope at high PDs is 1, indicating linearity in the UCL and saturation of the iQY.

According to the simplified model presented here, the anomalous behaviour observed in certain upconverting systems indicates that one of the transition points  $\rho_i$  is significantly larger than the excitation PDs used in the experiments. This can be expressed by the inequality shown in Eq. (2.24),

$$\rho_i \gg \rho(1 + \varphi_k). \quad (2.24)$$

### 2.2.5 A detailed comparison with the model proposed by Liu et al.

Applying the general solution to an ETU2 process, the iQY can be expressed by Eq. (2.25)<sup>4</sup>,

$$\eta_2 = \frac{\phi_{2o}}{\alpha N_a} \frac{\rho}{(\rho + \rho_1)(\rho + \rho_2)}, \quad (2.25)$$

where  $\rho_1$  and  $\rho_2$  represent the transition points of the ETU2 luminescence with respect to the excitation PD. The solution suggests that for PDs below both transition points, the UCL exhibits predominantly quadratic behaviour. However, between the two transition points, the UCL becomes linear and saturates above both transition PD points. It should be noted that in practical cases, such as in bulk upconverting particles, the saturation of the UCL is typically not observed, suggesting that one of the two transition PD points<sup>5</sup> is above the experimental ranges of PDs.

When comparing the results to the model proposed by Liu et al. [1], it is observed that the transition PD point related to the first excited energy state |1), denoted as  $\rho_1$ , is equivalent to the value of  $\rho_b$  found in their study. However, in Liu et al.'s model, they neglected the ET coefficient  $W_2$ , which is responsible for exciting the activator's electrons to the state |3)<sup>6</sup>. By disregarding  $W_2$ , the slope  $\kappa_2$  at high PDs was found to have a minimum value of 1, consistent with the anomalous PD dependence observed in various UCNPs. This approach is valid for systems where no UCL arises from an ETU3 process. However, many UCNPs exhibit a mixed emission spectrum involving both ETU2 and higher processes. For these systems, it is crucial not to neglect  $W_2$ , therefore both  $\rho_1$  and  $\rho_2$  are present in the solution. Although it may be presumed that  $\rho_1$  is small and the PDs in reported measurements for ETU2 never reached  $\rho_2$ , observations of downconversion luminescence indicate that the UCL from the first excited state |1) exhibits linear behaviour throughout the observed range. On the other hand, the UCL from the second state |2) transitions from quadratic to linear behaviour. This implies that  $\rho_2$  is indeed reached, while  $\rho_1$  represents the larger transition PD point. Further discussion and analysis are presented in Paper III.

### 2.2.6 A numerical example

A numerical approach was employed to simulate the ET process in a sodium fluoride UCNP system codoped with 20% Yb<sup>3+</sup> and 1% Tm<sup>3+</sup> ions ( $\beta$ -NaYF<sub>4</sub>:20%Yb<sup>3+</sup>,1%Tm<sup>3+</sup>). The selection of the concentration and structure was based on typical highly efficient UCNPs[81, 82]. The total electronic population densities of the sensitizers and activators were calculated based on the given concentration, assuming a hexagonal unit cell with typical lattice parameters:  $a = 5.91 \text{ \AA}$  and  $c = 3.53 \text{ \AA}$ [83]. UC-NPs with this composition are known to exhibit light emission at multiple wavelengths, involving processes ranging from ETU1 to ETU4. The absorption cross-section and decay times of the excited states of the Tm<sup>3+</sup> ions were obtained from Villanueva-Delgado et al.[77]. The ET constant  $W_0$  was taken from the work of Liu et al.[21], while the other ET constants were calculated based on the transition PD points obtained by fitting the experimental UCL data to the general model. The determined transition PD values are approximately  $\rho_1 = 20 \text{ kW/cm}^2$ ,  $\rho_2 = 40 \text{ W/cm}^2$ , and  $\rho_3 = 190 \text{ W/cm}^2$ . The constants used in the simulation, along with their respective sources, are summarized in Tab. 2.1.

<sup>4</sup>The approximation  $\rho \ll R_b/\alpha$  was taken into account.

<sup>5</sup>One of the two because  $\rho_1$  is not necessarily lower than  $\rho_2$ .

<sup>6</sup>For sanity test, one can replace  $W_2$  by 0 in the Eq. (2.25) and verify that it reduces to the iQY equation proposed by Liu et al., Eq. (2.5).

Table 2.1: Simulation UC constants and their respective source.  $N_S$  and  $N_A$  represent the total electronic population densities of  $\text{Yb}^{3+}$  and  $\text{Tm}^{3+}$ , respectively.  $\sigma$  denotes a typical absorption cross-section for the electronic transition from the ground state to the excited state of  $\text{Yb}^{3+}$  under 976 nm excitation light.  $\tau_j$  and  $W_j$  correspond to the decay time and ET rate for the excited state  $|j\rangle$ , where  $j \in \{1, 2, 3, 4\}$ .

Quantity		Source
$N_S$	$1.87 \cdot 10^{21} \text{ cm}^{-3}$	Calculated
$N_A$	$9.36 \cdot 10^{19} \text{ cm}^{-3}$	Calculated
$\sigma$	$1 \cdot 10^{-21} \text{ cm}^{-2}$	[77]
$\tau_b$	$2.3 \cdot 10^{-3} \text{ s}$	[77]
$\tau_1$	$12 \cdot 10^{-3} \text{ s}$	[77]
$\tau_2$	$2 \cdot 10^{-3} \text{ s}$	[77]
$\tau_3$	$675 \cdot 10^{-6} \text{ s}$	[77]
$\tau_4$	$500 \cdot 10^{-6} \text{ s}$	[77]
$W_0$	$1.6 \cdot 10^{-18} \text{ cm}^{-3} \text{ s}^{-1}$	[21]
$W_1$	$1.9 \cdot 10^{-19} \text{ cm}^{-3} \text{ s}^{-1}$	Calculated
$W_2$	$5.9 \cdot 10^{-16} \text{ cm}^{-3} \text{ s}^{-1}$	Calculated
$W_3$	$3.7 \cdot 10^{-16} \text{ cm}^{-3} \text{ s}^{-1}$	Calculated
$W_4$	$\approx 0 \text{ cm}^{-3} \text{ s}^{-1}$	ETU5 neglected

Using the numerical values of the constants listed in Tab. 2.1, the Eqs. (2.9) and (2.10) were implemented in a computational script using the Python programming language. This script was used to calculate the population density of the energy levels in their steady states. The population density of the activator's ground state  $|0\rangle$  was assumed to be constant and equal to the total electronic population density of the activator  $N_A$  across the entire PD range studied, which ranged from  $10^{-3}$  to  $10^3 \text{ W/cm}^2$ . The results are shown in Fig. 2.3 using a double logarithmic representation.

At PDs below  $\rho_2$ , the slope  $\kappa$  is equal to the index of the excited state, reflecting the number of absorbed photons involved in the ETU process. As the PD increases above  $\rho_2$  and  $\rho_3$ ,  $\kappa$  transitions from its maximum value to its minimum value of 1 for states  $|2\rangle$  and  $|3\rangle$ , and to 2 for state  $|4\rangle$ . The minimum slope of state  $|4\rangle$  does not reduce to 1 due to the approximation  $W_4 \approx 0$ , which results in an infinite value of  $\rho_{b,4}$ . Therefore, the minimum value of  $\kappa$  for state  $|4\rangle$  is 2.

The iQYs, calculated using equation Eq. (1.2) and normalised by their maximum value  $\eta_o$ , are depicted in Fig. 2.4. In the low PD limit, the slopes of the iQY curves in a double logarithmic representation are equal to the index of the excited state minus 1, as the number of absorbed photons exhibits a linear dependence on PD. At high PDs, the iQY curves reach a saturation point represented by the constant  $\eta_{i,o}$  for states  $|2\rangle$  and  $|3\rangle$ . In the case of state  $|4\rangle$ , the slope reaches its minimum value of 1 at high PDs.

One limitation of this model arises in the high PD limit due to the assumption of a constant population density  $N_0$  for the ground state. In Fig. 2.3, it can be observed that the population density of state  $|1\rangle$  becomes very close to that of the ground state  $|0\rangle$  at extremely high PDs, which occurs above  $10^3 \text{ W/cm}^2$  for the constants used in this simulation.

### 2.3 Dynamics

Applications in biophotonics involving UCNP often require the use of laser beams for nanoparticle excitation. However, due to safety considerations, living tissues have an average exposure limit of a few hundred  $m\text{W/cm}^2$  [84, 85], which is significantly below the maximum iQY satu-

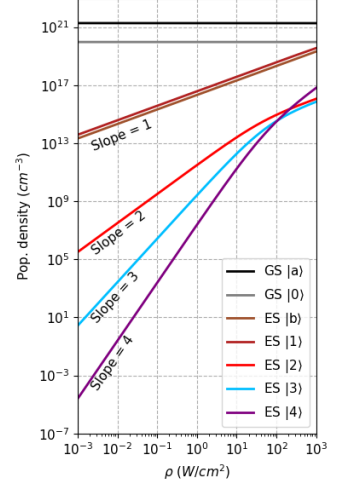


Figure 2.3: Population densities of the energy states of the  $\text{Yb}^{3+}$  and  $\text{Tm}^{3+}$  ions are shown in the plot, covering a PD range from  $10^{-3}$  to  $10^3 \text{ W/cm}^2$ . The plot is displayed on a double logarithmic scale. The highlighted slopes  $\kappa$  represent the behaviour of the population densities in the low PD limit. The population density of the ground state  $|0\rangle$  of the activator ions, denoted as  $N_0$ , is assumed to be constant and equal to  $N_A$ .

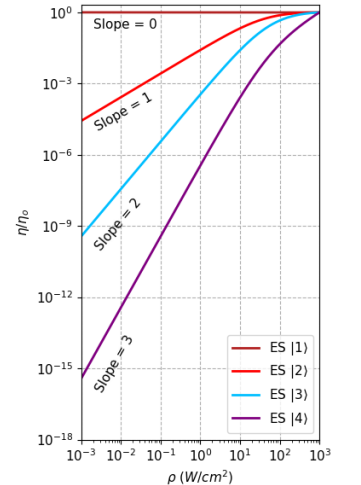


Figure 2.4: Normalised iQY for the UC of the activator's excited states. The slopes of the iQY curves versus PD are highlighted in the graph, which is plotted in a double logarithmic scale.

ration level  $\eta_o$  of UCNPs. When photons are absorbed by tissue, they locally increase the temperature, which is primarily dissipated through the bloodstream [86]. CW excitation delivers photons continuously to the tissue, while pulsed laser excitation applies light for a short duration followed by a dark period, allowing the tissue to cool down. By increasing the excitation power while reducing the laser-on time, the average delivered power can be kept constant. The average excitation power  $P_{avg}$  for a pulsed laser, as a function of the peak power  $P_{peak}$ , on-time duration  $\Delta t$ , and pulse period  $T$ , is given by Eq. (2.26),

$$P_{avg} = P_{peak} \frac{\Delta t}{T}, \quad (2.26)$$

where the ratio of  $\Delta t$  to  $T$  represents the duty cycle, which is commonly expressed as a percentage. Pulsed excitation offers advantages due to the unique non-linear characteristics of UC. For instance, when using pulsed excitation with a peak power  $P_{peak}$  that is twice as high as the average power  $P_{avg}$  and a duty cycle of 50%, the average power remains constant. However, in the case of an ETU3 process, the UCL should increase by a factor of eight ( $2^3$ ) during the on-time duration  $\Delta t$ . This holds true if  $\Delta t$  is sufficiently long to allow the excited levels to populate and reach their steady state.

Therefore, gaining an understanding of the mechanisms involved in populating and depopulating the energy levels in UC processes is crucial for various applications in biophotonics, including PDT and optogenetics. Additionally, this understanding is necessary for obtaining highly accurate measurements of the iQY.

### 2.3.1 Numerical approach

Obtaining analytical solutions for the rate equations in the time domain can be complex. Therefore, a numerical procedure based on the Euler method was implemented to calculate the rise and decay times of the energy states in an UC process. The Euler method involves discretising the time domain into smaller intervals, denoted as  $\delta t$ . Using smaller intervals leads to improved precision and accuracy of the results [87]. By applying the mathematical definition of a derivative, the following relation for a general state  $|j\rangle$  can be derived, as shown in Eq. (2.27):

$$\lim_{\delta t \rightarrow 0} N_j(t + \delta t) = \lim_{\delta t \rightarrow 0} \left[ \delta t \frac{dN_j(t)}{dt} + N_j(t) \right], \quad (2.27)$$

where  $N_j$  represents the population density of state  $|j\rangle$  and  $\delta t$  is the time interval. The rate  $\frac{dN_j}{dt}$  is given by the set of rate equations defined by Eq. (2.8). By knowing the initial state, i.e., the population density of the energy states at  $t = 0$ , the subsequent values of  $N_j$  after intervals of  $\delta t$  can be determined. Thus, this relation allows for the numerical evaluation of the rate of change of the population density over time.

Using the aforementioned definition, the model was implemented in a Python script to simulate the behaviour of the sodium-fluoride UCNP system, which is co-doped with 20%  $\text{Yb}^{3+}$  and 1% of  $\text{Tm}^{3+}$  ( $\beta\text{-NaYF}_4:20\%\text{Yb}^{3+},1\%\text{Tm}^{3+}$ ), as described in the previous subsection. The simulation utilized the constants listed in Tab. 2.1. A laser pulse with a power of  $500 \text{ mW/cm}^2$  and an average frequency of  $5 \text{ Hz}$ , with a duty cycle of 50%, was prepared. The time interval  $\delta t$  was set to  $1 \cdot 10^{-5} \text{ s}$ . By iterating through the simulation, the population density of the energy states was calculated at each time step. The resulting population density values were then plotted against time on a logarithmic scale along the simulated laser pulse, as illustrated in Fig. 2.5.

The results reveal that the population densities of the excited states are at least three orders of magnitude lower than those of the ground

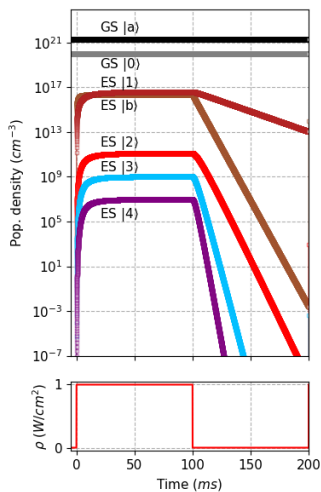


Figure 2.5: Population density of the energy states, represented in the logarithmic scale of the y-axis, is shown in the top plot. The bottom plot displays the pulse profile of the simulated excitation. Despite the fact that all energy states reach their steady state within a time interval of less than 100 ms, the excited state |1> exhibits a significant population remaining within the same time frame after the laser excitation is switched off.

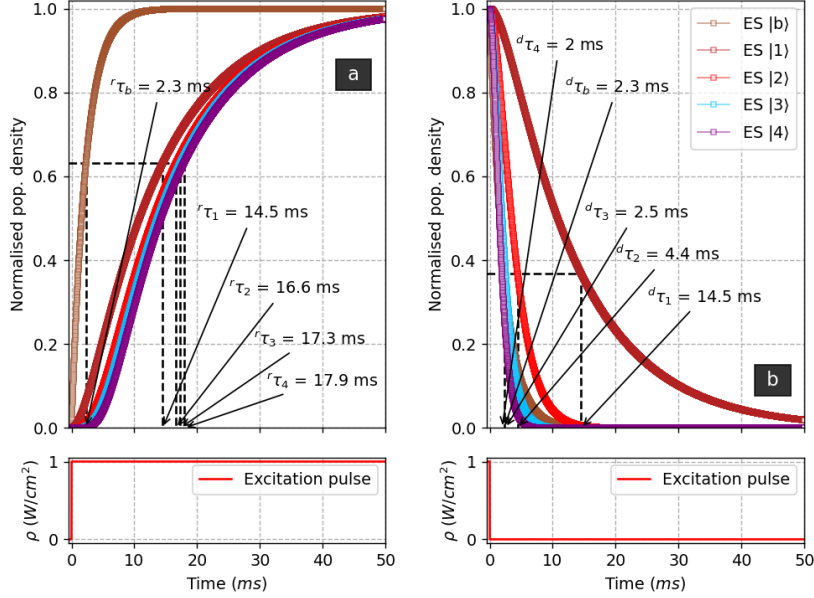


Figure 2.6: Normalised population densities of the excited states of the sensitizer and activator are depicted in the left and right plots, respectively, representing the first 50 ms of the rise and decay processes. The laser pulse profiles are shown at the bottom of the plots. Arrows indicate the time it takes for the population densities to reach 63% of the steady state level during the rise process and to decay to 37% of the steady state level during the decay process.

states for both the sensitizer and activator. Additionally, the absolute value of the slope of the decay curve for the excited states increases with higher energy states, as observed in the steady state results for the logarithmic population densities versus the logarithmic PDs.

Fig. 2.6 illustrates the population densities of the excited states, normalised by their maximum values at steady state. In Fig. 2.6.a, the population densities are shown during the first 50 ms of the rise process, while Fig. 2.6.b displays the first 50 ms of the decay process. The pulsed laser profile is depicted at the bottom of each plot.

The rise time  $r_\tau$  and decay time  $d_\tau$ , shown in Fig. 2.6, were determined based on the ratio of population densities relative to their saturation level. In the decay of a two-level system pumped by a resonant photon, the depopulation of either state can be described by a simple exponential equation,  $e^{-t/\tau}$ . When the time  $t$  is equal to the lifetime  $\tau$ , the population of the state reaches approximately 37% of the total electronic population. Similarly, the population of the state being populated accounts for the remaining 63%. This relationship holds true for the sensitizer's energy states, resulting in equal rise and decay times. However, for the activator's excited states, the mechanisms of population and depopulation depend on the population densities of the energy state  $|b\rangle$  and the immediately lower energy state from which the electrons are excited,  $|j-1\rangle$ , as given by the product in Eq. (2.28),

$$W_{j-1}N_{j-1}N_b. \quad (2.28)$$

Hence, the use of a simple exponential equation is inadequate for determining the rise and decay times of these energy states. This is evident from the shapes of the curves in Fig. 2.6. The population density of energy state  $|b\rangle$  exhibits a decreasing slope during the populating process,

Table 2.2: Rise and decay times for each of the excited energy levels are compared to their respective natural lifetimes, which were obtained through lifetime measurements at the tail of the decay curves by Villanueva-Delgado et al.[77].

Energy state	Natural lifetime $\tau$	Rise time ${}^r\tau$	Decay time ${}^d\tau$
$ b\rangle$	$2.3 \text{ ms}$	$\sim 2.3 \text{ ms}$	$\sim 2.3 \text{ ms}$
$ 1\rangle$	$12 \text{ ms}$	$\sim 14.5 \text{ ms}$	$\sim 14.5 \text{ ms}$
$ 2\rangle$	$2 \text{ ms}$	$\sim 17 \text{ ms}$	$\sim 4.4 \text{ ms}$
$ 3\rangle$	$675 \mu\text{s}$	$\sim 17 \text{ ms}$	$\sim 2.5 \text{ ms}$
$ 4\rangle$	$500 \mu\text{s}$	$\sim 18 \text{ ms}$	$\sim 2 \text{ ms}$

while the population densities of the remaining energy states initially increase with time before eventually decreasing towards their saturation level. Due to the lack of an analytical equation that accurately describes the rise and decay curves, the rise and decay times were defined as the points where the population densities reached 63% and 37% of their saturation level, respectively. The obtained results are visually depicted in Fig. 2.6 and compared to the decay times used as input in the simulation, as shown in Tab. 2.2.

During the populating process, the rise curves of the activator's excited states are strongly influenced by the rise curve of state  $|1\rangle$ . An excited state  $|j\rangle$  of the activator only reaches the saturation level when the energy state immediately below it,  $|j-1\rangle$ , and the energy state  $|b\rangle$  are in their steady states. This correlation arises due to the ET process described by the product in Eq. (2.28). As the excited state  $|b\rangle$  reaches its steady state before the excited state  $|1\rangle$ , the latter becomes the limiting factor for the higher excited states to reach saturation, hence the strong correlation with excited state  $|1\rangle$ . On the other hand, during the decay process, the activator's excited states can still be populated through ET while the energy state  $|b\rangle$  is relaxing, even in the absence of excitation light. The activator's excited states will only exhibit relaxation when the product in Eq. (2.28) becomes zero, which can be achieved by either one of the states involved becoming zero. Since  $N_b$  decays faster than  $N_1$ , the energy states above  $|1\rangle$  show a strong correlation with the energy state  $|b\rangle$  instead of state  $|1\rangle$ .

Therefore, the ET term explained by Eq. (2.28) accounts for the difference between the rise and decay times of the energy states above  $|1\rangle$ . In contrast, the rise and decay of state  $|1\rangle$  are the same because this state primarily depends on the population of the ground state, which remains relatively constant for the applied excitation PD.

## 2.4 Summary

In summary, this chapter presents a comprehensive analytical model to describe the PD dependence of UC and QY in ETU processes. The model is based on the concept of transition PD points and iQY saturation, providing a framework for the characterisation of upconverting materials. By utilizing the steady-state solutions provided by the model, one can effectively compensate for the influence of the excitation beam profile on iQY, thereby eliminating its impact on the final results to obtain the UC efficiency as an intrinsic material characteristic. The challenges associated with QY characterisation of UCNPs, including the limited availability of commercially viable equipment capable of capturing all pertinent QY parameters, will be further explored in the subsequent chapter.

The numerical approach employed in this study provides valuable insights into the disparities between rise and decay times. These findings hold significant importance for applications involving pulsed laser excitation of UCNPs in living tissues. Conventionally, the pulse duration is matched with the emission wavelength's lifetime. However, the results presented in this chapter demonstrate the inaccuracy of this approach, as the limited lifetime interval fails to ensure full population of excited states, given the considerably shorter decay times compared to the corresponding rise times.



---

# A SEMI-RELATIVE QUANTUM YIELD SYSTEM

---

Despite significant efforts to enhance the efficiency of UCL, evaluating the QY of UCNPs experimentally remains a challenging task due to several factors that affect the measurement. At low PDs, the UCL signal is relatively weak, and its non-linearity becomes more pronounced. Accurate beam profile compensation is required to address the strong dependence of QY on excitation PD. Additionally, power losses caused by scattering pose challenges, particularly for powder samples and colloidal samples with particles suspended in water. Water itself exhibits high absorption in a wavelength range that overlaps with the absorption of  $\text{Yb}^{3+}$ , which is the most commonly used sensitizer for UCNPs. Furthermore, temperature exerts opposing effects on small and large UCNPs, with UCL being enhanced at higher temperatures for particles smaller than 20-30 *nm*, while being quenched for larger particles [88]. Currently, there is no commercially available system that comprehensively addresses all of these critical parameters and provides accurate QY evaluations for UCNPs across a wide dynamic range of excitation PDs, spanning from the non-linear to the linear range. The typical QY evaluation involves using two separate setups: an absorption spectrometer and a luminescence spectrometer. For luminescence measurements, two distinct approaches are recommended, as per standard protocols, which are explained below [89].

## 3.1 Absolute QY evaluation

Absolute measurements have been the most commonly used technique to measure the resulting UCL of UCNPs [49, 89]. Referred to as "absolute QY measurement" or simply "absolute QY", this technique involves collecting the emitted light in all directions from a transparent sample positioned at the centre of an integrating sphere, combined with a commercial fluorometer [70]. In recent years, the importance of this method has grown as standalone integrating spheres have become commercially available, eliminating the need for a standard sample with a known QY as a reference [89]. Despite this advantage, the efficient reflections inside the sphere make it impossible to accurately assess the PD of the excitation light reaching the sample.

## 3.2 Relative QY evaluation

Another method for determining the UC efficiency of UCNPs is the relative method, which involves comparing the UCL of a sample to a reference

sample with similar optical properties, and a known QY, measured under identical conditions [89]. Typically, fluorescent dyes are used as standard samples, although they have limitations such as decreased efficiency over time and susceptibility to photo-bleaching, necessitating dark and refrigerated storage. This requirement leads to the need for freshly prepared standard samples for each characterisation. Relative measurements rely on fluorometers and have been extensively employed to characterise the QY of fluorescent materials. Unlike absolute measurements, only a fraction of the emitted light within a small solid angle of detection is collected in relative measurements. Although this technique is more complex to implement, it offers greater control over the PD across the excitation beam and allows for easy assessment. A detailed explanation and comparison of these methods are presented in a protocol reported by Würth et al. [89].

### 3.3 A semi-relative multi-characterisation setup

Given the critical importance of controlling and characterising the excitation beam profile, a QY system was initially developed in the laboratory based on a previously reported relative QY setup for UCNPs by [49]. The authors followed the protocol for QY characterisation of transparent samples reported by Würth et al., but they incorporated a CCD camera at a  $90^\circ$  angle from the excitation path. A beamsplitter was carefully positioned equidistant from the sample centre and the camera, enabling the measurement of the excitation beam profile in addition to the UCL and transmission, which are essential for computing the QY of UCNPs. In their study, the authors experimentally demonstrated the significance of beam profile compensation by comparing QY results with non-compensated ones for the 804 *nm* emission wavelength of a Yb-Tm-codoped UCNP [49]. This paved the way for exploring the QY of specific ET processes in UCNPs as an intrinsic characteristic of the compound, rather than simply the UCL efficiency of the sample.

Therefore, a semi-relative multi-characterisation QY setup was designed to integrate other important characterisation functions into their system, addressing the following key improvement points:

- (i) Expanded dynamic range of excitation PDs to allow exploration of both the non-linear and linear regimes of UCL;
- (ii) Multi-variable characterisation, including absorption, scattering, and emission spectra, to compensate for their influence on UCL;
- (iii) Speckle-free excitation beam profile;
- (iv) High signal-to-noise ratio (SNR) in the low PD range;
- (v) Fine resolution step size of laser excitation power to discern subtle features and enhance understanding of the UCL process;
- (vi) Fully automated and well-controlled experimental setup for consistent excitation and acquisition of transmission and emission under the same conditions at various PDs;
- (vii) Simultaneous or individual characterisation of multiple emission wavelengths for different excitation PDs;
- (viii) Simultaneous transmission measurements of the UCNP sample and a blank compound as a reference to determine the absorbed power by the UCNPs alone;
- (ix) Simultaneous measurement of UCL and emission spectra at different excitation PDs;

- (x) Time-domain measurements of UCL to study the dynamics of UC processes;
- (xi) Reduced reliance on a reference dye by implementing stable setup calibration, performed only when necessary.

### 3.3.1 The system

Initially, a preliminary version of the QY system was implemented, incorporating the enhancements outlined in points (i) to (vi), as described in detail in Paper II. Subsequently, a second iteration of the system was developed, integrating additional improvements as specified in points (vii) to (xi). To protect the engineering aspects of the speckle-free excitation beam shaping, a patent was also published. This advancement is crucial for enabling the characterisation of materials exhibiting non-linear responses to the excitation PD.

A simplified diagram of the most recent iteration of the QY setup is depicted in Fig. 3.1. For a comprehensive overview of the optical elements in the diagram, refer to Tab. 3.1. The QY setup consists of two primary macro-components: the illumination component, encompassing the collimation pack and beam shaping pack, and the measurement component, comprising various arms for beam profiling, absorption, scattering, transmission, emission spectra, and luminescence. The measurement macro component is constructed within a cage system utilizing 30 mm dark tubes to support both optical and non-optical elements. This configuration ensures alignment of the components and prevents external light from interfering with the measurements. Lens L6 is situated in an open space but securely attached to the cage system, allowing fine adjustment of the beam focus at the centre of the cuvette holders. The illumination macro component consists of multiple cage systems, each housing the necessary optical elements and facilitating precise beam guiding and alignment via free-space assembled mirrors. The **collimation pack** incorporates three distinct narrow wavelength lasers used for both UCNP sample excitation and reference dye excitation. The excitation lines are transmitted from the collimation pack to the measurement component using silver mirrors assembled in free space. The **beam shaping pack** offers the option of speckle-free excitation with a wider beam profile, which is particularly advantageous for low PD measurements as it enhances the SNR. The **beam profile arm** diverts a fraction of the light from the main laser path towards a CMOS camera, enabling the capture of the excitation beam profile reaching the centre of the cuvette containing the UCNPs. The **blank arm** serves as a reference for absorption measurements in conjunction with the **transmission arm**. The **scattering arm**, in combination with a broad-band white light source (WL) and two narrow-band lasers, is utilized to measure the scattering spectrum of the UCNPs. The **emission spectra** arm is responsible for capturing the emission spectra of the UCNPs or dyes. Lastly, the **luminescence arm** facilitates the measurement of UCL dynamics and steady-state. Further details of the individual components, as well as comprehensive description of the system's characterisation and calibration, will be presented in following subsections.

#### Collimation pack

The collimation pack was assembled to generate collimated laser beams at three specific wavelengths, allowing for their subsequent manipulation and shaping based on the experimental requirements at both low and high PDs. Each laser arm within the collimation pack serves the purpose of exciting a different type of compound. The 976 nm excitation

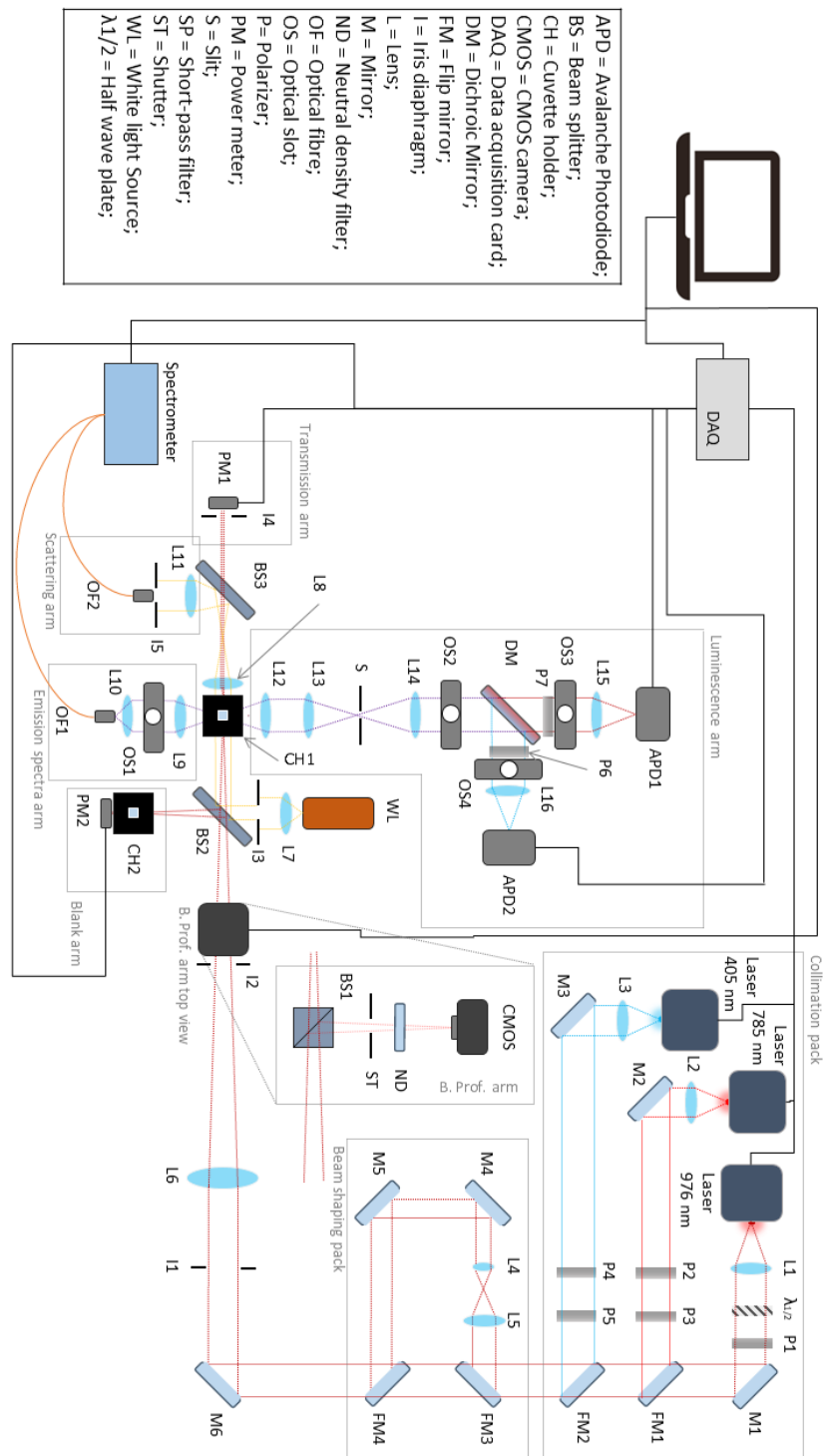


Figure 3.1: Simplified diagram depicting the most recent iteration of the QY setup, showcasing the optical components and laser lines employed for the excitation of UCNPs and reference dyes. The highlighted groups of components enable complete characterisation of UCNPs within a unified system. This characterisation encompasses UCL, absorption, scattering, emission spectra, dynamics across various excitation PDs, as well as the excitation beam profile for subsequent compensation of the iQY.

Table 3.1: List of optical components with their part code and description. All the components used in the QY system were procured from Thorlabs Inc.

Comp.	Part code	Details
BS1	CM1-BP108	98:2 Pellicle beam splitter
BS2,3	BSN11R	90:10 beam splitter plate
DM	DMLP550R	550 nm cut-on dichroic mirror
FM, M	PF05-03-P01	Silver mirror
L1	AC254-050-AB	AB-coated lens f. 50 mm
L2,3,5,7-15	AC254-030-AB	AB-coated lens f. 30 mm
L4	AC050-008-B-ML	AB-coated lens f. 8 mm
L6	AC508-300-AB	AB-coated lens f. 300 mm
ND	NDUV40B	Neutral density filter OD4
P1	LPNIRB100	Speckle free B-coated Lin. Polariser
P2,3,7	LPNIRE100-B	B-coated Lin. Polariser
P4,5,6	LPVISE100-A	A-coated Lin. Polariser
$\lambda_{1/2}$	WPH05M-980	Half-wave plate

is necessary for UCNPs, while the other two wavelengths are utilised for standard dye excitation. The 785 nm excitation is employed to excite a dye emitting in the NIR range, while the 405 nm excitation is used for a dye emitting in the visible range. Both dyes are necessary for calibrating the avalanche photodiodes (APD1 and APD2) within the high responsivity detection range. The 976 nm and 785 nm arms consist of temperature-stabilized, single-mode fibre-coupled diode lasers (Thorlabs, BL976-PAG500 and Thorlabs, FPL785S-250) with emission peaks at 976 nm and 785 nm, respectively. These diode lasers are mounted on a Thorlabs CLD1015 compact laser driver. The laser in the 405 nm arm is a Thorlabs L405P150 laser diode with an emission peak at 405 nm, connected to a Thorlabs SR9B-DB9 protection and relief cable, which is then connected to a Thorlabs LDC205C current controller.

The lasers were mounted within a cage system at the focal point of lenses, which served to collimate the laser beams. Specifically, lenses L1, L2, and L3 were carefully selected, along with lens L6 in the main excitation path, to achieve a resulting beam waist of approximately 100  $\mu\text{m}$  at the focal point in the centre of the cuvettes (CH1 and CH2). Fine adjustments to the beam waist can be made by moving L6 along the illumination path. This fine adjustment is only possible because L6 has a large focal length of 300 mm, meaning that small changes in the focal point within the cuvette do not significantly alter the symmetry of the beam waist in the central volume of the cuvette.

Two polarisation-dependent optical elements were positioned in front of the lens along the collimated path for two purposes. Firstly, they provide polarised light, which, when combined with a polariser placed in the luminescence arm oriented at a magic angle ( $54.7^\circ$ ) relative to the excitation polarisation, ensures that the measurement results are independent of any anisotropy in the UCNPs [89, 90]. Secondly, they enable precise control of the excitation intensity by rotating the optical element preceding the polariser at the end of the collimation arm. To facilitate the rotation of these optical elements, precise rotation mounts (Thorlabs, CRM1T/M) were utilised during the assembly.

The selection of optical elements in the collimation pack was based on factors such as cost, wavelength range of operation, and quality. Therefore, the half-wave plate and polariser P1 were chosen for the 976 nm excitation arm as they do not introduce speckles to the transmitted beam, although they are relatively more expensive compared to polarisers P2 and P3. Mirrors M1 to M3 and flipping mirrors FM1 and FM2 were

strategically positioned within the collimation pack in free space to align and orient the beams towards the main excitation path. The choice of which laser line is used to excite the sample in the cuvette holders can be easily made by flipping the appropriate mirror (FM1 or FM2) up or down. Further details regarding the optical elements can be found in Tab. 3.1.

### Centre illumination path

The core of the QY setup is the centre illumination path, to which all the other measurement arms are attached at a  $90^\circ$  angle. This path is constructed within a two-inch cage system and spans from iris I1 to iris I4, incorporating iris I2, two lenses (L6 and L8), cuvette holder CH1 (Thorlabs, CVH100), and beam-splitter plates BS2 and BS3. The beam-splitter plates are mounted in kinematic cubes, allowing for the interchangeability of optic elements (Thorlabs, DFM2/M). Lens L6 focuses the collimated excitation beam precisely at the centre of the cuvette holders CH1 and CH2 (Thorlabs, CVH100). Following its passage through CH1, lens L8 collects the diverging transmitted beam from the laser source and collimates it, thus preventing signal loss, until it reaches the transmission arm.

### Beam shaping pack

The beam shaping pack provides the option to excite the sample using a larger beam waist by flipping up the mirrors FM3-4. The mirrors M4-5 and FM-4 are assembled in free space, while the lenses L4-5 are mounted in a cage system for easy alignment. The lenses are positioned at a fixed distance from each other so that their focal points overlap, resulting in collimated laser light after passing through them. The focal lengths of the lenses are chosen to produce a resultant beam waist with a diameter of  $500 \mu\text{m}$  at the centre of the cuvette holders. The larger illumination area inside the cuvette enables the UCL that reaches the APDs to cover a greater portion of their sensors, thereby increasing the SNR of the luminescence measurements. Fine adjustment of the beam waist at the centre of the cuvette holders can be achieved by moving lens L4 slightly along the axis parallel to the excitation path.

### Beam profiler arm

The beam profiler arm consists of a pellicle beam-splitter BS1 (Thorlabs, CM1-BP108) that reflects approximately 2% of the excitation light at a  $90^\circ$  angle from the excitation path directly to the NIR monochrome CMOS camera (Thorlabs, DCC3240M). The camera is precisely positioned at the same distance from BS1 as the distance between BS1 and the centre of CH1. This ensures that the excitation profile captured by the camera accurately represents the profile that is illuminating the centre of the cuvette containing the sample. The vertical arrangement of the arm is necessary due to the strong polarisation dependence of the reflectance of BS1. As a result, the arm is assembled based on the vertical polarisation angles of P1, P3, and P5, which are set and fixed in a vertical orientation. To prevent saturation and potential damage to the CMOS sensor, a neutral density (ND) filter is placed in front of the camera to attenuate the beam intensity. Additionally, a shutter (ST), which is a diaphragm iris with no transmission when fully closed, remains closed during high PD measurements to protect both the sensor and the ND filter from damage.

### Blank arm and transmission arm

The blank arm and transmission arm serve distinct purposes in the QY setup. The blank arm comprises CH2 and a photodiode sensor (Thorlabs, S121C) connected to a digital optical power metre PM2 (Thorlabs, PM100D). It functions as a reference arm for absorption measurements. This segment of the setup is designed based on a double beam absorption spectrometer concept. In this configuration, the transparent compound, dispersed or dissolved in a solvent, is exposed to a fraction of the excitation power of the beam, while the blank (consisting of the solvent only) is irradiated by the remaining small fraction [89]. To ensure accurate measurements, CH2 and BS2 are strategically positioned to maintain equidistance between BS2 and both cuvette holders CH1 and CH2. This alignment guarantees that the beam profiles at the centre of both cuvette holders are identical. PM2, positioned behind CH2, captures the transmitted beam, while PM1 (identical to PM2), located at the transmission arm, measures the transmitted beam after passing through CH1. By comparing the signals obtained from both power metres and referencing the transmitted signal when the cuvette holders are empty, one can quantitatively assess the absorbed power attributed solely to the compound.

### Emission spectrum arm

The emission spectrum arm consists of two lenses, L9 and L10, with an optical filter slot positioned between them. The selection of the filter is based on the specific requirements, such as eliminating stray light from the excitation source and/or choosing a specific wavelength range for emission measurements. At the end of this arm, a commercial spectrometer (Bundle QEPro ABS) is connected using a 200  $\mu\text{m}$  multi-mode optical fibre (Thorlabs, BFL200LS02), which is precisely aligned with the focal point of the outermost lens L10.

### Scattering arm and the white light source

The scattering measurements are conducted in transmission mode using a broadband stabilized tungsten-halogen white light WL source (Thorlabs, SLS201L/M). The WL source is connected to an aperture in front of BS2 via a 200  $\mu\text{m}$  multi-mode optical fibre (Thorlabs, BFL200LS02) and a fibre adapter with a lens mount (Thorlabs, CVH100-COL). BS2 reflects the WL towards CH1, and the iris I5 can be adjusted to achieve an optimal aperture size, controlling the intensity of the WL and minimizing internal reflections within the cuvette containing the sample. Another 200  $\mu\text{m}$  multi-mode optical fibre is used to connect a spectrometer (Bundle QEPro ABS) to the optical output positioned in front of lens L11, which collimates the diverging transmitted light from cuvette holder CH1.

### Luminescence arm

The luminescence arm is designed to simultaneously measure two distinct wavelengths of the UCL at different sensors by utilizing a combination of a dichroic mirror and specific optical filters. UCNPs typically emit light at narrow band wavelengths due to a series of ETU processes. The luminescence arm allows for the investigation of the complexity of different ETUs individually and how they interact with each other at various excitation PDs.

The arm comprises a set of lenses L12-16, a slit S, a kinematic cage cube for interchangeable optics (Thorlabs, DFM2/M), such as dichroic mirrors or beamsplitter plates, as well as round spectral filters and/or polarisers. Additionally, it includes two APDs labelled as APD1 (Thorlabs,

APD410A/M) and APD2 (Thorlabs, APD440A2), all assembled within a 30 mm cage system with light-shielding tube connectors.

L12, positioned at the focal distance from the centre of cuvette holder CH1, collects the luminescence signal. L13 focuses the light onto a 1.0 mm wide vertical slit S (Thorlabs, VA100C/M), which suppresses any light originating from regions outside the excitation focal volume at the centre of the cuvette. This ensures that the detected luminescence originates within the waist of the excitation beam. The aperture of the slit is set to match the diameter of the APDs' sensors, maximizing light detection across the entire sensor area. L14, located at the focal distance from the slit aperture, collimates the light before it passes through a series of filters and polarisers. These optical elements are placed inside the optical slots of the kinematic cage cube, as well as additional slots positioned before and after the cube OS2-4 (Thorlabs, CFH2R). The selection of filters and polarisers is based on the sample to be analysed, the wavelengths to be measured by the APDs, and the excitation wavelength.

A dichroic mirror plate, arranged at a 45° angle within the cube, reflects a specific range of wavelengths to APD2 while allowing the remaining emission spectrum band to transmit to APD1. Lenses L15 and L16, situated just before the APDs, focus the light onto the round sensors. An opportunity for improvement here is to replace lenses L15 and L16 with lenses of shorter focal length. This adjustment would decrease the ratio of the illuminated area on the APD's sensor to the aperture of the slit, enabling the aperture to be increased and allowing for greater collection of luminescent light from the centre of the cuvette. Since UC-NPs have relatively low upconversion intensity, this enhancement would enable the system to detect weaker signals and accurately characterise the UC QY at lower excitation PDs.

The long focal length of lens L6 minimizes significant distortions of the beam waist along the 1 cm excitation path inside the cuvette. As a result, the slit aperture can be expanded to accommodate larger dimensions.

### Data acquisition and equipment control

Each function module of the QY system has its own method of data acquisition and control, but can be integrated into a single system when necessary. The laser drivers (Thorlabs, CLD1015 for the 976 nm and 785 nm lasers, and Thorlabs, LDC205C for the 405 nm laser) in the collimation pack are connected to an analogue input (AI) channel of a USB data acquisition card (DAQ) (National Instruments, NI-USB6218) via a BNC cable. Only one analogue output (AO) channel of the DAQ is used to control one laser driver at a time, so the cables are switched to a different driver as needed. A feedback of the AO signal is established through a tee BNC connector and a BNC cable linking the AO to a separate AI channel. The feedback signal is used to monitor the voltage set for laser driver modulation.

For beam profiling, the CMOS camera is connected to the laptop via USB, and the data acquisition and control are performed using the camera's software, which can be downloaded from the manufacturer's website. The QEPro Spectrometer used for broadband measurements (scattering arm and emission spectrum arm) is connected to the laptop via a USB port. Simple data acquisition for a specific PD of excitation is done using a software provided by the manufacturer, while a Python script is written to automate the acquisition of emission spectra for a range of PDs of excitation. The script combines a spectrometer controller (using the `seabreeze` Python library along with the Visual Studio developer tools with C++ libraries) with a DAQ controller (using the `nidaqmx` Python library), which modulates the laser. This setup allows

for setting a routine to vary the laser power and subsequently request the spectrometer to acquire and transfer data to the laptop.

There are various variables related to UCNPs that can rapidly change and influence their absorption and luminescence, such as temperature and scattering. Therefore, simultaneous measurement of transmission and luminescence is required to monitor these fast changes. The APDs and power meters are connected to four independent AI channels of the DAQ, and a Python controller with a simple terminal interface is developed. The controller utilises the specific Python library `nidaqmx` to communicate with the DAQ drivers and establish control over AO and AI channels, as well as certain functions of the DAQ. The terminal interface allows the user to adjust measurement settings, run the routine, and visualise the data before saving.

A typical routine for UCL measurement as a function of PDs of excitation involves setting a laser power range to be ramped up in fixed steps. The time per step must be long enough for the UCNPs to reach a steady state and for the power meters to stabilise, which may take a few milliseconds. The APDs are much faster, with the slowest (APD2) having a sampling rate of 100 *kHz*. Once the routine is configured and the controller is running, the script sets an initial voltage modulation through the AO (corresponding to an initial laser power) and requests a predetermined number of data points from all connected AI channels. The data is then stored locally in the laptop's memory, and the script repeats the process by incrementing the voltage modulation by one step. The process continues until the maximum voltage is set and the last data points are collected. The maximum modulation voltage depends on each laser driver, and it is important to know this in advance to avoid damaging the laser diodes with excessive current.

Another measurement mode is the pulsed mode, which can be used to study the dynamics of the populating and depopulating mechanisms involved in UCL. The pulsed mode allows for quick visualisation of the process, but it is limited by the sampling rate of the DAQ. Therefore, a function generator and an oscilloscope are more suitable for faster measurements.

### 3.3.2 Alignment of the excitation and luminescence beams

This step is crucial to ensure the long-term stability of the system's calibration. Proper alignment guarantees that all laser beams travel along the same path in the centre illumination arm and are focused on the centre of the cuvette. In addition, the luminescence image originating from the centre of the cuvette must be accurately projected onto the APD sensors for precise detection. Therefore, the setup alignment should follow the following steps:

- (i) Firstly, adjust lens L1 to achieve long-distance collimation of the 976 *nm* laser line.
- (ii) Next, align the laser line with respect to the irises I1 and I4 using mirrors M1 and M6, while keeping only the necessary FM's active.
- (iii) Place a four-window quartz cuvette containing a sample of UCNPs in cuvette holder CH1, and select the appropriate filters in the cage cube of the luminescence arm. Then, maximize the voltage signals from the APDs by fine-tuning the mirrors and the position of lens L6. Real-time verification of the APDs' signals can be done using an oscilloscope.

- (iv) Turn on the CMOS camera and adjust its x-y position to ensure that the beam spot remains at the centre of the image. Make a note of the position of the centre of the beam spot for aligning the other laser lines.
- (v) Flip up mirrors FM3 and FM4, and use mirrors M4 and M5 to align the laser beam with respect to iris I1 and the position of the centre of the previous beam spot in the CMOS camera image. Fine alignment is achieved by using a cage x-y stage to orient the centre axis of lens L4 along the laser beam path.
- (vi) Repeat steps (i), (ii), and (iii) for the other two laser lines, but use the annotated position of the centre of the previous beam spot instead of I4 in step (ii). In step (iii), change the filters accordingly and use the appropriate dye for each laser beam instead of the UCNPs sample.

### 3.3.3 Calibration

Not all functions of the QY setup need to be calibrated, only those related to the QY evaluation, namely transmission (which determines the number of absorbed photons) and luminescence. Therefore, the power metre sensors and the APDs were calibrated appropriately, as described in the following subsections.

#### Power metre sensors

Power metre sensors are well calibrated by the manufacturer, with the calibration curves provided with the power metre devices. This allows for quick and accurate readings of laser light on the device's screen. However, when connected to the DAQ via a BNC connection, the raw signal is provided in units of volts and requires calibration to rescale the reading values. The voltage output ranges from 0 to 2.0 V regardless of the power range and detection wavelength.

To calibrate the power metre readings, several power ranges were initially selected to ensure complete detection range for the system's lasers at wavelengths of 976 nm, 785 nm, and 405 nm. A table was prepared with recorded laser powers (readings from the power metre screen) and their corresponding voltage outputs. These data points were fitted to linear curves, as illustrated in Fig. 3.2. The angular coefficients  $m$  and the coefficients of determination  $R^2$  for the calibration curves are presented in Tab. 3.2. The angular coefficients represent the calibration factors that convert the voltage readings to power values in milliwatts  $mW$ .

Table 3.2: Calibration coefficients and respective coefficients of determination for both power metre sensors at different power ranges and wavelengths.

Power-metre	Wavelength	Range	$m_{PM}$	$R^2$
PM1	976 nm	60 mW	30.4 mW/V	0.999990
PM1	976 nm	600 mW	304 mW/V	0.999995
PM1	785 nm	9.1 mW	4.60 mW/V	0.999976
PM1	405 nm	0.23 mW	0.115 mW/V	0.999999
PM2	976 nm	61 mW	30.7 mW/V	0.999902
PM2	785 nm	0.95 mW	0.478 mW/V	0.999980
PM2	405 nm	2.2 mW	1.13 mW/V	0.999999

## APDs

The calibration of the APDs involved the use of two standard dyes with known QY: DY-785, an organic dye with a main emission peak at  $804\text{ nm}$ , for APD1, and DY-405, another organic dye with a main emission peak at  $470\text{ nm}$ , both obtained from Creative Diagnostics and characterised following the IUPAC protocol [89]. The choice of dyes was based on the spectral detection range of each APD, as detailed in Subject. 3.3.1. Calibrating the APDs required special attention. Although the voltage response of the APD is linear with respect to the incident light intensity, its sensitivity is dependent on the wavelength. This wavelength dependence must be taken into account due to the wide spectral range of dye luminescence. Moreover, the parameter of interest for calibration is the integrated luminescence from all directions originating from the volume at the centre of the cuvette, rather than the fraction of luminescence reaching the APD sensor. The light emitted from the central volume of the cuvette travels through the liquid solution, undergoing wavelength-dependent reabsorption<sup>1</sup>. Subsequently, only a fraction of the light is collected within a small solid angle of detection. In addition, the luminescence signal is attenuated by various optical components along the path to the APD sensor in the luminescence arm. Therefore, all these parameters were properly considered, and the following steps were followed to calibrate APD1 and APD2 consecutively:

- (i) **System preparation** - Firstly, the laser at  $785\text{ nm}$  was powered on and left to stabilise at the required temperature while preparing the dye solution. To narrow down the range of wavelengths reaching the APDs' sensors and minimise distortions in their voltage response, the band-pass filter BP800 (Thorlabs, FB800-10) was inserted into the optical spectrometer OS3.
- (ii) **Sample preparation** - A total of  $1\text{ mg}$  of the DY-781 dye was fully dissolved in  $10\text{ ml}$  of high purity ethanol to create a mother

<sup>1</sup>This process, known as spectral colouring, is also of particular interest in photoacoustic imaging due to its significant impact on the interpretation of output signals [91].

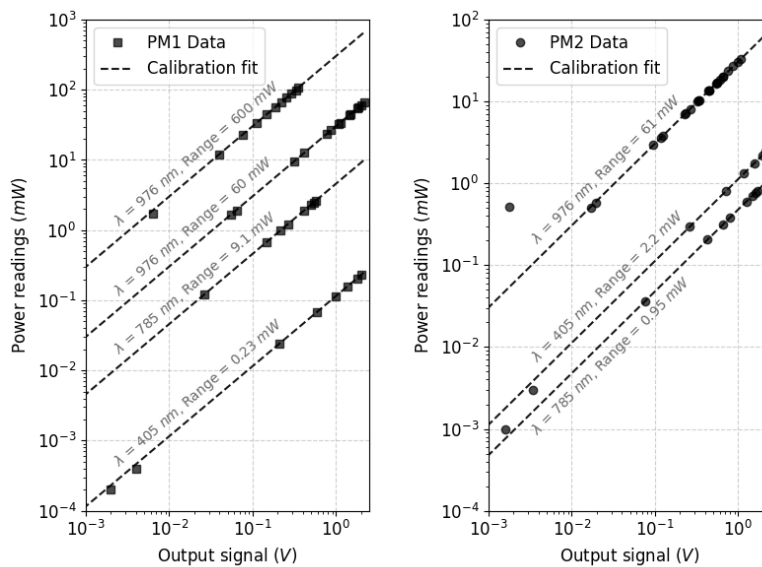


Figure 3.2: Calibration curves of the sensors at various wavelengths and power ranges. The left plot shows the curves for sensor PM1, while the right plot shows the curves for sensor PM2.

solution. Subsequently, 1 ml of ethanol was added to each of two four-window quartz cuvettes (Thorlabs, CV10Q35F). One cuvette was designated as a reference (blank cuvette) for absorption measurements, while the other cuvette was used to prepare a diluted dye sample. The latter cuvette was placed in the cuvette holder CH1, and the laser was set to its maximum power. The mother solution was then added to the ethanol in small increments using a pipette while monitoring the voltage output of APD1 with an oscilloscope. The addition of the mother solution continued until the voltage signal reached approximately 1 V (the maximum voltage signal of the APDs is 2 V before saturation).

- (iii) **Voltage output and transmission acquisition** - APD1 was reconnected to the DAQ, and the laser power was set to 0. The cuvettes containing the dye solution and reference sample were initially set aside for background measurements with empty cuvette holders. Next, the excitation laser power was incrementally increased from 0 to its maximum using the Python controller, which simultaneously recorded data from the power metres, and APDs. The acquired data was saved, and the same process was repeated with the dye sample in CH1 and the reference sample in CH2.
- (iv) **Emission spectra** - The luminescence spectrum of the dye was attenuated by the BP800 filter in the luminescence arm. The transmission factor, which accounts for the fraction of transmitted light as a function of wavelength, needed to be determined for subsequent analysis. To accomplish this, the optical fibre OF1 was connected to the spectrometer, and the laser power was set to an intermediate value sufficient to observe a well-resolved spectrum. Measurements were taken with the optical spectrometer OS1 empty and with the BP800 filter inserted. The ratio of the areas under the curves of these two spectra provided the transmission factor.
- (v) **Absorption spectrum** - The absorption spectrum was obtained by illuminating the sample in transmission mode using broadband white light. The optical fibre OF2 was connected to the spectrometer, and spectra were acquired first with the blank cuvette in CH1 and then with the sample cuvette. This measurement was essential to determine the reabsorption ratio for the APD calibration, particularly for the DY-781 dye, which exhibits significant overlap between its absorption and emission spectra.
- (vi) The previous steps were repeated to calibrate APD2 using the DY-415 dye and the band-pass filter BP470 (Semrock, FF02-472/30-25).

With all the data collected, the following analysis was conducted. According to the manufacturer's manual, the voltage response of the APD to light is given by Eq. (3.1),

$$V_{out} = \int_{\lambda_0}^{\lambda_1} G \cdot S(\lambda) \cdot P_{\lambda} d\lambda, \quad (3.1)$$

where  $G$  is the internal impedance constant represented in ohms ( $\Omega$ ),  $S(\lambda)$  is the wavelength-dependent sensitivity in amperes per watt ( $A/W$ ) shown in Fig. 3.3, and  $P_{\lambda}$  is the power reaching the APD's sensor at the wavelength  $\lambda$ .

On the other hand, the power reaching the APD can be represented in terms of the resultant luminescence by Eq. (3.2):

$$P_{\lambda} = L_r \cdot T_f \cdot (1 - \alpha_{\lambda}) \cdot g \cdot \theta, \quad (3.2)$$

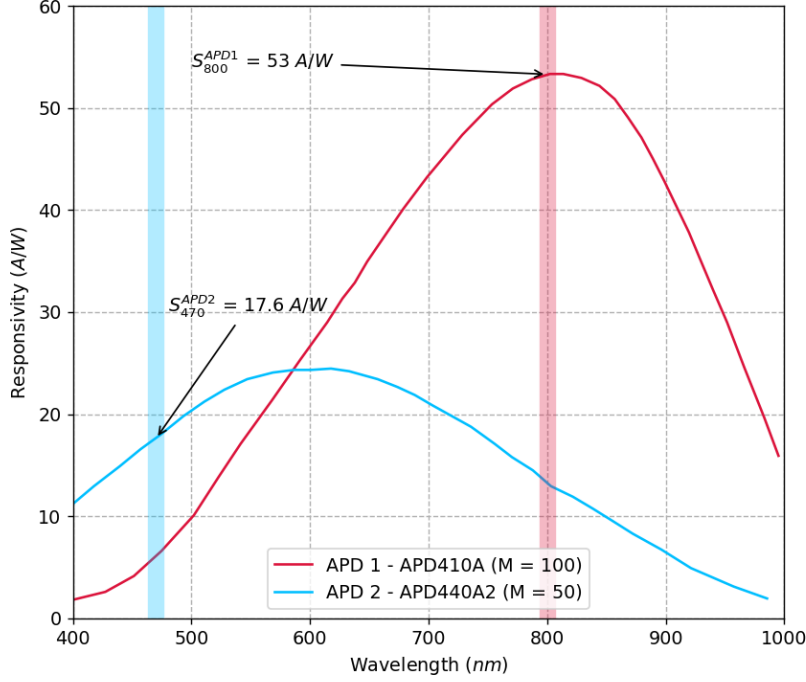


Figure 3.3: Wavelength-dependent sensitivities of the APDs utilised for luminescence detection (Data provided by Thorlabs). The vertical bands indicate the selected wavelength ranges in which the calibrations were conducted using two distinct fluorescent dyes.

where  $L_r$  is the resultant luminescence integrated in all directions and originated from the volume in the centre of the cuvette.  $\alpha_\lambda$  is the re-absorption coefficient,  $T_f$  represents the transmittance of the band-pass filters that are only present in the luminescence arm during calibration and not during the measurement of UCL,  $g$  is the geometry factor that accounts for the narrow solid angle of detection, and  $\theta$  is the coefficient of light attenuation due to the remaining common optics while measuring the luminescence of dyes or UCNPs. The use of a band-pass filter eliminates the wavelength effect on the results by narrowing down the wavelength range of detection, thus reducing Eq. (3.1) to Eq. (3.3),

$$V_{out} = G \cdot S(\lambda_0) \cdot P_{\lambda_0}. \quad (3.3)$$

Thus, by rearranging the equations, one can establish the relationship between the resultant luminescence and the APD's voltage output, as shown in Eq. (3.4),

$$L_r \cdot T_f \cdot (1 - \alpha_{\lambda_0}) = m_0 \cdot V_{out}, \quad (3.4)$$

where the left-hand side of the equation represents the integrated luminescence in all directions, corrected for the reabsorption coefficient and the transmittance coefficient of the filters. On the right-hand side,  $m_0$  represents the calibration coefficient at the calibration wavelength  $\lambda_0$ . This coefficient encompasses all the parameters present in the luminescence arm, as defined in Eq. (3.5),

$$m_0 = \frac{1}{g \cdot \theta \cdot G \cdot S(\lambda_0)}. \quad (3.5)$$

Finally, the wavelength-dependent calibration curve for the luminescence arm can be retrieved by the Eq. (3.6),

$$m_{APD}(\lambda) = \frac{m_0 \cdot S(\lambda_0)}{S(\lambda)}. \quad (3.6)$$

**Determining  $L_r$**  - The determination of the resultant luminescence  $L_r$  involves calculating the total number of photons absorbed by the volume in the centre of the cuvette and multiplying it by the QY of the dye. In terms of power,  $L_r$  can be expressed using Equation Eq. (3.7):

$$L_r = \eta_D \cdot P_{abs} \cdot \frac{\lambda_e}{\lambda_a}, \quad (3.7)$$

where,  $\eta_D$  represents the QY of the dye,  $P_{abs}$  is the total absorbed power by the volume at the centre of the cuvette, and  $\lambda_e$  and  $\lambda_a$  are the wavelengths at the peak of emission and absorption, respectively. For more information on the measurement and calculation of  $P_{abs}$ , refer to the measurement protocol (Subsect. 3.3.4) and the analysis protocol (Subsect. 3.3.5), which provide detailed procedures for measurements and data analysis.

**Determining the transmission coefficient of the filters  $T_f$**  - The transmission coefficient  $T_f$  of the band-pass filters represents the fraction of light transmitted through the filters. It can be obtained by comparing the integrated emission spectrum measured after the filters to the integrated emission spectrum measured without any filter. The spectra of both dyes, along with the signal filtered by the narrow band-pass filters used for calibration, are shown in Fig. 3.4. The resulting transmission coefficients are presented in Tab. 3.3.

Table 3.3: Filter transmission factors for the dyes DY-781 and DY-415.

Dye	$T_f$
DY-781	10.34%
DY-415	14%

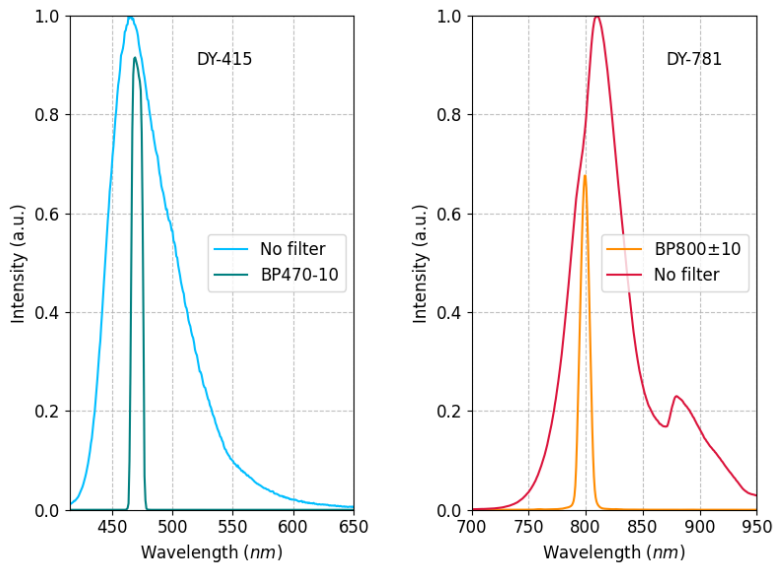


Figure 3.4: Emission spectra of the dye DY-415 (on the left) and DY-781 (on the right) are compared to curve of emission transmitted through the a band-pass filters used in each measurement.

**Determining the reabsorption ratio  $\alpha_r$**  - The reabsorption ratio was determined through a two-step process. Firstly, the absorption coefficients  $\mu_a$  were calculated for both dyes at the wavelengths of the excitation lasers used during the luminescence measurements. Secondly, the normalised absorption spectra, provided by the manufacturer, were

scaled proportionally to the absorption coefficients obtained at the corresponding wavelengths. The rescaled absorption spectra were then used to calculate the emitted spectra after undergoing reabsorption within the liquid path. This calculation was performed using the Beer-Lambert's law, as shown in Eq. (3.8),

$$L'(\lambda) = L_r(\lambda)e^{-\mu_a(\lambda)l/2}, \quad (3.8)$$

where  $L'(\lambda)$  represents the equivalent intensity of the resultant luminescence originating at the centre of the cuvette,  $L_r(\lambda)$  represents the initial luminescence,  $l$  is the length of the cuvette, and  $\mu_a$  is the absorption coefficient of the dye in units of  $cm^{-1}$ . Please refer to the Subjects. 3.3.4 and 3.3.5 for detailed information on the measurement procedure and the calculation of  $\mu_a$ . Figure Fig. 3.5 illustrates the absorption spectra and normalised emission spectra (represented by solid lines) for both dyes. The dashed lines depict the calculated attenuated emission spectra after passing through the cuvette. The reabsorption ratios, defined as the fraction of the area between the attenuated emission curves with respect to the emission curve without attenuation, are presented in Tab. 3.4.

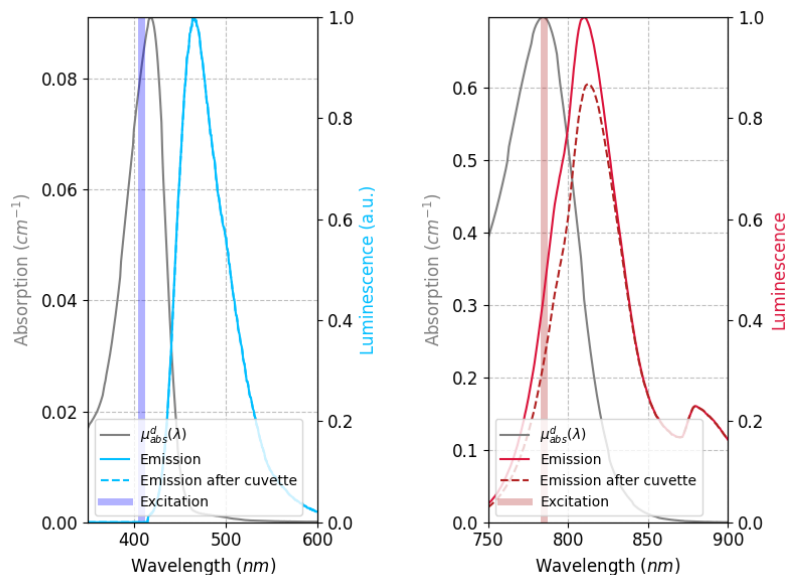


Figure 3.5: Emission and absorption spectra of the dye DY-415 (on the left) and DY-781 (on the right). The dashed curves represent the amount of light leaving the cuvettes after the reabsorption attenuation. Because of minimum overlap of the absorption and emission spectra of the DY-415, only 2% of the total emission is reabsorbed by the dye.

Table 3.4: Reabsorption ratios calculated for both dyes utilised on the calibration of the luminescence arm.

Dye	$\alpha_r$
DY-781	19.7 %
DY-415	2 %

**Determining the calibration coefficient  $m_0$**  - The calibration coefficients  $m_0$  are obtained for a narrow range of wavelengths defined by the band-pass filters. This process involved fitting the resultant luminescence  $L_r$ , corrected for the reabsorption ratio  $\alpha_r$  and the filter transmission ratio  $T_f$ , against the raw voltage output of the APDs to a linear curve described by equation Eq. (3.4). The calibration data and their corresponding fitted curves are depicted in Fig. 3.6 using a double-logarithmic representation. The calibration coefficients, along with the calibration parameters and their respective coefficient of determination, are presented in Tab. 3.5.

Finally, the wavelength dependent coefficients of calibration  $m_{APD}(\lambda)$  were retrieved according to Eq. (3.6) and plotted in the Fig. 3.7.

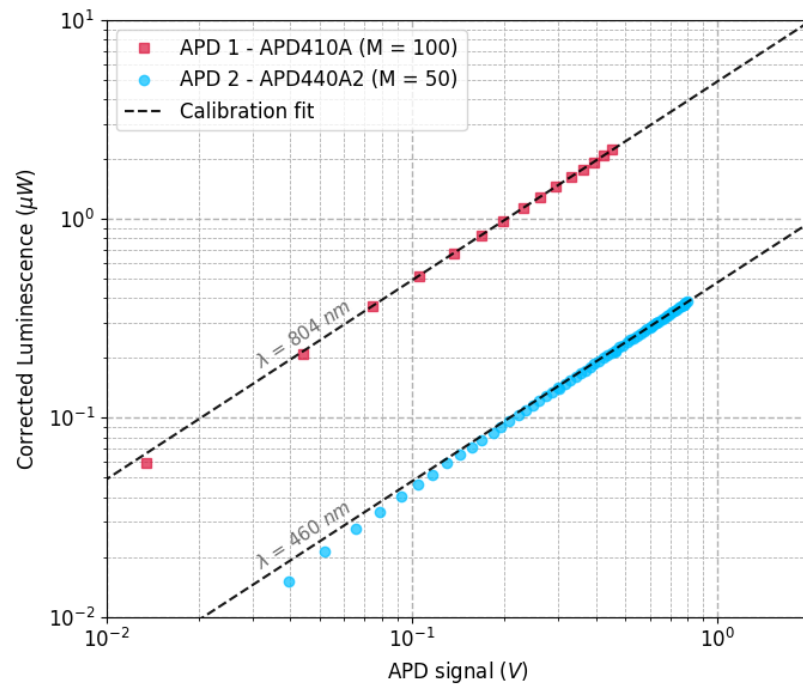


Figure 3.6: Calibration curves of the luminescence arms ending at APD1 and APD2.

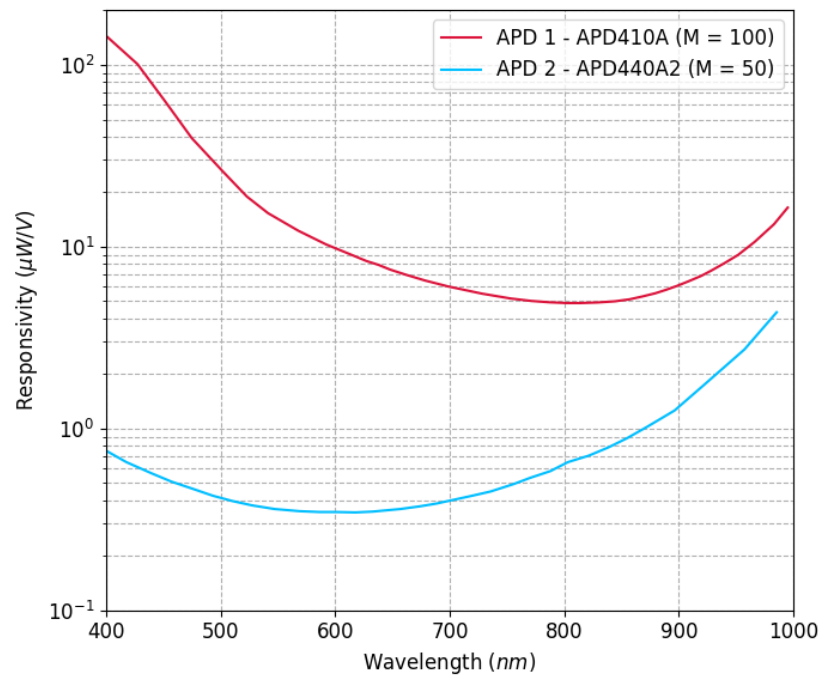


Figure 3.7: Wavelength dependent coefficients of calibration for the luminescence arm ending on APD1 and APD2. These coefficients convert the APD signals from units of volts ( $V$ ) to micro-watts ( $\mu W$ ).

Table 3.5: Calibration coefficients and respective coefficients of determination for both APDs at their respective wavelengths of calibration.

APD	Wavelength range	Gain	$m_0$	$R^2$
APD 1	$800 \pm 10 \text{ nm}$	100	$4.92 \mu\text{W}/V$	0.99994
APD 2	$470 \pm 10 \text{ nm}$	50	$0.48 \mu\text{W}/V$	0.99984

### 3.3.4 Measurement protocol

#### Sample preparation

The QY setup is designed for liquid solutions of UCNPs, therefore the UCNPs need to be dispersed in a solvent (such as water or toluene) and prepared according to the following steps:

- (i) Transfer approximately 1 *ml* (or enough to fill a volume where the laser light can pass through the sample without being affected by surface reflections) of the solution into a cuvette with four clear sides.
- (ii) Prepare another cuvette with the same amount of pure solvent (this will be used as a reference for absorption measurements).
- (iii) Sonicate the cuvette containing the UCNPs for approximately 15 minutes. This will disperse any aggregates present in the solution.

#### Emission spectrum

- (i) Place the cuvette containing the UCNPs in CH1.
- (ii) Keep mirrors FM1-4 flipped down.
- (iii) Connect the OF1 to the QEPro spectrometer.
- (iv) Place the short-pass filter (SP890 Semrock, FF01-890/SP-25) in OS1.
- (v) Turn on the 976 nm laser. The laser power can be manually selected on the display of the laser driver according to the experimental requirements.
- (vi) Connect the spectrometer to a computer using a USB cable. The QEPro has its own software for data acquisition that can be installed and easily used. For power dependence measurements, the measurement process can be automated using a Python script available for download on Github, Appendix ii.

The Fig. 3.8 shows an example of a measurement performed with the QY system, depicting the emission spectrum of a Yb-Tm-codoped UCNP.

#### Beam Profile

For the beam profile measurements the polarisers in the collimation pack are used to attenuate the laser light and prevent damage to the sensor of the camera.

- (i) Set a low power directly on the display of the laser driver for the expected wavelength to be measured.
- (ii) Attenuate the light by rotating the polarisers in the collimation pack. The power can be read on the display of PM1.

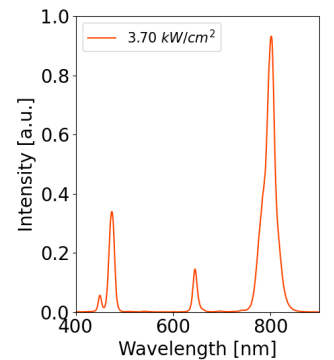


Figure 3.8: Example of emission spectrum acquired with the QY system.

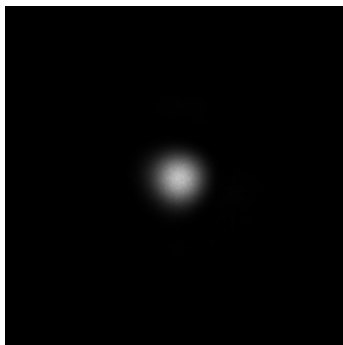


Figure 3.9: Example of beam profile acquired with the CMOS camera. The image was cropped around the beam spot.

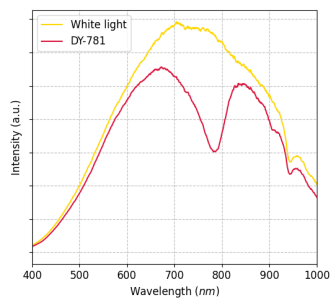


Figure 3.10: Example of raw data of the broadband light measurement. The dip in the DY-781 curve represents the attenuation due to absorption process of the dye.

- (iii) Select the narrow or wide beam profile by flipping up or down mirrors FM3 and FM4.
- (iv) Connect the CMOS camera to the computer using a USB cable. The ThorCam software, available for download from the manufacturer's website, is used for image acquisition.
- (v) With ThorCam running, open the shutter in front of the camera and acquire the images.

### Light attenuation measurements

For the scattering measurements, the WL source is utilised.

- (i) Ensure the lasers are switched off and turn on the WL source.
- (ii) Connect the spectrometer to OF2.
- (iii) Take a measurement of the spectrum of the WL source.
- (iv) Place the cuvette with the solvent in CH1.
- (v) Repeat the measurement for the solvent.
- (vi) Place the cuvette with UCNP in CH1.
- (vii) Repeat the measurement for the UCNP.

Simultaneous luminescence and transmission measurements are conducted using the Python controller, which can be downloaded from Github. The transmission measurements are used to calculate the attenuation of light as it passes through the sample. In some UCNP samples, high scattering can be present, and its contribution can be subtracted based on the measurements from the previous sub-section. Therefore, the remaining contribution to the attenuation is due to absorption.

- (i) Switch on the 976 nm laser, the power meters, and the APDs. Ensure that they are all connected to the DAQ channels, and connect the DAQ to the computer using its USB cable.
- (ii) Open the Python controller and adjust the sweep settings as required. For improved SNR, it is recommended to set the option *samples per step* to 1000, which instructs the DAQ to acquire 1000 data samples for each step of excitation power.
- (iii) Perform a measurement with empty cuvette holders (CH1 and CH2) to obtain the power of the laser before it reaches the cuvettes.
- (iv) Place the cuvette containing the UCNP in CH1 and the cuvette containing the solvent in CH2.
- (v) Run the measurement and plot the data using the *plot* option before saving the results.

### 3.3.5 Analysis protocol

The analysis protocol involves the evaluation of the UCL and transmission data to determine the QY of UCNPs. Additionally, it covers the compensation of beam profiles and the determination of transition PD points. These aspects of UCNPs characterisation consist of several steps that will be explained in detail in the following subsections. The UC emission spectrum, which is necessary for identifying the centre wavelengths of the main UCL and selecting appropriate spectral filters for the APDs, is straightforward to obtain. Therefore, no further details will be presented in this section.

#### Background removal

The background level of the transmitted power measurements (voltage output of the PMs) and UCL signal (voltage signal of the APDs) is determined by calculating the average of data points when the laser is switched off. Similarly, for beam profile measurements, the background is obtained by averaging the intensities of a dark region in the image captured by the CMOS camera. Subsequently, the background values are subtracted from their respective data sets.

#### Noise treatment

The UCL luminescence signal can be very weak at low PDs, which is why multiple data samples are acquired using the DAQ for each excitation power step. To reduce noise in the signal, the data points for each step are averaged. However, this process requires attention. Both the PMs and the samples take a few milliseconds to reach stability and the steady state, respectively. Therefore, the averaging of data points is performed only after the curves have reached the flat portion for each step.

#### Calibration of the PM and APD channels

The signal output obtained from the PMs and APDs is measured in volts (V) and needs to be converted to power units using the calibration constants that have been previously determined and are provided in Tab. 3.2 and Tab. 3.5.

#### Absorbed power

The calculation of the absorbed power is performed for a specific volume located at the centre of the cuvette, corresponding to a 1 mm length along the excitation path where the UCL is collected by the APDs. The absorbed power, denoted as  $P_{abs}$ , is determined by multiplying the power at the centre of the cuvette,  $P_c$ , by the absorption coefficient of the UCNPs,  $\mu_a$ , and the excitation path length,  $l = 0.1$  cm. This relationship is expressed in Eq. (3.9),

$$P_{abs} = P_c \mu_a l, \quad (3.9)$$

where  $P_c$  represents the square root of the product of the incident excitation power  $P_o$  to the power transmitted through the sample  $P$ , as shown in Eq. (3.10),

$$P_c = \sqrt{P_o P}, \quad (3.10)$$

and  $\mu_a$  is obtained from the Beer-Lambert's law by subtracting the contribution of scattering<sup>2</sup>, which can be present in some turbid samples, Eq. (3.11),

---

<sup>2</sup> $\mu_s$  is obtained from WL transmission measurements. A detailed example of this calculation can be found in the supplementary material of the Paper I

$$\mu_a = \ln \frac{P_o}{P} - \mu_s. \quad (3.11)$$

### External QY

The external QY is a measure of the efficiency of UCL in relation to the absorbed power. It is determined by the ratio of UCL power  $L_r$  to the total absorbed power  $P_{abs}$  at the centre of the cuvette, normalised by the excitation  $\lambda_{ex}$  and emission  $\lambda_{em}$  wavelengths, as described by Eq. (3.12),

$$\eta = \frac{L_r \lambda_{em}}{P_{abs} \lambda_{ex}}. \quad (3.12)$$

It is important to note that the QY curves obtained from different measurements using distinct beam profiles are not expected to overlap when plotted against the PDs of the laser beam. This is due to the non-linear weighted sum of UCNPs experiencing different local PDs across the beam profile. To obtain the UCNPs efficiency independent of the excitation beam profile, it is necessary to perform beam profile compensation. Detailed information and explanations regarding beam profile compensation methods will be presented in the next chapter.

### The transition PD points

The final steps of the analysis involve determining the transition PD points and the saturation level of the QY from the measured luminescence data as a function of excitation power at the centre of the cuvette. To obtain these parameters accurately, it is necessary to fit an equation that considers beam profile compensation to the experimental data. The transition points heavily depend on the power profile of the beam, and underestimating the QY saturation level can occur, as demonstrated by Mousavi et al. and discussed in Paper I.

A detailed explanation of the steps to obtain the beam-profile compensated resultant luminescence will be presented in the next chapter. However, assuming that the equation for the beam-profile compensated resultant luminescence is known at this point, the analysis should be conducted as follows.

First, fit the resultant luminescence emitted from the lowest energy level. Then, use the results of this fitting as boundary conditions to fit the resultant luminescence from higher levels, if necessary. Lower energy levels typically have fewer free parameters to adjust, making it easier for the results to converge to a solution. For example, consider a sample of UCNPs with emissions from ETU1, ETU2, and ETU3. The ETU1 process has only two parameters to fit, but it often exhibits a linear behaviour with respect to the excitation power density due to anomalous power density dependence. Consequently, the transition point for ETU1 may be extremely large and may not be detectable within the range of power densities used in the measurement. The absence of the first transition point can be used as a boundary condition in fitting ETU2. The ETU2 curve has three parameters, but with the boundary condition, it is reduced to two free parameters to fit. Once the ETU2 luminescence curve is adjusted, the same strategy is applied to ETU3 and so on.

### Internal quantum yield iQY

Finally, the iQY, which is an intrinsic characteristic of the material, is independent of the beam profile. It can be represented in terms of the transition PD points and the saturation level of the QY, as shown in Chap. 2. The beam-profile compensation, which will be explained in the next chapter, utilises the locally calculated PDs at each pixel level of the

CMOS camera. Therefore, the iQY is obtained by applying the beam profile-independent equation for the QY to all the local PDs, using the transition PD points and saturation levels obtained in the previous step.

The complete analysis can be extensive; however, a Python module has been developed to facilitate the process. This module can be imported into another script or a Jupyter notebook, and its methods can be used individually. The code is available on GitHub, and an example of its application in a Jupyter notebook for a comprehensive analysis is provided in the appendix.

### 3.4 Summary

This chapter describes the development of a semi-relative QY system for characterising upconverting materials in liquid solutions. The innovative system incorporates various features necessary for comprehensive characterisation of the iQY across a wide range of PDs. Additionally, the setup is designed to reduce reliance on a reference dye while still allowing assessment of the excitation beam profile. Unlike existing relative and absolute QY systems, the engineered device overcomes critical challenges and enables characterisation of the iQY as an intrinsic property of upconverting materials.

The compensation of beam profile effects on the iQY measurement is an important consideration, and the assessment of the excitation beam profile represents the initial step in this process. The compensation requires a thorough understanding of the UC behaviour with respect to PDs, as presented in Chap. 2. The subsequent chapter will provide detailed explanations of beam profile compensation and present an example of iQY characterisation for an ETU2 process in an UCNP sample using the developed QY setup.



---

# THE EXCITATION BEAM PROFILE-COMPENSATION AND HIGH DYNAMIC RANGE OF PDS

---

Experimental evaluation of iQY requires precise compensation of the excitation beam profile. An unmodified laser beam typically exhibits a Gaussian shape or the presence of speckles across its cross-section, leading to variations in the PD distribution. Consequently, different regions of a sample experience different PDs, and the non-linear relationship between iQY and PD results in significant variations in UC emissions depending on the position within the sample.

From an experimental perspective, accurately representing the QY as a function of excitation PD requires a precise definition of the beam radius. PD is determined by the ratio of power to the illuminated area. However, for a typical non-modified laser beam with a Gaussian-like profile, measuring its radius is often subjective and lacks standardisation.

The beam width of a Gaussian profile is commonly quantified as the full width at half maximum (FWHM), which represents the width of an equivalent profile with a uniform PD distribution and the same total power as the Gaussian profile. This definition is suitable for determining the total luminescence of materials exhibiting a linear response to the excitation PD, as the luminescence and excitation normalised profiles perfectly overlap. Consequently, a top-hat excitation profile with the same radius as the FWHM of a Gaussian profile will produce the same total luminescence.

However, for non-linear systems such as UC, the luminescence and excitation profiles differ. Therefore, the FWHM definition for calculating the excitation PD does not accurately represent the UCL of UCNPs irradiated with a top-hat illumination of the same PD. An attempt to address this issue was proposed by May and Berry, who introduced an alternative approach for defining the excitation beam width in the context of two-photon-process UC. Instead of considering the FWHM diameter, they found that taking the beam width at a distance equal to 1.8 standard deviations ( $1.8\sigma$ ) from the centre of the cross-section yielded better results[92].

It is important to note that this approach is only valid for the UC non-linear ETU2 regime. As UCNPs transition to the linear regime, the method deviates, and the FWHM once again becomes the preferred choice. Fig. 4.1 illustrates a simulation comparing the luminescence profiles of ETU processes at two different regimes. The top panel depicts the excitation profile with maximum PD below the first transition PD point, where the non-linearity of UC is at its maximum for all emission wave-

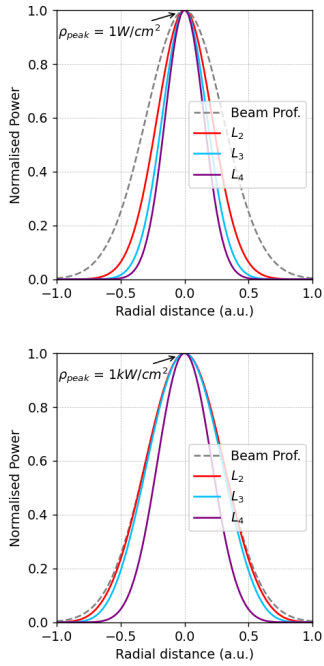


Figure 4.1: Profiles of the excitation beam and luminescence intensities for ETU2, ETU3, and ETU4 processes are shown. The continuous lines represent the normalised luminescence profiles under the same excitation beam, which has a Gaussian profile represented by the dashed lines. The excitation beam has a maximum PD at the peak of the beam equal to  $1 \text{ W/cm}^2$  (top panel), which is below the first transition PD point of  $40 \text{ W/cm}^2$ , and  $1 \text{ kW/cm}^2$  (bottom panel), which is above the detectable transition PD points and below the last transition PD point (considered infinite due to  $W_4$  being considered null).

lengths. In contrast, the bottom panel represents the excitation profile with maximum power above the detectable transition PD points. Under this regime, the ETU2 and ETU3 processes exhibit linearity across most PDs within the cross-section of the excitation beam, while the ETU4 process shows quadratic behaviour, assuming neglect of the ETU5 transition ( $W_4$  is considered null, leading to  $\rho_4$  approaching infinity). This simulation was implemented using the rate equations and rate constants presented in Chap. 2.

Another beam profile compensation strategy was initially proposed by Mousavi et al., who conducted a detailed comparison between a non-compensated QY curve and a compensated one for the  $800 \text{ nm}$  emission in an ETU2 process[49]. The approach by Mousavi et al. was based on the model proposed by Liu et al. for the ETU2 process[1]. In the following section, the concept introduced by Mousavi et al. is applied to a general ETU $j$  process using the model presented in Chap. 2. This approach offers advantages as it is valid for the entire PD range, including both the non-linear and linear regimes, as well as the transitions between them.

#### 4.1 The excitation beam profile compensation

Consider an arbitrary volume  $V$  of UCNP emitting light in all directions. The total power emitted by the UCNP at a certain wavelength  $\lambda_{em}$  due to an ETU $j$  process, denoted as  $L_{r_j}$ , can be calculated by integrating the local UCL  $L_j$  over the entire volume, as shown in Eq. (4.1),

$$L_{r_j} = \int_V L_j dV, \quad (4.1)$$

where  $L_j$  is determined using Eq. (4.2), which is obtained from the expansion of Eq. (2.16). In Eq. (4.2), the photon flux  $\phi_j$  is replaced with Eq. (2.14), and the equation is rewritten in terms of the absorption coefficient  $\mu_a$  as well as the excitation and emission wavelengths,  $\lambda_{ex}$  and  $\lambda_{em}$ , respectively,

$$L_j = \frac{\phi_{j_o}}{\alpha N_a} \mu_a \frac{\lambda_{ex}}{\lambda_{em}} \prod_{i=1}^j \frac{\rho(x, y, z)}{\rho(x, y, z) + \rho'_i}. \quad (4.2)$$

Let us consider a collimated excitation beam that traverses the sample along the  $z$ -axis, covering a path length denoted by  $l$ . Assume that the length  $l$  is sufficiently small so as to neglect any attenuation of the beam along its path. In this scenario, the volume integral in Eq. (4.1) can be simplified to an integral over the cross-sectional area of the beam multiplied by the path length  $l$ . Furthermore, the experimental measurement of the beam profile is performed discretely using a CMOS camera sensor, which captures the intensity values at multiple pixels. Since the area of each pixel, denoted by  $A_{px}$ , is much smaller compared to the overall illumination area, it is reasonable to approximate the local power density measured at each pixel, denoted by  $\rho_{px}$ , as approximately constant over the area  $A_{px}$ . As a result, the volume integral can be further simplified by summing over all  $m$  pixels that constitute the illuminated area on the  $xy$ -plane of the defined volume. This simplification can be mathematically expressed as shown in Eq. (4.3),

$$L_{r_j} = \frac{\phi_{j_o}}{\alpha N_a} \mu_a \frac{\lambda_{ex}}{\lambda_{em}} A_{px} l \sum_{px} \prod_{i=1}^j \frac{\rho_{px}}{\rho_{px} + \rho'_i}. \quad (4.3)$$

In order to determine the local power density  $\rho_{px}$ , it is necessary to calculate the product of the total power at the cross-section of the beam

profile at the centre of the cuvette, denoted as  $P_c$ , with the intensity measured at the pixel  $px$ , normalised by the total intensity of the excitation beam measured by the camera. This normalised profile can be represented as a matrix  $\Gamma$  with  $m$  elements,  $\gamma_{px}$ . Mathematically, the expression for  $\rho_{px}$  can be written as shown in Eq. (4.4),

$$\rho_{px} = P_c \gamma_{px}. \quad (4.4)$$

By replacing  $\rho_{px}$  in Eq. (4.3) with the expression given in Eq. (4.4) and fitting the resulting luminescence data against the power at the centre of the cuvette, the constants  $\eta_{j_o}$  and  $\rho'_i$ , which correspond to the transition PDs, can be determined. These constants play a crucial role in determining the iQY of the UCNPs, independent of the excitation profile. The equation representing the iQY, as derived in Chap. 2, is given by Eq. (4.5),

$$\eta_{j_{px}} = \frac{\phi_{j_o}}{\alpha N_a} \rho_{px}^{j-1} \prod_{i=1}^j \frac{1}{\rho_{px} + \rho'_i}. \quad (4.5)$$

The main distinction between the beam profile compensation approach presented in this section and the approach proposed by Mousavi et al. is that the authors of the previous study performed compensation by fitting the non-compensated QY curve with the excitation PD obtained from the FWHM definition of the beam radius. While their approach is suitable for highlighting the issues associated with using non-compensated QY for evaluating UC efficiency and comparing different samples, it is less practical in terms of analysis and introduces additional errors to the results due to unnecessary calculation steps.

## 4.2 Expanding the PD dynamic range of the excitation illumination

It is important to note that the method described in this section enables the retrieval of the UCL at a local level, specifically at the pixel level. This is achieved by utilising the excitation PD distribution across the cross-section of the illumination area to fit the resulting luminescence curve. This approach effectively extends the dynamic range of the PD evaluation by combining the dynamic range of the camera (represented by various  $\rho_{px}$  values) with the dynamic range of the laser (represented by various  $P_c$  values).

Each  $P_c$  value is distributed over a specific area of illumination, which is measured by the camera. Consequently, the evaluation at the pixel level allows for the study of the UCL and the QY of the UCNPs at lower PDs. Furthermore, high PDs can be achieved by confining the laser power within a small beam profile, while low PDs can be attained by distributing the power over a larger area of the beam profile. This approach increases the SNR of the measurement.

By combining the aforementioned method with two distinct measurements – one using a narrow beam profile and another using a wide profile – one can effectively study the properties of UCNPs across a wide range of power densities. This approach allows for the investigation of the non-linear and linear regimes of UCNPs, as well as the transitional range between them.

## 4.3 An example study

To illustrate this type of strategy, a water-soluble  $\beta$ - $\text{NaYF}_4:\text{Yb}^{3+}, \text{Yb}^{3+}\text{Tm}$  core-shell UCNP in aqueous solution, optimised for the 804 nm emission (an ETU2 process), was characterised using

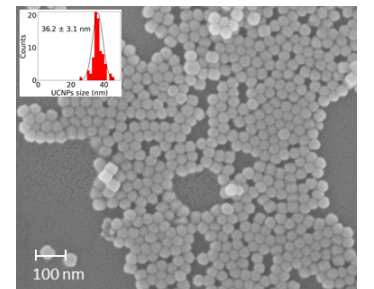


Figure 4.2: SEM image of the UCNPs.

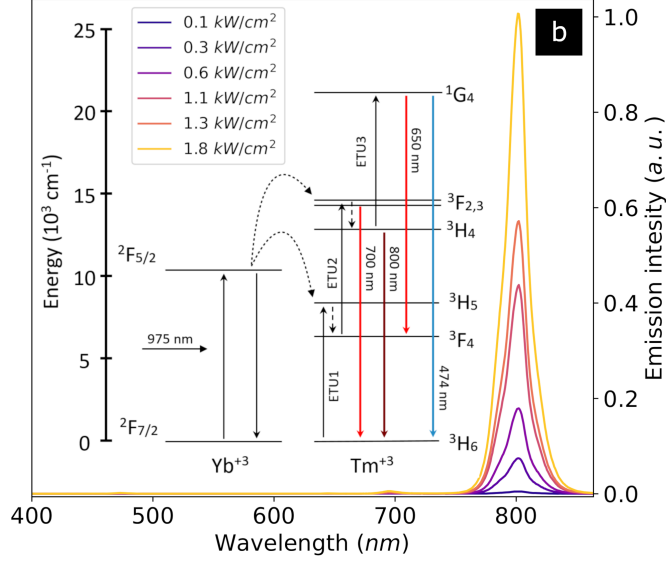


Figure 4.3: Luminescence spectra of the UCNPs under 976 *nm* excitation. The PDs shown in the legend of the figure were calculated using the FWHM definition of beam radius.

the first version of the QY system, as described in Paper II. The comprehensive results of this study were published in Paper I and are summarised as follows.

The morphology, structure, and size distribution of the UCNPs were analysed using a scanning electron microscope (SEM). The acquired image, shown in Fig. 4.2, displays hexagonal nanoparticles with an average size of 36 *nm*. To improve imaging, the UCNPs were coated with a thin layer of AuPd to prevent discharge.

The emission spectra were measured for the UCNP sample under various excitation PDs ranging from 100 *W/cm*<sup>2</sup> to 2000 *W/cm*<sup>2</sup>. The results are presented in Fig. 4.3, which also includes a diagram illustrating the electronic transitions commonly found in Yb-Tm-codoped UCNPs. The absence of any significant emission lines other than the 804 *nm* peak suggests that the UC process in this sample is predominantly governed by an ETU2 process. Therefore, the model proposed by Liu et al.[1] was employed for beam profile compensation. Consequently, the Eqs. (4.3) and (4.5) were simplified to Eqs. (4.6) and (4.7), respectively,

$$L_{2r} = 2\eta_b\mu_a \frac{\lambda_{ex}}{\lambda_{em}} A_{px} I P_c^2 \sum_{px}^m \frac{\gamma_{px}^2}{P_c \gamma_{px} + \rho_b}, \quad (4.6)$$

$$\eta_{2px} = 2\eta_b \frac{\rho_{px}}{\rho_{px} + \rho_b}. \quad (4.7)$$

The underlying physical mechanism behind the balancing PD point  $\rho_b$ , as proposed by Liu et al., has not been discussed or investigated in this study. It is worth noting that regardless of whether  $\rho_b$  corresponds to the transition point  $\rho_1$  or  $\rho_2$ , it leads to the same calculated iQY results.

The luminescence emitted by the UCNP sample was measured for various excitation powers ranging from 0 to approximately 200 *mW*, with an increment of 1.5 *mW*. The experiment was conducted twice, using two different beam profiles: a narrow beam referred to as BP1 and a wide beam referred to as BP2, with diameters of 106  $\mu\text{m}$  and 530  $\mu\text{m}$ , respectively. It is important to note that the beam diameters were determined based on the FWHM for reference purposes at this stage. The normalised profiles of the two beam profiles are illustrated in Fig. 4.4.

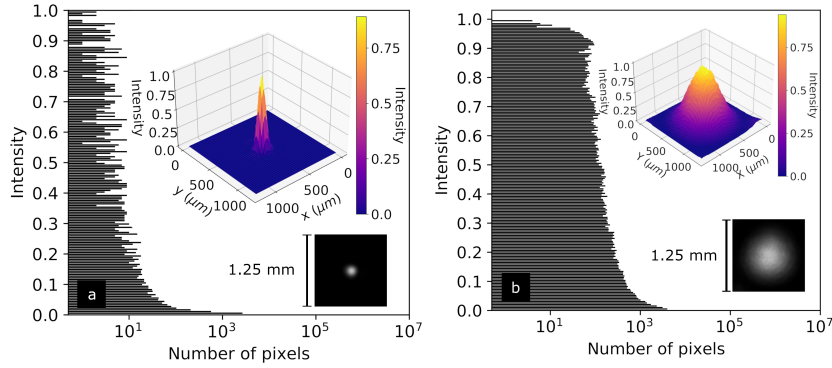


Figure 4.4: Profiles of the excitation beams (a) BP1 and (b) BP2 are shown in the figures. The histograms depict the number of pixels with identical intensities, which are also visualised by the 3D Gaussian surface in the inset. In the bottom-right corner of the figures, the original images captured by the CMOS camera were cropped to highlight the beam spots, with a length of 1.25 mm, for size comparison.

Table 4.1: Adjusted parameters obtained from the fitting of the resultant luminescence versus power at the centre of the cuvette for the UCNPs under BP1 and BP2 illumination.

Beam profile	$\eta_b$ (%)	$\rho_b$ ( $W/cm^2$ )
BP1	$2.28 \pm 0.02$	$43.7 \pm 3.2$
BP2	$2.29 \pm 0.06$	$43.8 \pm 2.0$

The resultant luminescence obtained under both profiles is presented in Fig. 4.5 as a function of the absorbed power at the centre of the cuvette, expressed in terms of power per unit volume. Despite being irradiated with the same power, the sample exhibited different emission characteristics. These findings clearly demonstrate the dependence of the UCL on the excitation beam profile, underscoring the significance of accurate beam profile compensation in determining the iQY of UCNPs.

By adjusting the parameters  $\eta_b$  and  $\rho_b$ , the curve described by Eq. (4.6) was fitted to the experimental luminescence data as a function of the power at the centre of the cuvette. The fitted results are presented in Tab. 4.1, and the corresponding fitted curves are represented by solid lines in Fig. 4.5. The close similarity and accuracy of the fitting parameters for both profiles demonstrate the consistency of the model in describing the underlying physics of the UC process. This justifies the application of the model to calculate the iQY as an intrinsic characteristic of these particles.

For PDs below the balancing point  $\rho_b = \sim 44 W/cm^2$ , the UCL exhibits a predominantly quadratic dependence on the PD. However, above  $\rho_b$ , the UCL demonstrates a linear behaviour.

#### 4.4 Detailed comparison of different compensation approaches

By applying the adjusted parameters to the iQY equation, Eq. (4.7), for the PDs at the pixel level  $\rho_{px}$  obtained from both BP1 and BP2 measurements, the compensated iQY curve (represented by the square data points) was derived. This curve was then plotted in a double-logarithmic scale in Fig. 4.6. The PDs ( $\rho_{px}$ ) at each pixel were used as the x-axis values for the iQY.

In addition, other curves in Fig. 4.6 were obtained by calculating the QY using different definitions for the beam radius, such as the FWHM,

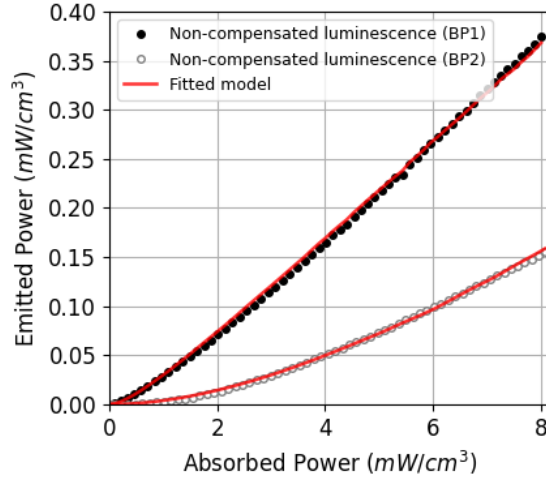


Figure 4.5: Resultant UCL measured under the BP1 and BP2 profiles as a function of the total power absorbed by the sample. The discrete circles represent the experimental data, while the continuous lines are the best fitted curves obtained from Eq. (4.6). The fitted constants are shown in the Tab. 4.1.

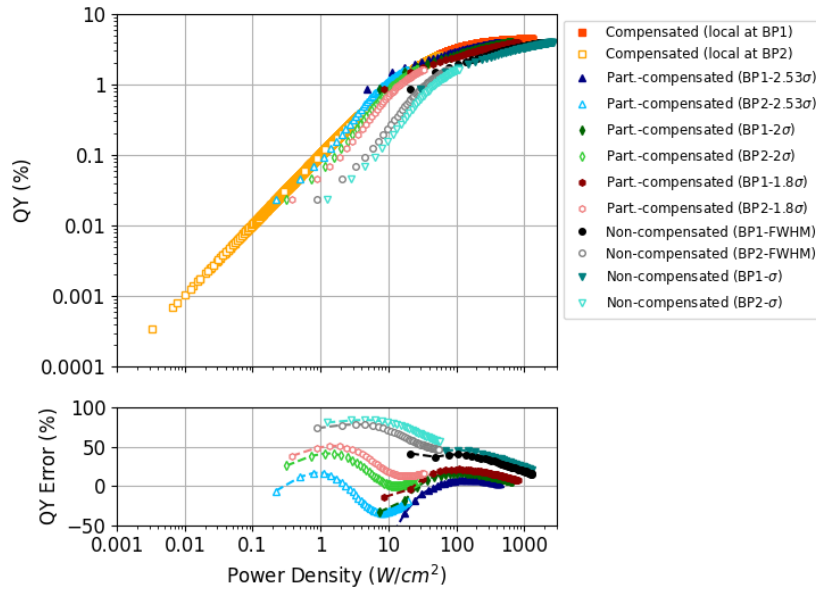


Figure 4.6: The compensated iQY of the UCNPs is compared to the non-compensated QY (with the beam radius defined as the FWHM), as well as to partially compensated QYs using different definitions of beam radius proportional to the standard deviation of the Gaussian representation of the beam profile ( $1\sigma$ ,  $1.8\sigma$ ,  $2\sigma$ , and  $2.53\sigma$ ).

and various distances from the centre of the beam proportional to the standard deviation of the Gaussian distribution. The power densities for these curves were determined based on different beam width definitions. Considering the iQY as the reference QY for a uniform power density illumination, the associated errors for each beam width definition were calculated and plotted at the bottom of Fig. 4.6.

The partially compensated QYs provide a more accurate approximation to the iQY compared to the non-compensated approach (FWHM), resulting in reduced errors. The FWHM method underestimates the QY by up to 75% at low PDs. The representation using  $2\sigma$  as the beam ra-

dius shows the lowest absolute error at PDs around  $10 \text{ W/cm}^2$ . However, at lower PDs, the error increases slightly due to the sample exhibiting a deviation from quadratic behaviour in the non-linear regime. Conversely, as the PD increases, all the methods tend to converge towards the saturation QY, leading to a rapid decrease in errors towards zero. The compensation method proposed by May and Berry[92] using  $1.8\sigma$  provides a good approximation in the non-linear regime, as it is optimised for the quadratic PD dependence of the UCL. However, as the power density increases and the UCL transitions to the linear regime, the error increases.

## 4.5 Summary

The beam profile compensation method presented in this chapter expands upon the work of Mousavi et al. for an arbitrary order ETU process. By utilising the model described in Chap. 2, the general equation was applied to experimental UC data of UCNPs measured using the initial version of the QY system. The results presented for the ETU2 process serve as an illustration of how the dynamic range of the camera can be combined with the use of two different beam profiles to extend the range of PDs over which the iQY is evaluated. Further details are provided in Paper **I**. In the last chapter the reader will find a comprehensive iQY characterisation of an UCNP sample exhibiting UCL at multiple wavelengths, including both ETU2 and ETU3 processes. The results were obtained from UC data measured using the final version of the QY system and analysed using the beam profile compensation method presented in this chapter.



---

# A COMPLETE QY CHARACTERISATION OF UC EMISSIONS IN THE NIR AND VIS RANGES INCORPORATING MULTIPLE ETU PROCESSES

---

This concluding chapter presents a detailed QY characterisation of UC-NPs that emit light simultaneously at different wavelengths, involving an ETU2 and two ETU3 processes. The study exemplifies the successful application of the QY system described in Chap. 3 and demonstrates the use of the general model developed in Chap. 2 for the analysis. This analysis enables the determination of the PD points and QY saturation for the energy levels involved in the UC processes. The iQY of the UCNPs is then calculated by applying the beam profile compensation method presented in Chap. 4. The comprehensive analysis and results are presented in detail in Paper **IV** and summarised as follows.

## 5.1 Methodology

A  $\beta$ -NaYF<sub>4</sub>:Yb<sup>3+</sup>,Tm<sup>3+</sup> UCNP was selected for the measurements, exhibiting main emission peaks at 800 nm, 650 nm, 470 nm, and 450 nm. The 800 nm emission corresponds to an ETU2, while the 650 nm and 470 nm emission lines correspond to ETU3 processes. The 450 nm emission is an ETU4, but it is only detectable by the system at PDs above 1 kW/cm<sup>2</sup>. The UCNP sample, purchased from Creative Diagnostics, was characterised following the measurement and analysis protocols described in Subsects. 3.3.4 and 3.3.5 in Chap. 3. The detailed methodology and results are presented in Paper **IV** and summarised in this chapter.

Initially, the emission spectra of the sample were measured as a function of PD to determine the appropriate selection of spectral filters for each APD in order to isolate a single transition per measurement. Subsequently, the UCL and absorption measurements were performed under 976 nm excitation using a Gaussian-shaped laser beam with a FWHM of 96  $\mu$ m, denoted as BP1.

The UCL at 800 nm and 470 nm wavelengths were measured using APD1 and APD2, respectively, with the corresponding spectral filters: LP700 (Thorlabs, FELH0700), and BP470 (Semrock, FF02-472/30-25). Then, the UCL at 650 nm wavelength was acquired using APD1 with a bandpass filter BP650 (Thorlabs, FBH650-40). To ensure consistency, the 470 nm UCL wavelength was measured again with APD2 as a reference to the initial data acquisition. These measurements were repeated

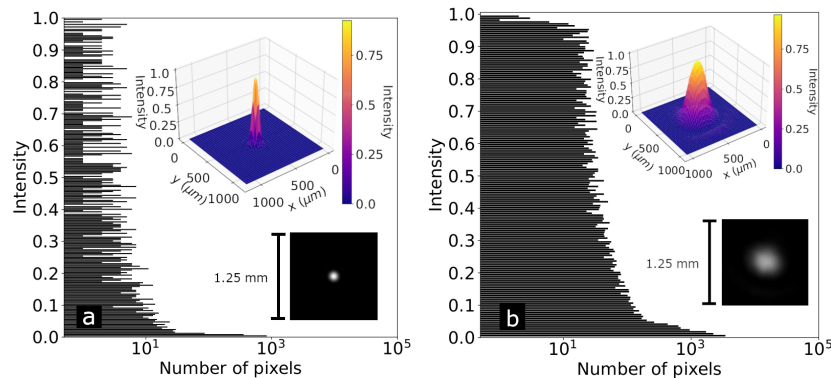


Figure 5.1: Profiles of the excitation beams, labelled as a) BP1 and b) BP2, are depicted. The pictures of the profiles, captured with the CMOS camera, are shown at the bottom right of the plots. The corresponding 3D surface plots illustrate the Gaussian shape of the beams. The histograms represent the distribution of the number of pixels with identical normalised intensities. BP1 and BP2 have beam widths of  $96 \mu\text{m}$  and  $300 \mu\text{m}$ , respectively, both measured as the FWHM.

using a second Gaussian beam profile, denoted as BP2, with a wider beam width of  $300 \mu\text{m}$  (FWHM). The beam profiles were designed to cover a wider dynamic range, following the same principles outlined in the previous chapter.

Fig. 5.1 illustrates the profiles of the excitation beams, with BP1 on the left and BP2 on the right. The bar charts depict the histograms of intensity distributions at the cross-sections of the beams, where the x-axes represent the number of pixels with identical intensities. The 3D surface insets display the Gaussian shapes of the beams, with the normalised intensities represented by the colour scale bar. The bottom right of the plots show pictures of the beam profiles taken with the CMOS camera, cropped around the beam spots.

## 5.2 Characterisation

Morphology, dispersion, and size distribution of the UCNPs were investigated using a scanning transmission electron microscope (STEM) to capture nanoparticle images. The UCNPs exhibited a hexagonal morphology with an average size of  $16 \pm 2 \text{ nm}$ , as shown in Fig. 5.2. The size distribution, presented as a histogram in the plot, was derived from the analysis of 100 nanoparticles.

Emission spectra were recorded across a range of PDs from  $0.2 \text{ kW/cm}^2$  to  $2.7 \text{ kW/cm}^2$  and are displayed in Fig. 5.3. The energy level diagram of  $\text{Yb}^{3+}$ , the sensitizer, and  $\text{Tm}^{3+}$ , the activator, highlights the electronic transitions involved in the UC processes. The UCNPs exhibited a prominent emission peak at  $800 \text{ nm}$ , resulting from the ETU2 transition from the energy level  $^5H_4$  to the ground state  $^3H_6$ . The secondary peaks at  $470 \text{ nm}$  and  $650 \text{ nm}$  corresponded to ETU3 processes, involving electronic decay from the  $^3G_4$  energy level to the ground state  $^3H_6$  and to an intermediate state  $^3F_4$ , respectively.

Additionally, an ETU4 process at  $450 \text{ nm}$  was observed, arising from the electronic decay from the  $^3D_2$  energy level to the intermediate state  $^3F_4$ . Due to the relatively low intensities of the ETU4 transition, its QY was not evaluated in this study.

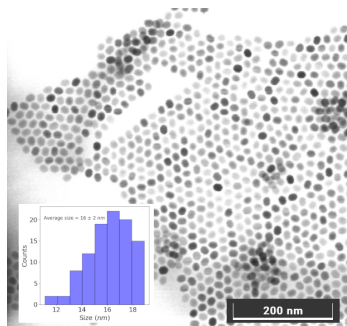


Figure 5.2: STEM image of the UCNPs exhibiting a hexagonal morphology. The nanoparticles displayed excellent dispersion with no clustering observed. The inset depicts the size distribution of 100 randomly selected UCNPs, as determined through post-image analysis.

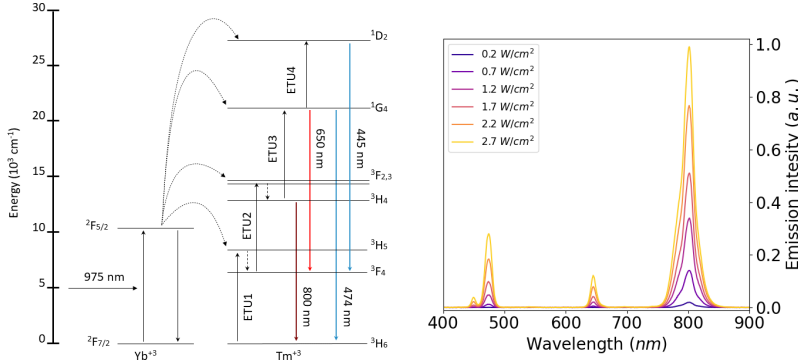


Figure 5.3: The energy level diagram displayed in the left panel highlights the electronic transitions involved in the ETU processes, while the right panel shows the emission spectra with distinct peaks at wavelengths of 800 nm, 650 nm, 470 nm, and 450 nm, corresponding to these electronic transitions.

### 5.2.1 The transition PD points

The transition PD points for the UCNPs under BP1 and BP2 illuminations are illustrated in Fig. 5.4. The transitions at 470 nm (top panel), 650 nm (middle panel), and 800 nm (bottom panel) are presented. The y-axes depict the emitted power from the UCNPs within the central volume of the cuvette, while the x-axis represents the total excitation power. The filled markers represent measurements taken under BP1 illumination, while the empty markers correspond to BP2 illumination.

By comparing the y-axes of the three graphs in Fig. 5.4, it is evident that the 800 nm transition exhibits the highest intensity, followed by the 470 nm and 650 nm transitions. This is consistent with the relative intensities of the peaks observed in the emission spectra shown in Fig. 5.3. Similar to what has been discussed in Chap. 4, the displacement of the curves in each plot indicates the dependence of the UCL on the beam profile, resulting from the non-linear behaviour of the UC process. The similar shape of the 470 nm curves with the 650 nm curves under the same beam profile suggests that both transitions have the same PD dependence, in agreement with the theoretical expectation that the PD dependence is determined by the order of the ETU process, with both being ETU3 transitions. In contrast, the 470 nm and 650 nm curves differ from the 800 nm curve, which corresponds to an ETU2 process. Furthermore, it can be observed that the 800 nm UCL reaches linearity earlier than the ETU3 curves under the same beam profile illumination. This can be attributed to the lower order of the ETU process for the 800 nm transition.

The continuous lines in Fig. 5.4 represent the fittings of Eq. (4.3) to the experimental data. It is evident from the almost perfect overlapping of the fittings with the data points in that the theoretical model accurately describes the ETU processes involved in these UCNPs. This is further supported by the similarity of the fitted coefficients shown in Tab. 5.1 for different emission wavelengths and beam profiles.

To determine the transition PD points and saturation iQY values for each emission line, the free parameters of Eq. (4.3) were adjusted to the UCL data. In the case of the 800 nm emission, the ETU process order  $j$  was considered to be 2, while for the 470 nm and 650 nm curves,  $j$  was considered to be 3, corresponding to the orders of the ETU processes governing the UCL at each wavelength.

The fitting of each curve was performed independently, with an initial

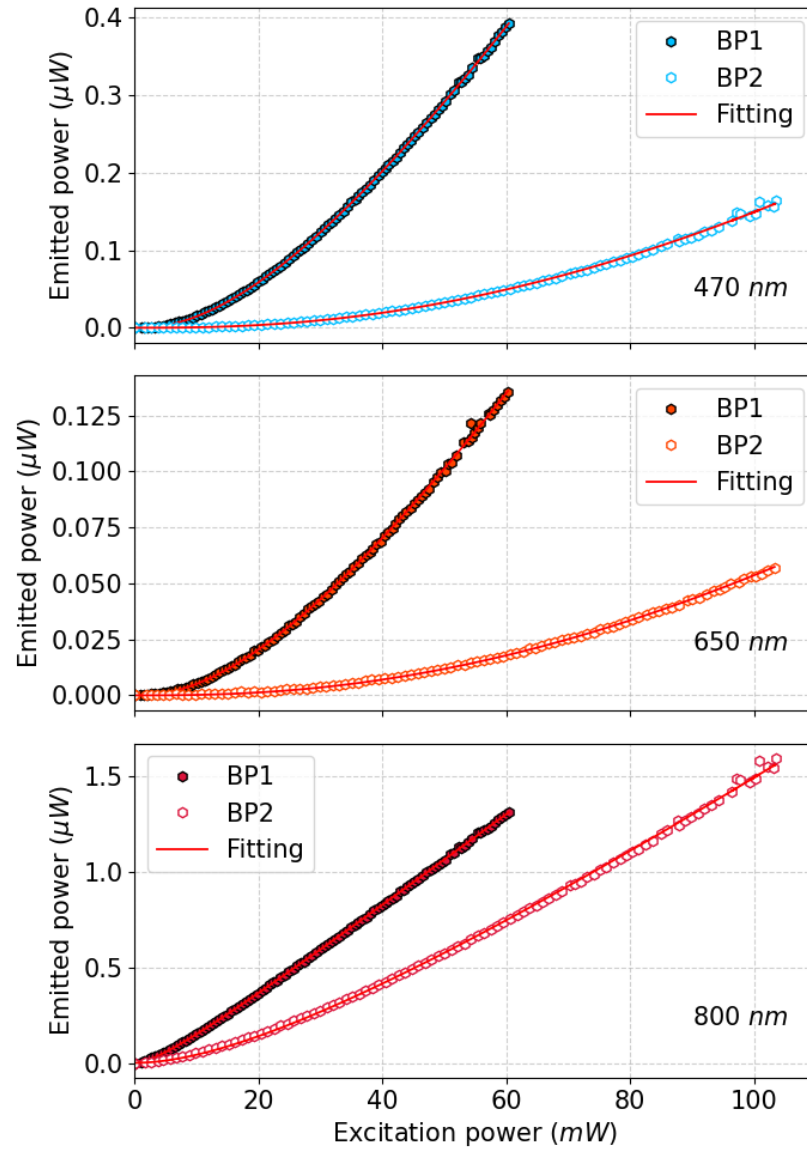


Figure 5.4: UCL measurements at 470 nm, 650 nm, and 800 nm are depicted. The filled markers represent measurements taken under BP1 illumination, while the empty markers correspond to BP2 illumination. The continuous curves represent the fitting curves with the best parameters, which are detailed in Tab. 5.1.

guess for the transition point  $\rho_1$  above  $5 \text{ kW/cm}^2$  as a boundary condition. This initial assumption was made due to the typical anomalous power density dependence observed in UCNPs. Alternatively, the same initial principle could be applied to  $\rho_2$  instead, yielding similar fittings. This interchangeability of  $\rho_1$  and  $\rho_2$  arises from the symmetry of these parameters in Eq. (4.3) for  $j > 1$ .

The determination of whether  $\rho_1$  or  $\rho_2$  corresponds to the larger parameter can only be concluded by measuring downconverted luminescence (luminescence wavelength higher than the excitation wavelength), if it is detectable for these UCNPs. If the downconverted luminescence curve exhibits a transition point from quadratic to linear behaviour coinciding with the transition point of the  $800 \text{ nm}$  emission curve, then the observed transition point corresponds to  $\rho_1$ . On the other hand, if the downconverted luminescence curve does not show any transition at this point, then the transition point of the  $800 \text{ nm}$  emission corresponds to  $\rho_2$ .

Table 5.1: Adjusted parameters obtained from fitting the resultant luminescence versus power at the centre of the cuvette for the UCNPs under BP1 and BP2 illumination, as shown in the Fig. 5.4.

<b>B. Prof.</b>	$\lambda_{em}$ (nm)	$\rho_1$ ( $W/cm^2$ )	$\rho_2$ ( $W/cm^2$ )	$\rho_3$ ( $W/cm^2$ )	$\eta_S$ (%)
BP1	470	$5.7 \times 10^4$	31	$3.7 \times 10^2$	0.30
BP1	650	$5.6 \times 10^4$	31	$3.6 \times 10^2$	0.14
BP1	804	$6.2 \times 10^4$	31	-	0.82
BP2	470	$6.1 \times 10^4$	31	$4 \times 10^2$	0.28
BP2	650	$6.0 \times 10^4$	31	$4 \times 10^2$	0.14
BP2	804	$6.2 \times 10^4$	33	-	0.78

The lowest transition PD point was found to be approximately  $31 \text{ W/cm}^2$ , followed by the second lowest value,  $\rho_3$ , which was approximately  $4 \times 10^2 \text{ W/cm}^2$ , and finally the largest value, around  $6 \times 10^4 \text{ W/cm}^2$ . The order of magnitude difference between  $\rho_3$  and  $\rho_2$  is consistent with the low intensity of the ETU4 emission line.  $\rho_3$  is directly proportional to the ratio of the decay rate  $R_3$  (from the third excited state) to the ET rate  $W_3$  (from the third excited state to the fourth excited state). A larger ratio indicates a lower population density of the fourth excited state, resulting in fewer emitted photons for the ETU4 process, which explains the weak intensity of the  $450 \text{ nm}$  emission peak. The precise value of  $\rho_1$  requires further analysis for accurate determination as it falls outside the measured excitation PD range.

The parameter that was fitted with a reasonable confidence interval in the analysis is the saturation iQY,  $\eta_S$ . This constant is defined as the ratio of the UCL saturation to the largest transition PD point,  $L_S/\rho_1$ . Therefore, there exist multiple solutions for  $L_S$  and  $\rho_1$  that satisfy the saturation level of the iQY. Regardless of the exact value of  $\rho_1$ , it is sufficiently large to remain undetected within the measurement range. This finding is consistent with the lower QY observed in UCNPs compared to bulk materials, which typically do not exhibit the anomalous PD dependence.

Reducing  $\rho_1$  can be achieved by decreasing the decay rate from the first excited state  $R_1$  or increasing the ET rate from the first excited state to the second excited state  $W_1$ . Both scenarios lead to higher population densities in all energy states above, resulting in increased quantum yield for the ETU processes. Therefore,  $\rho_1$  not only affects the linearity/non-linearity of the UCL at all wavelengths but also contributes to the low quantum yield of the UCNPs.

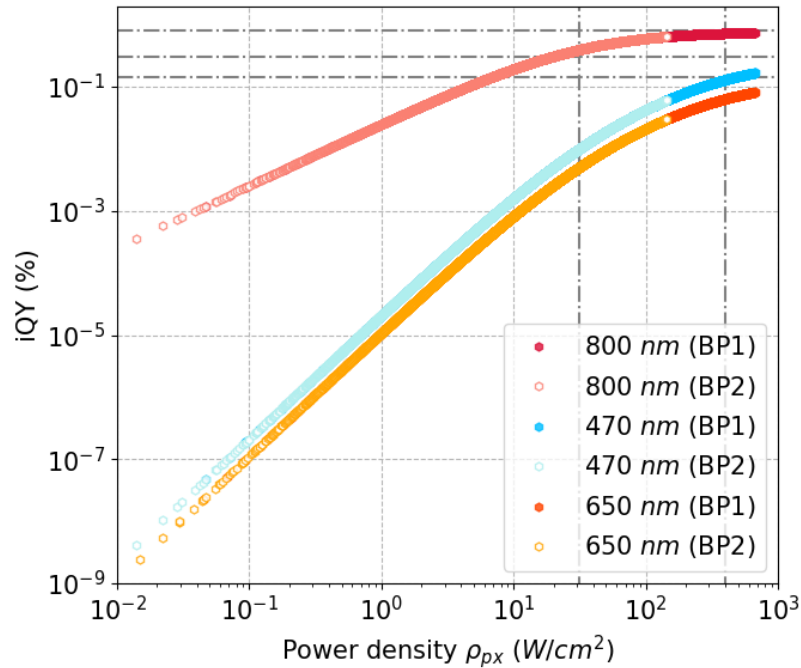


Figure 5.5: iQY curves of the 470 nm, 650 nm and 800 nm transitions of the UCNPs under the excitation profiles BP1 and BP2. The full markers correspond to the BP1 illumination whereas the empty markers correspond to the BP2. The vertical dashed lines indicate the transition PD points, and the horizontal lines represent the iQY saturation levels of the curves.

The impact of decay rates and ET rates on the QY of upconversion is well known among condensed matter researchers striving to engineer more efficient UCNPs. However, the quantification and formal relationship between QY and the PD dependence of UC is presented here for the first time using the general model introduced in this study.

### 5.2.2 The beam profile compensated iQY

Finally, the iQY curves were obtained by substituting the fitted values from Tab. 5.1 into the constants of Eq. (4.5), corresponding to the various local excitation PDs measured at the CMOS camera pixels. As previously mentioned,  $j$  was set to 2 for the 800 nm wavelength, and  $i$  was set to 3 for the 470 nm and 650 nm wavelengths. The iQY curves for the three emission wavelengths are presented in Fig. 5.5. The discrete hexagons represent the iQY values, while the vertical dashed lines indicate the first and second transition PD points. The first transition point is relevant for all three wavelengths, while the second transition point only applies to the 470 nm and 650 nm wavelengths, corresponding to the ETU3 processes. The horizontal dashed lines represent the iQY saturation levels for each wavelength.

Within the PD range of the measurement, the iQY for the 800 nm emission reaches its saturation level at high PDs. On the other hand, the iQY for the other two wavelengths is still transitioning towards saturation at the highest PDs achieved with the narrow excitation profile BP1.

Below the first transition point, the iQY for the 800 nm emission predominantly exhibits a linear behaviour, while the iQYs for the other two wavelengths demonstrate a quadratic power density dependence. This is a direct consequence of the PD dependence of the QY, which is one order

lower than the PD dependence of the UCL.

Above the first transition point  $\rho_2$ , the iQY for the 800 nm emission undergoes a transition and eventually reaches saturation. The second transition point  $\rho_3$  primarily affects higher ETU transitions. The 470 nm and 650 nm emissions exhibit linearity within a limited range of PDs between the two transition points. As the excitation PD increases beyond  $\rho_2$ , the ETU3 emissions transition to linearity and quickly become influenced by the second transition point  $\rho_3$ . Consequently, the slope of the iQY curves for both wavelengths, represented in a double logarithmic plot, changes from 2 to values lower than 1 as the PD approaches and exceeds the second transition point.

### 5.3 Summary

This chapter provides a summary of the research conducted during the PhD project. The comprehensive iQY characterisation of the UCNPs sample with multiple wavelength emissions demonstrates the capability of the QY system to perform simultaneous measurements at different wavelengths. The UCL data showcase the high resolution and wide dynamic range achieved in excitation PD through the successful implementation of the system, coupled with accurate analysis and theoretical modelling. Furthermore, the congruent results obtained for the transition PD points and the excellent agreement between the fitted curves and empirical data strengthen the analytical solutions for representing iQY in terms of transition points and saturation levels. However, the determination of whether  $\rho_1$  or  $\rho_2$  is the larger parameter remains an open question, which can be resolved by evaluating the downconverted light. Nevertheless, the improved understanding of the UC process opens up opportunities for further exploration, and the engineering of optimal UCNPs.



# CONCLUSIONS AND FUTURE PERSPECTIVE

---

---

The low QY remains a significant barrier to the widespread utilisation of UCNPs in biomedical applications, and limited research has been conducted thus far to understand the PD dependence of UC and its relationship to QY. Non-linearity is an intriguing property of UC, but its characterisation has proven to be a circular problem, where the development of equipment capable of measuring non-linearity depends on a thorough understanding of UC behaviour. Conversely, the study of such behaviour typically requires an in-depth empirical investigation into the physical nature of UC and UCNPs.

Over the course of the past four years, this research has systematically addressed these challenges by breaking down the problem into smaller tasks. The initial version of the QY system provided valuable relative QY results measured under different excitation beam profiles. These data were extensively compared to various mathematical models, including complex analytical and numerical solutions that represented potential UC behaviours as a function of excitation PDs. Only with the development of the second version of the QY setup was a complete analytical model achieved.

The optimal model, as demonstrated in Chap. 2, is the simplest one, encompassing only the population and depopulation rates of the electronic energy states of the ions involved in the ETU processes. The second version of the QY system, described in Chap. 3, not only introduced new features, such as simultaneous measurements at different wavelengths, but also implemented important improvements to optimise the analysis process. The software controller of the system enabled instant visualisation of results as data were acquired. This step was crucial for alignment and calibration, which needed to be performed before each UCNP sample characterisation.

The presented analytical model elegantly connects microscopic characteristics of the RE elements embedded within the host matrix with macroscopic luminescence observations. The determination of transition PD points enables the quantification of boundaries that delineate distinct regimes of PD dependence for various ETU processes. The mathematical solutions offer a wide range of possibilities for future research, ranging from characterisation and simulations to the study of population and depopulation dynamics of energy levels in upconverting materials.

Time-resolved analysis, particularly of the rise time, is critical for biophotonics applications. The rise time of an UC process tends to be longer than the decay time due to the multiple steps required to populate an energy state, while radiative decay occurs in a single step, resulting in a shorter decay time. The utilisation of pulsed laser light can reduce heating of living tissues during exposure while increasing the amount of UC light delivered to cells. This is a consequence of the non-linearity of UC, where a one-order-of-magnitude increase in PD results in a three-

order-of-magnitude gain in UCL for the cubic regime of an ETU3 process, for example. However, such gains can only be achieved by matching the laser pulse duration with the rise time of the energy states responsible for UC emissions. Research in this direction is of utmost importance, particularly for higher-order ETU processes, such as those applied in optogenetics, which benefit from the blue emission of UCNPs.

In conclusion, the findings presented in this thesis represent a critical and substantial contribution to the advancement of the UC field, bridging the perspectives of condensed matter physics and biophotonics. These two disciplines must work together for the successful utilisation of UCNPs in biomedical applications.

# COMMENTS ON THE PAPERS

---

## **I Evaluation of relative beam-profile-compensate quantum yield of upconverting nanoparticles over wide dynamic range of power densities**

This paper presents a beam profile compensation method based on rate equations for a two-photon energy transfer upconversion process (ETU2). The method was applied to evaluate the 800 *nm* emission of a Yb-Tm-codoped upconverting nanoparticle (UNCP) over a wide dynamic range of power densities. The measured internal quantum yield (iQY) results were compared to the non-compensated and partially-compensated quantum yields to emphasize the significance of accurate measurements and evaluation in studying and comparing the efficiency of different UCNPs. During the validation phase of the quantum yield system, I proposed this method after conducting an extensive analysis of the upconversion data under distinct excitation profiles. I was primarily responsible for data collection and performed all data analysis, including coding the scripts for data pre-processing. Additionally, I took the lead in writing the manuscript.

## **II Multi-variable compensated quantum yield measurements of upconverting nanoparticles with high dynamic range: a systematic approach**

This paper describes the development of a quantum yield (QY) system for measuring the efficiency of the upconversion process in the near-infrared emission range of UCNPs. The initial setup was based on a device previously constructed by the group in another research centre. I made significant contributions to the assembly, testing, validation, and data collection stages of the system. Moreover, I performed all data analysis and contributed to the manuscript writing. It is important to note that the latest version of the QY system is not discussed in this paper.

### III Generalised analytical model of the transition power densities of the upconversion luminescence and quantum yield

This work presents an analytical model for evaluating the quantum yield (QY) of a general energy transfer upconversion process in upconverting nanoparticles (UCNPs). While initially studying the model for a two-photon process, I discovered that it could not accurately describe the two-photon process in UCNPs with multiple wavelength emissions, including higher-order processes such as Tm-UCNPs with near-infrared and blue emission. This led to the expansion of the existing model to include other wavelengths, resulting in the QY characterisation based on transition power density points. The study includes a detailed analysis of microscopic quantities and their relationship to the distinct properties observed in UCNPs and their bulk counterparts. I derived the mathematical solutions and was responsible for data collection, analysis, and manuscript preparation.

### IV Beam-profile compensation for quantum yield characterisation of Yb-Tm codoped upconverting nanoparticles emitting at 474 nm, 650 nm and 804 nm (Submitted for publication)

In this study, the analytical general model was applied to perform beam-profile compensation and obtain the internal quantum yield (iQY) of an upconverting nanoparticle (UCNP) material with multiple wavelength emissions, including ETU2 (800 nm emission) and ETU3 processes (470 nm and 650 nm emissions). Transition power density points and QY saturation levels were determined and compared among the different ETU processes. I was responsible for building the latest version of the quantum yield system used for these measurements, which involved project planning, assembly, testing, and validation. In addition, I developed the automated Python controller for data acquisition and storage. The data analysis was conducted by me, and I wrote the manuscript.

# COMMENTS ON THE PATENTS

---

## **I Optical system and method**

To date, there is currently no commercially available system capable of accurately measuring the quantum yield of upconverting materials. The non-linear nature of upconversion necessitates the shaping and evaluation of the excitation beam profile prior to quantum yield analysis. As a result, this patent has been granted, covering the apparatus and method for conducting optical characterisation of luminescent particles within a sample.



# ACKNOWLEDGEMENTS

---

I would like to express my deepest gratitude to my supervisors, **Stefan Andersson-Engels** and **Silvia Melgar**, who guided me in conducting this research project. I am truly thankful for their invaluable support, guidance, and expertise throughout this journey. I am grateful to the **Science Foundation Ireland (SFI)**, the **Irish Photonics Centre (IPIC)**, the **Physics department at University College Cork**, and **Tyndall National Institute** for providing the funding and facilities that made this research possible. Their contributions have been instrumental in the success of this project. I extend my sincere appreciation to the **examiners** for their time and effort in reviewing this work. Their valuable feedback and insights have greatly contributed to the refinement and quality of this thesis.

During my time in the Biophotonics team, I have had the privilege of working with exceptional individuals whom I am also grateful to. Special thanks to **Kasia**, my research advisor, for sharing your laboratory skills, engaging in insightful discussions, and motivating me to write manuscripts. To all the members of the UCNP group, especially **Sana**, **Gokhan**, and **Kho**, with whom I have spent most of my time working, it has been a pleasure collaborating with you all. I would also like to thank **Marcelo** for the moments we shared speaking in our native language amid our work. To **Siddra** and **Michael Amissah**, thank you for the enjoyable experiences of teaching undergraduate students at UCC.

I want to express my gratitude to **Andrea** for being a wonderful friend, sharing a passion for Science, and your amazing coffee cake. To **Kon**, thank you for your assistance with LabView skills. **Simon**, your insights on rate equations provided me with a clear direction for initiating simulations. **Baptiste**, I appreciate your friendship, valuable advice on implementing optics solutions, and your expertise in Matlab.

I would like to thank **Marinara** for the insightful discussions we had during the launch of SmartEdu. I have learned a great deal from your talent and expertise.

Lastly, I am indebted to my **friends** who have always believed in me and supported me throughout this journey. To my parents, **Terezinha** and **Benedito**, thank you for your unwavering efforts in enabling me to pursue higher education. I am aware of the sacrifices you made, working seven days a week on the farm. I acknowledge that your dedication and hard work were more challenging than my PhD. **Giulia**, your support has been invaluable, and your encouragement has always propelled me forward, pushing me to reach new heights.



# REFERENCES

---

- [1] Haichun Liu, Can T. Xu, David Lindgren, Haiyan Xie, Diana Thomas, Carsten Gundlach, and Stefan Andersson-Engels. Balancing power density based quantum yield characterization of upconverting nanoparticles for arbitrary excitation intensities. *Nanoscale*, 5(11):4770–4775, 2013. ISSN 20403364. doi: 10.1039/c3nr00469d.
- [2] Qi Pian, Chao Wang, Xueli Chen, Jimin Liang, Lingling Zhao, Ge Wang, and Xavier Intes. Multimodal biomedical optical imaging review: Towards comprehensive investigation of biological tissues. *Current Molecular Imaging*, 3:72–87, 11 2014. ISSN 22115552. doi: 10.2174/2211555203666141117231651.
- [3] Jiating Xu, Arif Gulzar, Piaoping Yang, Huiting Bi, Dan Yang, Shili Gai, Fei He, Jun Lin, Bengang Xing, and Dayong Jin. Recent advances in near-infrared emitting lanthanide-doped nanoconstructs: Mechanism, design and application for bioimaging. *Coordination Chemistry Reviews*, 381:104–134, 2019. ISSN 00108545. doi: 10.1016/j.ccr.2018.11.014. URL <https://doi.org/10.1016/j.ccr.2018.11.014>.
- [4] Alper Corlu, Regine Choe, Turgut Durduran, Mark A. Rosen, Martin Schweiger, Simon R. Arridge, Mitchell D. Schnall, and Arjun G. Yodh. Three-dimensional in vivo fluorescence diffuse optical tomography of breast cancer in humans. *Opt. Express*, 15(11):6696–6716, May 2007. doi: 10.1364/OE.15.006696. URL <http://opg.optica.org/oe/abstract.cfm?URI=oe-15-11-6696>.
- [5] Vivek Venugopal and Xavier Intes. Recent advances in optical mammography. *Current Medical Imaging Reviews*, 8:244–259, 08 2012. doi: 10.2174/157340512803759884.
- [6] Ting Ai, Wenting Shang, Hao Yan, Chaoting Zeng, Kun Wang, Yuan Gao, Tianpei Guan, Chihua Fang, and Jie Tian. Near infrared-emitting persistent luminescent nanoparticles for hepatocellular carcinoma imaging and luminescence-guided surgery. *Biomaterials*, 167:216–225, 2018. doi: 10.1016/j.biomaterials.2018.01.031.
- [7] Rogério Alves Costa, Mirian Skaf, Luiz Alberto Soares Melo, Daniela Calucci, José Augusto Cardillo, Jarbas C. Castro, David Huang, and Maciej Wojtkowski. Retinal assessment using optical coherence tomography. *Progress in Retinal and Eye Research*, 25:325–353, 2006.
- [8] Chinmay D. Darne, Yujie Lu, and Eva M. Sevick-Muraca. Small animal fluorescence and bioluminescence tomography: a review of approaches, algorithms and technology update. *Physics in Medicine and Biology*, 59:R1 – R64, 2014.
- [9] Frederic Leblond, Scott C. Davis, Pablo A. Valdés, and Brian W. Pogue. Pre-clinical whole-body fluorescence imaging: Review

- of instruments, methods and applications. *Journal of Photochemistry and Photobiology B: Biology*, 98(1):77–94, 2010. ISSN 1011-1344. doi: <https://doi.org/10.1016/j.jphotobiol.2009.11.007>. URL <https://www.sciencedirect.com/science/article/pii/S1011134409002061>.
- [10] Yu Chen, Shuai Yuan, Jerry Wierwille, Chao-Wei Chen, Tiffany R. Blackwell, Paul T. Winnard, Venu Raman, and Kristine Glunde. Integrated optical coherence tomography (oct) and fluorescence laminar optical tomography (flot) for depth-resolved subsurface cancer imaging. In *Biomedical Optics and 3-D Imaging*, page BSuD9. Optica Publishing Group, 2010. doi: 10.1364/BIOMED.2010.BSuD9. URL <http://opg.optica.org/abstract.cfm?URI=BIOMED-2010-BSuD9>.
- [11] Yurong Wei, Xiangdong Yang, Yurou Ma, Shengfu Wang, and Quan Yuan. Lanthanide-doped nanoparticles with near-infrared-to-near-infrared luminescence for bioimaging. *Chinese Journal of Chemistry*, 34(6):558–569, 2016. doi: <https://doi.org/10.1002/cjoc.201500755>. URL <https://onlinelibrary.wiley.com/doi/abs/10.1002/cjoc.201500755>.
- [12] Lin Yuan, Weiyang Lin, Kaibo Zheng, and Sasa Zhu. Fret-based small-molecule fluorescent probes: Rational design and bioimaging applications. *Accounts of Chemical Research*, 46(7):1462–1473, 2013. doi: 10.1021/ar300273v. URL <https://doi.org/10.1021/ar300273v>. PMID: 23419062.
- [13] John V Frangioni. In vivo near-infrared fluorescence imaging. *Current Opinion in Chemical Biology*, 7(5):626–634, 2003. ISSN 1367-5931. doi: <https://doi.org/10.1016/j.cbpa.2003.08.007>. URL <https://www.sciencedirect.com/science/article/pii/S1367593103001091>.
- [14] Andrew M. Smith, Michael C. Mancini, and Shuming Nie. Second window for in vivo imaging. *Nature Nanotechnology*, 4(11):710–711, Nov 2009. ISSN 1748-3395. doi: 10.1038/nnano.2009.326. URL <https://doi.org/10.1038/nnano.2009.326>.
- [15] Jie Shen, Guanying Chen, Anne-Marie Vu, Wei Fan, Osman S. Bilsel, Chun-Chih Chang, and Gang Han. Engineering the upconversion nanoparticle excitation wavelength: Cascade sensitization of tri-doped upconversion colloidal nanoparticles at 800 nm. *Advanced Optical Materials*, 1(9):644–650, 2013. doi: <https://doi.org/10.1002/adom.201300160>. URL <https://onlinelibrary.wiley.com/doi/abs/10.1002/adom.201300160>.
- [16] Jiaying Wu, Zhenxiong Shi, Linlin Zhu, Jie Li, Xu Han, Man Xu, Shiping Hao, Yibo Fan, Tao Shao, Hua Bai, Bo Peng, Wenbo Hu, Xiaowang Liu, Chuanhao Yao, Lin Li, and Wei Huang. The design and bioimaging applications of nir fluorescent organic dyes with high brightness, 4 2022. ISSN 21951071.
- [17] Sandhya Vardharajula, Zulfikar Ali Shaik, Pooja Tiwari, Erdal Eroglu, Komal Vig, Vida Dennis, and Shree Singh. Functionalized carbon nanotubes: Biomedical applications. *International journal of nanomedicine*, 7:5361–74, 10 2012. doi: 10.2147/IJN.S35832.
- [18] Xiaohu Gao, Yuanyuan Cui, Richard M. Levenson, Leland W. K. Chung, and Shuming Nie. In vivo cancer targeting and imaging with semiconductor quantum dots. *Nature Biotechnology*, 22(8):969–976, Aug 2004. ISSN 1546-1696. doi: 10.1038/nbt994. URL <https://doi.org/10.1038/nbt994>.

- [19] Zhuang Liu, Corrine Davis, Weibo Cai, Lina He, Xiaoyuan Chen, and Hongjie Dai. Circulation and long-term fate of functionalized, biocompatible single-walled carbon nanotubes in mice probed by raman spectroscopy. *Proceedings of the National Academy of Sciences*, 105(5):1410–1415, 2008. doi: 10.1073/pnas.0707654105. URL <https://www.pnas.org/doi/abs/10.1073/pnas.0707654105>.
- [20] Eva Hemmer, Nallusamy Venkatachalam, Hiroshi Hyodo, Akito Hattori, Yoshie Ebina, Hidehiro Kishimoto, and Kohei Soga. Up-converting and nir emitting rare earth based nanostructures for nir-bioimaging. *Nanoscale*, 5:11339–11361, 2013. doi: 10.1039/C3NR02286B. URL <http://dx.doi.org/10.1039/C3NR02286B>.
- [21] Haichun Liu, Can T. Xu, Gökhan Dumlupinar, Ole B. Jensen, Peter E. Andersen, and Stefan Andersson-Engels. Deep tissue optical imaging of upconverting nanoparticles enabled by exploiting higher intrinsic quantum yield through use of millisecond single pulse excitation with high peak power. *Nanoscale*, 5(20):10034–10040, 2013. ISSN 20403364. doi: 10.1039/c3nr01917a.
- [22] Jie Shen, Liang Zhao, and Gang Han. Lanthanide-doped upconverting luminescent nanoparticle platforms for optical imaging-guided drug delivery and therapy. *Advanced drug delivery reviews*, 65(5): 744–755, May 2013. ISSN 0169-409X. doi: 10.1016/j.addr.2012.05.007. URL <https://doi.org/10.1016/j.addr.2012.05.007>.
- [23] Yujia Liu, Yiqing Lu, Xusan Yang, Xianlin Zheng, Shihui Wen, Fan Wang, Xavier Vidal, Jiangbo Zhao, Deming Liu, Zhiguang Zhou, Chenshuo Ma, Jiajia Zhou, James A. Piper, Peng Xi, and Dayong Jin. Amplified stimulated emission in upconversion nanoparticles for super-resolution nanoscopy. *Nature*, 543:229–233, 3 2017. ISSN 14764687. doi: 10.1038/nature21366.
- [24] Qiuqiang Zhan, Sailing He, Jun Qian, Hao Cheng, and Fuhong Cai. Optimization of optical excitation of upconversion nanoparticles for rapid microscopy and deeper tissue imaging with higher quantum yield. *Theranostics*, 3:306–316, 2013. ISSN 18387640. doi: 10.7150/thno.6007.
- [25] Andries Meijerink and Freddy T Rabouw. Giant photon avalanches in tiny particles. *Nature News & views*, 2021.
- [26] Niagara Muhammad Idris, Muthu Kumara Gnanasammandhan, Jing Zhang, Paul C. Ho, Ratha Mahendran, and Yong Zhang. In vivo photodynamic therapy using upconversion nanoparticles as remote-controlled nanotransducers. *Nature Medicine*, 18(10):1580–1585, 2012. ISSN 10788956. doi: 10.1038/nm.2933.
- [27] Yuhui Wang, Lei Bao, Zhihong Liu, and Dai Wen Pang. Aptamer biosensor based on fluorescence resonance energy transfer from up-converting phosphors to carbon nanoparticles for thrombin detection in human plasma. *Analytical Chemistry*, 83(21):8130–8137, 2011. ISSN 00032700. doi: 10.1021/ac201631b.
- [28] Yanqiu Tao, Arthur J Y Huang, Yuki Hashimoto-dani, Masanobu Kano, Angelo H All, Iku Tsutsui-kimura, Kenji F Tanaka, Xiaogang Liu, and Thomas J Mchugh. Near-infrared deep brain stimulation via upconversion nanoparticle-mediated optogenetics. 684:679–684, 2018.

- [29] Jikai Wang, Ni He, Yanli Zhu, Zhengbin An, Ping Chen, Craig A. Grimes, Zhou Nie, and Qingyun Cai. Highly-luminescent eu,sm,mn-doped cas up/down conversion nano-particles: Application to ultra-sensitive latent fingerprint detection and: In vivo bioimaging. *Chemical Communications*, 54:591–594, 2018. ISSN 1364548X. doi: 10.1039/c7cc07790d.
- [30] Feng Wang, Renren Deng, Juan Wang, Qingxiao Wang, Yu Han, Haomiao Zhu, Xueyuan Chen, and Xiaogang Liu. Tuning up-conversion through energy migration in core-shell nanoparticles. *Nature Materials*, 10(12):968–973, 2011. ISSN 14764660. doi: 10.1038/nmat3149. URL <http://dx.doi.org/10.1038/nmat3149>.
- [31] Shihui Wen, Jiajia Zhou, Kezhi Zheng, Artur Bednarkiewicz, Xiaogang Liu, and Dayong Jin. Advances in highly doped upconversion nanoparticles. *Nature Communications*, 9(1):2415, Jun 2018. ISSN 2041-1723. doi: 10.1038/s41467-018-04813-5. URL <https://doi.org/10.1038/s41467-018-04813-5>.
- [32] Verónica Bastos, Párastu Oskoei, Elina Andresen, Maysoon I. Saleh, Bastian Rühle, Ute Resch-Genger, and Helena Oliveira. Stability, dissolution, and cytotoxicity of nayf4-upconversion nanoparticles with different coatings. *Scientific Reports*, 12, 12 2022. ISSN 20452322. doi: 10.1038/s41598-022-07630-5.
- [33] Qiuqiang Zhan, Jun Qian, Huijuan Liang, Gabriel Somesfalean, Dan Wang, Sailing He, Zhiguo Zhang, and Stefan Andersson-Engels. Using 915 nm laser excited Tm<sup>3+</sup>/Er<sup>3+</sup>/Ho<sup>3+</sup>-doped NaYbF<sub>4</sub> up-conversion nanoparticles for in vitro and deeper in vivo bioimaging without overheating irradiation. *ACS Nano*, 5(5):3744–3757, 2011. ISSN 19360851. doi: 10.1021/nn200110j.
- [34] Akshaya Bansal, Haichun Liu, Muthu Kumara Gnanasammandhan Jayakumar, Stefan Andersson-Engels, and Yong Zhang. Quasi-Continuous Wave Near-Infrared Excitation of Upconversion Nanoparticles for Optogenetic Manipulation of *C. elegans*. *Small*, 12(13):1732–1743, 2016. ISSN 16136829. doi: 10.1002/smll.201503792.
- [35] Can T. Xu, Pontus Svenmarker, Haichun Liu, Xia Wu, Maria E. Messing, L. Reine Wallenberg, and Stefan Andersson-Engels. High-resolution fluorescence diffuse optical tomography developed with nonlinear upconverting nanoparticles. *ACS Nano*, 6(6):4788–4795, 2012. ISSN 19360851. doi: 10.1021/nn3015807.
- [36] Bin Dong, Baosheng Cao, Yangyang He, Zhuang Liu, Zhipeng Li, and Zhiqing Feng. Temperature sensing and in vivo imaging by molybdenum sensitized visible upconversion luminescence of rare-earth oxides. *Advanced Materials*, 24(15):1987–1993, 2012. ISSN 09359648. doi: 10.1002/adma.201200431.
- [37] Eduardo Martínez, Carlos Brites, Luís Carlos, A. García-Flores, R. Urbano, and Carlos Rettori. Electrochromic switch devices mixing small- and large-sized upconverting nanocrystals. *Advanced Functional Materials*, 29, 02 2019. doi: 10.1002/adfm.201807758.
- [38] J. De Wild, J. K. Rath, A. Meijerink, W. G.J.H.M. Van Sark, and R. E.I. Schropp. Enhanced near-infrared response of a-Si:H solar cells with  $\beta$ -NaYF<sub>4</sub>:Yb<sub>3</sub> (18%), Er<sub>3</sub> (2%) upconversion phosphors. *Solar Energy Materials and Solar Cells*, 94(12):2395–2398, 2010. ISSN 09270248. doi: 10.1016/j.solmat.2010.08.024. URL <http://dx.doi.org/10.1016/j.solmat.2010.08.024>.

- [39] Tim F. Schulze and Timothy W. Schmidt. Photochemical upconversion: Present status and prospects for its application to solar energy conversion. *Energy and Environmental Science*, 8(1):103–125, 2015. ISSN 17545706. doi: 10.1039/c4ee02481h.
- [40] Dandan Li, Shu Hong Yu, and Hai Long Jiang. From UV to Near-Infrared Light-Responsive Metal–Organic Framework Composites: Plasmon and Upconversion Enhanced Photocatalysis. *Advanced Materials*, 30(27):1–7, 2018. ISSN 15214095. doi: 10.1002/adma.201707377.
- [41] Michael D. Wisser, Stefan Fischer, Chris Siefe, A. Paul Alivisatos, Alberto Salleo, and Jennifer A. Dionne. Improving Quantum Yield of Upconverting Nanoparticles in Aqueous Media via Emission Sensitization. *Nano Letters*, 18(4):2689–2695, 2018. ISSN 15306992. doi: 10.1021/acs.nanolett.8b00634.
- [42] Denitza Denkova, Martin Ploschner, Minakshi Das, Lindsay M. Parker, Xianlin Zheng, Yiqing Lu, Antony Orth, Nicolle H. Packer, and James A. Piper. 3D sub-diffraction imaging in a conventional confocal configuration by exploiting super-linear emitters. *Nature Communications*, 10(1):1–12, 2019. ISSN 20411723. doi: 10.1038/s41467-019-11603-0. URL <http://dx.doi.org/10.1038/s41467-019-11603-0>.
- [43] Changhwan Lee, Emma Z. Xu, Yawei Liu, Ayelet Teitelboim, Kaiyuan Yao, Angel Fernandez-Bravo, Agata M. Kotulska, Sang Hwan Nam, Yung Doug Suh, Artur Bednarkiewicz, Bruce E. Cohen, Emory M. Chan, and P. James Schuck. Giant nonlinear optical responses from photon-avalanching nanoparticles. *Nature*, 589: 230–235, 1 2021. ISSN 14764687. doi: 10.1038/s41586-020-03092-9.
- [44] Chao hao Chen, Lei Ding, Baolei Liu, Ziqing Du, Yongtao Liu, Xi-angjun Di, Xuchen Shan, Chenxiao Lin, Min Zhang, Xiaoxue Xu, Xiaolan Zhong, Jianfeng Wang, Lingqian Chang, Benjamin Halkon, Xin Chen, Faliang Cheng, and Fan Wang. Exploiting dynamic non-linearity in upconversion nanoparticles for super-resolution imaging. *Nano Letters*, 9 2022. ISSN 1530-6984. doi: 10.1021/acs.nanolett.2c02269.
- [45] Lothar Schermelleh, Alexia Ferrand, Thomas Huser, Christian Eggeling, Markus Sauer, Oliver Biehlmaier, and Gregor P.C. Drummen. Super-resolution microscopy demystified, 1 2019. ISSN 14764679.
- [46] Gabriella Tessitore, Gabrielle A. Mandl, Mikhail G. Brik, Wounghang Park, and John A. Capobianco. Recent insights into upconverting nanoparticles: Spectroscopy, modeling, and routes to improved luminescence, 7 2019. ISSN 20403372.
- [47] Theodore A. Henderson and Larry D. Morries. Near-infrared photonic energy penetration: Can infrared phototherapy effectively reach the human brain?, 8 2015. ISSN 11782021.
- [48] François Auzel. Upconversion and Anti-Stokes Processes with f and d Ions in Solids. *Chemical Reviews*, 104(1):139–173, 2004. ISSN 00092665. doi: 10.1021/cr020357g.
- [49] Monirehalsadat Mousavi, Björn Thomasson, Meng Li, Marco Kraft, Christian Würth, Ute Resch-Genger, and Stefan Andersson-Engels. Beam-profile-compensated quantum yield measurements of upconverting nanoparticles. *Physical Chemistry Chemical Physics*, 19(33): 22016–22022, 2017. ISSN 14639076. doi: 10.1039/c7cp03785f.

- [50] J. S. Matias, K. Komolibus, S. Konugolu-Venkata-Sekar, and S. Andersson-Engels. Evaluation of relative beam-profile-compensated quantum yield of upconverting nanoparticles over a wide dynamic range of power densities. *Nanoscale*, 14:2230–2237, 2022. ISSN 20403372. doi: 10.1039/d1nr06129a.
- [51] François E. Auzel. Materials and Devices Using Double-Pumped Phosphors with Energy Transfer. *Proceedings of the IEEE*, 61(6):758–786, 1973. ISSN 15582256. doi: 10.1109/PROC.1973.9155.
- [52] N. Bloembergen. Solid state infrared quantum counters. *Phys. Rev. Lett.*, 2:84–85, Feb 1959. doi: 10.1103/PhysRevLett.2.84. URL <https://link.aps.org/doi/10.1103/PhysRevLett.2.84>.
- [53] François E. Auzel. Compteur Quantique par Transfert d’Energie Entre Deux Ions de Terres Rares dans un Tungstate Mixte et dans un Verre. *C. R. Acad. Sci.*, 262:1016–1019, 1966.
- [54] V. V. Ovsyankin and P. P. Feofilov. Mechanism of Summation of Electronic Excitations in Activated Crystals. *ZhETF Pisma Redaktsiiu*, 3:494, June 1966.
- [55] Th. Förster. Zwischenmolekulare energiewanderung und fluoreszenz. *Annalen der Physik*, 437(1-2):55–75, 1948. doi: <https://doi.org/10.1002/andp.19484370105>. URL <https://onlinelibrary.wiley.com/doi/abs/10.1002/andp.19484370105>.
- [56] D. L. Dexter. A theory of sensitized luminescence in solids. *The Journal of Chemical Physics*, 21(5):836–850, 1953. doi: 10.1063/1.1699044. URL <https://doi.org/10.1063/1.1699044>.
- [57] C. Kittel. *Elementary Statistical Physics*. Dover Books on Physics Series. Dover Publications, 2004. ISBN 9780486435145. URL <https://books.google.ie/books?id=5sd9SAoRjgQC>.
- [58] Marvin J. Weber. Luminescence Decay by Energy Migration and Transfer: Observation of Diffusion-Limited Relaxation. *Physical Review B*, 4(9):2934–2939, 1971.
- [59] Eiichiro Nakazawa and Shigeo Shionoya. Cooperative luminescence in YbPO<sub>4</sub>. *Physical Review Letters*, 25:1710–1712, 1970. ISSN 00319007. doi: 10.1103/PhysRevLett.25.1710.
- [60] P. A. Franken, A. E. Hill, C. W. Peters, and G. Weinreich. Generation of optical harmonics. *Physical Review Letters*, 7(4):118–119, 1961. ISSN 00319007. doi: 10.1103/PhysRevLett.7.118.
- [61] Maria Göppert-Mayer. Über elementarakte mit zwei quantensprüngen. *Annalen der Physik*, 401(3):273–294, 1931. doi: <https://doi.org/10.1002/andp.19314010303>. URL <https://onlinelibrary.wiley.com/doi/abs/10.1002/andp.19314010303>.
- [62] W. Kaiser and C. G. B. Garrett. Two-photon excitation in  $\text{CaF}_2:\text{Eu}^{2+}$ . *Phys. Rev. Lett.*, 7:229–231, Sep 1961. doi: 10.1103/PhysRevLett.7.229. URL <https://link.aps.org/doi/10.1103/PhysRevLett.7.229>.
- [63] Jay S. Chivian, W. E. Case, and D. D. Eden. The photon avalanche: A new phenomenon in  $\text{Pr}^{3+}$ -based infrared quantum counters. *Applied Physics Letters*, 35:124–125, 1979. ISSN 00036951. doi: 10.1063/1.91044.

- [64] A. F. García-Flores, J. S. Matias, D. J. Garcia, E. D. Martínez, P. S. Cornaglia, G. G. Lesseux, R. A. Ribeiro, R. R. Urbano, and C. Rettori. Crystal-field effects in  $\text{er}^{3+}$ - and  $\text{yb}^{3+}$ -doped hexagonal  $\text{nayf}_4$  nanoparticles. *Phys. Rev. B*, 96:165430, Oct 2017. doi: 10.1103/PhysRevB.96.165430. URL <https://link.aps.org/doi/10.1103/PhysRevB.96.165430>.
- [65] Hui Li, Xin Wang, Dingxin Huang, and Guanying Chen. Recent advances of lanthanide-doped upconversion nanoparticles for biological applications. *Nanotechnology*, 31, 2020. ISSN 13616528. doi: 10.1088/1361-6528/ab4f36.
- [66] Rui Shi, Eduardo D. Martinez, Carlos D.S. Brites, and Luís D. Carlos. Thermal enhancement of upconversion emission in nanocrystals: A comprehensive summary. *Physical Chemistry Chemical Physics*, 23(1):20–42, 2021. ISSN 14639076. doi: 10.1039/d0cp05069e.
- [67] Martin Kaiser, Christian Würth, Marco Kraft, Iko Hyppänen, Tero Soukka, and Ute Resch-Genger. Power-dependent upconversion quantum yield of  $\text{NaYF}_4:\text{Yb}^{3+},\text{Er}^{3+}$  nano- and micrometer-sized particles-measurements and simulations. *Nanoscale*, 9(28):10051–10058, 2017. ISSN 20403372. doi: 10.1039/c7nr02449e.
- [68] Michael S. Meijer, Paola A. Rojas-Gutierrez, Dmitry Busko, Ian A. Howard, Florian Frenzel, Christian Würth, Ute Resch-Genger, Bryce S. Richards, Andrey Turshatov, John A. Capobianco, and Sylvestre Bonnet. Absolute upconversion quantum yields of blue-emitting  $\text{LiYF}_4:\text{Yb}^{3+},\text{Tm}^{3+}$  upconverting nanoparticles. *Physical Chemistry Chemical Physics*, 20(35):22556–22562, 2018. ISSN 14639076. doi: 10.1039/c8cp03935f.
- [69] C. Würth, M. Kaiser, S. Wilhelm, B. Grauel, T. Hirsch, and U. Resch-Genger. Excitation power dependent population pathways and absolute quantum yields of upconversion nanoparticles in different solvents. *Nanoscale*, 9(12):4283–4294, 2017. ISSN 20403372. doi: 10.1039/c7nr00092h.
- [70] John Christopher Boyer and Frank C.J.M. Van Veggel. Absolute quantum yield measurements of colloidal  $\text{NaYF}_4:\text{Er}^{3+},\text{Yb}^{3+}$  upconverting nanoparticles. *Nanoscale*, 2(8):1417–1419, 2010. ISSN 20403364. doi: 10.1039/c0nr00253d.
- [71] Daniel O. Faulkner, Srebri Petrov, Doug D. Perovic, Nazir P. Kherani, and Geoffrey A. Ozin. Absolute quantum yields in  $\text{nayf}_4:\text{er},\text{yb}$  upconverters-synthesis temperature and power dependence. *Journal of Materials Chemistry*, 22:24330–24334, 2012. ISSN 09599428. doi: 10.1039/c2jm33457g.
- [72] Björn Thomasson. High Accuracy Relative Luminescence Quantum Yield Measurements of Upconverting Nanoparticles. Master’s thesis, Lund University, 2015.
- [73] Natalia Kiseleva, Dmitry Busko, Bryce S. Richards, Mikhail A. Filatov, and Andrey Turshatov. Determination of Upconversion Quantum Yields Using Charge-Transfer State Fluorescence of Heavy-Atom-Free Sensitizer as a Self-Reference. *Journal of Physical Chemistry Letters*, 11(16):6560–6566, 2020. ISSN 19487185. doi: 10.1021/acs.jpcclett.0c01902.
- [74] Stefan Fischer, Noah J.J. Johnson, Jothirmayanantham Pichaandi, Jan Christoph Goldschmidt, and Frank C.J.M. Van Veggel. Upconverting core-shell nanocrystals with high quantum yield under

- low irradiance: On the role of isotropic and thick shells. *Journal of Applied Physics*, 118(19):193105, 2015. ISSN 10897550. doi: 10.1063/1.4936119.
- [75] J. F. Suyver, A. Aebischer, S. García-Revilla, P. Gerner, and H. U. Güdel. Anomalous power dependence of sensitized upconversion luminescence. *Phys. Rev. B*, 71:125123, Mar 2005. doi: 10.1103/PhysRevB.71.125123. URL <https://link.aps.org/doi/10.1103/PhysRevB.71.125123>.
- [76] M. Pollnau, D. Gamelin, S. Lüthi, H. Güdel, and M. Hehlen. Power dependence of upconversion luminescence in lanthanide and transition-metal-ion systems. *Physical Review B - Condensed Matter and Materials Physics*, 61:3337–3346, 2000. ISSN 1550235X. doi: 10.1103/PhysRevB.61.3337.
- [77] Pedro Villanueva-Delgado, Karl W. Kramer, and Rafael Valiente. Simulating Energy Transfer and Upconversion in  $\beta$ -NaYF<sub>4</sub>: Yb<sup>3+</sup>, Tm<sup>3+</sup>. *Journal of Physical Chemistry C*, 119:23648–23657, 2015. ISSN 19327455. doi: 10.1021/acs.jpcc.5b06770.
- [78] Jan Bergstrand, Qingyun Liu, Bingru Huang, Xingyun Peng, Christian Würth, Ute Resch-Genger, Qiuqiang Zhan, Jerker Widengren, Hans Ågren, and Haichun Liu. On the decay time of upconversion luminescence. *Nanoscale*, 11:4959–4969, 2019. ISSN 20403372. doi: 10.1039/c8nr10332a.
- [79] Christian Würth, Stefan Fischer, Bettina Grauel, A. Paul Alivisatos, and Ute Resch-Genger. Quantum yields, surface quenching, and passivation efficiency for ultrasmall core/shell upconverting nanoparticles. *Journal of the American Chemical Society*, 140:4922–4928, 2018. ISSN 15205126. doi: 10.1021/jacs.8b01458.
- [80] M. Pokhrel, G. A. Kumar, and D. K. Sardar. Highly efficient nir to nir and vis upconversion in er<sup>3+</sup> and yb<sup>3+</sup> doped in m<sub>2</sub>o<sub>2</sub>s (m = gd, la, y). *Journal of Materials Chemistry A*, 1:11595–11606, 10 2013. ISSN 20507488. doi: 10.1039/c3ta12205k.
- [81] Tianying Sun, Ronghua Ma, Xvsheng Qiao, Xianping Fan, and Feng Wang. Shielding upconversion by surface coating: A study of the emission enhancement factor. *ChemPhysChem*, 17(5): 766–770, 2016. doi: <https://doi.org/10.1002/cphc.201500724>. URL <https://chemistry-europe.onlinelibrary.wiley.com/doi/abs/10.1002/cphc.201500724>.
- [82] S. Heer, K. Kömpe, H.-U. Güdel, and M. Haase. Highly efficient multicolour upconversion emission in transparent colloids of lanthanide-doped nayf<sub>4</sub> nanocrystals. *Advanced Materials*, 16(23-24):2102–2105, 2004. doi: <https://doi.org/10.1002/adma.200400772>. URL <https://onlinelibrary.wiley.com/doi/abs/10.1002/adma.200400772>.
- [83] Lewis E. Mackenzie, Jack A. Goode, Alexandre Vakurov, Padmaja P. Nampi, Sikha Saha, Gin Jose, and Paul A. Millner. The theoretical molecular weight of nayf<sub>4</sub> :re upconversion nanoparticles. *Scientific Reports*, 8, 12 2018. ISSN 20452322. doi: 10.1038/s41598-018-19415-w.
- [84] Markolf H. Niemz. *Light and Matter*, pages 9–43. Springer Berlin Heidelberg, Berlin, Heidelberg, 1996. ISBN 978-3-662-03193-3. doi: 10.1007/978-3-662-03193-3\_2. URL [https://doi.org/10.1007/978-3-662-03193-3\\_2](https://doi.org/10.1007/978-3-662-03193-3_2).

- 
- [85] Shuhei Okuyama, Tadanobu Nagaya, Fusa Ogata, Yasuhiro Maruoka, Kazuhide Sato, Yuko Nakamura, Peter L Choyke, and Hisataka Kobayashi. Avoiding thermal injury during near-infrared photoimmunotherapy (nir-pit): the importance of nir light power density, 2017. URL [www.impactjournals.com/oncotarget/](http://www.impactjournals.com/oncotarget/).
- [86] Gerald L. DeNardo and Sally J. DeNardo. Turning the heat on cancer, 12 2008. ISSN 10849785.
- [87] K. E. Atkinson. *An Introduction to Numerical Analysis*. Numerical Analysis. John Wiley and Sons, 1989. ISBN 9780471500230.
- [88] Dongdong Li, Qiyue Shao, Yan Dong, and Jianqing Jiang. Anomalous temperature-dependent upconversion luminescence of small-sized  $\text{NaYF}_4:\text{Yb}^{3+}, \text{Er}^{3+}$  nanoparticles. *The Journal of Physical Chemistry C*, 118(39):22807–22813, 2014. doi: 10.1021/jp507804h. URL <https://doi.org/10.1021/jp507804h>.
- [89] Christian Würth, Markus Grabolle, Jutta Pauli, Monika Spieles, and Ute Resch-Genger. Relative and absolute determination of fluorescence quantum yields of transparent samples. *Nature Protocols*, 8(8):1535–1550, 2013. ISSN 17502799. doi: 10.1038/nprot.2013.087.
- [90] Joseph Lakowicz. *Principles of Fluorescence Spectroscopy*, volume 1. 01 2006. ISBN 978-0-387-31278-1. doi: 10.1007/978-0-387-46312-4.
- [91] Benjamin T. Cox, Jan G. Laufer, Paul C. Beard, and Simon R. Arridge. Quantitative spectroscopic photoacoustic imaging: a review. *Journal of Biomedical Optics*, 17(6):1 – 23, 2012. doi: 10.1117/1.JBO.17.6.061202. URL <https://doi.org/10.1117/1.JBO.17.6.061202>.
- [92] P. Stanley May and Mary Berry. Tutorial on the acquisition, analysis, and interpretation of upconversion luminescence data. *Methods and Applications in Fluorescence*, 7(2):023001, 2019. ISSN 20506120. doi: 10.1088/2050-6120/ab02c6.



# APPENDIX

---

## 1. Github repos with some of the codes developed along the research

- (i) **QY DAQ Interface** – Python code to control the QY system and acquire data.

<https://github.com/Biophotonics-Tyndall/QY-DAQInterface.git>

- (ii) **QEPro Controller** – A simple Python controller to help on automating data collection with a QEPro spectrometer. <https://github.com/Biophotonics-Tyndall/QY-QEProController.git>

- (iii) **QY Virtuallab** – A python script to simulate ETU processes. It allows one to study the dynamic and the steady states of the energy levels. <https://github.com/Biophotonics-Tyndall/QY-VirtuaLabForUCNPs.git>

- (iv) **QY analysis framework** – A Python framework to help on the analysis of the data acquired with the QY System <https://github.com/Biophotonics-Tyndall/QY-AnalysisFramework.git>

## 2. Quantum yield analysis example

The following pages contain a Jupyter notebook with an example of the QY analysis utilizing the **QY analysis framework** available to download and installation on GitHub, link above.

## Quantum Yield Analysis →

Author: Jean Matias  
 UCNP Sample: s019  
 spot sizes: 254um  
 Acquired on: 2022/06/29  
 Analysed on: 2022/07/01

In [1]:

```
%matplotlib notebook
import sys
sys.path.append('../scripts/')
from lab import Analysis, BeamProfile, PowerMeters
# Importing the classes responsible for the analysis from the ../scripts/ folder
from calibration import *
```

For details on the analysis protocol and calculation:  
 >>> help(Analysis)  
 >>> help(Sample)

In [3]:

```
# Further details regarding the main codes can be obtained with the help function
help(Analysis)
```

```
compound in a certain range within the cuvette.
**Dye**:
```

7. Get emitted power - Knowing its quantum yield the emitted power is calculated.
8. Get apd power - It calculates the power reaching the apd after the light passes through a long pass filter.
9. Fit apd power vs apd voltage (apd) - It calibrates the apd output.

```
**UCNP**:
```

7. Calibrate the apd - Using a dye calibration curve it calculates the power reaching the apd.
8. Get emitted power - Calculates the power before the short pass filter, i.e. emitted power.
9. Get kappa - Calculates the slope of the emission curve vs power density at centre in log scale.
10. Get quantum yield - Calculates the quantum yield of a sample from its emitted power and absorbed power.

Methods defined here:

```
__init__(self, dataPath='../data/raw-data/')
Builds an object for analysis
```

## Beam Profile analysis

In [2]:

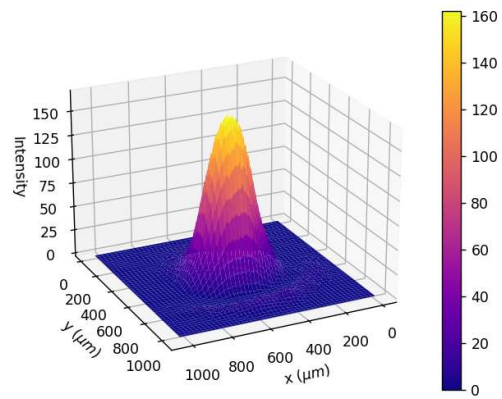
```
# Loading the beam profile data (acquired with the CMOS camera)
beam_profile = BeamProfile('20220629_976nm_S2.png')

# Cropping it around the spot
beam_profile.trim(2) #

# Removing background noise
beam_profile.removebackground(3)
```

In [3]:

```
# Quick visualisation of the 3d Gauss profile
beam_profile.plotsurf()
```



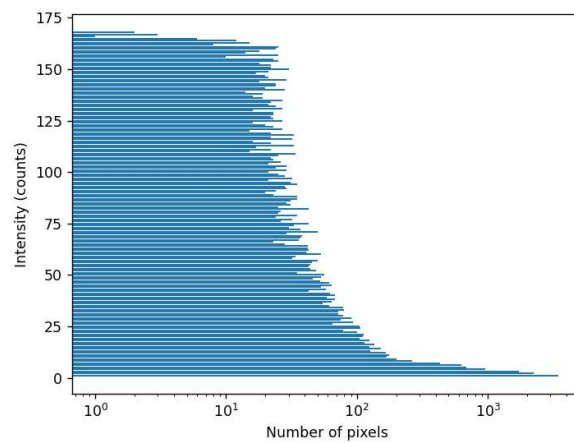
In [4]:

```
# Info regarding beamwidth and calculation method
print(f'BP: {beam_profile.beamwidth():.3e} cm')
print(f'BP: {beam_profile.beamarea():.3e} cm^2')
print(f'Method: {beam_profile.beamWidthMethod} ') # if none -> FWHM
```

```
BP: 2.544e-02 cm
BP: 5.083e-04 cm^2
Method: None
```

In [5]:

```
_ = beam_profile.histprofile(show=True)
```



## Load data

In [7]:

```
# Initialise the analysis object: This class includes all the methods required to Load,
# treat and analyse the data
data = Analysis()
```

In [8]:

```
# Loading the UCNP and empty background data by their ID.
# The data were acquired with the QY system stored in a folder with all
# their details save in a separated file and related to them by their IDs.

# The loaddata method also loads the details of teh experiemnts
data.loaddata(sampleType='ucnp', dataIds='20220629-121143') # s2
data.loaddata(sampleType='empty', dataIds='20220629-120601') # s2
```

In [9]:

```
# Visualizing the main details
data.details(full=False)
```

Out[9]:

	exp_id	type	sample	reference	apd1_gain	apd2_gain	apd1_wavelength	apd2_wavelength	pms_range	pmr_range	laser_wavelength	spot_size
0	20220629-121143	ucnp	s019	toluene	max	max	800nm	472nm	690mW	61mW	976nm	s2
1	20220629-120601	empty	empty	empty	max	max	800nm	472nm	690mW	61mW	976nm	s2

In [10]:

```
# Linking the beam proifile with the data
data.get('setbeamprofile', dict(bp=beam_profile))
```

20220629-121143: UCNP - Success!

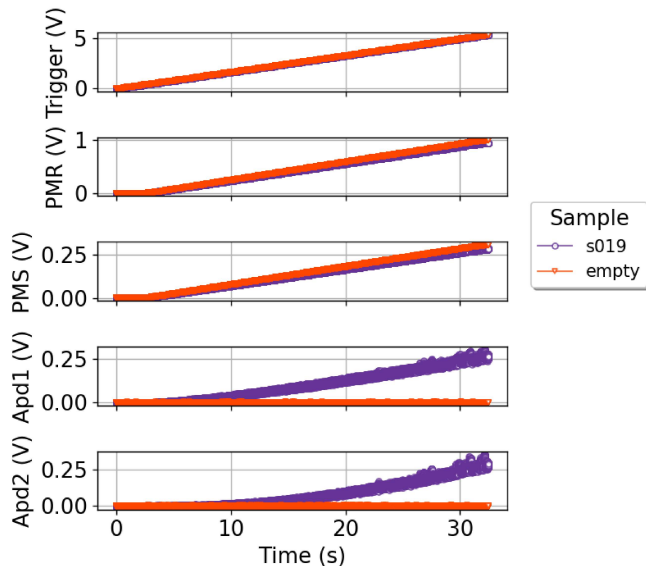
In [11]:

```
# Adding the details related to filter transmittance and reabsorption.
for s in data._sampleList:
    s.filterTransmittance = 0.97 #
    s.reabsorption = 0.00 #
```

### Quick view of raw data

In [12]:

```
_ = data.view(label='sample', includeEmpty=True)
```



In [15]:

```
# Removing background from all measurements
# The background level is obtained from the first points where there's no
# Laser Light
data.get('removebackground', dict(channel='pmr'), includeEmpty=True)
data.get('removebackground', dict(channel='pms'), includeEmpty=True)
data.get('removebackground', dict(channel='apd1'))
data.get('removebackground', dict(channel='apd2'))

20220629-121143: UCNP - Success!
20220629-120601: CuvetteHolder - Success!
20220629-121143: UCNP - Success!
20220629-120601: CuvetteHolder - Success!
20220629-121143: UCNP - Success!
20220629-121143: UCNP - Success!
```

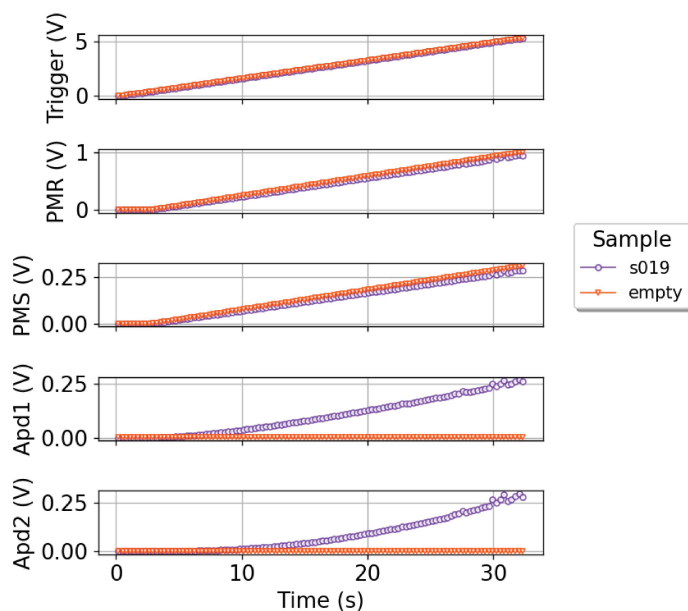
In [14]:

```
# Averaging the data points to reduce the noise.
# For each Laser power there are 1000 data points.
# The first 100 are eliminated since the power meters
# and UCNPs take some time to stabilise
data.get('steadydata', dict(fromPt=100, toPt=1000), includeEmpty=True)

20220629-121143: UCNP - Success!
20220629-120601: CuvetteHolder - Success!
```

In [16]:

```
# Quick view
_ = data.view(label='sample', includeEmpty=True)
```



## Powermeter calibration

In [17]:

```
# Powermeter calibration data
# ALL the constants were previously obtained during the calibration process of the QY system
PowerMeters.data
```

Out[17]:

	power_meter	wavelength_nm	range_mW	m_mW/V	b	Rsqr
0	pm1	976	600.00	303.698372	-0.230276	0.999995
1	pm1	976	60.00	30.396345	-0.012825	0.999990
2	pm1	785	9.10	4.601155	-0.000037	0.999976
3	pm1	405	0.23	0.115223	-0.000027	0.999999
4	pm2	976	61.00	30.689235	0.023667	0.999902
5	pm2	785	0.95	0.478520	-0.000759	0.999980
6	pm2	405	2.20	1.127430	-0.000571	0.999998

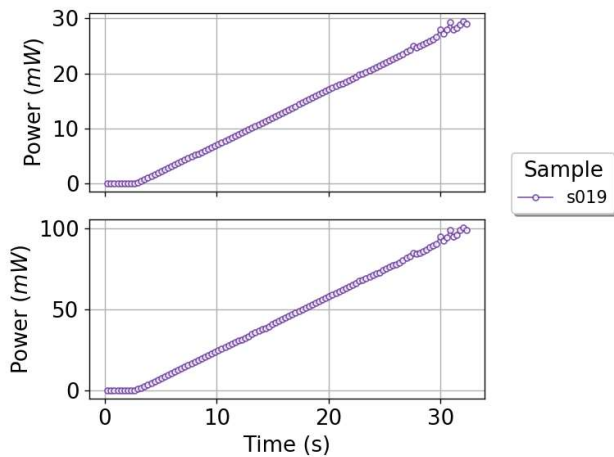
In [18]:

```
for s in data._sampleList:
    pm1Range = float(s.details['pms_range'][:-2])
    pm2Range = float(s.details['pmr_range'][:-2])
    wavel = float(s.details['laser_wavelength'][:-2])

    calFunc1 = PowerMeters.calibration('pm1', wavel, pm1Range)
    calFunc2 = PowerMeters.calibration('pm2', wavel, pm2Range)
    s.calibrate(calibFunction=calFunc1, channel='pms')
    s.calibrate(calibFunction=calFunc2, channel='pmr')
```

In [18]:

```
fig, ax = data.view(x='time', yList=['transmitted_power_r', 'transmitted_power_s'], label='sample')
```



## APD calibration

In [19]:

```
m01 = 0.00492 # mW/V
m02 = 0.00448 # mW/V
m01 = 0.00575 # mW/V
m02 = 0.00054 # mW/V

apd1CalibFunc = lambda x: m01 * x
apd2CalibFunc = lambda x: m02 * x

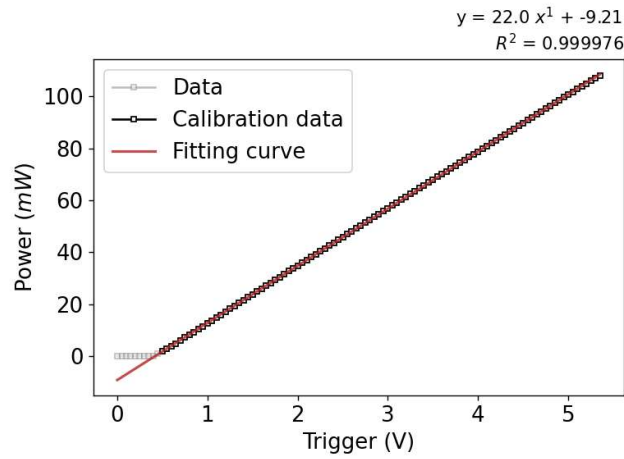
data.get('calibrate', dict(calibFunction=apd1CalibFunc, channel='apd1'))
data.get('calibrate', dict(calibFunction=apd2CalibFunc, channel='apd2'))
```

```
20220629-121143: UCNP - Success!
20220629-121143: UCNP - Success!
```

### Calibrate trigger to obtain incident power

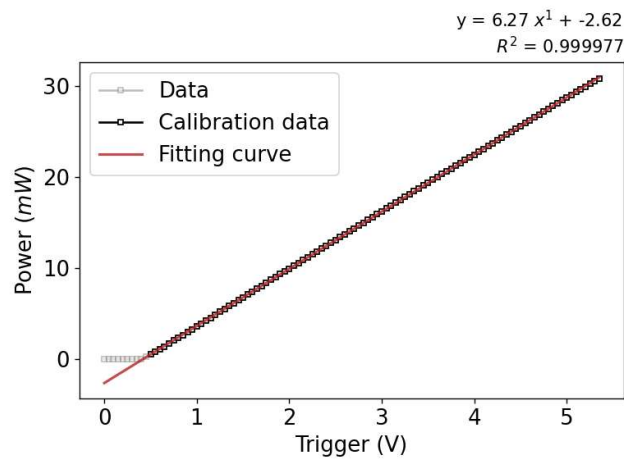
In [20]:

```
coeffs, rsqr, msg= data.sample(1).generatecalibration(x='trigger', y='transmitted_power_s',
                                                    degree=1, condition='x>0.5', show=True)
triggerFuncS = lambda x: coeffs[0] * x + coeffs[1]
```



In [21]:

```
coeffsR, rsqrR, msgR= data.sample(1).generatecalibration(x='trigger', y='transmitted_power_r',
                                                         degree=1, condition='x>0.5', show=True)
triggerFuncR = lambda x: coeffsR[0] * x + coeffsR[1]
```



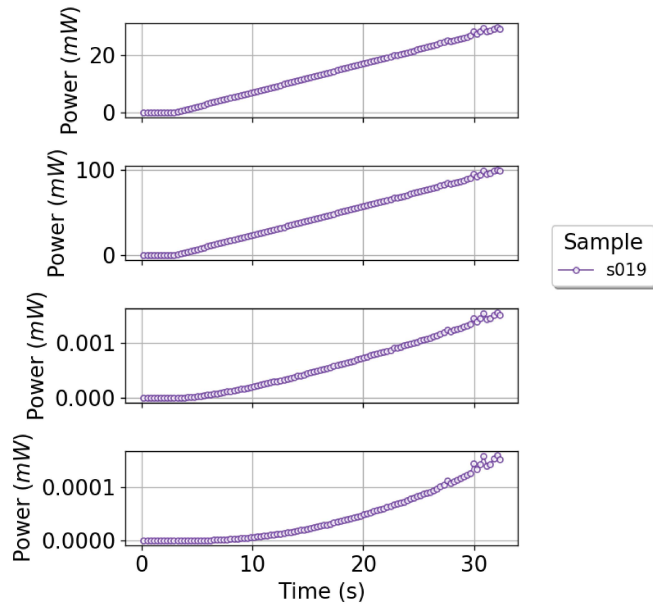
In [22]:

```
data.get('calibrate', dict(calibFunction=triggerFuncR, channel='trigger', cuvette='reference', recalculate=True))
data.get('calibrate', dict(calibFunction=triggerFuncS, channel='trigger', cuvette='sample', recalculate=True))
```

```
20220629-121143: UCNP - Success!
20220629-121143: UCNP - Success!
```

In [23]:

```
_= data.view(x='time', ylist=['transmitted_power_r', 'transmitted_power_s', 'power_at_apd1', 'power_at_apd2'],
            includeReference=True, label='sample')
```



In [24]:

```
# Calculates the power at the centre of the cuvette
data.get('poweratcentre', dict(method='incident power', recalculate=True))
```

20220629-121143: UCNP - Success!

In [25]:

```
# Calculates the PD at the centre. It uses the beam width
# provided by the beam_profile object
data.get('powdensatcentre', dict(recalculate=True))
```

20220629-121143: UCNP - Success!

In [26]:

```
# Calculates the absorbed power by the volume at the centre of the cuvette
data.get('absorbedpower', dict(recalculate=True))
```

20220629-121143: UCNP - Success!

## Absorption

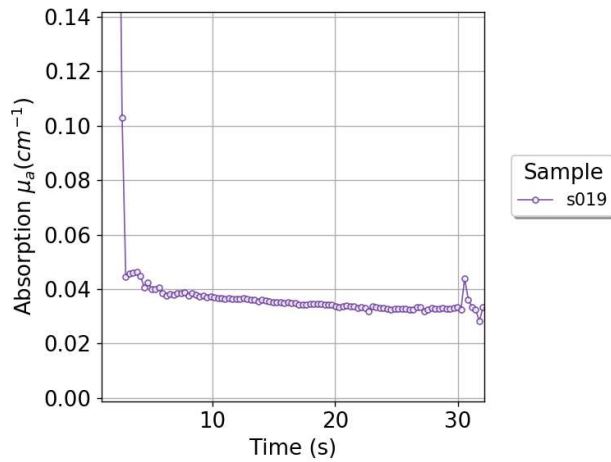
In [27]:

```
data.get('absorptioncoeff', dict(method='reference', filterQuery='time > 15', recalculate=True))
# The filterQuery parameter is used to remove the initial points to get only
# stable data. The data is averaged to a single value to be used later.
```

20220629-121143: UCNP - Success!

In [28]:

```
fig, ax = data.view(x='time', yList=['absorption_coeff'], label='sample')
```



In [29]:

```
# Average value
data.sample(0)._absorptionCoeff
```

Out[29]:

```
0.03363005164574406
```

## Luminescence

In [30]:

```
# Calculates the UCL (800 nm at APD1) right after the sample,
# i.e. before the attenuation by the optics
data.get('emittedpower', dict(apd=1, wavelength=800, recalculate=True))
```

```
20220629-121143: UCNP - Success!
```

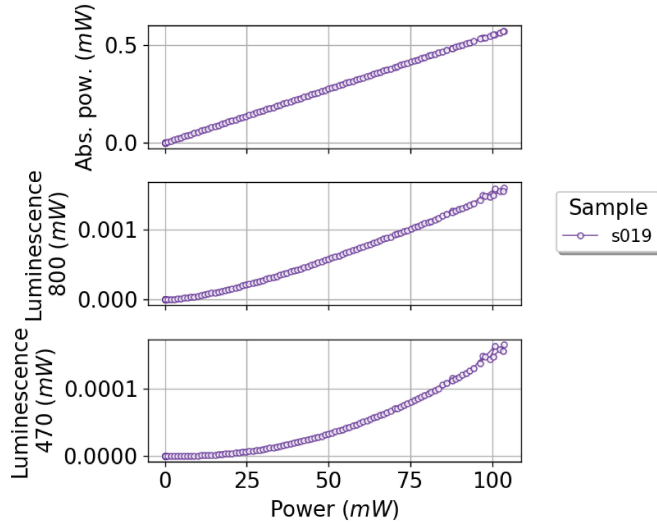
In [31]:

```
# Calculates the UCL (470 nm at APD2) right after the sample,
# i.e. before the attenuation by the optics
data.get('emittedpower', dict(apd=2, wavelength=470, recalculate=True))
```

```
20220629-121143: UCNP - Success!
```

In [32]:

```
fig, ax = data.view(x='power_at_centre_s',
  yList=['absorbed_power', 'emitted_power_800nm', 'emitted_power_470nm'],
  label='sample')
```



In [41]:

```
pl.tight_layout()
```

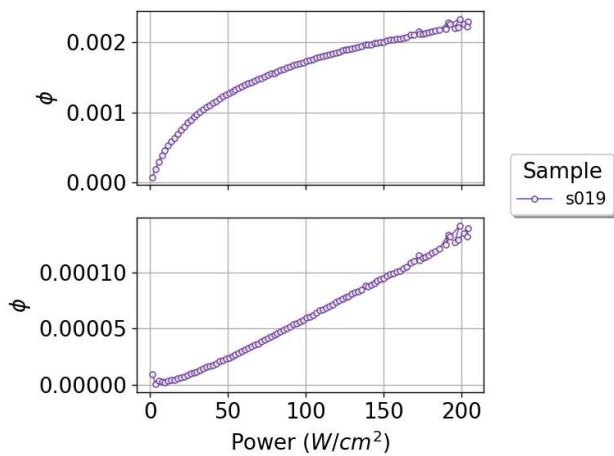
In [33]:

```
data.get('equantumyield', dict(apd=1, wavelength=800, recalculate=True))
data.get('equantumyield', dict(apd=2, wavelength=470, recalculate=True))
```

20220629-121143: UCNF - Success!  
 20220629-121143: UCNF - Success!

In [34]:

```
fig, ax = data.view(x='pow_dens_at_centre_s', yList=['eQY_800nm', 'eQY_470nm'], label='sample')
```



## Beam profile correction

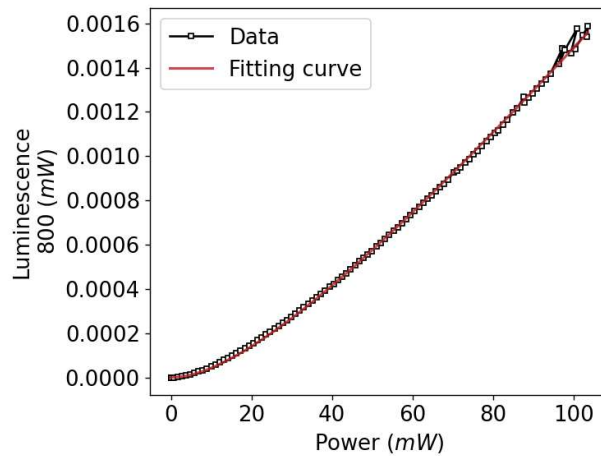
In [35]:

```
def printparams(popt):
    """Prints the results in a nice representation.
    """
    etas = popt[0] / popt[1] * 100 # %
    paramsStr = f'Results:\netas = {etas:.2f} %\n'
    paramsStr += f'etao = {popt[0]/1000:.2g} W/cm2\n'
    i = 1
    for v in popt[1:]:
        paramsStr += f'rhub{i} = {v/1000:.2g} W/cm2\n'
        i += 1
    print(paramsStr)
```

## 800nm emission

In [39]:

```
popt, pcov, fittedFunc800bp1, _ = data.sample(0). \
    fitemission(wavelength=800, etu=2, bounds=(0, 2.5e7, 0), [np.inf, np.inf, np.inf]), show=True)
printparams(popt)
```

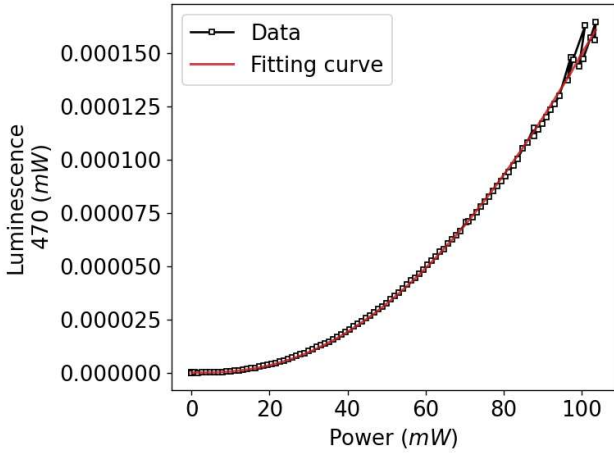


```
Results:
etas = 0.58 %
etao = 3.1e+02 W/cm2
rhub1 = 5.4e+04 W/cm2
rhub2 = 30 W/cm2
```

### 470nm emission

In [40]:

```
popt, pcov, fittedFunc470bp1, _ = data.sample(0). \
    fitemission(wavelength=470, etu=3,
                bounds=([0, 5.7e7, 3.1e4, 0], [np.inf, 6.2e+07, 3.5e4, np.inf]), show=True)
printparams(popt)
```



Results:  
 etas = 0.25 %  
 etao = 1.6e+02 W/cm2  
 rhob1 = 6.2e+04 W/cm2  
 rhob2 = 31 W/cm2  
 rhob3 = 5e+02 W/cm2

### Further analysys

Further analysis can be conducted with the data if needed.

In [41]:

```
# All the calculations are stored in dataframe of the samples
data.sample(0).data
```

Out[41]:

	time	trigger	pms	pmr	apd1	apd2	time_daq	time_std	trigger_std	pms_std	...	incident_power_r	incident_pov
0	0.192652	-0.000028	0.000000e+00	0.000000e+00	0.000000	0.000000	0.164852	0.091138	0.000271	0.000318	...	0.000000	0.00
1	0.539693	0.049826	7.306646e-07	1.351730e-05	0.000005	0.000058	0.489155	0.077982	0.000271	0.000311	...	0.000000	0.00
2	0.839281	0.099965	-6.575982e-06	1.461329e-06	-0.000028	-0.000031	0.789157	0.077831	0.000287	0.000306	...	0.000000	0.00
3	1.140777	0.149812	-1.688494e-05	-7.758943e-06	-0.000042	0.000048	1.089010	0.078672	0.000270	0.000299	...	0.000000	0.00
4	1.441162	0.199969	-6.483018e-06	4.191536e-07	-0.000011	0.000015	1.388263	0.077639	0.000263	0.000322	...	0.000000	0.00
...	...	...	...	...	...	...	...	...	...	...	...	...	...
103	31.141287	5.150287	2.716071e-01	9.109652e-01	0.247365	0.258272	31.089738	0.077987	0.000269	0.000327	...	29.655493	104.00
104	31.441443	5.200172	2.745743e-01	9.201232e-01	0.250475	0.264624	31.389891	0.077727	0.000275	0.000347	...	29.968101	105.10
105	31.740991	5.250357	2.822989e-01	9.419027e-01	0.260776	0.282516	31.689443	0.077984	0.000281	0.005933	...	30.282582	106.20
106	32.039940	5.299955	2.864448e-01	9.606194e-01	0.268150	0.295693	31.988396	0.076859	0.000273	0.008253	...	30.593388	107.30
107	32.327200	5.350130	2.822593e-01	9.463910e-01	0.259908	0.280105	32.275799	0.071779	0.000284	0.000520	...	30.907815	108.40

108 rows x 28 columns



In [43]:

```
# Details of the calculations are generated automatically and can be accessed
# in the 'metadata' attribute.
data.sample(0)._metadata
```

Out[43]:

	field_name	data_type	data_format	example	standard_units	plot_label	description
0	time	float	^[0-9]?\.?[1-9][0-9]*\$	123423.98270	seconds	Time (s)	Positive float number for time acquired with p...
1	trigger	float	^[^-]?([0-9]?\.?[1-9][0-9]*\$)	-1.99834	volts	Trigger (V)	Daq input channel
2	pms	float	^[^-]?([0-9]?\.?[1-9][0-9]*\$)	-1.99834	volts	PMS (V)	Daq input channel
3	pmr	float	^[^-]?([0-9]?\.?[1-9][0-9]*\$)	-1.99834	volts	PMR (V)	Daq input channel
4	apd1	float	^[^-]?([0-9]?\.?[1-9][0-9]*\$)	-1.99834	volts	Apd1 (V)	Daq input channel
5	apd2	float	^[^-]?([0-9]?\.?[1-9][0-9]*\$)	-1.99834	volts	Apd2 (V)	Daq input channel
6	time_daq	float	^[^-]?([0-9]?\.?[1-9][0-9]*\$)	0.02938	s	Time (s)	Time acquired from the Daq internal clock
7	transmitted_power_s	float	^[0-9]*\.[0-9]*\$	5.50000	mW	Power (mW)	Transmitted Power S - Obtained from pms calibr...
8	transmitted_power_r	float	^[0-9]*\.[0-9]*\$	5.50000	mW	Power (mW)	Transmitted Power R - Obtained from pmr calibr...
9	power_at_apd1	float	^[0-9]*\.[0-9]*\$	5.50000	mW	Power (mW)	Power At Apd1 - Obtained from apd1 calibration.
10	power_at_apd2	float	^[0-9]*\.[0-9]*\$	5.50000	mW	Power (mW)	Power At Apd2 - Obtained from apd2 calibration.
11	incident_power_r	float	^[0-9]*\.[0-9]*\$	5.50000	mW	Power (mW)	Incident Power R - Obtained from trigger calib...
12	incident_power_s	float	^[0-9]*\.[0-9]*\$	5.50000	mW	Power (mW)	Incident Power S - Obtained from trigger calib...
13	power_at_centre_s	float	^[0-9]*\.[0-9]*\$	100.56500	mW	Power (mW)	Power at the center of the sample cuvette.
14	pow_dens_at_centre_s	float	^[0-9]*\.[0-9]*\$	10000.56500	W/cm <sup>2</sup>	Power (W/cm <sup>2</sup> )	Power density at the center of the sample cuve...
15	absorption_coeff	float	^[0-9]*\$	0.40000	(cm <sup>-1</sup> )	Absorption $\mu_a$ (cm <sup>-1</sup> )	Absorption coefficient obtained $\mu_a = \ln(P_{f...}$
16	absorbed_power	float	^[0-9]*\$	0.40000	mW	Abs. pow. (mW)	Absorbed power given by $P_{abs} = I \mu_a P_{c\$}$
17	emitted_power_800nm	float	^[0-9]*\.[0-9]*\$	10.56500	mW	Luminescence/n800 (mW)	Total emitted power in all directions.
18	emitted_power_470nm	float	^[0-9]*\.[0-9]*\$	10.56500	mW	Luminescence/n470 (mW)	Total emitted power in all directions.
19	eQY_800nm	float	^[0-9]*\.[0-9]*\$	10000.56500	-	$\phi$	External Quantum yield: $(E * \lambda_{da_e}) / (\lambda^* ...$
20	eQY_470nm	float	^[0-9]*\.[0-9]*\$	10000.56500	-	$\phi$	External Quantum yield: $(E * \lambda_{da_e}) / (\lambda^* ...$

In [ ]:



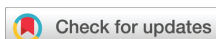
# PAPERS



**Evaluation of relative beam-profile-compensate quantum yield of upconverting nanoparticles over wide dynamic range of power densities**

J. S. Matias, K. Komolibus, S. Konugolu, and S. Andersson-Engels.  
*Nanoscale* **14**, 2230-2237 (2022).





Cite this: DOI: 10.1039/d1nr06129a

## Evaluation of relative beam–profile-compensated quantum yield of upconverting nanoparticles over a wide dynamic range of power densities†

J. S. Matias,<sup>a</sup> K. Komolibus,<sup>a</sup> S. Konugolu-Venkata-Sekar<sup>a</sup> and S. Andersson-Engels<sup>a,b</sup>

The presented work uses a discrete strategy of beam profile compensation to evaluate the local internal quantum yield (iQY) of upconverting nanoparticles (UCNPs) at the pixel level of the beam profile using a compact CMOS camera. The two-photon process of upconversion with a central emission peak at 804 nm was studied for a  $\beta$ -phase core–shell Tm-codoped UCNP under 976 nm excitation. At the balancing power density point,  $\rho_b$ , found to be  $44 \pm 3 \text{ W cm}^{-2}$ , the iQY,  $\eta_b$ , was obtained as  $2.3 \pm 0.1\%$ . Combining the power density dynamic range provided by the pixel depth of the camera with the dynamic range achieved using two distinct beam profiles to excite the UCNPs, the iQY was evaluated throughout a range of  $10^4$  in the iQY scale (from 0.0003% to 4.6%) and  $10^6$  in power densities of excitation (from 0.003  $\text{W cm}^{-2}$  to 1050  $\text{W cm}^{-2}$ ). To the best of our knowledge, these are the lowest values ever obtained as QY results have never been reported under 0.02% or at excitation power densities below 0.01  $\text{W cm}^{-2}$ .

Received 17th September 2021.

Accepted 17th December 2021

DOI: 10.1039/d1nr06129a

rsc.li/nanoscale

### 1. Introduction

Great attention has begun to be paid in the last decades to lanthanide doped inorganic nanocrystals (e.g.  $\text{NaYF}_4\text{:RE}$ ,  $\text{LuPO}_4\text{:RE}$ , etc. with  $\text{RE} = [\text{Yb}, \text{Tm}, \text{Er}, \text{Ho}, \text{etc.}]$ ),<sup>1</sup> known as upconverting nanoparticles (UCNPs), because of their distinct optical properties and promising applications in several fields including temperature sensing,<sup>2</sup> solar energy,<sup>3,4</sup> photocatalysis,<sup>5</sup> optogenetics,<sup>6</sup> diffuse optical tomography,<sup>7</sup> biosensors,<sup>8</sup> *in vivo* and *in vitro* biological imaging,<sup>9</sup> photodynamic therapy,<sup>10</sup> and super-resolution microscopy.<sup>11,12</sup> UCNPs feature a sharp emission band due to an anti-Stokes spectral shift, named upconversion (UC), which consists of multiple long wavelength photon absorption events followed by the emission of a single shorter-wavelength photon.<sup>13</sup> Accordingly, UC provides a series of benefits in the near infrared range, such as autofluorescence rejection,<sup>14,15</sup> increased light penetration depth in living tissue<sup>16</sup> and improved spatial image resolution.<sup>12</sup> In addition, UCNPs also allow surface functionalisation,<sup>17</sup> present low cytotoxicity,<sup>18</sup> and photo<sup>19</sup> and chemical stability.<sup>20</sup>

Despite all potentialities, UCNPs have poor UC efficiency and its evaluation has been a big challenge in terms of both experimental methodology as well as data analysis. At low power densities, the non-linearity of UC is more profound and its luminescence signal is relatively low. The characterisation at low power densities is extremely important for biomedical applications, especially deep in tissue. Living tissues can be exposed to limited irradiation, therefore, this poses a requirement for accurate and sensitive devices to evaluate the UC efficiency, also known as quantum yield (QY). However, currently, there are no available commercial systems able to tackle all the important parameters shown to affect the UCNPs' QY (e.g. excitation beam profile, scattering, and temperature<sup>21–23</sup>). Several groups have measured the QY absolutely using integrating spheres,<sup>24–26</sup> and other groups have performed relative measurements using a material with known QY as a reference.<sup>7,21,27,28</sup> Integrating spheres capture most of the emitted light from all directions, however, evaluating the excitation beam profile that reaches the UCNP sample can be difficult, considering that inside an integrating sphere the excitation laser beam can back-reflect and cross the sample multiple times. On the other hand, relative measurements are more versatile allowing for wavelength selectivity, and easier beam profile evaluation, although only a fraction of the emitted light is acquired within a small solid angle. The lack of standardisation leads to different approaches including different QY terminologies and definitions.<sup>29–32</sup> The internal quantum yield, referred to simply as iQY for the scope of this

<sup>a</sup>Biophotonics@Tyndall, IPIC, Tyndall National Institute, Cork, Ireland.

E-mail: jean.matias@tyndall.ie

<sup>b</sup>Department of Physics, University College Cork, Cork, Ireland

†Electronic supplementary information (ESI) available. See DOI: 10.1039/d1nr06129a

paper, is an accurate parameter to characterise and compare the UC efficiency of different UCNPs and is defined by the ratio of the number of emitted photons to the number of absorbed photons.

Regardless of the chosen method or terminology, one has to measure absorption and luminescence to evaluate UCNP efficiency. Absorption can be calculated from transmission measurements, however, the power losses due to scattering can be tricky to address. This is especially important in the case of powder samples or colloidal samples with the particles suspended in water. Water has high absorption in the near infrared range, overlapping with the absorption of the most common sensitizer in UCNPs,  $\text{Yb}^{3+}$ . In addition, measuring colloidal samples usually requires high concentrations, which causes the UCNPs to quickly precipitate, changing the scattering on the illumination path. For emission quantification, the beam profile strongly influences the UCNP's luminescence as UC has a non-linear behaviour with respect to the excitation power density. An unmodified laser beam has non-uniform power density distribution along its cross section, thus the particles irradiated by a laser beam experience distinct power densities and present distinct iQYs. May *et al.*<sup>33</sup> recently presented a detailed study on the importance of the excitation irradiance and power density definition for the evaluation of the iQY of UCNPs. In their paper, the authors pointed out the subjective determination of the radius of the excitation beam cross section, wherein different groups had chosen it arbitrarily (*e.g.* one standard deviation, *i.e.*  $1\sigma$ ,  $2\sigma$  or one-half of the full-width-half-maximum (FWHM) for Gaussian beams). As a conclusion, they suggested that the choice of a radius equal to  $1.8\sigma$  for Gaussian beams represents a certain kind of beam profile compensation for a two-photon UC process. However, this approach is only valid for Gaussian beams and does not correct irregularities such as speckles or interference. Therefore implementing an accurate beam profile compensation to evaluate the iQY of UC is extremely important, especially at low power densities where UC non-linearity is more profound. Among the vast literature reporting remarkable approaches to improve QY or to tune UC luminescence,<sup>34–37</sup> only a few papers have reported the influence of the beam profile on the QY of UCNPs.<sup>21,33,38,39</sup> In addition, because of the difficulties of measuring low UC signals and the excitation beam profile, the QY of UCNPs has not yet been deeply studied under low power density ranges, which are particularly interesting for biomedical applications, as previously mentioned.

Hence, using a discrete analysis obtained from a rate equation based model, this paper aims to present the beam profile compensated iQY for a two-photon UC process (804 nm centre emission peak) of a commercial core-shell UCNP ( $\beta\text{-NaYF}_4\text{:Yb}^{3+},\text{Tm}^{3+}$ ) for a wide dynamic range of power densities of the excitation beam, covering the linear regime at high power densities, down to the non-linear regime at extreme low power densities. In addition, we demonstrate how it is possible to explore the iQY of UCNPs locally within the beam profile and expand the results below the power density

limit of the excitation beam using a compact CMOS camera. To the best of our knowledge, QY results under 0.02% or at excitation power densities below  $0.01\text{ W cm}^{-2}$  have never been reported before.

## 2. Materials and methods

### 2.1. Sample characterisation

Water soluble  $\beta\text{-NaYF}_4\text{:Yb}^{3+},\text{Tm}^{3+}$  core-shell UCNPs in aqueous solution, purchased from Creative Diagnostics, were chosen for the experiments. Before studying the QY characteristics of these UCNPs, morphology and size were evaluated using a commercial scanning electron microscope (SEM). The UCNPs were drop cast over a 5 mm silicon piece and coated with a  $4 \pm 1$  nm layer of Au/Pd (95 : 5 in atomic proportion) to avoid charging of the UCNPs surface. Then, images of the surface of the silicon piece containing the UCNPs were acquired accordingly. Following that, 1 ml of the  $10\text{ mg ml}^{-1}$  as-purchased sample was transferred to a four clear window quartz cuvette and sonicated long enough that the particles were homogeneously dispersed and no aggregation was visually observed in the aqueous solution. The sample was left to rest for around 15 min in order that any possible existing cluster could settle down to the bottom and the whole sample could reach thermal equilibrium with the room temperature before absorption, luminescence, and emission spectrum measurements were conducted. These UCNPs are synthesised in such a way that the 804 nm emission intensity is maximised. This is a two-photon process named “energy transfer upconversion 2” (ETU2), however, Tm doped UCNPs can also have emission in the 470 nm range, an ETU3 process. Thus, to verify that, the sample in the same quartz cuvette was irradiated with a 976 nm laser line and its emission spectrum was measured with a commercial spectrometer (Ocean Optics – QEPRO-FL) at  $90^\circ$  to the excitation path.

### 2.2. QY evaluation

In order to calculate the iQY of the 804 nm emission peak; absorption, luminescence and beam profile measurements were performed using a QY system built in the lab based on a similar setup reported elsewhere.<sup>21</sup> Briefly, the system consists of two detection paths, for luminescence and transmission, oriented at  $90^\circ$  and along the excitation line, respectively (see Fig. S1 and Table S1 in the ESI† for more details). The beam profiles of a 500 mW CW 976 nm excitation laser diode (Thorlabs – BL976-PAG500), controlled by a digital driver (Thorlabs – CLD1015), were acquired using an 8-bit compact CMOS camera (Thorlabs – DCC3240-X) with  $5.30\text{ }\mu\text{m}$  square pixel size. In the luminescence path, an avalanche photodiode (APD, Thorlabs – APD410A) was precisely placed at the end of the detection arm. The QY procedure was calibrated by replacing the sample with the organic dye DY-781-01 (Dyomics, GmbH) see section S1 in the ESI.† The calibration procedure followed a standard protocol for the determination of fluorescence QYs of transparent samples,<sup>40</sup> and based on the pub-

lished QY of this dye (12.4%).<sup>21</sup> The APD was aligned with the centre of the cuvette using a 1 mm slit placed along the emission path to eliminate the contribution of any light coming from any part along the excitation beam outside this 1 mm range. The region at the centre of the cuvette will be referred to in this paper as the region of interest (ROI) and corresponds to 1 mm<sup>3</sup> in volume ensuring to include the full beam profile. For data acquisition, the laser driver, APD and power meter (Thorlabs – PM100D) were connected to a DAQ card (National instruments – NI USB 6212), which was connected to an external computer *via* USB. A Python application was developed to fully control the DAQ, in order to sweep up the laser power and collect the transmission and luminescence data simultaneously.

Given the described setup, transmission and luminescence were measured simultaneously, as well as sequentially under two distinct Gaussian beam profiles, labelled as BP1 and BP2. The scattering losses on transmission and luminescence were compensated with the UCNPs' scattering coefficient, which was determined by white light measurements (see section S3 and Fig. S3 in the ESI†). BP1 was prepared with the smallest possible beamwidth (106 μm taken as FWHM) without compromising its measurement given the resolution limit of the CMOS camera. In contrast, to improve the signal-to-noise ratio for the low beam power density range, BP2 was arranged with the largest possible spot size (530 μm, FWHM), yet smaller than the APD sensor size (1 mm<sup>2</sup>) to avoid luminescence signal loss. The same total power range (2–175 mW) was scanned for both beam profiles, thus, the two beamwidths were chosen appropriately to cover as wide beam power density range as possible. At this point, the excitation power density was evaluated by simply dividing the total excitation power by the area of the beam cross section ( $\pi r^2$ , where  $r$  is either  $1.8\sigma$  or one-half of the beamwidth taken as the FWHM). In this paper, the term “beam power density” will refer to this definition with  $r$  equal to one-half of the FWHM unless explicitly mentioned otherwise, while the term “local power density” will refer to the power density at a specific “pixel” of the beam profile. The local power density evaluation was made by measuring the beam profile with the CMOS camera and it was used to perform the discrete beam profile compensation. The full description of this strategy is explained in more detail below.

### 2.3. Data analysis and theoretical background

The beam profile compensation was performed by evaluating the local UC luminescence at each point of the beam profiles using a rate equation based model. According to the literature,<sup>21,38,39</sup> the uniform power density dependent iQY,  $\eta(\rho)$ , can be described by eqn (1) for a two-photon UC process:

$$\eta(\rho) = \frac{2\eta_b\rho}{\rho_b + \rho} \quad (1)$$

where  $\rho$  represents a uniform power density distribution, and  $\eta_b$  represents the iQY at the power density balancing point,  $\rho_b$ .

At  $\rho_b$ , the iQY is precisely half of its maximum saturation value at very high power densities.

On the other hand, the iQY is defined as the ratio between the number of photons emitted and the number of photons absorbed, and it can be described in terms of power by eqn (2),

$$\eta = \frac{L\lambda_e}{P_{\text{abs}}\lambda_a} \quad (2)$$

where  $L$  is the luminescence,  $P_{\text{abs}}$  is the absorbed power, and  $\lambda_e = 804$  nm and  $\lambda_a = 976$  nm are the emission and excitation wavelengths, respectively. Because absorption is a linear process for the studied power density range (see Fig. S2 in the ESI†),  $P_{\text{abs}}$  can be expressed as a function of power densities as stated by eqn (3),

$$P_{\text{abs}}(\rho) = l\mu_a\rho A \quad (3)$$

where  $l = 0.1$  cm is the length of the illumination path,  $A$  is the irradiated area, and  $\mu_a$  represents the absorption coefficient per centimetre obtained according to Beer–Lambert's law from transmission data using water as the reference. Rearranging eqn (1), (2) and (3), the uniform power density dependent luminescence becomes eqn (4),

$$L(\rho) = 2\eta_b\alpha A(\lambda_a/\lambda_e) \frac{\rho^2}{\rho_b + \rho} \quad (4)$$

where  $\alpha$  is the product of  $l\mu_a$  corresponding to the absorption factor under  $\lambda_a$  illumination. Notice that the magnitude of  $\rho_b$  determines the threshold of the UC's non-linearity/linearity. At high power densities where  $\rho \gg \rho_b$ ,  $L(\rho)$  becomes linear as shown by eqn (5):

$$\lim_{\rho_b/\rho \rightarrow 0} L(\rho) = 2\eta_b\alpha A(\lambda_a/\lambda_e)\rho. \quad (5)$$

For the ROI with non-uniform illumination, the resultant luminescence,  $L_r$ , is obtained from the APD's signal.  $L_r$  is the sum of all the local  $L$  contributions from UCNPs experiencing different local power densities. Therefore,  $L_r$  can be expressed as an integration over the volume of the ROI. However, for symmetry and simplicity, a discrete approximation was adopted. Dividing the ROI in  $N$  identical sub-regions with length  $l$  oriented along the excitation path and assuming that each sub-region has a small enough area in such a way that it presents uniform local power density,  $L_r$  is reduced to a linear combination of the individual luminescence contributions, as shown by eqn (6),

$$L_r = 2\eta_b\alpha A_{\text{px}}(\lambda_a/\lambda_e) \sum_k^N \frac{\rho_k^2}{\rho_b + \rho_k} \quad (6)$$

where  $\rho_k$  represents the power density at the centre of the  $k$ th sub-region and is given by the power measured by the  $k$ th pixel on the sensor of the CMOS camera divided by the area of the pixel  $A_{\text{px}}$ . The assumption here is that  $A_{\text{px}}$  is small enough to satisfy the local uniform power density condition. In addition,  $\rho_k$  taken at the centre of the ROI accounts for any power attenu-

ation, which can be considered linear along a small path length, such as  $l$ . Following the same principle, the total power absorbed by the UCNPs in the ROI,  $P_{\text{abs},r}$  is given by eqn (7),

$$P_{\text{abs},r} = l\mu_a P_c \quad (7)$$

where  $P_c$  is the total excitation power at the centre of the ROI and it is equivalent to the sum of all local powers.

Having  $L_r$  defined,  $\rho_b$  and  $\eta_b$  were obtained by fitting eqn (6) to the luminescence measured by the APD over a series of excitation powers for BP1 and BP2. First, the images taken with the CMOS camera were cropped around the ROI and had their background removed. Each resultant intensity matrix was converted to a vector of power densities,  $\rho_k$ , for each beam power data point. According to eqn (5), the UC luminescence curve in the linear regime provides more information regarding  $\eta_b$  and little regarding  $\rho_b$ . Because of that, the beam profile compensation was performed recursively:  $\eta_b$  obtained from the fitting of the UC luminescence due to BP1 illumination was used as the maximum accepted value to fit the UC luminescence of the UCNPs under BP2, and  $\rho_b$  obtained from the fitting due to BP2 was used as the minimum accepted value to fit the UC luminescence due to BP1. Finally, having the fitted parameters, the beam profile compensation was conducted by calculating the local contributions for each beam profile. The local absorption and local luminescence were obtained applying the eqn (3) and (4) to the local power densities,  $\rho_k$ . The local iQY was obtained by the iQY definition represented by eqn (2).

### 3. Results and discussion

The SEM image of the UCNPs, shown in Fig. 1a, exhibits hexagonal nanoparticles with an average size of  $36 \pm 3.1$  nm. The histogram with the size distribution of 150 UCNPs is displayed in the inset of Fig. 1a. The UCNPs presented a main UC luminescence peak at 804 nm (ETU2 with  ${}^3\text{H}_4 \rightarrow {}^3\text{H}_6$  electronic transition) under 976 nm excitation for various beam power densities, with secondary low intensity peaks at 695 nm (ETU2 with  ${}^3\text{F}_2 \rightarrow {}^3\text{H}_6$  transition), 646 nm (ETU3 with  ${}^4\text{G}_4 \rightarrow {}^3\text{F}_4$  transition), and 474 nm (ETU3 with  ${}^1\text{G}_4 \rightarrow {}^3\text{H}_6$  transition) shown in Fig. 1b. The 646 nm and 474 nm emission peaks represent a maximum of 0.2% and 0.5% of the total emission at 1800  $\text{W cm}^{-2}$  (see Fig. S4 in the ESI†) and thus the results indicate that the ETU3 process can be neglected, confirming that the simplified rate equation model could be applied in the iQY analysis of this material.

The characterisation of the beam profiles is shown in Fig. 2. The histograms represent the number of pixels with same intensity, and the 3D projections give the intensity spatial distribution of the images acquired with the CMOS camera, shown in the bottom right of the Fig. 2a and b. BP1 and BP2 have Gaussian-shape with beamwidths taken as the FWHM of 106  $\mu\text{m}$  and 530  $\mu\text{m}$ , respectively. Because of the smaller area of BP1, higher beam power densities were reached (21–1930  $\text{W cm}^{-2}$ ) throughout the range of the laser

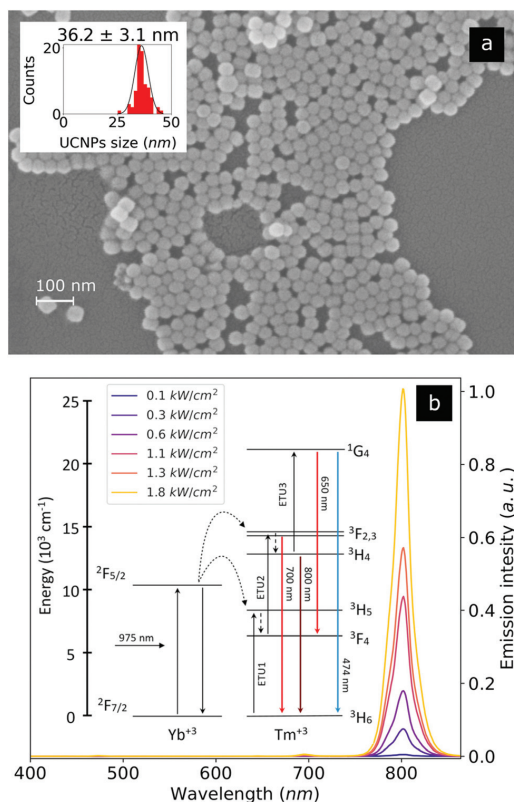


Fig. 1 SEM image and luminescence spectrum of the UCNPs. (a) The SEM image shows the UCNPs with  $36.2 \pm 3.1$  nm in size and hexagonal morphology. Its inset displays their size distribution histogram accounting for 150 nanoparticles. The Au/Pd coating used on the SEM technique was  $4 \pm 1$  nm in thickness. (b) The luminescence spectra of the UCNPs under 976 nm excitation, for various beam power densities, show main peak at 804 nm with secondary low intensity peaks at 695 nm, 646 nm and 474 nm. At 1800  $\text{W cm}^{-2}$  the secondary peaks represent altogether less than 1% of the intensity of the main emission peak. The transition for each luminescence is depicted on the energy level diagram (Jablonski diagram, inset of (b)).

power used. In contrast, the broader spot size of BP2 provided lower beam power densities (1–80  $\text{W cm}^{-2}$ ). Notice that there is an overlapping region between the two beam power density ranges, which was used to evaluate the accuracy of the beam profile compensation and of the rate equations based model on representing the UCNPs' behaviour under the linear and the non-linear regimes.

After the beam profiles were characterised, the parameters  $\rho_b$  and  $\eta_b$  were obtained by fitting eqn (6) to the resultant luminescence data. After four iterations, the results converged to the values and their respective least square errors associated as shown in Table 1. The small errors presented by the results reflect directly on the accurate fitting of the curves shown in

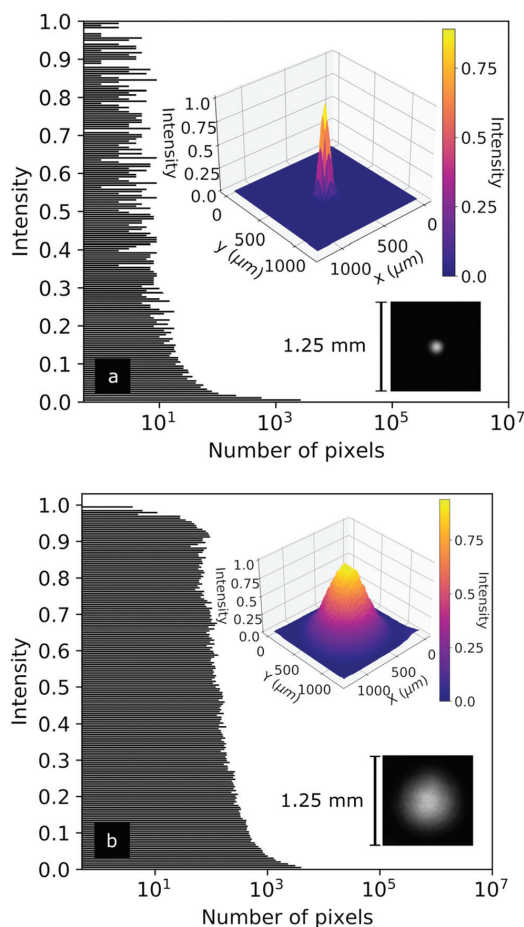


Fig. 2 Characterization of (a) BP1 (106  $\mu\text{m}$  at FWHM) and (b) BP2 (530  $\mu\text{m}$  at FWHM). The pictures acquired with the CMOS camera and cropped around the ROI of the beam spots are represented in the bottom right of each graph. The 3D projection of each beam shows their Gaussian profile. The histograms represent the number of pixels with the same normalised intensity in the log scale.

**Table 1** Fitting results obtained for the resultant luminescence of the UCNP's under BP1 and BP2 illumination. The parameter  $\eta_b$  is the iQY at the balancing power density point  $\rho_b$

Beam profile	$\eta_b$ (%)	$\rho_b$ ( $\text{W cm}^{-2}$ )
BP1	$2.28 \pm 0.02$	$43.7 \pm 3.2$
BP2	$2.29 \pm 0.06$	$43.8 \pm 2.0$

Fig. 3. The fitting process was performed on luminescence (in mW) versus a series of powers at the centre of the cuvette,  $P_c$  (in mW), converted to vectors of  $\rho_k$ , as previously described. Then, the luminescence data and the resultant fitted curves

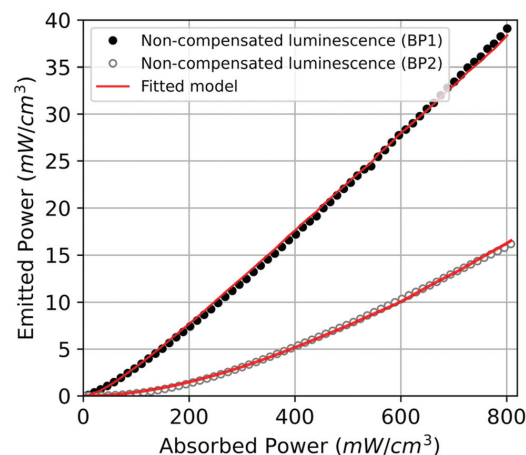
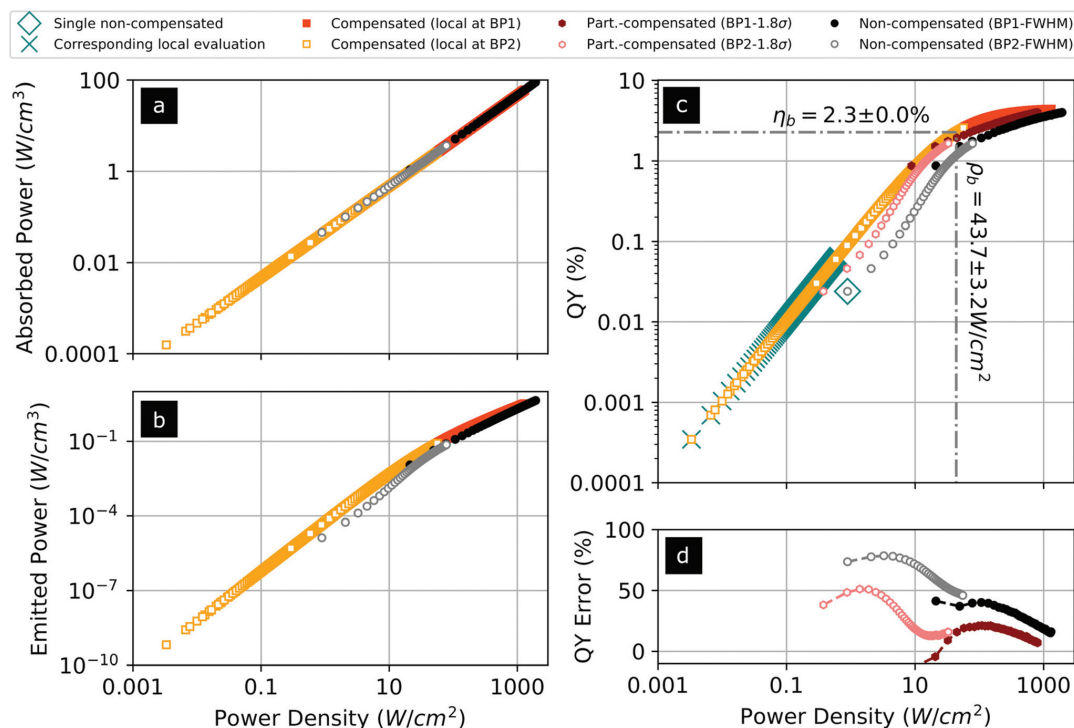


Fig. 3 Emitted power of the UCNP's in the ROI under two distinct beam profiles, BP1 and BP2. Under BP1 illumination, the UCNP's exhibited higher QY over the entire studied range. The distinct behaviour under different beam profiles evidences the need of the beam profile compensation on the QY analysis. The best fitted curves utilised a rate equations based model for the beam profile compensation. The results of the fitting are shown in Table 1.

were plotted versus the total absorbed power in Fig. 3, all converted to units of volume by dividing them by the volume of the ROI ( $1 \times 10^{-3} \text{ cm}^3$ ) for better visualisation and understanding. The total absorbed power was computed as stated by eqn (7) with the absorption coefficient  $\mu_a$  equal to  $(4.9 \pm 0.4) \times 10^{-2} \text{ cm}^{-1}$ , see Fig. S3.† Because of the linearity of absorption and because the sample was exposed to the same range of total laser powers in both measurements, the absorbed power range in the x-axis is identical for both curves. On the other hand, the difference in the UC luminescence for both beam profiles makes evident its strong beam profile dependence. Even though less UCNP's are exposed to the effective illuminated volume under BP1 than under BP2, the UC luminescence under BP1 is much higher for the whole absorbed power range, which translates to higher QY. Under BP1, the UCNP's experience higher local power densities and most of the UC luminescence curve exhibits linear behaviour. This means that the local power densities of BP1 are mostly above the non-linear threshold determined by  $\rho_b$ . In contrast, the local power densities of BP2 are mainly below this threshold, as observed by the deeper curvature of the UC luminescence plot. The strategy of using these two different beam profiles allowed for exploring the two extreme regimes of the UC luminescence.

In order to be able to compare the local results with the non-compensated ones, luminescence and absorbed power were divided by the effective illuminated volume and plotted versus the excitation power densities in Fig. 4a and b. The effective illuminated volume is given by the product  $l \times A$ , while the excitation power density is given by excitation power divided by  $A$ , where  $A$  is the area of a pixel, for the local



**Fig. 4** Power density dependence of (a) absorption, (b) luminescence and (c) QY of the UCNPs under BP1 and BP2 illumination. The square markers (in orange and dark orange) represent the local compensated ones at the pixel level (plotted versus the local power density at each pixel), the circles (in black and grey) are related to the non-compensated values (plotted versus beam power density defined with one-half of the FWHM as the radius of the beam cross section), and the hexagons (in light red and dark red) represent the partially compensated QY (plotted versus beam power density defined with  $1.8\sigma$  as the radius of the beam cross section). In (c) the large diamond highlights a single data point of the non-compensated QY as a result of the entire ROI and the x markers show its corresponding local iQY values at the pixel level for the same measurement. The iQY underestimation is shown in (d) as error percentage of the local iQY for both non-compensated and partially compensated QY.

results, and the area of the beam cross-section, for the non-compensated curves. For the iQY evaluation in Fig. 4c, the eqn (2) was applied. It is worth noting that the ratio of  $L$  and  $P_{\text{abs}}$  should be kept dimensionless. Since absorption is a linear process and the FWHM determination is usually used for linear processes, no divergence exists between the local and the non-compensated curves in Fig. 4a. On the other hand, the non-compensated luminescence curve is always under the local luminescence at the pixel level as seen in Fig. 4b. As a consequence, the non-compensated QY is underestimated, as shown in Fig. 4c. The non-compensated QY is an external property representing the efficiency of the sample within the ROI under its specific beam profile illumination. Although useful for certain applications, the non-compensated QY cannot be considered an intrinsic characteristic of the UCNPs, therefore it is not useful as a figure of merit to compare the efficiency of distinct UCNPs. The partial compensation, given by choosing the radius of the beam cross section as  $1.8\sigma$ , provides a better approximation to the local iQY in agreement

with May *et al.*<sup>33</sup> However, the QY curve represented by this definition still underestimates the iQY for the studied excitation power density range. The magnitude of underestimation was calculated and presented in Fig. 4d as the error percentage in respect to the iQY. At low power densities, where the UCNPs are in the non-linear regime, the error increases significantly reaching 75% and 50% underestimation for the non-compensated and partially compensated curves, respectively, under BP2 at  $5 \text{ W cm}^{-2}$ . Other methods of determining the beam power density ( $1\sigma$ ,  $2\sigma$ , and  $2.53\sigma$  - *i.e.* 4% of the maximum of the beam) are shown in Fig. S5 in the ESI.† On the opposite side of the curve, both non-compensated and compensate curves tend to merge to the iQY saturation point equal to 4.6%, *i.e.*  $2 \times \eta_b$ . At high beam power densities, more UCNPs are in the linear regime where the iQY is constant, however, regardless of how high the beam power density of a Gaussian profile is, it is not possible to obtain a flat non-compensated QY curve. The tails of a Gaussian profile will always have low power densities below the linear threshold. The underestima-

tion of the non-compensated QY confirms what was first reported by Mousavi *et al.*<sup>21</sup> The authors reported  $\rho_b = 14 \text{ W cm}^{-2}$  and  $\eta_b = 0.4\%$  for this class of material synthesised and prepared in-house, however, the analysed data were presented for a limited excitation power density range within the non-linear regime ( $1\text{--}30 \text{ W cm}^{-2}$ ). In addition, unlike their sample, the sample used for this paper is optimised for the 804 nm emission, presenting predominantly the ETU2 process, as shown by Fig. 1b. QY results for UCNP with more similar emission spectrum were recently reported by May *et al.*<sup>32</sup> The authors investigated samples of  $\beta\text{-NaYF}_4:0.5\% \text{ Tm}$ , 25% Yb core and  $\beta\text{-NaYF}_4:0.5\% \text{ Tm}$ , 25% Yb@ $\text{NaYF}_4$  core-shell dispersed in toluene over an excitation power density range of approximately ( $0\text{--}75 \text{ W cm}^{-2}$ ), in which they presented mainly the 804 nm emission. Their core and core-shell samples showed a maximum iQY of around  $4.0 \pm 0.5\%$  and  $10.0 \pm 1.2\%$ , respectively, above  $70 \text{ W cm}^{-2}$ , the highest studied power density. Under this excitation the samples seem to be at, or close to their saturation point; however, exact values for  $\eta_b$  and  $\rho_b$  are not shown on their report since they have used different methods to evaluate the iQY using the  $\text{Yb}^{3+}$  emission as an internal standard.

Comparing the non-compensated values with the local compensated results, it is also possible to notice that the local values allow exploring at least 2 orders of magnitude more in power densities towards low intensities. The power density gain occurs because of the  $10^2$  dynamic range of the CMOS camera. The relation between a single non-compensated measurement with its corresponding local iQY results is exemplified in Fig. 4c (see section S6 in the ESI† for more details). The large diamond marker highlights a single non-compensated QY data point at the lowest BP2 power density and the  $\times$  markers highlight the corresponding reconstructed local iQY at the pixel level for the same measurement. The retrieved iQY for this single beam power density spans through  $10^2$  QY dynamic range below the lowest value of the non-compensated QY ( $0.02\%$  at  $1 \text{ W cm}^{-2}$ ). Iterating the analysis for all the non-compensated data points, the full local iQY curve is reconstructed covering a wide dynamic range of  $10^4$  in the iQY scale, from  $0.0003\%$  to  $4.6\%$ , and  $10^6$  of excitation power densities, from  $0.003 \text{ W cm}^{-2}$  to  $1050 \text{ W cm}^{-2}$ . This strategy is a powerful tool, which allows one to accurately determine the iQY in the non-linear regime of UCNP below the luminescence detection limit. The lowest UC luminescence detected by the APD was limited to  $\sim 10^{-5} \text{ W cm}^{-3}$  at  $\sim 1 \text{ W cm}^{-2}$ , however, by decomposing it to the pixel level, the local UC luminescence was evaluated down to  $10^{-9} \text{ W cm}^{-3}$ , a gain of 4 orders of magnitude.

## 4. Conclusion

This paper presented a discrete strategy of beam profile compensation to evaluate the iQY of an ETU2 process. With this approach, the iQY of a commercial core-shell UCNP ( $\text{NaYF}_4:\text{Yb}^{3+},\text{Tm}^{3+}$ ) was evaluated over a  $10^6$  dynamic range of power densities (from  $0.003 \text{ W cm}^{-2}$  to  $1050 \text{ W cm}^{-2}$ ) covering both

extremes of the non-linear and linear regime. The non-compensated QY varies considerably with the excitation beam profile. In addition, the beam profile compensated iQY was compared to the non-compensated QY (which takes one-half of the FWHM to define radius of the excitation beam and then uses it to determine the beam power density) and to the partially compensated QY (which takes  $1.8\sigma$  as the radius). The non-compensated QY is highly underestimated, reaching 75% error at low power densities as demonstrated by the results. On the other hand, the partial compensation reduced the error for the entire power density range; however, the results still showed a high error of 50% at low power densities. As a conclusion, implementing the beam profile compensation is essential for determining the QY as an intrinsic characteristic of materials with non-linear luminescence. Exploring UC at low excitation power densities is extremely important for biomedical applications and the approach of decomposing the non-compensated luminescence into local sub-regions with uniform illumination pushed the results downwards to QY values never reported before (under  $0.02\%$  or at excitation power densities below  $0.01 \text{ W cm}^{-2}$ ). It is critical to drive research to improve QY analysis and develop devices with high resolution and sensitivity that are able to accurately characterise UCNP without external influences (such as scattering and beam profile) in order to improve their low QY, tune their luminescence and compare results among different laboratories in a meaningful way. Furthermore, this methodology opens opportunities to explore even lower power densities by replacing the compact CMOS camera with cameras or beam profilers with higher pixel depths, covering higher dynamic ranges.

## Author contributions

Conceptualisation, J. S. M., K. K., S. K. V. S. and S. A. E.; data curation, J. S. M. and K. K.; formal analysis, J. S. M.; funding acquisition, S. A. E.; investigation, J. S. M. and K. K.; methodology, J. S. M.; project administration, K. K., S. K. V. S. and S. A. E.; software, J. S. M.; supervision, K. K. and S. A. E.; validation, J. S. M., K. K. and S. K. V. S.; visualisation, J. S. M.; writing – original draft, J. S. M. and K. K.; writing – review and editing, J. S. M., K. K., S. K. V. S. and S. A. E.

## Conflicts of interest

The authors declare that they have no conflict of interest.

## Acknowledgements

The authors would like to thank the Electron Microscopy Technician, Davinder Singh, for acquiring the SEM images of the UCNP, and his prompt response as well as Monirehalsadat Mousavi for helpful discussions. This project was funded by SFI/15/RP/2828.

## References

- 1 F. Wang and X. Liu, *Chem. Soc. Rev.*, 2009, **38**, 976–989.
- 2 B. Dong, B. Cao, Y. He, Z. Liu, Z. Li and Z. Feng, *Adv. Mater.*, 2012, **24**, 1987–1993.
- 3 J. De Wild, J. K. Rath, A. Meijerink, W. G. Van Sark and R. E. Schropp, *Sol. Energy Mater. Sol. Cells*, 2010, **94**, 2395–2398.
- 4 T. F. Schulze and T. W. Schmidt, *Energy Environ. Sci.*, 2015, **8**, 103–125.
- 5 D. Li, S. H. Yu and H. L. Jiang, *Adv. Mater.*, 2018, **30**, 1–7.
- 6 A. Bansal, H. Liu, M. K. G. Jayakumar, S. Andersson-Engels and Y. Zhang, *Small*, 2016, **12**, 1732–1743.
- 7 C. T. Xu, P. Svenmarker, H. Liu, X. Wu, M. E. Messing, L. R. Wallenberg and S. Andersson-Engels, *ACS Nano*, 2012, **6**, 4788–4795.
- 8 Y. Wang, L. Bao, Z. Liu and D. W. Pang, *Anal. Chem.*, 2011, **83**, 8130–8137.
- 9 Q. Zhan, J. Qian, H. Liang, G. Somesfalean, D. Wang, S. He, Z. Zhang and S. Andersson-Engels, *ACS Nano*, 2011, **5**, 3744–3757.
- 10 N. M. Idris, M. K. Gnanasamandhan, J. Zhang, P. C. Ho, R. Mahendran and Y. Zhang, *Nat. Med.*, 2012, **18**, 1580–1585.
- 11 M. D. Wisser, S. Fischer, C. Siefe, A. P. Alivisatos, A. Salleo and J. A. Dionne, *Nano Lett.*, 2018, **18**, 2689–2695.
- 12 D. Denkova, M. Ploschner, M. Das, L. M. Parker, X. Zheng, Y. Lu, A. Orth, N. H. Packer and J. A. Piper, *Nat. Commun.*, 2019, **10**, 1–12.
- 13 D. R. Gamelin and H. U. Gudel, *Topics in Current Chemistry*, Springer, Berlin, Heidelberg, 2001, vol. 214, ch. Upconversion, pp. 1–54.
- 14 F. Auzel, *Chem. Rev.*, 2004, **104**, 139–173.
- 15 J. Xu, A. Gulzar, P. Yang, H. Bi, D. Yang, S. Gai, F. He, J. Lin, B. Xing and D. Jin, *Coord. Chem. Rev.*, 2019, **381**, 104–134.
- 16 N.-N. Dong, M. Pedroni, F. Piccinelli, G. Conti, J. E. Ramirez-hernández, L. M. Maestro and M. Carmen, *ACS Nano*, 2011, **2**–3.
- 17 B. Zhou, B. Shi, D. Jin and X. Liu, *Nat. Nanotechnol.*, 2015, **10**, 924–936.
- 18 L. Xiong, T. Yang, Y. Yang, C. Xu and F. Li, *Biomaterials*, 2010, **31**, 7078–7085.
- 19 N. M. Idris, Z. Li, L. Ye, E. K. Wei Sim, R. Mahendran, P. C. L. Ho and Y. Zhang, *Biomaterials*, 2009, **30**, 5104–5113.
- 20 S. Wilhelm, M. Kaiser, C. Würth, J. Heiland, C. Carrillo-Carrion, V. Muhr, O. S. Wolfbeis, W. J. Parak, U. Resch-Genger and T. Hirsch, *Nanoscale*, 2015, **7**, 1403–1410.
- 21 M. Mousavi, B. Thomasson, M. Li, M. Kraft, C. Würth, U. Resch-Genger and S. Andersson-Engels, *Phys. Chem. Chem. Phys.*, 2017, **19**, 22016–22022.
- 22 C. M. S. Jones, N. Panov, A. Skripka, J. Gibbons, F. Hesse, J.-W. G. Bos, X. Wang, F. Vetrone, G. Chen, E. Hemmer and J. Marques-Hueso, *Opt. Express*, 2020, **28**, 22803.
- 23 R. Shi, E. D. Martinez, C. D. Brites and L. D. Carlos, *Phys. Chem. Chem. Phys.*, 2021, **23**, 20–42.
- 24 J. C. Boyer and F. C. Van Veggel, *Nanoscale*, 2010, **2**, 1417–1419.
- 25 M. S. Meijer, P. A. Rojas-Gutierrez, D. Busko, I. A. Howard, F. Frenzel, C. Würth, U. Resch-Genger, B. S. Richards, A. Turshatov, J. A. Capobianco and S. Bonnet, *Phys. Chem. Chem. Phys.*, 2018, **20**, 22556–22562.
- 26 C. Würth, M. Kaiser, S. Wilhelm, B. Grauel, T. Hirsch and U. Resch-Genger, *Nanoscale*, 2017, **9**, 4283–4294.
- 27 B. Thomasson, MSc thesis, Lund University, 2015.
- 28 N. Kiseleva, D. Busko, B. S. Richards, M. A. Filatov and A. Turshatov, *J. Phys. Chem. Lett.*, 2020, **11**, 6560–6566.
- 29 Y. Zhou, F. N. Castellano, T. W. Schmidt and K. Hanson, *ACS Energy Lett.*, 2020, **5**, 2322–2326.
- 30 S. Fischer, N. J. Johnson, J. Pichaandi, J. C. Goldschmidt and F. C. Van Veggel, *J. Appl. Phys.*, 2015, **118**, 193105.
- 31 M. Pokhrel, A. K. Gangadharan and D. K. Sardar, *Mater. Lett.*, 2013, **99**, 86–89.
- 32 P. S. May, A. Baride, M. Y. Hossan and M. Berry, *Nanoscale*, 2018, **10**, 17212–17226.
- 33 P. S. May and M. Berry, *Methods Appl. Fluoresc.*, 2019, **7**, 023001.
- 34 S. Schietinger, T. Aichele, H. Q. Wang, T. Nann and O. Benson, *Nano Lett.*, 2010, **10**, 134–138.
- 35 F. Wang, R. Deng, J. Wang, Q. Wang, Y. Han, H. Zhu, X. Chen and X. Liu, *Nat. Mater.*, 2011, **10**, 968–973.
- 36 H. Liu, C. T. Xu, G. Dumlupinar, O. B. Jensen, P. E. Andersen and S. Andersson-Engels, *Nanoscale*, 2013, **5**, 10034–10040.
- 37 Y. Wang, R. Deng, X. Xie, L. Huang and X. Liu, *Nanoscale*, 2016, **8**, 6666–6673.
- 38 H. Liu, C. T. Xu, D. Lindgren, H. Xie, D. Thomas, C. Gundlach and S. Andersson-Engels, *Nanoscale*, 2013, **5**, 4770–4775.
- 39 M. Kaiser, C. Würth, M. Kraft, I. Hyppänen, T. Soukka and U. Resch-Genger, *Nanoscale*, 2017, **9**, 10051–10058.
- 40 C. Würth, M. Grabolle, J. Pauli, M. Spieles and U. Resch-Genger, *Nat. Protoc.*, 2013, **8**, 1535–1550.

**Multi-variable compensated quantum yield  
measurements of upconverting nanoparticles with  
high dynamic range: a systematic approach**

S. Konugolu, J. S. Matias, K. Komolibus, and S. Andersson-Engels.  
*Opt Express.* **30(10)**, 16572-16584 (2022).



# Multi-variable compensated quantum yield measurements of upconverting nanoparticles with high dynamic range: a systematic approach

SANATHANA KONUGOLU VENKATA SEKAR,<sup>1,4\*</sup> JEAN S. MATIAS,<sup>1,2,4</sup> GOKHAN DUMLUPINAR,<sup>1,2</sup> LORENZO NIEMITZ,<sup>1,2</sup> MONIREHALSADAT MOUSAVI<sup>3</sup>, KATARZYNA KOMOLIBUS,<sup>1</sup> AND STEFAN ANDERSSON-ENGELS<sup>1,2</sup>

<sup>1</sup>*Biophotonics@Tyndall, IPIC, Tyndall National Institute, Cork, Ireland*

<sup>2</sup>*Department of Physics, University College Cork, Cork, Ireland*

<sup>3</sup>*Department of Physics, Lund University, Lund, Sweden*

<sup>4</sup>*Equally contributed to this work*

\*[sanathana.konugolu@tyndall.ie](mailto:sanathana.konugolu@tyndall.ie)

**Abstract:** Non-linear materials like upconverting nanoparticles (UCNPs) are emerging technology with fast-growing applications in various fields. The power density dependence of the emission quantum yield (QY) of these non-linear materials makes them challenging to characterize using currently available commercial QY systems. We propose a multimodal system, which takes into account and compensates for various distorting parameters (scattering, beam profile, inner filter effect and bandwidth of emission lines) over the entire dynamic range ( $1:10^4$ ) of the QY curve. The novel beam shaping approach enabled speckle free beam profiles of various sizes (530  $\mu\text{m}$  or 106  $\mu\text{m}$ ). This provides low noise high-resolution QY curves. In particular, at low power densities, the signal to noise ratio  $>50$  was found. A Tm-based core-shell UCNP with excitation at 976 nm and emission at 804 nm was investigated with the system.

© 2019 Optical Society of America under the terms of the [OSA Open Access Publishing Agreement](#)

## 1. Introduction

The use of upconverting nanoparticles (UCNPs) has developed rapidly and today spans a wide range of research fields including, among others, molecular interactions in cell biology, specific staining of tissue slides, *in vivo* luminescence imaging, and photodynamic therapy [1-10]. Each of these avenues of research stems from the discovery of the upconversion (UC) process by Bloembergen [11] and an early series of studies conducted by Auzel [12-14]. UC is the unique feature of certain materials to generate a high energy photon as a consequence of the sequential absorption of multiple low energy photons. UC capable nanomaterials have demonstrated remarkable optical features, which have facilitated the generation of high impact findings in various fields of research in biomedicine.

Due to the varying requirements in different biomedical applications, both material design and optimization of these particles are playing key roles in framing further research. To date, numerous properties of UCNPs have been investigated, including crystal composition and structure, surface functionality, and biocompatibility [15-20]. Recently, one of the important areas of UCNP-related research has focused on understanding the non-linear behaviour of UCNPs and their luminescence efficiency. The low quantum yield (QY) nature of UCNPs has

been a limiting factor in the extensive adoption of UCNPs in biomedical applications. QY is typically in the range of a few percent at high excitation power densities and decreases dramatically to a fraction percent in the low power density regime [21]. The power dependence of the QY is critically important, especially for deep tissue applications - where the excitation light is heavily attenuated by intrinsic biomolecules and where low power densities are required. Various factors influence the QY of UCNPs, including crystal properties (*e.g.* host matrix, size, phase, and dopant ratio), surface properties, and dispersion medium [22-27]. Hence, extensive research aimed at improving the QY of UCNPs to obtain a stronger signal is well motivated. Many different approaches have been applied to increase QY, including but not limited to optimization of particle composition [28], engineering of the excitation source [9, 29, 30], and implementation of core-shell structures [31, 32].

The efforts in improving the luminescence efficiency of UCNPs make standardized QY measurements essential. More recently, the importance of the excitation beam profile in such measurements was reported [3-37]. Traditionally, integrating sphere instruments are used to measure the absolute QY, as these can collect emission in all directions. The alternative would be to use a detector measuring at a limited solid angle. This can then yield the QY by referring to measurements of a dye with a known QY in the same measurement geometry, assuming that the spatial distribution of the emission from the two samples are identical. The advantage of the latter relative QY technique is that the power density across the beam profile can be controlled to a greater degree, which is of significant importance as the QY depends on the power density of the excitation light. The efficient reflections within an integrating sphere, together with a complication in measuring the actual beam profile in an integrating sphere, make it difficult to control the exact beam profile of the excitation light in this type of setup. Also, the QY measurements using an integrating sphere provide poor signal-to-noise ratio (SNR) owing to the fraction of emitted light collected by the sphere, making it hard to measure at low power densities, which is critical for biomedical application.

Currently, there is no complete system that adequately characterizes the QY of UCNPs. Therefore, there is a high demand for a compact QY characterization system specifically designed to characterize non-linear materials. The ideal system should include:

1. a speckle free excitation beam profile for power density compensation,
2. a multi-variable characterisation namely absorption, scattering, emission spectra for compensation of their influence on QY curves,
3. a high SNR in low power density region to enable low noise, repeatable and reproducible characterisation in this important regime of operation,
4. a high-resolution step size of laser excitation power to resolve subtle features that would enhance the understanding of the QY curve,
5. a wide dynamic range of QY curves,
6. a broad spectral range of excitation and detection to allow for measurements of all emission lines of interest,
7. a systematic QY characterization protocol that would allow for direct comparisons between different materials that are developed by various research groups,
8. and a fully automated and well-controlled experimental setup with a subroutine to excite and acquire absorption and emission under the same experimental conditions across various power densities.

In this work, we present, to the best of our knowledge, a novel multi-modal QY system that addresses the above-mentioned challenges in characterizing the QY of non-linear material like UCNP. It compensates for various distorting parameters (scattering, beam profile, inner filter effect, the limited bandwidth of emission lines) and provides well-resolved high dynamic range QY curves. The system provides the means to measure the absorption, scattering, emission spectra of samples and the beam profile employed in the excitation. Importantly, the method also eliminates the influence of uneven and uncontrolled power density distribution due to speckles of a coherent excitation laser by cleverly managing the illumination path design. It

also provides high SNR, in particular, at low power density by changing the beam size. Tm-based core-shell UCNPs with excitation at 976 nm and emission at 804 nm were investigated using the system.

## 2. Material and Methods

### 2.1 System Setup

Figure 1 shows the schematic layout of the multi-modal QY system. The system consists of 6 arms designed to shape the beam (arms 1 and 2) and acquire the beam profile (arm 3) and characterize various optical parameters (absorption and scattering, emission spectra, and luminescence signal) of the UCNP sample (arms 4, 5, 6, respectively). Arm 1 (UCNP excitation arm) consists of temperature stabilized single-mode fibre-coupled diode laser (Thorlabs, BL976-PAG500) at 976 nm and an optical arrangement to achieve speckle free beam profile of adjustable size. Two sets of optics in arm 1 (L1  $f = 30$  mm; L2  $f = 30$  mm or nil; L3  $f = 6$  mm or nil; and L4  $f = 200$  mm) were used to achieve two different spot sizes: 530  $\mu\text{m}$  or 106  $\mu\text{m}$  in beam diameter (full width at half maximum-FWHM). The two spot sizes were chosen to achieve a high SNR in the low power density region, the high dynamic range of power densities while also having an optimal overlap of the two QY curves generated. A filter F1 (CM1-BP145B2) was employed to further increase the range of QY curves at low power densities for a given spot size. Lenses L1 and L3 on arm 1 were mounted on XY stages (Thorlabs CXY1) for precise alignment of the beam spot in the middle of the cuvette holder. A pair of irises (I1 and I2) were used to align the spot in the middle of the cuvette. A polarizer P1 (Thorlabs, LPNIRE200-B) was placed in between lenses L1 and L2 to vertically polarize the light impinging on the sample. A power meter PM (Thorlabs, PM100D) was attached at the distal end of the cuvette holder to measure the power of the light passing through the sample. Arm 2 (reference dye excitation arm) is a replica of arm 1 with a single-mode fibre-coupled 785 nm laser (Thorlabs FPL785S-250 at 785 nm) used for excitation. The arm is enabled by flipping the flip mirror (FM2). The purpose of this arm is to acquire the luminescence signal from the dye whose emission line is similar to the emission of the UCNP. The QY value of the dye used was well known from the literature (11.9%) [34, 38], which enables the relative QY assessment by calibrating the experimentally obtained QY values from the UCNP.

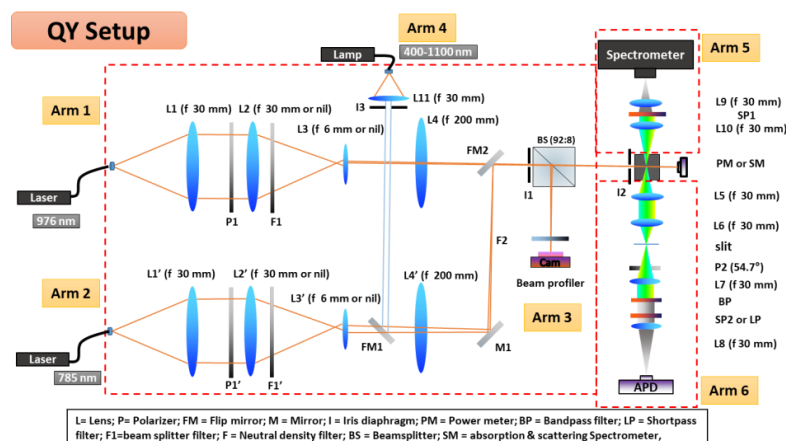


Fig. 1 Optical layout of multimodal QY system. Arm 1 and 2 are identical excitation arms used to shape the excitation beams: 976 nm and 785 nm for the excitation of the UCNP and reference dye, respectively. Arm 3 collects a fraction of the laser light for beam profile measurements.

Arm 4 includes a broadband white light to the main excitation path to perform scattering measurements, replacing the power meter, PM, with a spectrometer. Arm 5 is used for emission spectrum evaluation and arm 6 is used to collect the luminescence signal from UCNPs or Dye (once for calibration).

Arm 3 (beam profile arm) consists of a compact high-resolution CMOS camera (Thorlabs DCC3240M) and a set of neutral density filters to acquire the beam profile of the excitation light employed, identical to the beam profile in the cuvette. A pellicle beam splitter (BS, Thorlabs, CM1-BP108, 92:8) was used to split the rays and the camera was placed equidistant to the center of the cuvette holder thus acquiring a beam profile resembling the midpoint of the sample cuvette. Arm 4 (scattering spectra arm) provides a broadband light source (Ocean Optics HL 2000) to enable a wide range of absorbance spectra to estimate the scattering contribution of the sample. This arm is enabled by flip mirrors (FM1 and FM2) which guide the white light to the sample in the sample holder. For this measurement, the power meter (PM) was replaced with a fiber bundle (Thorlabs BFL200HS02) which was connected to the spectrometer (Ocean Optics QE Pro, 350-1100 nm). The intensity and spot size of this arm is controlled using an iris (I3). Arm 5 collects the luminescence light from the sample and sends it to the fiber-coupled (Thorlabs BFL200HS02) spectrometer (Ocean Optics QE Pro) to measure the emission spectra of UCNP samples. The arm consists of lenses (L9, L10  $f = 30$  mm), and a short pass filter SP1 (Thorlabs, FES0900) to remove excitation stray light at 976 nm. Arm 6 is the luminescence arm, which collects the luminescence light emitted by the sample using a set of lenses (L5, L6, L7, L8 = 30 mm) and focuses that light onto an avalanche photodiode (APD) detector (Thorlabs, APD410A). A slit (1 mm) is placed between L6 and L7 to limit the measured light to the emission generated in the center of the cuvette and also manage to avoid luminescence signals overfilling the APD. A polarizer P2 (Thorlabs, LPNIRE100-B) is kept at  $54.7^\circ$  with respect to the linear polarizer in excitation arms to remove distortion caused due to any anisotropic nature of the samples. A set of two filters, a bandpass BP (Thorlabs, FBH800-40) and a short pass SP2 (Thorlabs, FES0900) are placed in the path to filter excitation light and only allow the luminescence signal (804 nm) to pass and be focused on the APD active area. Similarly, a bandpass BP (Thorlabs, FBH800-40) and long pass LP (Semrock - LP02-785RE-25) filters are adopted to avoid excitation light while measuring the reference dye signal. An XY stage (Thorlabs CXY1) was used to precisely center the APD detector and thereby enable accurate alignment. A data acquisition (DAQ) device (National Instruments, USB-6216) along with a preamplifier (Femto – DLPVA) was used to acquire the signal from the APD. All parameters varied in the system (e.g. laser current, power meter settings, beam profile, spectrometer settings) and the measurement routine are controlled and automated using a user-specified Python script interface.

## 2.2 Samples preparation

The samples used for this study were water-soluble  $\text{NaYF}_4:\text{Tm}$  core-shell UCNP samples procured from Creative Diagnostics at a concentration of 10 mg/ml. These UCNPs were optimized during the synthesis for enhancement of the 804 nm emission transition. The reference dye used to calibrate the UCNPs signal was procured from Dyomics (Dy-781-01). The dye has been chosen to match the emission wavelength of the UCNPs (804 nm) and a factory tabulated QY of 11.9% (in ethanol) has been provided by the manufacturer. In addition, this dye has been previously characterised [34] following standard protocols from certified laboratories for linear fluorescent materials [35]. The dye was diluted in ethanol solvent in a concentration that yielded luminescence values similar to 10 mg/ml UCNP samples used for this study. Two dedicated cuvettes with water and ethanol solvents were prepared as blank references to obtain absorption values of pure UCNPs and dye. A volume of 1 ml was the minimum quantity needed to perform the measurement. Therefore, 2 ml of each sample were placed in a quartz cuvette (Thorlabs, CV10Q3500FS).

### 2.3 Measurement protocol and data analysis

A systematic procedure was adopted for both, the collection of data from the sample and the analysis algorithm to extract compensated QY values. The workflow for data collection and analysis is depicted in Figure 2.

#### Measurement protocol

At first, the UCNP and dye samples were prepared as mentioned in section 2.2. and sonicated for 15 minutes. The broadband (350-1100 nm) emission spectrum of the UCNPs was acquired using arm 5. This was followed by broadband transmission measurements of samples in the following order: UCNPs, reference water, empty cuvette, dye sample, reference ethanol. Then the system was set up to create spot size S1 in both arms 1 and 2. The beam profile of S1 was captured using arm 3 with the beam profile camera, followed by luminescence signal measurements of UCNPs in arm 6 at various laser currents (976 nm, 0 - 800 mA, step size 12 mA). The same process was directly repeated thereafter for the dye sample at various laser currents (785 nm, 0 - 250 mA, step size 1.5 mA). The whole procedure of measuring the luminescence signal of UCNPs and dye at S1 was repeated with filter F1 & F1' in the respective arms. Then, the whole sequence of measurements was repeated for beam profile S2. In total, eight luminescence measurement series were conducted in the following order: UCNP-S1, dye-S1, UCNP-S1-F1, dye-S1-F1', UCNP-S2, dye-S2, UCNP-S2-F1, dye-S2-F1'. This completes the measurement sequence of the multimodal system. The outputs of the measurement sequence are the emission spectrum of UCNPs, in total five transmission data of UCNP and dye samples, two beam profiles of S1 and S2, and eight luminescence signals of UCNPs and dye combined.

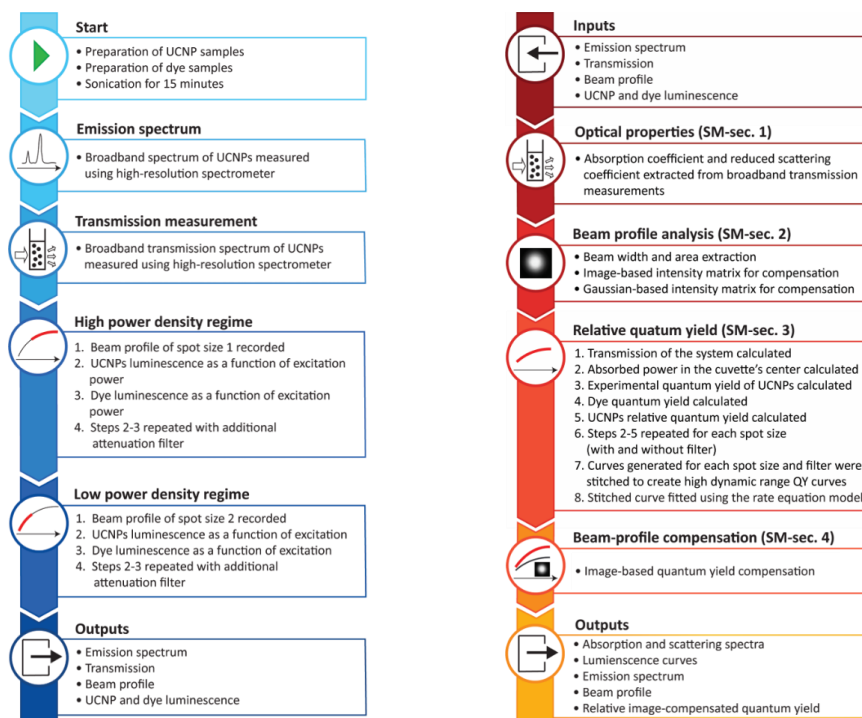


Fig. 2 Schematic flow chart depicting the measurement protocol and analysis algorithm. The left side shows the measurement protocol and the right side provides the outline of analysis methods.

#### *Analysis methods*

The analysis algorithm takes all the outputs of the measurements as inputs and calculates various optical parameters (wide dynamic range QY, absorption, scattering, the processed emission spectra, beam profile) and subsequently uses the calculated data to compensate for possible distortions in the estimated high dynamic range QY values of UCNPs. The steps are briefly described in this section, more detailed equations and calculation steps could be found in the supplementary material (SM). The first step is to calculate the absorption and scattering spectra of UCNPs from the transmission measurement data. Beer Lamberts' and Mie scattering laws were used for the estimation of absorbance and scattering spectra of the samples as described in the SM-sec.1. The compensated absorption of UCNPs at 976 nm was used as input to the QY calculations. The acquired beam profiles of the 976 nm laser (S1 and S2) were employed to create i) image-based intensity matrix (SM-sec.2), utilized to calculate the image compensated QY value of UCNP. The experimental QY (not compensated with dye QY) is obtained by taking the ratio of luminescence signal of UCNP to the absorbed power per unit length in the centre of the cuvette (SM-sec.3). The relative QY is estimated by calibrating the UCNP experimental QY values with dye QY values (SM-sec.3). The above process to find the relative QY was repeated for all spot sizes (S1, S2) and filter (nil, F1) configurations which provides in total four QY curves. The relative QY curves were stitched without any fitting parameters to provide a high dynamic range relative QY curve. The relative QY curves were compensated for the beam profile to avoid underestimating the QY values. This compensation was implemented by solving the QY for each pixel in the beam profile using a 2-level rate equation for the 804 nm line. The balancing power density ( $\rho_b$ ) and balancing QY ( $\phi_b$ ) for all dynamic range relative QY curves (uncompensated, and image compensated) were calculated. The details of compensation methods are discussed in SM-sec.4.

### **3. Results and Discussion**

### 3.1 Temporal and Spatial Beam profile characterization

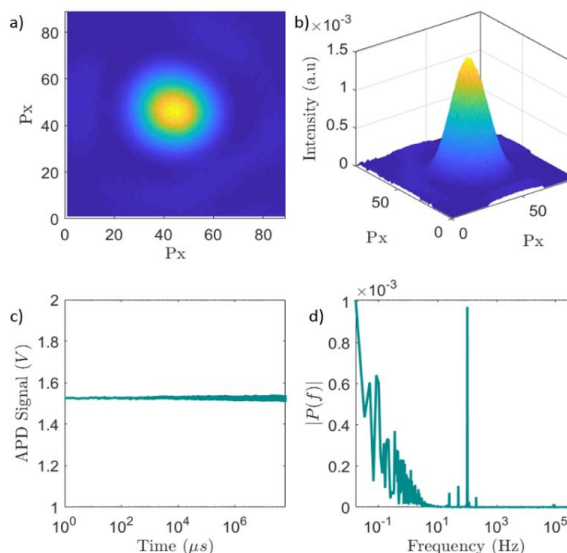


Fig. 3 Beam profile characterization a) Beam profile image b) Beam profile in 3D plot c) Raw temporal signal from one pixel of the beam profile shows no temporal fluctuations in laser intensity d) Fourier transform of the temporal signal show low frequency  $1/f$  noise and harmonics of power supply.

One of the key features of the system is the ability to obtain a speckle free uniform beam profile for a given spot size. This is achieved by using a single-mode fiber followed by an optical beam shaping lens set up to obtain spot size while preserving the speckle free beam profile. It is critical to have the power density (light intensity) across the beam profile as uniform and stable as possible. Such a profile will lead to fewer compensations and thereby accurate estimations of relative QY values of non-linear material. Figure 3(a-b) shows the beam profile acquired by the camera equidistant to the midpoint of the sample cuvette. The smooth speckle-free profile enables the algorithm to easily compensate for the beam-profile-based distortion to the evaluated QY curves. However, it is also important to ensure that the laser is temporally stable over the entire measurement period. To test this, the power meter at the distal end of the sample holder was temporarily replaced by a single-mode fiber ( $6 \mu\text{m}$  core diameter) with the other end of the fiber connected to an APD detector. The small fraction of light collected by the APD detector was acquired for 60 sec by using a DAQ card at a collection rate of 1 Mega sample/sec. Figure 3c shows the raw data acquired by the APD detector. The variation in the amplitude of the laser during one minute is less than 0.5%. To understand the key variation frequencies we performed a Fast Fourier transform (FFT) of the acquired signal. The results are shown in Figure 3d where  $1/f$  noise is evident and signal at 50 Hz is observed which might be corresponding to the power supply frequency (50 Hz). The generation of such a speckle free beam profile to avoid beam profile speckle related distortion, along with shaping beam width to increase SNR at various power density ranges were not found in the QY system published in the literature to date [34]. This novel design proposed in this work can achieve high dynamic range, speckle distortion-free QY values have the potential to bring insights to various works explored in literature, in particular, standardization efforts of UCNP emission across the community [39].

### 3.2 Multi-modal measurements and compensation

The accuracy of the estimated QY values of UCNPs depends on the accurate evaluation of various optical properties of UCNPs and optimal compensation for all contributing factors. It is ideal to measure all parameters of UCNPs simultaneously using a well-calibrated system to avoid possible changes in sample properties over time. The developed measurement protocol (section 2.3) allows for the efficient collection of data while minimizing delay, thereby maximizing accuracy when compensating for various contributing factors.

#### Absorption and Scattering Compensation

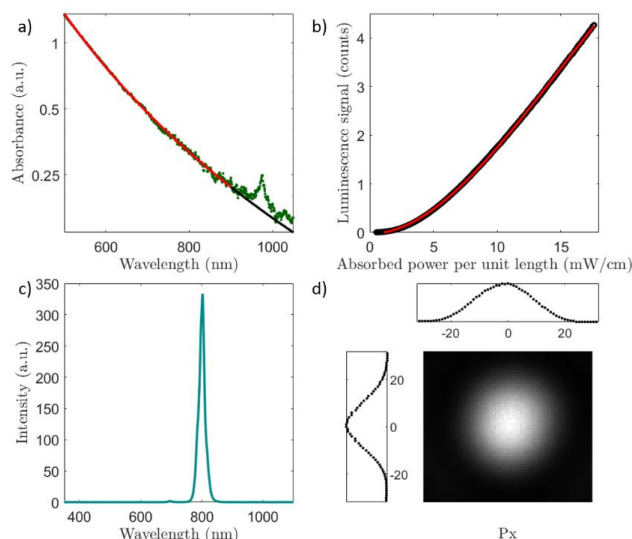


Fig. 4 Multimodal features of QY system a) Absorbance (green dots) and fitted scattering (red line indicating fitting range) spectra b) Raw Luminescence signal (black dots), second-order polynomial fitted curve (red line) of UCNP sample c) Emission spectrum of UCNP d) Beam profile of 976 nm laser.

The UCNP absorbance spectrum measured by arm 5 contains both the absorption and scattering contribution. The measured transmission spectrum was fit to the wavelength dependence of Mie scattering. Figure 4a (red, black line) shows the Mie-scattering fit to the transmitted spectrum. The difference between the fitted scattering and the measured transmission spectra yields the actual absorption of the UCNP sample. To understand the importance of simultaneous measurement of scattering, we have performed extensive measurements on the sample by changing variables like sonication, and intra-day variation. Under various conditions, the absorption of our sample is estimated to be around 10 % percent of the sample's attenuation. In the absence of scattering compensation, the UCNP QY would be underestimated by 90% at low power densities. The uncompensated QY curves were described in the supplementary material (SM-sec.5). The literature work on the QY system has considered to some extent the effect of scattering compensation. However, this compensation was limited to non-simultaneous measurements. In this work, we quantify the error of uncompensated scattering under various experimental conditions (SM-sec.5). The errors for these tests on QY were found to be fluctuating by 100% under certain conditions, these results emphasise the necessity to perform simultaneous scattering measurements using a multimodal system. Figure 4b, shows an example curve of the change in luminescence signal for the absorbed power per unit length by the UCNP for a given spot size  $S_2$ . The UCNP emission line (804 nm) explored

in this paper follows two photon process, the emission is known to be proportional to  $\rho^n$  where  $n$  is the number of photons involved in the upconversion process [34], the red line Figure 4b shows the fitted curve.

#### *Reference dye calibration and emission filter compensation*

A calibration reference dye was used to convert the experimentally measured QY values to corrected relative QY values. For this to be accurate the spatial and spectral distribution of the luminescence emission needs to be the same for both samples. Both samples should emit isotropically, so the spatial assumption is believed to be fulfilled. In addition, the detection filters have to be compensated for, as the emission of the dye, in particular, is broader than the optical detection filter. For both samples, the percentage of the incident light was corrected by calculating the fraction of the emission profile being transmitted through the filters. It is also important to use a dye with a similar emission profile to the UCNPs as possible so that this correction factor can be minimized (yielding as small an error as possible). The emission spectrum of the UCNPs (acquired at  $1.8 \text{ W/cm}^2$ ), shown in Figure 4c is processed with filters transmission spectra to account for errors related to limited spectral bandwidth emission filters. This correction procedure is described in detail in SM-sec.3.

#### *Beam profile compensation*

The luminescence signal (e.g. Figure 2b) at all spot sizes provide raw data for QY values calculations (described in SM-sec.3). The shape of the beam profile and characteristics of the laser affects the estimated QY values. The absence of speckle and a smooth Gaussian beam profile is evident from Figure 4d. Importantly, any presence of speckles results in a random distribution of a light speckle pattern with different power densities across the beam profile. This makes it difficult to accomplish accurate compensation for the beam profile. The system in this work is effectively free of both temporal and spatial speckles. The beam profile compensation algorithm (described in SM-sec.4) can thereby accurately compensate for the different power densities across the beam profile. In the absence of compensation, the beam profile related error can be as much as 50% at low power density values. A similar approach for beam profile compensation can be found in literature and it was limited to single spot size low dynamic range measurements [34]. In this work, we have extended the compensation to multi-spot size which enabled accurate estimation of QY values over a high dynamic range of power densities.

#### *High dynamic range and SNR of QY curves*

Figures 5(a-d) show the relative QY values estimated for different spot sizes and filter combinations. Unlike dyes, the QY of UCNPs is dependent on the excitation power density. In order to determine the QY of UCNPs for a broad range of power densities is of great value. For example, Figure 5 (a-b) have valuable inputs for *in vivo* studies of deep tissue, as it needs QY values for low power densities limited by light attenuation in tissue and safe human exposure levels whereas the microscope studies need to understand QY values at high power density. Depending on the microscope objective and sample, Figure 5(c-d) provides insights into the emitted light from the sample. The system described in this paper has been designed to perform QY measurements over a broad range of power densities ( $1:10^4$ ). This is achieved by using two different spot sizes ( $S_1, S_2$ ) in combination with/without the use of an ND filter. In total 4 measurement series were conducted for each sample to extract QY values of UCNPs at a range of power densities and the results were stitched without any fitting parameter to obtain high dynamic range QY curves. Figure 5e shows the stitched experimental QY curve along with the image beam profile compensated QY curve. The balance point of the image compensated curve is estimated to be  $40 \text{ W cm}^{-2}$  balancing power density ( $\rho_b$ ) and 4% balancing QY ( $\phi_b$ ). The dynamic range can be further extended by adding new beam width to the setup by proper choice of lenses that can cover higher or lower dynamic range.

Examples of high dynamic range QY measurements can be found in the literature [39]. However, all of them suffered from high noise, leading to large error bars in measured data, in particular, at low power density region, which is critical for light-sensitive applications like deep tissue imaging for biomedical applications. The proposed system effectively overcomes this challenge by employing a beam profile of large width (530  $\mu\text{m}$ ) to excite with a large number of photons with low power density. This effectively increases the signal level (25 times in area) of UCNP emitted light as compared to the small beam width (106  $\mu\text{m}$ ). The SNR of the system at the low power density region was found to be SNR ( $>50$ ). To the best of our knowledge, this is the first demonstration of a high dynamic range with superior SNR at low power densities.

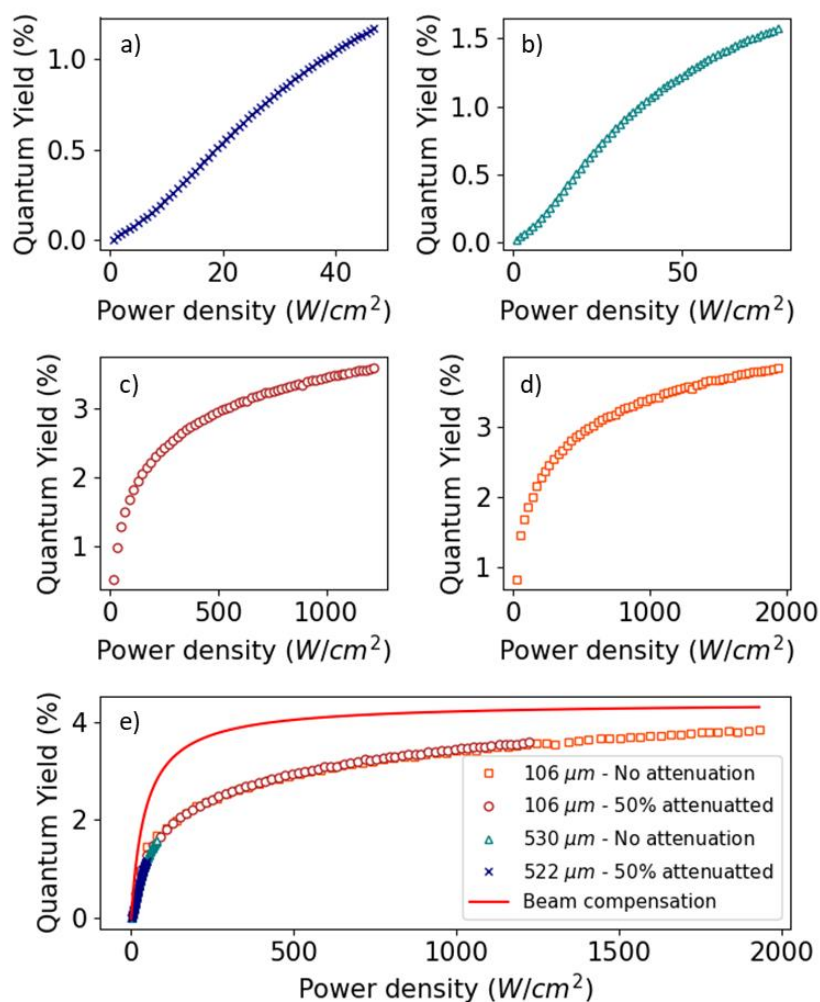


Fig. 5 High dynamic range QY curve of UCNP a) Spot size S2 with filter F1, b) Spot size S2 without filter F1 c) Spot size S1 with filter F1 d) Spot size S1 without filter F1 e) Stitched experimentally (discrete markers), image compensated (red line).

### 3.5 Future outlook

In this work, we consider only the 804 nm emission line of the NaYF<sub>4</sub>:Tm UCNPs. An extension to other emission lines could be achieved easily, by changing emission filters in the system and by selecting a proper dye matching the emission wavelength of UCNPs. The UCNP laser remains the same, while the excitation laser of the reference dye needs to be chosen based on the measurement protocol used for the tabulated QY of the selected dye. Importantly, the rate equations (2 photon transition) developed for the 804 nm emission line may no longer

be valid for other lines, as these lines might involve 3, 4 or 5 photon transitions. Hence, the image-based beam compensation algorithms will no longer be valid for those transitions. Therefore there is an obvious demand for rate equation models that take into account these higher order transitions. In the current configuration of the system, the sample and solvent are measured in sequence. Changes in the intensity of the light source may be present, leading to errors in the assessed optical properties and the obtained QY. This could be avoided by adding an extra arm with a cuvette holder for the blank sample containing solvent only. This would permit the transmittance spectral measurements to be performed simultaneously, thus avoiding possible errors. Also, a careful look into state-of-the-art detection technology might make it possible to further increase the dynamic range of the measured QY curves. To thoroughly validate the system we were using two different arms for UCNP laser 976 nm and dye reference laser 785 nm. However, the purpose of the dye arm is purely related to the calibration of the QY of UCNPs. This calibration factor will remain constant, provided, the system is robustly built and well tested under different experimental conditions. Therefore, the need for a reference arm could be eliminated once the calibration factor at each emission line is robustly estimated. Another possibility is to make transparent long-lasting solid phantoms with UCNP which can be used as a calibration tool [40]. Another important parameter influencing the optical properties of UCNPs and solvents is temperature. The future system could potentially include temperature stabilization to avoid errors when performing measurements in different laboratories under various conditions

#### 4. Conclusions

In this work, we have presented for the first time high resolution and high SNR QY curves of UCNPs by carefully compensating for various distorting effects (scattering, beam profile, inner filter effect, bandwidth of filters) which influence the accuracy of estimated QY values. The study revealed that obtained QYs of UCNPs could vary by 90% in the absence of the multi-modal corrections. A systematic and standardized measurement and analysis protocol is proposed and tested on the commercially available core-shell UCNPs sample. The key results obtained in this work point to the importance of multi-modal measurements and compensation to achieve accurate and consistent QY values for UCNPs. With the increasing innovation rate in the field of UCNPs, we believe our work can act as a precursor for standardizing the measurements of QY values.

#### Funding

Science Foundation Ireland targeted professorship award SFI/15/RP/2828.

#### Disclosures

The authors declare no conflicts of interest.

#### References

1. Zijlmans, H.J.M.A.A., et al., *Detection of Cell and Tissue Surface Antigens Using Up-Converting Phosphors: A New Reporter Technology*. Analytical Biochemistry, 1999. **267**(1): p. 30-36.
2. Chatterjee, D.K., A.J. Rufaihah, and Y. Zhang, *Upconversion fluorescence imaging of cells and small animals using lanthanide doped nanocrystals*. Biomaterials, 2008. **29**(7): p. 937-943.
3. Wang, M., et al., *Immunolabeling and NIR-Excited Fluorescent Imaging of HeLa Cells by Using NaYF<sub>4</sub>:Yb,Er Upconversion Nanoparticles*. ACS Nano, 2009. **3**(6): p. 1580-1586.
4. Kobayashi, H., et al., *In vivo multiple color lymphatic imaging using upconverting nanocrystals*. Journal of Materials Chemistry, 2009. **19**(36): p. 6481-6484.

5. Liu, K., et al., *Covalently Assembled NIR Nanoplatform for Simultaneous Fluorescence Imaging and Photodynamic Therapy of Cancer Cells*. ACS Nano, 2012. **6**(5): p. 4054-4062.
6. Zhang, P., et al., *Versatile Photosensitizers for Photodynamic Therapy at Infrared Excitation*. Journal of the American Chemical Society, 2007. **129**(15): p. 4526-4527.
7. Wang, C., et al., *Near-infrared light induced in vivo photodynamic therapy of cancer based on upconversion nanoparticles*. Biomaterials, 2011. **32**(26): p. 6145-6154.
8. Qiu, H., et al., *Recent Progress in Upconversion Photodynamic Therapy*. Nanomaterials (Basel, Switzerland), 2018. **8**(5): p. 344.
9. Wang, D., et al., *808 nm driven Nd<sup>3+</sup>-sensitized upconversion nanostructures for photodynamic therapy and simultaneous fluorescence imaging*. Nanoscale, 2015. **7**(1): p. 190-197.
10. Liu, Q., et al., *Sub-10 nm Hexagonal Lanthanide-Doped NaLuF<sub>4</sub> Upconversion Nanocrystals for Sensitive Bioimaging in Vivo*. Journal of the American Chemical Society, 2011. **133**(43): p. 17122-17125.
11. Bloembergen, N., *Solid State Infrared Quantum Counters*. Physical Review Letters, 1959. **2**(3): p. 84-85.
12. Auzel, F., *Upconversion and Anti-Stokes Processes with f and d Ions in Solids*. Chemical Reviews, 2004. **104**(1): p. 139-174.
13. Auzel, F., *Multiphonon-assisted anti-Stokes and Stokes fluorescence of triply ionized rare-earth ions*. Physical Review B, 1976. **13**(7): p. 2809-2817.
14. Auzel, F.E., *Materials and devices using double-pumped-phosphors with energy transfer*. Proceedings of the IEEE, 1973. **61**(6): p. 758-786.
15. Haase, M. and H. Schäfer, *Upconverting Nanoparticles*. Angewandte Chemie International Edition, 2011. **50**(26): p. 5808-5829.
16. Wang, F., et al., *Upconversion nanoparticles in biological labeling, imaging, and therapy*. Analyst, 2010. **135**(8): p. 1839-1854.
17. Liu, T.-M., et al., *Smart NIR linear and nonlinear optical nanomaterials for cancer theranostics: Prospects in photomedicine*. Progress in Materials Science, 2017. **88**: p. 89-135.
18. Dong, H., L.-D. Sun, and C.-H. Yan, *Energy transfer in lanthanide upconversion studies for extended optical applications*. Chemical Society Reviews, 2015. **44**(6): p. 1608-1634.
19. Gnach, A. and A. Bednarkiewicz, *Lanthanide-doped up-converting nanoparticles: Merits and challenges*. Nano Today, 2012. **7**(6): p. 532-563.
20. Sedlmeier, A. and H.H. Gorriss, *Surface modification and characterization of photon-upconverting nanoparticles for bioanalytical applications*. Chemical Society Reviews, 2015. **44**(6): p. 1526-1560.
21. Pollnau, M., et al., *Power dependence of upconversion luminescence in lanthanide and transition-metal-ion systems*. Physical Review B, 2000. **61**(5): p. 3337-3346.
22. Soukka, T., et al., *Photochemical Characterization of Up-Converting Inorganic Lanthanide Phosphors as Potential Labels*. Journal of Fluorescence, 2005. **15**(4): p. 513-528.
23. Krämer, K.W., et al., *Hexagonal Sodium Yttrium Fluoride Based Green and Blue Emitting Upconversion Phosphors*. Chemistry of Materials, 2004. **16**(7): p. 1244-1251.
24. Wang, F., J. Wang, and X. Liu, *Direct Evidence of a Surface Quenching Effect on Size-Dependent Luminescence of Upconversion Nanoparticles*. Angewandte Chemie International Edition, 2010. **49**(41): p. 7456-7460.
25. Zhao, J., et al., *Upconversion luminescence with tunable lifetime in NaYF<sub>4</sub>:Yb,Er nanocrystals: role of nanocrystal size*. Nanoscale, 2013. **5**(3): p. 944-952.
26. Niu, W., S. Wu, and S. Zhang, *A facile and general approach for the multicolor tuning of lanthanide-ion doped NaYF<sub>4</sub> upconversion nanoparticles within a fixed composition*. Journal of Materials Chemistry, 2010. **20**(41): p. 9113-9117.
27. Bogdan, N., et al., *Synthesis of Ligand-Free Colloidally Stable Water Dispersible Brightly Luminescent Lanthanide-Doped Upconverting Nanoparticles*. Nano Letters, 2011. **11**(2): p. 835-840.
28. Wang, F., et al., *Simultaneous phase and size control of upconversion nanocrystals through lanthanide doping*. Nature, 2010. **463**: p. 1061.
29. Liu, H., et al., *Deep tissue optical imaging of upconverting nanoparticles enabled by exploiting higher intrinsic QY through use of millisecond single pulse excitation with high peak power*. Nanoscale, 2013. **5**(20): p. 10034-10040.
30. Zhan, Q., et al., *Using 915 nm Laser Excited Tm<sup>3+</sup>/Er<sup>3+</sup>/Ho<sup>3+</sup>-Doped NaYbF<sub>4</sub> Upconversion Nanoparticles for in Vitro and Deeper in Vivo Bioimaging without Overheating Irradiation*. ACS Nano, 2011. **5**(5): p. 3744-3757.
31. Yi, G.-S. and G.-M. Chow, *Water-Soluble NaYF<sub>4</sub>:Yb,Er(Tm)/NaYF<sub>4</sub>/Polymer Core/Shell/Shell Nanoparticles with Significant Enhancement of Upconversion Fluorescence*. Chemistry of Materials, 2007. **19**(3): p. 341-343.
32. Qian, H.-S. and Y. Zhang, *Synthesis of Hexagonal-Phase Core-Shell NaYF<sub>4</sub> Nanocrystals with Tunable Upconversion Fluorescence*. Langmuir, 2008. **24**(21): p. 12123-12125.
33. Boyer, J.-C. and F.C.J.M. van Veggel, *Absolute QY measurements of colloidal NaYF<sub>4</sub>: Er<sup>3+</sup>, Yb<sup>3+</sup> upconverting nanoparticles*. Nanoscale, 2010. **2**(8): p. 1417-1419.
34. Mousavi, M., et al., *Beam-profile-compensated QY measurements of upconverting nanoparticles*. Physical Chemistry Chemical Physics, 2017. **19**(33): p. 22016-22022.

35. Würth, C., et al., *Relative and absolute determination of fluorescence QYs of transparent samples*. Nature Protocols, 2013. **8**: p. 1535.
36. Würth, C., et al., *Integrating Sphere Setup for the Traceable Measurement of Absolute Photoluminescence QYs in the Near Infrared*. Analytical Chemistry, 2012. **84**(3): p. 1345-1352.
37. Thomasson, B., *High Accuracy Relative Luminescence QY Measurements of Upconverting Nanoparticles*. 2016, Lund University.
38. Dyomics, "QY of DY-781", <https://dyomics.com/en/products/nir-excitation/dy-781.html>.
39. Meijer, M. S., Rojas-Gutierrez, P. A., Busko, D., Howard, I. A., Frenzel, F., Würth, C., ... Bonnet, S. (2018). Absolute upconversion quantum yields of blue-emitting LiYF<sub>4</sub>:Yb<sup>3+</sup>, Tm<sup>3+</sup> upconverting nanoparticles. *Physical Chemistry Chemical Physics*, 20(35), 22556–22562. <https://doi.org/10.1039/c8cp03935f>
40. Sanathana Konugolu Venkata Sekar, Andrea Pacheco, Pierluigi Martella, Haiyang Li, Pranav Lanka, Antonio Pifferi, and Stefan Andersson-Engels, "Solid phantom recipe for diffuse optics in biophotonics applications: a step towards anatomically correct 3D tissue phantoms," *Biomed. Opt. Express* 10, 2090-2100 (2019)

## PAPER III

### **Generalised analytical model of the transition power densities of the upconversion luminescence and quantum yield**

J. S. Matias, K. Komolibus, S. Konugolu, W. Kho-Kiang and S. Andersson-Engels.

*Nanoscale Advances* **5**, 3279 - 3286 (2022).





Cite this: DOI: 10.1039/d2na00850e

## Generalised analytical model of the transition power densities of the upconversion luminescence and quantum yield

 J. S. Matias,<sup>1</sup> <sup>\*ab</sup> K. Komolibus,<sup>a</sup> K. W. Kho,<sup>a</sup> S. Konugolu-Venkata-Sekar<sup>a</sup> and S. Andersson-Engels <sup>ab</sup>

The quantum yield (QY) evaluation of upconverting nanoparticles (UCNPs) is an essential step in the characterisation of such materials. The QY of UCNPs is governed by competing mechanisms of populating and depopulating the electronic energy levels involved in the upconversion (UC), namely linear decay rates and energy transfer rates. As a consequence, at low excitation, the QY excitation power density ( $\rho$ ) dependence obeys the power law  $\rho^{n-1}$ , where  $n$  represents the number of absorbed photons required for the emission of a single upconverted photon and determines the order of the energy transfer upconversion (ETU) process. At high power densities, the QY transits to a saturation level independent of the ETU process and the number of excitation photons, as a result of an anomalous power density dependence present in UCNPs. Despite the importance of this non-linear process for several applications (e.g., living tissue imaging and super-resolution-microscopy), little has been reported in the literature regarding theoretical studies to describe the UC QY, especially for ETUs with order higher than two. Therefore, this work presents a simple general analytical model, which introduces the concept of the transition power density points and QY saturation to characterise the QY of an arbitrary ETU process. The transition power density points determine where the power density dependence of the QY and the UC luminescence changes. The results provided in this paper from fitting the model to experimental QY data of a Yb–Tm codoped  $\beta$ -UCNP for 804 nm and 474 nm emissions (ETU2 and ETU3 processes, respectively) exemplify the application of the model. The common transition points found for both processes were compared to each other showing strong agreement with theory, as well as, compared to previous reports when possible.

Received 25th November 2022  
Accepted 4th April 2023

DOI: 10.1039/d2na00850e

rsc.li/nanoscale-advances

This article is licensed under a Creative Commons Attribution-NonCommercial 3.0 Unported Licence.



## 1 Introduction

In the last few decades, upconverting nanoparticles (UCNPs) have been extensively studied due to their unique ability to convert low-energy photons to high-energy photons, an anti-Stokes non-linear process involving multi-photon absorption followed by the emission of a single photon with the total absorbed energy.<sup>1–3</sup> The upconversion luminescence (UCL) non-linearity is a unique property responsible for a breakthrough in super-resolution microscopy, where researchers achieved sub 70 nm imaging resolution utilising the giant non-linear response found in some UCNPs.<sup>4–7</sup> From clean energy to biophotonics, UCNPs have also been successfully applied to light harvesting,<sup>8,9</sup> photodynamic therapy (PDT),<sup>10</sup> diffuse optical imaging,<sup>11</sup> optogenetics,<sup>12,13</sup> biosensors,<sup>14</sup> and temperature sensing.<sup>15,16</sup> Despite their potential, the quantum yield (QY) of UCNPs remains low, especially at low excitation power densities

required for biological applications.<sup>17</sup> The internal quantum yield (iQY) is often used as a figure of merit to characterise UCNPs, and is defined as the ratio of the number of emitted photons to the number of absorbed ones.<sup>18–20</sup> At low excitation power densities the non-linear behaviour of UCL is more pronounced and, as a consequence, the iQY is power density dependent,<sup>20–23</sup> which adds further complexities to the evaluation of their efficiency. An accurate iQY evaluation is crucial for the development of optimal UCNPs, although, analytical and modelling studies on the excitation power density dependence of iQY are astonishingly scarce.<sup>22</sup>

The most efficient UCNPs have a sensitizer ion that strongly absorbs near-infrared (NIR) photons and transfers its energy to an activator ion *via* a phonon through the lattice of a host matrix.<sup>3</sup> This energy transfer upconversion (ETU) process excites the electrons from the ground state to an  $n^{\text{th}}$  excited state of the activators in a sequence of steps involving long-living intermediate states.<sup>24</sup> When the electrons relax radiatively from the excited state  $|n\rangle$  to lower states, an ETU process of order  $n$  (ETU $n$ ) is completed and a single photon is emitted with higher energy.<sup>1–3,25</sup> At low power densities the non-linear UCL is

<sup>a</sup>Biophotonics@Tyndall, IPIC, Tyndall National Institute, Cork, Ireland. E-mail: jean.matias@tyndall.ie

<sup>b</sup>Department of Physics, University College Cork, Cork, Ireland

proportional to  $\rho^n$ , where  $n$  represents the number of absorbed photons involved in the process and  $\rho$  is the uniform excitation power density of irradiated UCNPs. As the excitation power density is increased, the UCL transits to regimes of power density dependence with an exponent lower than  $n$ , and eventually reaches linearity, *i.e.*  $\rho^1$ . The UCL of upconverting micro-particles tends to saturate after reaching linearity as the power density is further increased.<sup>26,27</sup> Unlikely, the UCL of UCNPs typically does not show saturation, regardless of the number of excitation photons and number of energy transfers involved.<sup>21,28</sup> This behaviour seen in UCNPs, named as anomalous power (density) dependence for the first time by Suyver *et al.*, has been extensively observed experimentally as shown in the literature.<sup>20–22,27–33</sup> Yet, analytical studies exploring the phenomenon are nonexistent, especially with regard to the different power density regimes and the thresholds between them. The delimitation of the regimes has never been formally defined before, and thus far is based on subjective assessment in the literature; the authors refer to the ranges of non-linearity and linearity as being at the “low” and “high power densities”, respectively.<sup>18,21,22,27,28,34,35</sup> These subjective terms can well describe the UCL behaviour qualitatively, although a quantitative method is necessary for accurate characterisation, especially in applications where precise tuning of the UCL dynamics is crucial.<sup>36</sup> Recently, Liu *et al.*, while studying the ETU2 of a NIR UCL, have introduced the concept of the “balancing power density” as the transition point where the iQY is exactly half of its maximum QY value (the “QY saturation” level), which is reached at the linear regime of the UCL.<sup>22</sup> The balancing power density was the first concept of a quantitative parameter to define the threshold between the non-linear and linear regimes of ETU2 processes, highlighting its importance. In addition, their model reduced a complex power density dependent system, with numerous energy transfer and linear decay rates, to a simple equation with two variables: the balancing power density point and the QY saturation. The model proposed by the authors was based on two key studies<sup>21,28</sup> using an elegant but simple rate equation model to describe the population densities of the energy states involved in the UC. Later on, their model was utilised in the implementation of a beam-profile compensation on experimental QY and to demonstrate the need of the compensation for an accurate evaluation of the iQY.<sup>20,23</sup> Apart from Liu *et al.*'s study on ETU2, no study has been conducted on higher ETU processes. A precise modelling of the UCL and iQY is of particular importance to the optimisation of application-specific UCNPs. Therefore, this work presents a general analytical model for an ETU process of arbitrary order, and includes a detailed analysis of the how a transition power density point, such as the balancing power density, affects ETU processes of higher order. Applying the model to an ETU2 process, the found transition power density points were compared to the balancing point proposed by Liu *et al.* In addition, the distinct power density behaviour of UCNPs and that of their bulk counterparts are discussed in terms of their iQY saturation and transition power density points. Experimental results, supporting the findings, and exemplifying the application of the model to the characterisation of UCNPs, are

presented for the 804 nm and 474 nm emissions (ETU2 and ETU3 processes, respectively) of a Yb-Tm codoped  $\beta$ -UCNP.

## 2 Materials and methods

### 2.1 Sample characterisation

$\beta$ -NaYF<sub>4</sub>:YbTm core-shell UCNPs with multiple emission wavelengths dispersed in toluene, purchased from Creative Diagnostics, were chosen for the experiments. Morphology, dispersion and size were characterised with a scanning transmission electron microscope (STEM). The sample was drop-cast over 5 mm silicon and images were acquired in the transmission mode. For the emission spectra and QY measurements a 500 mW CW 976 nm excitation laser diode (Thorlabs – BL976-PAG500), controlled by a digital driver (Thorlabs – CLD1015) was utilised to irradiate the sample. The excitation beam was shaped to a Gaussian profile with 302  $\mu$ m diameter taken as full-width-at-half-maximum. The power densities of the excitation were calculated by the ratio of power to the area of the cross-section of the beam. The emission spectra of the sample were acquired for a few power densities ranging from 20 W cm<sup>-2</sup> to 100 W cm<sup>-2</sup> with a commercial spectrometer (Ocean Optics – QEPRO-FL) attached to the emission arm at 90° to the excitation path of a QY system built in the lab, which is reported elsewhere.<sup>35</sup> The QY system was calibrated with two commercial organic dyes: a NIR dye diluted in ethanol (Dyomics – DY-781-01) with an emission peak at 800 nm and known QY of 12.4%, obtained according to a standard protocol;<sup>20,23,31</sup> and a blue dye diluted in ethanol (Dyomics – DY-415-01) with an emission peak at 467 nm and QY of 20.2% characterised by the manufacturer. The calibration at these specific wavelengths accounts for the wavelength dependence of the APD sensitivities, and these dyes were chosen to match their emission wavelength with the UCNP emission wavelengths that were characterised with the QY system. The sample of UCNPs was prepared and characterised according to the process recently reported in the literature.<sup>20</sup> Experimentally, the iQYs were obtained according to the definition, which written in terms of wavelengths and power is given by eqn (1),

$$\eta_{\lambda_{em}} = \frac{L_{\lambda_{em}} \lambda_{em}}{P_a \lambda_{ex}}, \quad (1)$$

where  $L_{\lambda_{em}}$  [W] is the UCL for the wavelength of emission  $\lambda_{em}$  [nm],  $P_a$  [W] is the total absorbed power, and  $\lambda_{ex}$  [nm] is the excitation wavelength, 976 nm.

The iQY evaluation was conducted for the 804 nm and the 474 nm UCL peaks, which were measured simultaneously at two avalanche photodiodes (APDs) (Thorlabs – APD410A and APD440A2, respectively) attached to the QY system. The emission wavelengths, selected for the characterisation, were chosen accordingly as they were the most intense emission peaks for these UCNPs, and because, they arise from two distinct ETU processes (ETU2 and ETU3 processes). In addition, the NIR emission is widely used in most of the applications in the biophotonic field because of its high penetration depth in living tissues,<sup>17,37,38</sup> while the blue UC emission of UCNPs has shown promising utilisation to trigger neurons for less invasive



techniques in optogenetics.<sup>13,39,40</sup> Despite the beam-profile-compensation to be essential for the iQY characterisation, its mathematical derivation would deviate the focus of this work. Therefore, for the purpose of exemplifying the theoretical findings and keeping the message clear in this paper, the beam-profile-compensation was not accounted for in the experimental results.

### 3 Results and discussion

#### 3.1 A general theoretical model

The general model proposed here in its simplest form comprises a two-level sensitizer (S) and an activator (A) with an arbitrary number of energy levels  $m$  larger than two, as shown in Fig. 1. The electrons from the sensitizer's ground state  $|a\rangle$  are pumped to the excited energy level  $|b\rangle$  using an excitation source with power density  $\rho$  [ $\text{W cm}^{-2}$ ] and natural frequency  $\nu_{\text{ex}}$  [Hz]. The probability of a photon to be absorbed is given by the sensitizer's cross-section area  $\sigma_{\text{S}}$  [ $\text{cm}^2$ ]. As the sensitizer relaxes to the ground state  $|a\rangle$  with a constant rate  $R_{\text{b}}$  [ $\text{s}^{-1}$ ], phonons propagate through the lattice carrying energy until it encounters an activator and transfers the energy to the ions, exciting them from their current state  $|j-1\rangle$  to the next higher state  $|j\rangle$ . The energy transfer (ET) is the key process that determines the dynamics of the populating and depopulating mechanisms of the UC energy states.<sup>24</sup> Thus, the model considers that any energy state  $|j\rangle$  is populated only by ET with a constant rate  $W_{j-1}$  [ $\text{s}^{-1}$ ], and cross-relaxation is neglected. The depopulation of a  $|j\rangle$  state occurs *via* two

mechanisms, as such, a linear decay to the activator's ground state  $|0\rangle$  with a decay constant rate  $R_j$  [ $\text{s}^{-1}$ ], and an excitation to the next higher energy state  $|j+1\rangle$  by ET. The set of population density equations and their rate equations that encapsulates the concept of the proposed model is given by eqn (2),

$$\begin{aligned} N_{\text{S}} &= N_{\text{a}} + N_{\text{b}}, \\ \frac{dN_{\text{b}}}{dt} &= \alpha\rho N_{\text{a}} - N_{\text{b}}R_{\text{b}}, \\ N_{\text{A}} &= \sum_{i=0}^m N_i, \\ &\vdots \\ \frac{dN_j}{dt} &= W_{j-1}N_{j-1}N_{\text{b}} - W_jN_jN_{\text{b}} - N_jR_j, \\ &\vdots \end{aligned} \quad (2)$$

where  $N_j$  [ $\text{cm}^{-3}$ ] is the population density of an arbitrary  $|j\rangle$  state, for  $j \in \{1, 2, 3, \dots, m\}$ ;  $N_{\text{a}}$  [ $\text{cm}^{-3}$ ], and  $N_{\text{b}}$  [ $\text{cm}^{-3}$ ] are the population densities of the energy states  $|a\rangle$  and  $|b\rangle$ , respectively;  $N_{\text{S}}$  [ $\text{cm}^{-3}$ ], and  $N_{\text{A}}$  [ $\text{cm}^{-3}$ ] represent the total electronic density of the sensitizers and activators, respectively; and  $\alpha$  [ $\text{cm}^2 \text{J}^{-1}$ ] is the sensitizer's cross-section  $\sigma_{\text{S}}$  divided by Planck's constant  $\hbar$  [J s] times the natural frequency of the excitation photons  $\nu_{\text{ex}}$ , eqn (3).

$$\alpha = \frac{\sigma_{\text{S}}}{\hbar\nu_{\text{ex}}} \quad (3)$$

Solving the equations for the steady states, the population densities for the energy states  $|b\rangle$  and the  $|j\rangle$ 's are given by eqn (4) and (5), respectively.

$$N_{\text{b}} = \frac{\alpha\rho N_{\text{S}}}{R_{\text{b}} + \alpha\rho}, \quad (4)$$

$$N_j = \frac{W_{j-1}N_{j-1}N_{\text{b}}}{W_jN_{\text{b}} + R_j} \quad (5)$$

Being  $|j\rangle$  an arbitrary state, one can prove that eqn (5) is also a solution for the state  $|j-1\rangle$  by the principle of finite induction. Therefore, the population density for a  $|j\rangle$  state can be represented in terms of the population density of the ground state of the activators  $N_0$  [ $\text{cm}^{-3}$ ] by replacing recursively the solutions of all the energy states lower than  $|j\rangle$ , *i.e.*  $N_{j-1}, N_{j-2}, \dots, N_0$ , in eqn (5). The population density of the ground state barely changes during UC processes within the ranges of power densities utilised in most applications, and thus,  $N_0$  can be considered a constant of the order of magnitude of  $N_{\text{A}}$ . Furthermore, the power density dependent solution is obtained by replacing  $N_{\text{b}}$  in eqn (5) by eqn (4). This solution is valid for the limit where  $\rho \ll R_{\text{b}}/\alpha$  (typically  $R_{\text{b}}/\alpha > 5000 \text{ W cm}^{-2}$  for a range of values of  $\sigma_{\text{S}}$  and  $R_{\text{b}}$  found in the literature<sup>44,42</sup>). Within this limit, the population density of the sensitizer's ground state  $N_{\text{a}}$  is much larger than the population density of the excited state  $|b\rangle$ ,  $N_{\text{a}} \gg N_{\text{b}}$ , and thus,  $N_{\text{a}}$  can be considered a constant with the same order of magnitude of  $N_{\text{S}}$ . Therefore, the simplified solution is given by eqn (6),

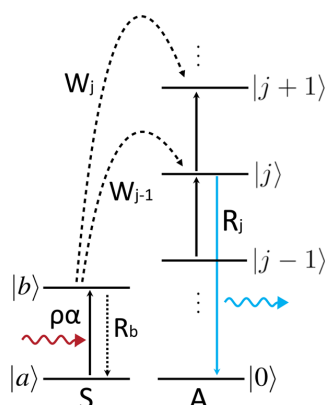


Fig. 1 Simplified energy levels scheme representing a two-level sensitizer (S) and an activator (A) with an arbitrary number of energy levels. The diagram represents the sensitizer's electrons being excited by ground state absorption and subsequent multiple energy transfers to equally spaced energy levels present in the activator (A) ion. Any  $|j\rangle$  excited state (*i.e.*  $j > 0$ ) is populated and depopulated by mechanisms of the same nature, and if  $j$  is equal to 1, the state  $|j-1\rangle$  coincides with the ground state  $|0\rangle$ . The curly arrows represent the excitation photon on the left, and the emitted photon on the right, whereas the arrows pointing up (down) represent the electronic transitions to a higher (lower) energy state. The dashed lines correspond to the energy transfers between the ions.



$$N_j = N_{js} \prod_{i=1}^j \frac{\rho}{\rho + \rho_i}, \quad (6)$$

where  $N_{js}$  [ $\text{cm}^{-3}$ ] is the saturated population density for the energy state  $|j\rangle$ , given by eqn (7), and  $\rho_i$  [ $\text{W cm}^{-2}$ ] defines the power density transition point corresponding to a state  $|i\rangle$  for  $i \in \{1, 2, \dots, j\}$ , given by eqn (8),

$$N_{js} = \frac{W_0 N_0}{W_j}, \quad (7)$$

$$\rho_i = \frac{R_i R_b}{W_i \alpha N_a}, \quad (8)$$

where  $W_0$  [ $\text{s}^{-1}$ ] is the energy transfer rate responsible for the electronic excitation from the energy state  $|0\rangle$  to the first excited state  $|1\rangle$ .

The population density saturation is reached at excitation power densities much higher than the constants  $\rho_i$ , where these transition constants can be neglected. A  $\rho_i$  constant determines the threshold where the slope of the population density versus the excitation power density in a double logarithmic scale for a particular  $|i\rangle$  state transits from  $i$  to  $i - 1$ , as the excitation power density is increased. Notice that a particular transition point  $\rho_i$  influences the population density of its correspondent energy state  $|i\rangle$  and the population densities of all the energy states above. However, it does not affect any energy state below it. For example, taking  $j$  equal to 1, the product in the solution of eqn (6) is reduced to a single element with the transition point  $\rho_1$ . Now, taking  $j$  equal to 2, one can notice that the population density solution is dependent on the transition points  $\rho_1$  and  $\rho_2$ . Thus, the constant  $\rho_2$  does not influence the state  $|1\rangle$ , although it influences the energy state  $|2\rangle$ . Considering the solutions for the energy states above  $|2\rangle$ , one can verify that  $\rho_2$  also affects all the higher energy states.

The iQY for the emitted photons originated from an energy state  $|j\rangle$ ,  $\eta_j$  [-], is, by definition, the ratio of the number of emitted photons to the number of absorbed photons. The emitted photon density per second is proportional to the population density of this state multiplied by a constant factor  $R_j^{\text{rad}}$  [ $\text{s}^{-1}$ ] (which is the radiative decay rate from the energy state  $|j\rangle$ ), and the density of absorbed photons per second is given by the product  $\alpha N_a \rho$ . Thereby, the power density dependent iQY for each of these energy states is easily obtained as represented by eqn (9).

$$\eta_j = \frac{N_{js} R_j^{\text{rad}}}{\alpha N_a \rho} \rho^{j-1} \prod_{i=1}^j \frac{1}{\rho + \rho_i} \quad (9)$$

### 3.2 The power density limits and the anomalous power density dependence of UCNPs

At the limit where  $\rho \ll \rho_i$ ,  $\forall i \in \{1, \dots, j\}$ , the population density becomes proportional to  $\rho^j$ , and the iQY becomes proportional to  $\rho^{j-1}$ , obeying the power law observed experimentally.<sup>21,22,34</sup> At the other extreme, where the limit  $\rho \gg \rho_i$ ,  $\forall i \in \{1, \dots, j\}$  applies, the model indicates that the population density of the states  $|j\rangle$  reaches a saturation level, given by the constant  $N_{js}$ , and

therefore the iQY is quenched. This effect has been observed for upconverting microparticles,<sup>26,27</sup> although the typical behaviour of UCNPs indicates no saturation of the population densities at high power densities. Instead, the UCL of UCNPs exhibits linear power density dependence within this regime, *i.e.*  $\rho^1$ , independent of the energy state or the order of the ETU process,<sup>20-22,27-33</sup> as previously mentioned. Named as anomalous power dependence by Suyver *et al.*,<sup>21</sup> this phenomenon is explained if one of the transition power density points is significantly large and had never been reached experimentally in UCNPs. Suyver *et al.* showed a few experimental examples of UCNPs with different sensitizers and activators for which the anomalous behaviour occurs for all the upconverting states including the energy state  $|1\rangle$ , *i.e.* the states related to the down conversion. This suggests that the  $\rho_1$  was never reached during their experiments, and therefore one can conclude that the highest transition point is in fact  $\rho_1$ . Fig. 2 shows a schematic representation of the population densities, eqn (6), and iQY, eqn (9), for the UC of a four-level system in a double-logarithmic representation. The power density dependence of the regimes of each energy state is indicated in the plots. In this example,  $\rho_1$  is much larger than the other transition points. As a consequence, the population densities of all the energy states present linear power density dependence at power densities much higher than  $\rho_2$  and  $\rho_3$ , yet much lower than  $\rho_1$ . Having  $\rho_1$  much larger than the other transition points allows the linearity of all the energy states to be observed over a wide range of excitation power densities without any significant change in the slope of the experimental UCL curves, which represent the anomalous power density dependence observed in UCNPs.

Comparing the behaviours of UCNPs and upconverting microparticles, the results suggest that  $\rho_1$  is strongly increased as the size of the particles is reduced. For example, Kaiser *et al.* compared experimental iQY results of  $\beta\text{-NaYF}_4$ : 17%  $\text{Yb}^{3+}$ , 3%  $\text{Er}^{3+}$  upconverting microparticles and UCNPs. The iQY of the microparticles shows a saturation point at around  $30 \text{ W cm}^{-2}$ , and quenching at power densities above it. However, the iQY of UCNPs tends to saturation at the maximum power densities measured, around  $4000 \text{ W cm}^{-2}$ , which is far above the saturation power density range shown by the microparticles.<sup>27</sup> In addition, upconverting microparticles exhibit higher iQYs than those of UCNPs excited at the same power densities,<sup>33</sup> and the iQY saturation levels are also higher for microparticles.<sup>27</sup> These observations are also supported by numerical simulations, including experimental data, presented by Hossain *et al.*, where the authors compare luminescence and iQY of upconverting microparticles and UCNPs (core and core-shell).<sup>44</sup> This occurs because of the relation between the iQY saturation to the largest transition power density point, *i.e.*  $\rho_1$  for the anomalous power density dependence. Within the linear regime and below it, the iQY equation, eqn (9), can be further simplified. Applying the limit  $\rho_1 \gg \rho$ , the power density in the denominator that has  $\rho_1$  is reduced to  $\rho_1$ ,  $\rho + \rho_1 \rightarrow \rho_1$ , and eqn (10) is obtained,

$$\eta_j = \eta_{js} \rho^{j-1} \prod_{i=2}^j \frac{1}{\rho + \rho_i} \quad (10)$$



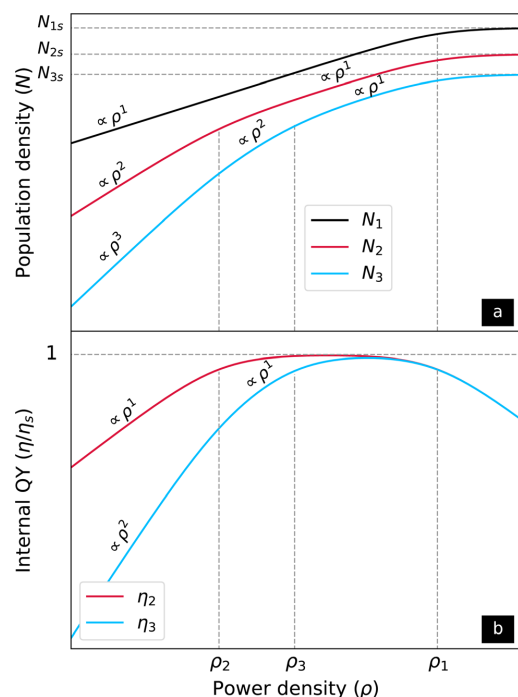


Fig. 2 Schematic representation of the (a) population densities, and (b) the iQYs versus the excitation power density in a double logarithmic scale for a four-level upconverting system. The horizontal dashed lines represent the saturation levels of the population densities and of the iQYs. The vertical dashed lines indicate the transition power density points. With  $\rho_1$  being higher than the other transition points, the population densities of all the energy states have linear behaviour at power densities much higher than  $\rho_2$  and  $\rho_3$ , yet much lower than  $\rho_1$ . A web application with free access was developed for simulating population densities, UCL, and iQY for a four-level up-converting system. It allows users to change the fundamental variables in eqn (2) and view the simulated data plotted in the interface. The programming code that powers the application is available on a GitHub repository accessible from the upper right corner of the web page.<sup>43</sup>

where  $\eta'_j$  [–] is the simplified iQY,  $\eta_{js}$  [–] is the iQY saturation, given by eqn (11) and obtained from the ratio of the constants outside the product in eqn (9) to the transition point  $\rho_1$ .

$$\eta_{js} = \frac{N_{js} R_j^{\text{rad}} W_1}{R_1 R_b} \quad (11)$$

Because the iQY saturation is inversely proportional to  $\rho_1$ , an upconverting material that has lower  $\rho_1$  is expected to have higher iQY saturation, which is exactly what is seen in UC microparticles compared to UCNPs.<sup>26,27</sup>

### 3.3 The ETU2 case for UCNPs

Liu *et al.*'s model for the ETU2 process<sup>22</sup> is a special case of the present general model with  $W_2 = 0$ , which neglects ETU3 and

higher processes. Placing this constant in eqn (8),  $\rho_2$  tends to infinity, however, expanding eqn (9) before considering  $W_2 = 0$ , this constant is cancelled out with the same constant in the denominator of the population density saturation constant  $N_{2s}$ . Thereby, the Liu *et al.*'s solution for the ETU2 process is obtained, eqn (12),

$$\eta_2 = \eta_s \frac{\rho}{\rho + \rho_b} \quad (12)$$

where  $\eta_s$  [–] gives the iQY saturation, eqn (13), and  $\rho_b$  [ $\text{W cm}^{-2}$ ] is the balancing power density point, named by Liu *et al.*, eqn (14).

$$\eta_s = \frac{W_0 N_0 R_2^{\text{rad}}}{R_2 R_b}, \quad (13)$$

$$\rho_b = \frac{R_1 R_b}{W_1 \alpha N_a} \quad (14)$$

From the practical perspective of fitting a QY data curve, eqn (10) for  $j = 2$  and eqn (12) result in the same numerical values for the QY saturation and the transition/balancing power density point. However, the physical nature of the constants can be misleading for the purpose of understanding and engineering optimal UCNPs. The assumption that  $W_2$  is null requires  $\rho_1$  to be measurable instead of  $\rho_2$ , in contrast to what is expected for UCNPs, which have an anomalous power density dependence. In any case, the determination of which constant is the highest one is only obtained by measuring the power density dependence of the down converted luminescence to evaluate the population density of the first excited state |1>. Moreover, several UCNPs have multiple wavelength UC emissions involving ETU2 and higher. For these materials, the ET constants responsible for the population of such higher energy states are required to be larger than zero, and therefore, the general solution is necessary.

### 3.4 An experimental example

The sample utilised in the experiments presented a hexagonal morphology and  $16 \pm 2$  nm of average size, as shown by the STEM image in Fig. 3. The histogram of size distribution shown in the inset of Fig. 3 was obtained from 100 nanoparticles measured by post analysis of the acquired image. The particles were well dispersed and only insignificant aggregation was observed. The emission spectra of the UCNPs, Fig. 4, show main emission peaks at 474, 650, and 804 nm (ETU3, ETU3 and ETU2 processes, respectively) for the power density range below  $100 \text{ W cm}^{-2}$ . An ETU4 process (450 nm emission peak) is also present in these UCNPs, although it was only seen for power densities above  $1000 \text{ W cm}^{-2}$  (data not shown). The inset of the figure shows the energy level diagram highlighting the electronic transitions of each emission peak.

The iQY curves for the 804 nm and 474 nm emission versus the excitation power density are shown in Fig. 5. The discrete markers correspond to the experimental data and the continuous curves represent the fitted model, eqn (10). The experimental data and the fitted results displayed in the figure were



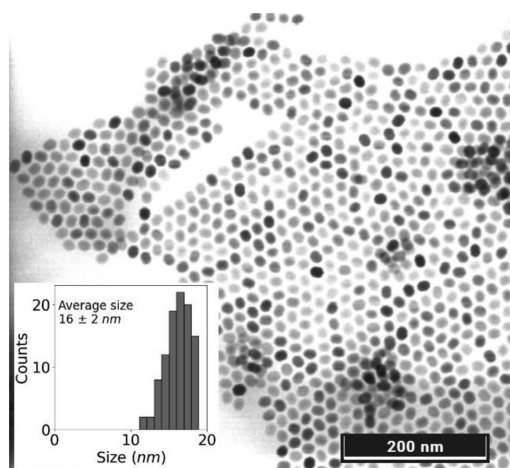


Fig. 3 The STEM image acquired in the transmission mode shows the UCNPs with an average size of  $16 \pm 2$  nm and hexagonal morphology. The inset displays their size distribution histogram taken from 100 nanoparticles.

normalised by their respective iQY saturation values, eqn (11), for a better comparison of the distinct behaviour of the two curves. The iQY saturation values and the transition power density points were obtained by fitting eqn (10) (with  $j = 2$  and  $j = 3$  for the 804 nm and 474 nm emission, respectively) to the experimental iQY data. The results of best fitted parameters are presented in Table 1. The first transition point  $\rho_2$  was found to be  $20 \text{ W cm}^{-2}$  and the second transition point  $\rho_3$  to be  $150 \text{ W cm}^{-2}$

$\text{cm}^{-2}$ . The iQY saturation values were found as 0.24% for the 474 nm emission, and 0.78% for the 804 nm emission.

Below the first transition point  $\rho_2$  the iQY curve for the 804 nm emission has a predominant linear power density dependence, whereas the iQY for the 474 nm emission has a predominant quadratic power density dependence. As the power density is increased above  $\rho_2$ , the iQY for the 804 nm emission transits to saturation, which was not reached within the power density range of the measurement. For the 474 nm emission, the iQY transits to a linear dependence before the power density approaches the next transition power density point  $\rho_3$ . Above  $\rho_3$ , the iQY for the 474 nm emission, finally, transits to saturation. Because, the iQY for an ETU2 process is independent of  $\rho_3$ , the curve for the 804 nm emission does not undergo any changes at power densities near this transition point.  $\rho_2$  and the iQY saturation for the 804 nm emission are in agreement with the balancing power density and iQY points previously reported in the literature for core-shell  $\beta$ -UCNPs with the same dopants and a similar emission spectrum (the iQY at the balancing point is exactly half of the iQY saturation<sup>20,22,23</sup>). Mousavi *et al.* reported  $\rho_b = 14 \text{ W cm}^{-2}$  and  $\eta_s/2 = 0.39\%$  obtained from a beam-profile-compensated QY for the 804 nm emission.<sup>23</sup> Liu *et al.* found  $\rho_b = 1.3 \text{ W cm}^{-2}$  and  $\eta_s = 2.6\%$  for the 804 nm emission of a non-beam-profile-compensated iQY.<sup>22</sup> The latter diverges from the results found here, although the transition power density points and the iQY saturation are strongly dependent on the concentration of the dopants, on the particle size, and on the profile of the excitation beam. Therefore, a more accurate comparison would require the beam profile compensation to be considered. As this is the first work to report the iQY for an ETU3 process in terms of transition

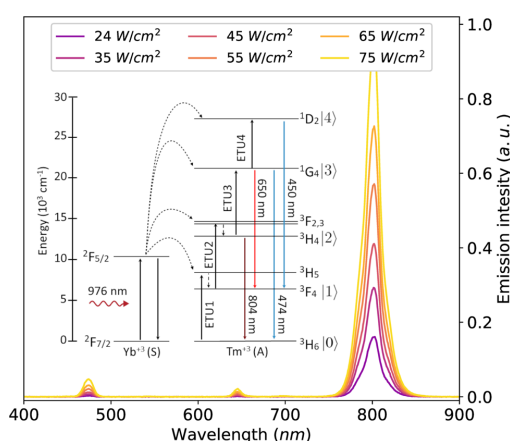


Fig. 4 Emission spectra of the UCNPs acquired for six different excitation power densities. The UCNPs showed the main emission peak at 804 nm and less intense peaks at 474 nm and 650 nm for the power density range of the measurements. The inset of the figure presents an energy level diagram indicating the electronic transitions corresponding to the emission spectra peaks.

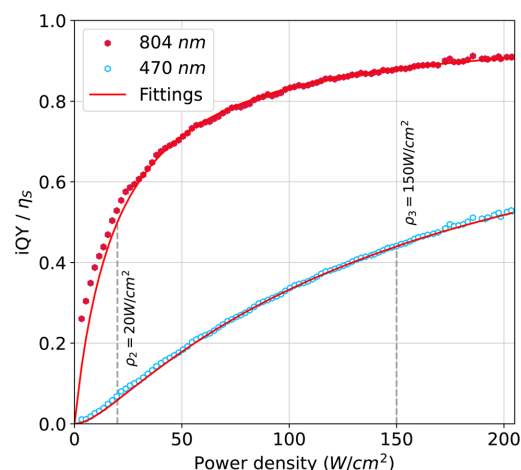


Fig. 5 Non-beam-profile-compensated-iQY data (discrete markers) for the 804 nm and 474 nm emission fitted with the general model (continuous curves) applied to the ETU2 and ETU3 processes, respectively. The results were normalised by their saturation values for a better comparison of the two curves. The iQY saturation values and the transition power density points are summarised in Table 1.



**Table 1** Transition power density points and iQY saturation obtained from fitting the general model approximated to the anomalous power density dependence to the iQY versus power density. The experimental data and the fitted curves are shown in Fig. 5

$\lambda_{\text{em}}$ (nm)	$\rho_2$ (W cm <sup>-2</sup> )	$\rho_3$ (W cm <sup>-2</sup> )	$\eta_s$ (%)
474	20	150	0.24
804	20	—	0.78

points and iQY saturation,  $\rho_3$  and the iQY saturation for the 474 nm emission cannot be compared with the existing literature. Comparing the iQY saturation of both emission wavelengths, the results are in agreement with the magnitude of the emission peaks in Fig. 4, and with typical UCNPs samples doped with Tm, which present much lower QYs for the 474 nm emission than that for the 804 nm emission.<sup>45</sup>

## 4 Conclusion

In conclusion, this paper presented a robust and simple analytical model for an arbitrary ETU process to characterise the iQY of upconverting materials in terms of the transition points of the curves and the iQY saturation level. To exemplify the application of the characterisation method, experimental results of iQY for the 804 nm and 474 nm emissions of a  $\beta$ -NaYF<sub>4</sub>:YbTm core-shell UCNPs were provided. As a result of the analysis of the model, the concepts of “power density transition points” and “iQY saturation” proposed in this work were found in terms of intrinsic properties of the energy levels of the sensitizer and activator ions. In addition, it was found that there is a strong relation between the iQY saturation and the highest power density transition point, which is associated with the first excited state of the activators for UCNPs with anomalous power density dependence. This finding suggests that the properties of the first excited state are related to the fact that upconverting microparticles typically have higher iQYs than UCNPs, and they present a transition power density point, above which, their iQY is reduced to values below the saturation level. The quantification of the transition points is not only important for the determination of the power densities where the behaviours of the UCL and iQY change, but also for the determination of the ET rates. Combining the UCL measurements with life-time measurements, the ET rates are easily obtained for upconverting systems with known activator and sensitizer concentrations. The authors believe that the model proposed in this work provides a powerful tool to accurately characterise upconverting materials and help engineering optimal UCNPs for specific applications, as well as, provide a better understanding of the UC mechanisms.

## Author contributions

Conceptualisation, J. S. M., K. K. and S. A. E.; data curation, J. S. M.; formal analysis, J. S. M.; funding acquisition, S. A. E.; investigation, J. S. M. and K. K.; methodology, J. S. M.; project

administration, K. K., W. K. K., S. K. V. S. and S. A. E.; software, J. S. M.; supervision, K. K. and S. A. E.; validation, J. S. M., K. K., W. K. K. and S. K. V. S.; visualisation, J. S. M.; writing – original draft, J. S. M.; writing – review & editing, J. S. M., K. K., W. K. K., S. K. V. S. and S. A. E.

## Conflicts of interest

The authors declare that they have no conflict of interest.

## Acknowledgements

The authors thank the electron microscopy technicians, Michael Schimth and Davinder Singh, for acquiring the STEM images of the UCNPs, and their prompt response. This project is funded by SFI/15/RP/2828.

## References

- 1 F. E. Auzel, *Proc. IEEE*, 1973, **61**, 758–786.
- 2 F. E. Auzel, *C. R. Acad. Sci.*, 1966, **262**, 1016–1019.
- 3 F. Auzel, *Chem. Rev.*, 2004, **104**, 139–173.
- 4 M. D. Wisser, S. Fischer, C. Siefe, A. P. Alivisatos, A. Salleo and J. A. Dionne, *Nano Lett.*, 2018, **18**, 2689–2695.
- 5 D. Denkova, M. Ploschner, M. Das, L. M. Parker, X. Zheng, Y. Lu, A. Orth, N. H. Packer and J. A. Piper, *Nat. Commun.*, 2019, **10**, 1–12.
- 6 C. Lee, E. Z. Xu, Y. Liu, A. Teitelboim, K. Yao, A. Fernandez-Bravo, A. M. Kotulska, S. H. Nam, Y. D. Suh, A. Bednarkiewicz, B. E. Cohen, E. M. Chan and P. J. Schuck, *Nature*, 2021, **589**, 230–235.
- 7 C. Chen, L. Ding, B. Liu, Z. Du, Y. Liu, X. Di, X. Shan, C. Lin, M. Zhang, X. Xu, X. Zhong, J. Wang, L. Chang, B. Halkon, X. Chen, F. Cheng and F. Wang, *Nano Lett.*, 2022, **22**, 7136–7143.
- 8 J. De Wild, J. K. Rath, A. Meijerink, W. G. Van Sark and R. E. Schropp, *Sol. Energy Mater. Sol. Cells*, 2010, **94**, 2395–2398.
- 9 T. F. Schulze and T. W. Schmidt, *Energy Environ. Sci.*, 2015, **8**, 103–125.
- 10 N. M. Idris, M. K. Gnanasammandhan, J. Zhang, P. C. Ho, R. Mahendran and Y. Zhang, *Nat. Med.*, 2012, **18**, 1580–1585.
- 11 C. T. Xu, P. Svenmarker, H. Liu, X. Wu, M. E. Messing, L. R. Wallenberg and S. Andersson-Engels, *ACS Nano*, 2012, **6**, 4788–4795.
- 12 A. Bansal, H. Liu, M. K. G. Jayakumar, S. Andersson-Engels and Y. Zhang, *Small*, 2016, **12**, 1732–1743.
- 13 T. Xia, *Sci. Bull.*, 2018, **63**, 405–407.
- 14 Y. Wang, L. Bao, Z. Liu and D. W. Pang, *Anal. Chem.*, 2011, **83**, 8130–8137.
- 15 B. Dong, B. Cao, Y. He, Z. Liu, Z. Li and Z. Feng, *Adv. Mater.*, 2012, **24**, 1987–1993.
- 16 E. Martinez, C. Brites, L. Carlos, A. Garcia-Flores, R. Urbano and C. Rettori, *Adv. Funct. Mater.*, 2019, **29**, 1807758–1807770.
- 17 T. A. Henderson and L. D. Morries, *Neuropsychiatr. Dis. Treat.*, 2015, **11**, 2191–2208.



- 18 S. Fischer, B. Fröhlich, K. W. Krämer and J. C. Goldschmidt, *J. Phys. Chem. C*, 2014, **118**, 30106–30114.
- 19 S. Fischer, N. J. Johnson, J. Pichaandi, J. C. Goldschmidt and F. C. Van Veggel, *J. Appl. Phys.*, 2015, **118**, 193105–193118.
- 20 J. S. Matias, K. Komolibus, S. Konugolu-Venkata-Sekar and S. Andersson-Engels, *Nanoscale*, 2022, **14**, 2230–2237.
- 21 J. F. Suyver, A. Aebischer, S. García-Revilla, P. Gerner and H. U. Güdel, *Phys. Rev. B: Condens. Matter Mater. Phys.*, 2005, **71**, 125123–125132.
- 22 H. Liu, C. T. Xu, D. Lindgren, H. Xie, D. Thomas, C. Gundlach and S. Andersson-Engels, *Nanoscale*, 2013, **5**, 4770–4775.
- 23 M. Mousavi, B. Thomasson, M. Li, M. Kraft, C. Würth, U. Resch-Genger and S. Andersson-Engels, *Phys. Chem. Chem. Phys.*, 2017, **19**, 22016–22022.
- 24 A. Teitelboim, B. Tian, D. J. Garfield, A. Fernandez-Bravo, A. C. Gotlin, P. J. Schuck, B. E. Cohen and E. M. Chan, *J. Phys. Chem. C*, 2019, **123**, 2678–2689.
- 25 G. Tessitore, G. A. Mandl, M. G. Brik, W. Park and J. A. Capobianco, *Nanoscale*, 2019, **11**, 12015–12029.
- 26 M. Pokhrel, A. K. Gangadharan and D. K. Sardar, *Mater. Lett.*, 2013, **99**, 86–89.
- 27 M. Kaiser, C. Würth, M. Kraft, I. Hyppänen, T. Soukka and U. Resch-Genger, *Nanoscale*, 2017, **9**, 10051–10058.
- 28 M. Pollnau, D. R. Gamelin, S. R. Lüthi, H. U. Güdel and M. P. Hehlen, *Phys. Rev. B: Condens. Matter Mater. Phys.*, 2000, **61**, 3337–3346.
- 29 D. O. Faulkner, S. Petrov, D. D. Perovic, N. P. Kherani and G. A. Ozin, *J. Mater. Chem.*, 2012, **22**, 24330–24334.
- 30 T. Jung, H. L. Jo, S. H. Nam, B. Yoo, Y. Cho, J. Kim, H. M. Kim, T. Hyeon, Y. D. Suh, H. Lee and K. T. Lee, *Phys. Chem. Chem. Phys.*, 2015, **17**, 13201–13205.
- 31 C. Würth, M. Kaiser, S. Wilhelm, B. Grauel, T. Hirsch and U. Resch-Genger, *Nanoscale*, 2017, **9**, 4283–4294.
- 32 A. Das, C. Mao, S. Cho, K. Kim and W. Park, *Nat. Commun.*, 2018, **9**, 4828–4839.
- 33 C. M. Jones, A. Gakamsky and J. Marques-Hueso, *Sci. Technol. Adv. Mater.*, 2021, **22**, 810–848.
- 34 I. N. Stanton, J. A. Ayres, J. T. Stecher, M. C. Fischer, D. Scharpf, J. D. Scheuch and M. J. Therien, *J. Phys. Chem. C*, 2018, **122**, 252–259.
- 35 S. K. V. Sekar, J. S. Matias, G. Dumlupinar, L. Niemitz, M. Mousavi, K. Komolibus and S. Andersson-Engels, *Opt. Express*, 2022, **30**, 16572–16584.
- 36 R. Deng, F. Qin, R. Chen, W. Huang, M. Hong and X. Liu, *Nat. Nanotechnol.*, 2015, **10**, 237–242.
- 37 M. Fitzgerald, S. Hodgetts, C. V. D. Heuvel, R. Natoli, N. S. Hart, K. Valter, A. R. Harvey, R. Vink, J. Provis and S. A. Dunlop, *Rev. Neurosci.*, 2013, **24**, 205–226.
- 38 J. R. Jagdeo, L. E. Adams, N. I. Brody and D. M. Siegel, *PLoS One*, 2012, **7**, 1–10.
- 39 X. Wu, Y. Zhang, K. Takle, O. Bilsel, Z. Li, H. Lee, Z. Zhang, D. Li, W. Fan, C. Duan, E. M. Chan, C. Lois, Y. Xiang and G. Han, *ACS Nano*, 2016, **10**, 1060–1066.
- 40 Y. Tao, A. J. Y. Huang, Y. Hashimoto-dani, M. Kano, A. H. All, I. Tsutsui-kimura, K. F. Tanaka, X. Liu and T. J. Mchugh, *Science*, 2018, **684**, 679–684.
- 41 P. Villanueva-Delgado, K. W. Krämer and R. Valiente, *J. Phys. Chem. C*, 2015, **119**, 23648–23657.
- 42 J. Bergstrand, Q. Liu, B. Huang, X. Peng, C. Würth, U. Resch-Genger, Q. Zhan, J. Widengren, H. Ågren and H. Liu, *Nanoscale*, 2019, **11**, 4959–4969.
- 43 J. Matias, *Upconversion Virtual Lab*, 2023, <https://jsmatias-qv-virtuallabapp-home-ch3fhq.streamlit.app/>.
- 44 M. Y. Hossan, A. Hor, Q. Luu, S. J. Smith, P. S. May and M. T. Berry, *J. Phys. Chem. C*, 2017, **121**, 16592–16606.
- 45 M. S. Meijer, P. A. Rojas-Gutierrez, D. Busko, I. A. Howard, F. Frenzel, C. Würth, U. Resch-Genger, B. S. Richards, A. Turshatov, J. A. Capobianco and S. Bonnet, *Phys. Chem. Chem. Phys.*, 2018, **20**, 22556–22562.



## PAPER IV

**Beam-profile compensation for quantum yield characterisation of Yb-Tm codoped upconverting nanoparticles emitting at 474 nm, 650 nm and 804 nm (Submitted for publication)**

J. S. Matias, K. Komolibus, S. Konugolu, W. Kho-Kiang and S. Andersson-Engels.

*Nanoscale* -, (2023).



## Journal Name

## ARTICLE TYPE

Cite this: DOI: 00.0000/xxxxxxxxxx

**Beam-profile compensation for quantum yield characterisation of Yb-Tm codoped upconverting nanoparticles emitting at 474 nm, 650 nm and 804 nm**<sup>†</sup>J. S. Matias,<sup>\*ab</sup> K. Komolibus,<sup>a</sup> W. K. Kiang,<sup>a</sup> S. Konugolu-Venkata-Sekar,<sup>a</sup> and S. Andersson-Engels<sup>ab</sup>

Received Date

Accepted Date

DOI: 00.0000/xxxxxxxxxx

Upconverting nanoparticles (UCNPs) have found widespread applications in biophotonics and energy harvesting due to their unique non-linear optical properties arising from energy transfer upconversion (ETU) mechanisms. However, accurately characterising the power density-dependent efficiency of UCNPs using the internal quantum yield (iQY) is challenging due to the lack of methods that account for excitation beam-profile distortions. This limitation hinders the engineering of optimal UCNPs for diverse applications. To address this, this work presents a novel beam profile compensation strategy based on a general analytical rate-equations model, enabling the evaluation of iQY for ETU processes of arbitrary order, such as ETU2, ETU3, and beyond. The method was applied to characterise the ETU2 and ETU3 processes corresponding to the main emission peaks (474 nm, 650 nm, and 804 nm) of a Yb-Tm codoped  $\beta$ -UCNP. Through this approach, the transition power density points (which delimit the distinct non-linear regimes of the upconversion luminescence (UCL)), and the saturation iQY values (which are reached at high excitation power densities above the transition points) were determined. The ETU2 process exhibits a single transition power density point, denoted as  $\rho_2$ , while the ETU3 processes involve two transition points,  $\rho_2$  and  $\rho_3$ . By compensating for the beam profile, we evaluate the iQY of individual lines across a wide dynamic range of excitation power densities (up to  $10^5 \text{ W/cm}^2$ ), encompassing both non-linear and linear regimes of UCL. This study introduces a valuable approach for accurately characterising the iQY of UCNPs, facilitating a deeper understanding of the upconversion and its performance. By addressing excitation beam-profile distortions, this method provides a comprehensive and reliable assessment of the power density-dependent iQY. The results highlight the applicability and effectiveness of this beam profile compensation strategy, which can be employed for a wide range of UCNPs. This advancement opens new avenues for the tailored design and application of UCNPs in various fields, especially for biophotonics.

**1 Introduction**

In the last decades, upconverting nanoparticles (UCNPs) have been extensively studied due to their unique ability to convert low-energy to high-energy light, an anti-Stokes process involving multi-photon absorption followed by the emission of a single photon with shorter wavelength<sup>1-3</sup>. This unique property makes UCNPs interesting for several applications, from renewable energy to biophotonics. UCNPs have been successfully ap-

plied to light harvesting<sup>4,5</sup>, photodynamic therapy<sup>6</sup>, diffuse optical imaging<sup>7</sup>, optogenetics<sup>8,9</sup>, biosensors<sup>10</sup>, and temperature sensing<sup>11,12</sup>. Despite their potential, their internal quantum yield (iQY) - used as a figure of merit to characterise UCNPs, defined as the ratio of number of emitted photons to the number of absorbed ones<sup>13-15</sup> - remains low, and its accurate evaluation can be challenging, especially at the low excitation power densities required for biological applications. The most efficient UCNPs contain a rare-earth element, known as the sensitiser, which absorbs the excitation photons and transfers the absorbed energy to another rare-earth element, known as the activator. After a series of energy transfers, the activator relaxes to the ground state by emitting upconverted light completing the process known as energy transfer upconversion (ETU). The order of the ETU pro-

<sup>a</sup> Biophotonics@Tyndall, IPIC, Tyndall National Institute, Cork, Ireland.

E-mail: jean.matias@tyndall.ie

<sup>b</sup> Department of Physics, University College Cork, Cork, Ireland<sup>†</sup> Electronic Supplementary Information (ESI) available.

See DOI: 00.0000/00000000.

cess is determined by the number of absorbed photons involved in the upconversion (UC), and as a result, the upconversion luminescence (UCL) exhibits non-linear behaviour with respect to the excitation power density. This non-linearity effect has led to breakthroughs in super-resolution microscopy, where researchers achieved sub-70 nm imaging resolution by utilising the giant non-linear response found in certain UCNPs<sup>16–19</sup>. However, the non-linear response of the UCL implies a power density dependence of the iQY of UCNPs, which requires its evaluation over a wide dynamic range of the excitation power density while accounting for the beam profile of the excitation beam. This is because different regions of a non-uniform excitation beam can have varying effects on the UCNPs within the illuminated volume, which can complicate the determination of the exact power density of excitation. Characterisation of iQY without beam-profile compensation can underestimate the value by up to 75% compared to compensated iQY characterisation<sup>15</sup>. Moreover, different beam profiles with the same total power can lead to different UCL results, which makes it difficult to compare different measurements (especially those performed at different laboratories<sup>20,21</sup>), understand the underlying UC properties of the material, and consequently impedes precise engineering of optimal UCNPs.

An attempt to compensate for the iQY of an ETU2 process for the excitation beam profile was presented by May and Berry. The authors studied different approaches to defining the radius of a Gaussian profile of the excitation beam to calculate the area of its cross-section, and finally compute the excitation power density. They showed that defining the radius taken at 1.8 times the standard deviation of the cross-section, instead of the conventional full-width-at-half-maximum (FWHM), is a way to compensate the QY for an ETU2 process in its non-linear regime, where the power density dependence of the UCL is quadratic<sup>21</sup>. However, the issue with this strategy is that the power density dependence of the UCL changes for different power density ranges, which are delimited by transition power density points<sup>22</sup>. Moreover, UCNPs typically have multiple wavelength emission, typically involving ETU processes with different orders of power density dependence<sup>23</sup>. For example, the UCL of an ETU3 process has a cubic behaviour at low power densities and becomes linear at high excitation, transiting to intermediate values within a power density range between transition power density points<sup>22</sup>. Another approach for compensation is to measure the excitation beam profile and utilise a model that describes the behaviour of the UCL. This method was firstly reported for an ETU2 process by Mousavi *et al.*, and further confirmed by Matias *et al.*<sup>15,24</sup>. This strategy is advantageous as it considers the different regimes presented by an ETU process, including the transition power density ranges between them. To date, research on the beam-profile-compensation has primarily focused on ETU processes of second-order due to the lack of an analytical model capable of accurately describing higher-order ETU. However, a recent publication introduced a general analytical model for arbitrary-order ETU, providing a crucial step towards characterising and compensating iQY for these processes<sup>22</sup>. Building on this development, we combined the general model with a beam profile compensation approach developed for ETU2 process to characterise the iQY of UCNPs over a

wide dynamic range of the excitation power density. This extends the beam profile compensation of the iQY for ETU processes of arbitrary order, which is crucial for the comprehensive characterisation of UCNPs for various biophotonic applications. For the first time, our method enables the characterisation of ETU processes of orders higher than 2, expanding the scope of UCNPs that can be characterised using this approach. We demonstrate the effectiveness of our method by accurately characterising the iQY of the 474 nm, 650 nm, and 804 nm emission peaks of a Yb-Tm-codoped  $\beta$ -UCNP. The beam-profile-compensated iQY of the ETU2 and ETU3 processes were obtained over a wide range of excitation power densities using our compensation method in conjunction with two distinct excitation beam profiles, as previously reported<sup>15</sup>. The iQY characterisation covers a wide range of excitation power densities, from the highly non-linear regime below the power density transition points, to the linear regimes at high power densities above the transition points. This work represents a significant advance towards the standardisation of UCNPs characterisation for a range of biophotonic applications. Of particular importance is the ability to characterise ETU processes of orders higher than 2, which are essential for optogenetics applications. Our method provides a powerful tool for accurately characterising UCNPs with any sensitiser or activator, enabling the optimisation of these materials for various biophotonic applications, including emerging uses in optogenetics.

## 2 Materials and methods

The core-shell  $\beta$ -NaYF<sub>4</sub> codoped with Yb<sup>3+</sup> and Tm<sup>3+</sup> UCNPs, which exhibit visible and near-infrared (NIR) emission wavelengths, were procured from Creative Diagnostics and prepared according to the experimental requirements. Firstly, the nanoparticles were subjected to scanning transmission electron microscopy (STEM) to determine their morphology, size, and dispersion. Subsequently, the emission spectra, luminescence, and absorption characteristics of the UCNPs were studied using a modified QY system described in the electronic supplementary material, which is based on a previously reported method<sup>25</sup>. Finally, the luminescence data were analysed by fitting them with the beam-profile-compensation equation. This approach enabled us to obtain the iQY curves for a wide range of excitation power densities. The experimental details, along with the theoretical background on the development of the beam-profile-compensation method, are presented in the following sections.

### 2.1 Sample characterisation

For morphology, size, and dispersion characterisation, the sample solution was drop-cast over a 5 mm silicon and brought to the STEM for image acquisition in the transmission mode. For the emission spectra, luminescence, and absorption characterisation, the sample was prepared according to the following steps, which are based on a procedure reported elsewhere<sup>15</sup>. First, 1 ml of the as-purchased UCNPs was transferred to a four-cleared-window quartz cuvette and sonicated for 15 minutes. The sample was allowed to rest for an additional 15 minutes to reach thermal equilibrium and to ensure that any residual aggregation could settle

to the bottom of the cuvette. The cuvette containing the UCNPs was placed inside CH1, and another identical cuvette containing only toluene (blank cuvette) was placed inside CH2 as a reference for absorption measurements. The laser beam was shaped to a narrow waist by keeping the mirrors FM3 and FM4 flipped down, and beam profile images were taken with the CMOS camera and labelled as BP1. Emission spectra were then collected for a range of power densities between 200-3000  $W/cm^2$ . The power density was determined by the ratio between the excitation power at the centre of the cuvette and the area of the cross-section of the beam, with the radius taken as the FWHM. Transmission and luminescence data for the 804  $nm$  and 474  $nm$  peaks were collected simultaneously for several excitation powers between 0-100  $mW$ . This step was repeated for the 650  $nm$  emission peak, replacing a 700  $nm$  long-pass filter with a 650  $nm$  band-pass filter in front of the APD1. The UCL signal of the 474  $nm$  peak was also acquired simultaneously with the 650  $nm$  as a reference to the previous measurement. This procedure for the three wavelengths was repeated for the large beam profile, labelled as BP2. Next, the UCL data was plotted versus the excitation power at the centre of the cuvette,  $P_c$  [W], which was obtained by taking the square root of the product between the incident power  $P_o$  [W] and the transmitted power  $P$  [W], as given by (Eq. 1),

$$P_c = \sqrt{P_o P} \quad (1)$$

The incident power  $P_o$  was obtained by running measurements (for BP1 and BP2) with empty cuvette holders. The experimental data were fitted with a beam-profile dependent UCL equation, which is described in detail below.

## 2.2 QY evaluation and theoretical background

The beam profile compensation method utilised in this study is based on a rate-equations-general-model for an ETU process of arbitrary order, which was recently reported in the literature<sup>22</sup>. The method involves determining the iQY saturation and the transition power density points of the UCL and iQY by fitting luminescence curves versus excitation power with an equation that takes into account the excitation beam profile. The fitting equation for a general ETU process was determined based on a previous report in the literature for an ETU2 process<sup>15</sup>. By definition, the iQY is the ratio of emitted photons to absorbed photons by the material. This relationship can be expressed in terms of power and wavelengths of excitation and emission using the (Eq. 2),

$$\eta_{\lambda_{em}} = \frac{L_{\lambda_{em}} \lambda_{em}}{P_a \lambda_{ex}} \quad (2)$$

where,  $\eta_{\lambda_{em}}$  [-] and  $L_{\lambda_{em}}$  [W] represent the iQY and UCL for the wavelength of emission  $\lambda_{em}$  [nm],  $P_a$  [W] is the absorbed power, and  $\lambda_{ex}$  [nm] is the excitation wavelength, which is 976  $nm$ . The absorbed power  $P_a$  is proportional to the excitation power density, given by (Eq. 3),

$$P_a = \mu_a l \rho A \quad (3)$$

where,  $\mu_a$  [ $cm^{-1}$ ] is the absorption coefficient obtained by the

Beer-Lambert's law,  $l$  [cm] is excitation path length of an uniform power density  $\rho$  [ $W/cm^2$ ] over an area  $A$  [ $cm^2$ ]. According to the general analytical model for UCNPs under uniform power density excitation and exhibiting anomalous power density dependence, the simplified iQY  $\eta_n(\rho)$  [-] equation for an ETUn process is given by (Eq. 4),

$$\eta_n(\rho) = \eta_{ns} \rho^{n-1} \prod_{i=2}^n \frac{1}{\rho + \rho_i} \quad (4)$$

where  $\eta_{ns}$  [-] is the iQY saturation, and  $\rho_i$  [ $W/cm^2$ ] are the transition power density points that define the different regimes of linearity and non-linearity of the UCL curve<sup>22</sup>. Now, by comparing equations (Eq. 2) and (Eq. 4) for  $n$ , the order of the ETUn process responsible for the UC emission wavelength  $\lambda_{em}$ , and isolating the power density and all the constants on the right-hand side of the equation, one can determine the power density dependent UCL  $L_{\lambda_{em}}(\rho)$ , as given by equation (Eq. 5),

$$L_{\lambda_{em}}(\rho) = \mu_a l A \frac{\lambda_{ex}}{\lambda_{em}} \eta_{ns} \rho^n \prod_{i=2}^n \frac{1}{\rho + \rho_i} \quad (5)$$

where,  $P_a$  was replaced by the (Eq. 3). This equation gives the emitted power for a uniform power density illumination. However, the resultant emitted power of a volume of UCNPs under non-uniform illumination can be obtained by integrating the emission over the entire volume. This volume integral can be simplified to an integral of area at the cross-section of the beam profile, by considering that the excitation power density does not change along the illumination path. Since the beam profile is measured with a camera having a discrete  $m$  number of pixels, we assume that the excitation power density is constant over the area of each pixel region. Thus, the integration can be further simplified to a summation over the  $m$  pixels, and the resultant UCL  $L_{\lambda_{emr}}$  [W] is represented by 6,

$$L_{\lambda_{emr}} = \mu_a l A_{px} \frac{\lambda_{ex}}{\lambda_{em}} \eta_{ns} \sum_{px}^m \rho_{px}^n \prod_{i=2}^n \frac{1}{\rho_{px} + \rho_i} \quad (6)$$

where,  $A_{px}$  [ $cm^2$ ] is the area of each pixel, and  $\rho_{px}$  [ $W/cm^2$ ] is the power density measured at each pixel region. Since the measurements are conducted over a wide range of excitation powers, it is convenient to represent the resultant UCL in terms of the excitation power at the centre of the illuminated volume,  $P_c$  [W]. The power density at each pixel can be related to the excitation power at the centre by (Eq. 7),

$$\rho_{px} = \frac{P_c \gamma_{px}}{A_{px}} \quad (7)$$

where,  $\gamma_{px}$  [-] is the normalised intensity of the beam profile at the pixel  $px$ , as given by (Eq. 8),

$$\gamma_{px} = \frac{\Gamma_{px}}{\sum_{px} \Gamma_{px}} \quad (8)$$

where  $\Gamma_{px}$  [a.u.] is intensity of the beam profile  $\Gamma$  at the pixel  $px$  in arbitrary units measured with the CMOS camera. Finally, the resultant UCL for an emission wavelength  $\lambda_{em}$  as a function of the beam profile and the excitation power at the centre of the region,

$L_{\lambda_{emr}}(P_c)$  [W], is given by the (Eq. 9),

$$L_{\lambda_{emr}}(P_c) = \mu_{al} \frac{\lambda_{ex}}{\lambda_{em}} \eta_{ns} \sum_{px} P_c^n \gamma_{px} \prod_{i=2}^n \frac{1}{P_c + \rho_i A_{px} / \gamma_{px}} \quad (9)$$

### 3 Results

The UCNPs exhibited a hexagonal morphology with an average size of  $16 \pm 2$  nm, as demonstrated by the STEM image in Fig. 1. The size distribution, shown in the inset of Fig. 1, was determined by analysing 100 randomly selected nanoparticles from the STEM image. The particles exhibited good dispersion, and no significant aggregation was observed.

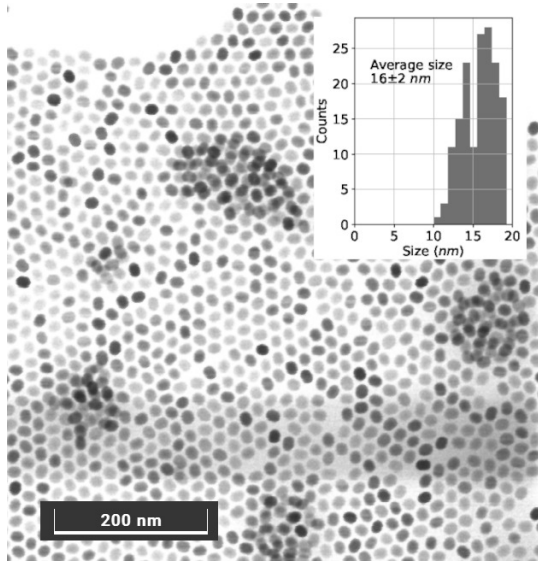


Fig. 1 STEM image acquired in transmission mode, revealing the hexagonal morphology of the UCNPs with an average size of  $16 \pm 2$  nm. The inset displays the size distribution histogram obtained from the analysis of 160 nanoparticles selected randomly.

Fig. 2.a displays an energy level diagram highlighting the electronic transitions responsible for each emission peak in the emission spectra of the UCNPs, shown in Fig. 2.b. The spectra exhibit prominent peaks at 450 nm, 474 nm, 650 nm, and 804 nm, which are typical emission peaks of the ion  $\text{Tm}^{3+20}$ . The emission peak at 450 nm could only be observed at power densities exceeding  $1000 \text{ W/cm}^2$  due to the less probable electronic transition decay from the excited state  $^1D_2$  to the ground state  $^3H_6$ , which corresponds to an ETU4 process. Due to its lower intensity compared to the other peaks, the UCL at the 450 nm wavelength was not measured. On the other hand, the 474 nm and 650 nm emission peaks originate from ETU3 processes, resulting from electronic decay transitions from the same excited state to the ground state ( $^1G_4 \rightarrow ^3H_6$ ) and to an intermediate excited state ( $^1G_4 \rightarrow ^3F_4$ ), respectively. Finally, the 804 nm emission corresponds to an ETU2 process, representing the electronic decay from the excited state  $^3H_4$  to the ground state  $^3H_6$ .

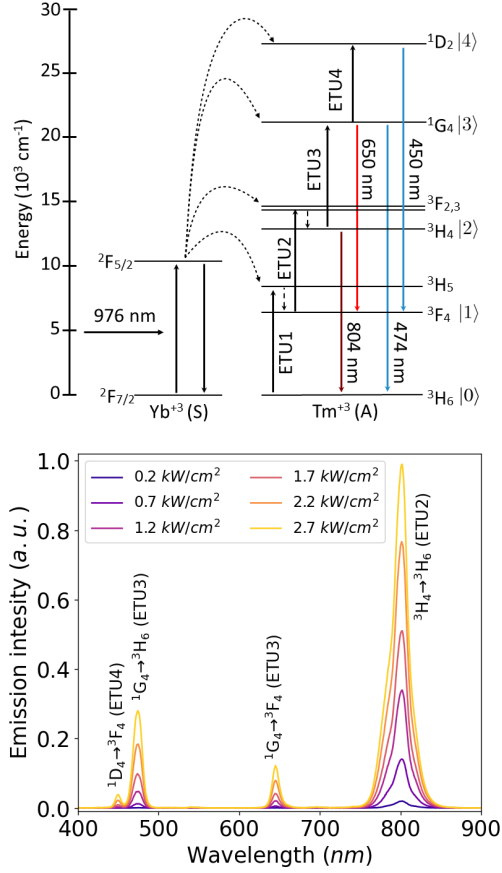


Fig. 2 Emission spectra of the UCNPs recorded under various excitation power densities. Panel a) illustrates an energy level diagram showcasing the electronic transitions corresponding to the observed emission peaks. Panel b) shows the UCNPs' primary emission peak at 804 nm, along with weaker peaks at 474 nm and 650 nm, which were detected within the investigated range of power densities.

On the left side of Fig. 3, the profiles of the excitation beams are presented, with BP1 shown at the top in panel a) and BP2 displayed at the bottom in panel b). On the right side, three plots depict the UCL curves in relation to the measured excitation powers under the BP1 and BP2 profiles. In panel c), the UCL for the 474 nm peak is shown, while panel d) displays the UCL for the 650 nm peak. At the bottom in panel e), the UCL plot for the 804 nm emission peak is presented. To fit the UCL data, the (Eq. 9) was employed with the corresponding beam profiles, where  $l$  represents the aperture of the slit ( $0.1 \text{ cm}$ ), and  $\mu_a$  is the absorption coefficient ( $0.05 \text{ cm}^{-1}$ ). The value of  $n$  was replaced by the order of the respective ETU processes for each emission peak. The continuous lines in Fig. 3 represent the fitted curves obtained from the fittings of the UCL curves. The best-fitted pa-

Table 1 Transition power density points and iQY saturation constants obtained from fitting the simplified general model for the anomalous power density dependence to the UCL versus excitation power. The experimental data and the fitted curves are shown in Fig. 3

Beam Profile	$\lambda_{em}$ (nm)	$\rho_2$ (W/cm <sup>2</sup> )	$\rho_3$ (W/cm <sup>2</sup> )	$\eta_S$ (%)
BP1	474	31	$3.7 \times 10^2$	0.30
BP1	650	31	$3.6 \times 10^2$	0.14
BP1	804	31	-	0.82
BP2	474	31	$4 \times 10^2$	0.28
BP2	650	31	$4 \times 10^2$	0.14
BP2	804	33	-	0.78

parameters for the transition power density points and the iQY saturation constants are provided in Table. 1.

Finally, the beam-profile-compensated iQY curves were obtained by applying the (Eq. 4) using the constants obtained from Table 1. These curves were plotted as a function of excitation power densities measured at the pixels of the CMOS camera. Fig. 4 presents the iQY results for the three emission peaks in a double-logarithmic representation. This highlights the iQY results at low excitation power densities. The high dynamic range of excitation power densities ( $10^5$ ) and of iQY values ( $10^8$ ) is evident as a result of combining the dynamic range of the camera with the dynamic range of laser power and power-meter. The vertical dashed lines in the plot represent the transition power density points ( $\rho_2$  and  $\rho_3$ ), while the horizontal dashed lines indicate the iQY saturation levels for the three curves.

#### 4 Discussion

As with any quantum process, ETU is probabilistic, and the UCL depends on the population densities of the energy levels. Higher-order ETU processes occur only if lower-order ETU processes have already occurred. Thus, as the excited energy level at which the electrons decay becomes higher, the probability of the event decreases. This can be observed by comparing the heights of the peaks in the emission spectra shown in Fig. 2. The ETU4 peak at 450 nm exhibits the lowest intensity and was only detected for power densities above 1000 W/cm<sup>2</sup>, while the other emission peaks were detected at power densities as low as a few mW/cm<sup>2</sup>. The ETU3 processes show higher intensities than the 450 nm peak but lower intensities than the 804 nm peak, which corresponds to an ETU2 process. When comparing the heights of the 474 nm and 650 nm peaks, which both result from decays from the same excited state, it can be observed that the 650 nm peak shows lower intensities. This preference for electronic transitions to lower energy levels indicates that transitions to the ground state are more likely to occur. These findings align with those reported by Meijer *et al.* in their investigation of the absolute QY of UCNP containing the same dopants (Yb<sup>3+</sup> and Tm<sup>3+</sup>) but embedded in a different host matrix (LiYF<sub>4</sub>)<sup>20</sup>. Despite the variations in host matrix, the authors examined the QY of UCNP with similar dopant compositions and presented a comparison of absolute QY measurements conducted at different research centres. Their results exhibited a main emission peak at 794 nm, followed by peaks at

451 nm, 480 nm, and 649 nm, which closely resemble the peaks observed in this study. The main difference lies in the higher intensity observed at 451 nm compared to 480 nm in their results. Additionally, their emission spectra displayed broader peaks with secondary peaks, indicating a potential stronger influence of the crystal field resulting from the LiYF<sub>4</sub> host matrix on the energy levels of the activator ions. Furthermore, a systematic study of the influence of Tm<sup>3+</sup> concentrations on the excitation power-dependent UCL of similar UCNP, *i.e.* same host matrix and same dopants, was reported by Kraft *et al.*<sup>26</sup>. Interestingly, our results exhibit emission spectra that closely resemble their sample with low Tm<sup>3+</sup> concentration (0.2%), matching most of the observed peaks and their intensities. At low Tm<sup>3+</sup> concentrations the 700 nm emission peak is suppressed and the relative intensity of the 450 nm peak is reduced, as shown in their results.

Comparing the absolute UCL values of these transitions, as shown in Fig. 3, allows for a similar analysis. Under the same beam profile and excitation power, the UCNP exhibit higher UCL at 804 nm compared to 474 nm and 650 nm, with the 650 nm wavelength having the lowest intensity. The dependence of the UCL curves on the beam profile is clearly evident. Each wavelength exhibits a higher intensity when excited by the BP1 beam profile compared to the BP2 profile, despite both profiles having the same excitation power. Although BP1 illuminates a smaller volume of the sample, containing fewer nanoparticles compared to the volume illuminated by BP2, the higher power density experienced by the UCNP excited by BP1 leads to increased luminescence. This effect is a direct result of the non-linear power density characteristics of UC. The effect is particularly pronounced for the ETU3 processes, which exhibit a cubic power density dependence at power density ranges below their power density transition points, while the ETU2 process displays quadratic behaviour. Additionally, it is worth noting that the 804 nm UCL curve under BP1 reaches linearity at lower excitation powers compared to the curve under BP2. This difference arises from the overall higher power density associated with BP1 in comparison to BP2. These observations align with findings in the literature<sup>15,24,27</sup> and underscore the significance of beam-profile compensation in accurately characterising the iQY of non-linear UC.

The UCL curves for the 474 nm and 650 nm exhibit identical shapes under the same excitation beam profile. This is because the UCL is proportional to the population density of the excited energy state from which the electrons decay. However, their absolute intensity values differ due to the iQY saturation constants, which depend on the radiative decay rates of the respective processes<sup>22</sup>. Since the electrons end up in different energy levels, their decay rates differ, consequently, their iQY saturation constants are distinct. In contrast, the 804 nm UCL curve shows a noticeably different shape. This is a result of the varying number of power density transition points associated with different ETU processes. As an ETU3 process, the 474 nm and 650 nm UCL curves share the same transition power density points,  $\rho_2$  and  $\rho_3$ , while the 804 nm UCL curve depends solely on one power density transition point,  $\rho_2$ .

The results obtained from fitting the parameters in Table. 1 reveal very similar values for the transition power density points

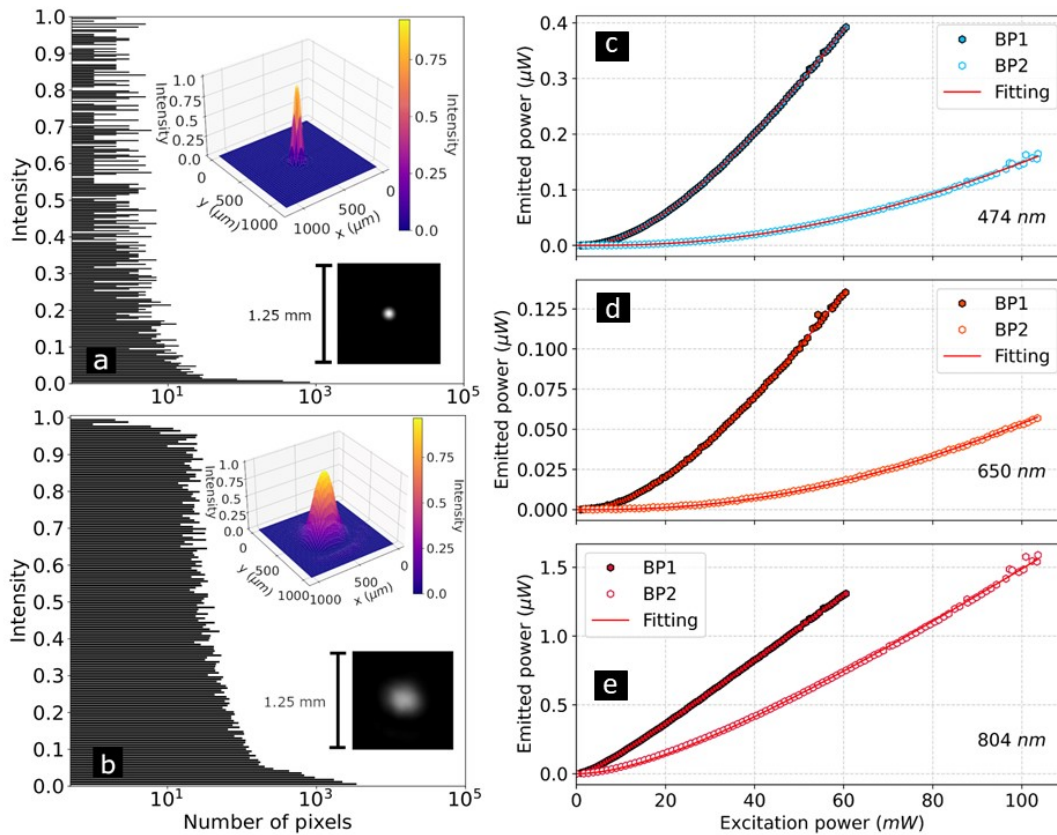


Fig. 3 Absolute UCL measured under different beam profiles: a) narrow beam profile (BP1) with a width of 100 μm (FWHM) and b) large beam profile (BP2) with a width of 300 μm. The UCL curves for the c) 474 nm, d) 650 nm, and e) 804 nm emission peaks are shown.

across all the experimental UCL curves. The value of  $\rho_2$  was found to be 31 W/cm<sup>2</sup> for the ETU3 processes, regardless of the excitation beam profile, and for the ETU2 process under BP1. For the ETU2 process under BP2,  $\rho_2$  was slightly higher at 33 W/cm<sup>2</sup>. The values of  $\rho_3$  were determined as 370 W/cm<sup>2</sup> and 360 W/cm<sup>2</sup> for the 474 nm and 650 nm UCL curves under BP1, respectively. Under BP2, both fittings yielded the same value of 400 W/cm<sup>2</sup> for  $\rho_3$ . Despite minor deviations, these values are consistent with the theoretical expectation that the transition power density points are independent of the beam profile and the order of the ETU process or emission wavelength. In contrast, the iQY saturation levels are wavelength-dependent but independent of the excitation beam profile, as confirmed by fitting the experimental results. The 804 nm UCL exhibits the highest iQY saturation, 0.82% and 0.78% for the BP1 and BP2 curves, respectively. The 474 nm UCL follows with iQY saturation values of 0.30% and 0.28% for BP1 and BP2, respectively. Finally, the iQY saturation for the 650 nm UCL falls in between, with a value of 0.14% for both excitation beam profiles. These results align with the probabilistic interpretation of the ETU processes discussed earlier. Furthermore,

the excellent agreement between the fitted curves and the experimental UCL data in Fig. 3 confirms the robustness of the general model in explaining the ETU processes. Therefore, the transition power density points and the iQY saturation constants accurately and consistently represent the power density-dependent iQY of these UCNPs for all the wavelengths analysed, as shown in Fig. 4. At power densities below the transition points, the UCNPs exhibit maximum UCL non-linearity, with the iQY of the ETU2 process being proportional to power density,  $\rho$ , while the iQY of the ETU3 process is proportional to  $\rho^2$ . As the excitation power density increases beyond  $\rho_2$ , the iQY transitions to saturation for the ETU2 process and to linear power density dependence ( $\rho$ ) for the ETU3 processes. Moreover, the iQYs of the ETU3 processes tend to saturate at excitation power densities above the  $\rho_3$  transition point. However, the ETU2 process does not undergo further changes beyond this point, as its iQY is independent of  $\rho_3$  (Eq. 4).

A comparison of the iQY values for the dominant emission peak (~ 800 nm) under 5 W/cm<sup>2</sup> excitation reveals notable differences between the results obtained in this study and those reported by Meijer *et al.*. The results presented by Meijer *et al.* ex-

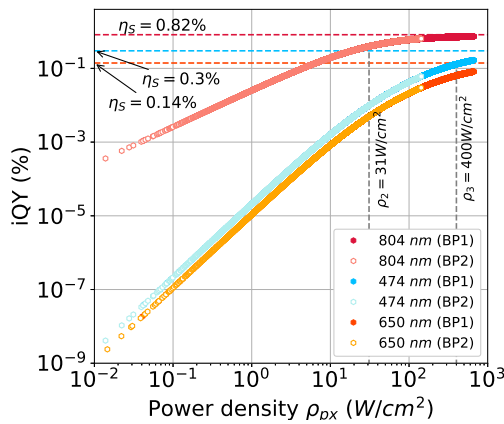


Fig. 4 Beam-profile-compensated iQY data for the 804 nm, 650 nm and 474 nm emission peaks versus the local excitation power densities measured at the pixels of the CMOS camera. The horizontal dashed lines represent the iQY saturation levels of the three curves. The vertical dashed lines represent the transition power density points,  $\rho_2$  common for all the curves, and  $\rho_3$  only affecting the iQY curves for the ETU3 processes (650 nm and 474 nm emission peaks).

hibits an approximately one order of magnitude higher quantum yield, approximately 2%, compared to the 0.1% iQY determined in our measurements. It should be noted, however, that Meijer *et al.*'s sample has different host matrix (LiYF<sub>4</sub> as mentioned previously), the dopants concentrations are probably different, and their sample is optimised for the NIR emission. Additionally, their reported values do not account for beam-profile compensation<sup>20</sup>. Contrasting to that, the iQY saturation level summed for all emission wavelengths, around 1.2%, falls between the results reported by Kraft *et al.* for the samples with 0.2% and 0.5% the Tm<sup>3+</sup> concentrations, which is consistent to the analysis comparing the emission spectra reported by the authors and this work. Although, their result suggest that the QYs reach saturation level around 70 W/cm<sup>2</sup><sup>26</sup>, which is below of what was found here, around 100 W/cm<sup>2</sup> for the most intense emission wavelength, 804 nm. Moreover, the results of the fittings for the ETU2 process show good agreement with the literature. The transition power density point ( $\rho_2$ ) and iQY saturation ( $\eta_{2S}$ ) obtained in this study align with the findings of Mousavi *et al.*<sup>24</sup>. While their reported iQY saturation is identical to the one found for BP2 in this work, it is important to note that the transition power density points and iQY saturation constants can vary depending on the dopant concentrations of the sensitizer and activator. Therefore, they are not necessarily expected to be the same. Regarding the ETU3 process, this study represents the first report of beam-profile-compensated QY, making direct comparisons to existing literature challenging. However, a previous study by the authors without beam-profile compensation, which introduce the general model utilised in this paper, reported lower transition power density points ( $\rho_2 = 20$  W/cm<sup>2</sup> and  $\rho_3 = 150$  W/cm<sup>2</sup>)<sup>22</sup>. These lower values further highlight the importance of accounting for beam-

profile compensation in accurately characterising iQY, as previously emphasised<sup>15,24</sup>. On the other hand, the iQY saturation levels were found to be similar, with  $\eta_{2S} = 0.3\%$  and  $\eta_{3S} = 0.78\%$ . This indicates that the saturation constants play a more significant role at power densities above the transition points, where the UCL enters the linear regime and both UCL and iQY become independent of the excitation beam profile.

## 5 Conclusion

In conclusion, this study presents a novel beam-profile compensation method based on a comprehensive analytical rate-equations-based model for the characterisation of the iQY of ETU processes of any order, encompassing various UCL wavelengths. The model's applicability extends beyond the specific sample analysed in this paper, as it can be employed for UCNP's with different codopants. In this study, the model was successfully applied to analyse the UCL peaks at 474 nm, 650 nm, and 804 nm in a core/shell Yb-Tm-codoped  $\beta$ -UCNP. By fitting the theoretical model to the experimental UCL data acquired under two distinct beam profiles, precise determination of the transition power density points and iQY saturation levels for the ETU2 and ETU3 processes was achieved.

The excellent agreement between the model fitting and experimental data, along with the consistent results of the transition power density points, highlight the robustness of the proposed model in precisely evaluating the power density-dependent iQY of UCNP's, regardless of the excitation beam profile. Given the low QY of UCNP's, which limits their potential for biomedical applications, the evaluation of iQY as an intrinsic property is crucial for standardising the characterisation of these materials and facilitating the engineering of optimal nanoparticles.

This work contributes to advancing the understanding of UC processes and provides a valuable tool for accurately assessing the iQY of UCNP's. The developed beam-profile compensation method has the potential to enhance the efficiency and reliability of future studies involving UCNP's, leading to the design and development of more efficient and tailored upconverting nanomaterials for a wide range of applications, especially the ones in biophotonics.

## Author contributions

Conceptualisation, J.S.M., K.K. and S.A.E.; Data curation, J.S.M.; Formal analysis, J.S.M.; Funding acquisition, S.A.E.; Investigation, J.S.M. and K.K.; Methodology, J.S.M.; Project administration, K.K., W.K.K., S.K.V.S. and S.A.E.; Software, J.S.M.; Supervision, K.K. and S.A.E.; Validation, J.S.M., K.K., W.K.K. and S.K.V.S.; Visualisation, J.S.M.; Writing - original draft, J.S.M.; Writing - review & editing, J.S.M., K.K., W.K.K., S.K.V.S. and S.A.E.

## Conflicts of interest

The authors declare that they have no conflict of interest.

## Acknowledgements

The authors thank the Electron Microscopy technicians, Michael Schimth and Davinder Singh, for acquiring the STEM images of the UCNP's, and their prompt response. This project is funded by SFI/15/RP/2828.

## References

- 1 F. E. Auzel, *Proceedings of the IEEE*, 1973, **61**, 758–786.
- 2 F. E. Auzel, *C. R. Acad. Sci.*, 1966, **262**, 1016–1019.
- 3 F. Auzel, *Chemical Reviews*, 2004, **104**, 139–173.
- 4 J. De Wild, J. K. Rath, A. Meijerink, W. G. Van Sark and R. E. Schropp, *Solar Energy Materials and Solar Cells*, 2010, **94**, 2395–2398.
- 5 T. F. Schulze and T. W. Schmidt, *Energy and Environmental Science*, 2015, **8**, 103–125.
- 6 N. M. Idris, M. K. Gnanasamandhan, J. Zhang, P. C. Ho, R. Mahendran and Y. Zhang, *Nature Medicine*, 2012, **18**, 1580–1585.
- 7 C. T. Xu, P. Svenmarker, H. Liu, X. Wu, M. E. Messing, L. R. Wallenberg and S. Andersson-Engels, *ACS Nano*, 2012, **6**, 4788–4795.
- 8 A. Bansal, H. Liu, M. K. G. Jayakumar, S. Andersson-Engels and Y. Zhang, *Small*, 2016, **12**, 1732–1743.
- 9 T. Xia, *Science Bulletin*, 2018, **63**, 405–407.
- 10 Y. Wang, L. Bao, Z. Liu and D. W. Pang, *Analytical Chemistry*, 2011, **83**, 8130–8137.
- 11 B. Dong, B. Cao, Y. He, Z. Liu, Z. Li and Z. Feng, *Advanced Materials*, 2012, **24**, 1987–1993.
- 12 E. Martínez, C. Brites, L. Carlos, A. García-Flores, R. Urbano and C. Rettori, *Advanced Functional Materials*, 2019, **29**, 1807758–1807769.
- 13 S. Fischer, B. Fröhlich, K. W. Krämer and J. C. Goldschmidt, *Journal of Physical Chemistry C*, 2014, **118**, 30106–30114.
- 14 S. Fischer, N. J. Johnson, J. Pichaandi, J. C. Goldschmidt and F. C. Van Veggel, *Journal of Applied Physics*, 2015, **118**, 193105–193117.
- 15 J. S. Matias, K. Komolibus, S. Konugolu-Venkata-Sekar and S. Andersson-Engels, *Nanoscale*, 2022, **14**, 2230–2237.
- 16 M. D. Wisser, S. Fischer, C. Siefe, A. P. Alivisatos, A. Salleo and J. A. Dionne, *Nano Letters*, 2018, **18**, 2689–2695.
- 17 D. Denkova, M. Ploschner, M. Das, L. M. Parker, X. Zheng, Y. Lu, A. Orth, N. H. Packer and J. A. Piper, *Nature Communications*, 2019, **10**, 1–12.
- 18 C. Lee, E. Z. Xu, Y. Liu, A. Teitelboim, K. Yao, A. Fernandez-Bravo, A. M. Kotulska, S. H. Nam, Y. D. Suh, A. Bednarkiewicz, B. E. Cohen, E. M. Chan and P. J. Schuck, *Nature*, 2021, **589**, 230–235.
- 19 C. Chen, L. Ding, B. Liu, Z. Du, Y. Liu, X. Di, X. Shan, C. Lin, M. Zhang, X. Xu, X. Zhong, J. Wang, L. Chang, B. Halkon, X. Chen, F. Cheng and F. Wang, *Nano Letters*, 2022, **22**, 7136–7146.
- 20 M. S. Meijer, P. A. Rojas-Gutierrez, D. Busko, I. A. Howard, F. Frenzel, C. Würth, U. Resch-Genger, B. S. Richards, A. Turshatov, J. A. Capobianco and S. Bonnet, *Physical Chemistry Chemical Physics*, 2018, **20**, 22556–22562.
- 21 P. S. May and M. Berry, *Methods and Applications in Fluorescence*, 2019, **7**, 023001–023015.
- 22 J. S. Matias, K. Komolibus, K. W. Kho, S. Konugolu-Venkata-Sekar and S. Andersson-Engels, *Nanoscale Advances*, 2023, –.
- 23 M. Kaiser, C. Würth, M. Kraft, I. Hyppänen, T. Soukka and U. Resch-Genger, *Nanoscale*, 2017, **9**, 10051–10058.
- 24 M. Mousavi, B. Thomasson, M. Li, M. Kraft, C. Würth, U. Resch-Genger and S. Andersson-Engels, *Physical Chemistry Chemical Physics*, 2017, **19**, 22016–22022.
- 25 S. K. V. Sekar, J. S. Matias, G. Dumlupinar, L. Niemitz, M. Mousavi, K. Komolibus and S. Andersson-Engels, *Opt. Express*, 2022, **30**, 16572–16584.
- 26 M. Kraft, C. Würth, E. Palo, T. Soukka and U. Resch-Genger, *Methods and Applications in Fluorescence*, 2019, **7**, 2–8.
- 27 H. Liu, C. T. Xu, D. Lindgren, H. Xie, D. Thomas, C. Gundlach and S. Andersson-Engels, *Nanoscale*, 2013, **5**, 4770–4775.

# PATENTS



## **Optical system and method**

S. Konugolu-Venkata-Sekar, S. Andersson-Engels, J. S. Matias and  
K. Komolibus.

*WIPO WO 2021/084137 A1*, (2021).



(12) INTERNATIONAL APPLICATION PUBLISHED UNDER THE PATENT COOPERATION TREATY (PCT)

(19) World Intellectual Property Organization  
International Bureau



(10) International Publication Number  
**WO 2021/084137 A1**

(43) International Publication Date  
06 May 2021 (06.05.2021)

(51) International Patent Classification:  
G01N 15/02 (2006.01) G02B 27/48 (2006.01)  
G01N 15/14 (2006.01) G01N 15/00 (2006.01)  
G01N 21/64 (2006.01) G01N 15/10 (2006.01)  
G02B 27/09 (2006.01)

(21) International Application Number:  
PCT/EP2020/080714

(22) International Filing Date:  
02 November 2020 (02.11.2020)

(25) Filing Language: English

(26) Publication Language: English

(30) Priority Data:  
1915957.3 01 November 2019 (01.11.2019) GB

(71) Applicant: UNIVERSITY COLLEGE CORK, NATIONAL UNIVERSITY OF IRELAND, CORK [IE/IE]; Western Road, Cork (IE).

(72) Inventors: KONUGOLU VENKATA SEKAR, Sanathana; Apartment 3, 2 Dean Street, Cork (IE). ANDERSSON-ENGELS, Stefan; 39 The Fastnet, Lancaster Gate, Cork (IE). MATIAS, Jean; c/o University College Cork, Western Road, Cork (IE). KOMOLIBUS, Katarzyna; c/o University College Cork, Western Road, Cork (IE).

(74) Agent: BARKER BRETTELL LLP; 100 Hagley Road, Edgbaston, Birmingham West Midlands B16 8QQ (GB).

(81) Designated States (unless otherwise indicated, for every kind of national protection available): AE, AG, AL, AM, AO, AT, AU, AZ, BA, BB, BG, BH, BN, BR, BW, BY, BZ, CA, CH, CL, CN, CO, CR, CU, CZ, DE, DJ, DK, DM, DO, DZ, EC, EE, EG, ES, FI, GB, GD, GE, GH, GM, GT, HN, HR, HU, ID, IL, IN, IR, IS, IT, JO, JP, KE, KG, KH, KN, KP, KR, KW, KZ, LA, LC, LK, LR, LS, LU, LY, MA, MD, ME, MG, MK, MN, MW, MX, MY, MZ, NA, NG, NI, NO, NZ, OM, PA, PE, PG, PH, PL, PT, QA, RO, RS, RU, RW, SA, SC, SD, SE, SG, SK, SL, ST, SV, SY, TH, TJ, TM, TN, TR, TT, TZ, UA, UG, US, UZ, VC, VN, WS, ZA, ZM, ZW.

(84) Designated States (unless otherwise indicated, for every kind of regional protection available): ARIPO (BW, GH, GM, KE, LR, LS, MW, MZ, NA, RW, SD, SL, ST, SZ, TZ, UG, ZM, ZW), Eurasian (AM, AZ, BY, KG, KZ, RU, TJ, TM), European (AL, AT, BE, BG, CH, CY, CZ, DE, DK, EE, ES, FI, FR, GB, GR, HR, HU, IE, IS, IT, LT, LU, LV, MC, MK, MT, NL, NO, PL, PT, RO, RS, SE, SI, SK, SM, TR), OAPI (BF, BJ, CF, CG, CI, CM, GA, GN, GQ, GW, KM, ML, MR, NE, SN, TD, TG).

Published:  
— with international search report (Art. 21(3))

WO 2021/084137 A1

(54) Title: OPTICAL SYSTEM AND METHOD

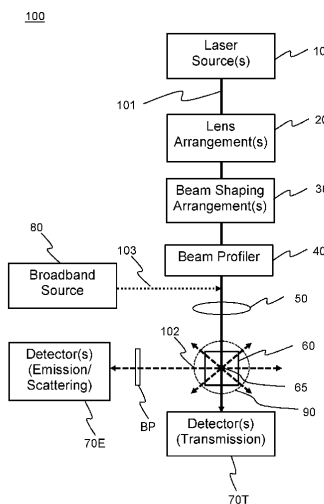


Figure 1

(57) Abstract: An apparatus and method for performing optical characterisation of luminescent particles within a sample is provided. The apparatus comprises a light source (10) configured to produce a first pump beam having a first centre wavelength and a substantially speckle-free beam profile for illuminating, along a first illumination optical path (101), a sample to thereby produce emitted light by the interaction of the first pump beam with the sample; a first detector (70E) for detecting pump-induced emitted light from a detection region (65) within the sample along a first detection optical path (102); and a first optical filter element in the first detection optical path (102) for attenuating light at the first centre wavelength. The method comprises illuminating the sample with the pump beam having the substantially speckle-free beam profile at a detection region (65) within the sample; and detecting light emitted from the detection region of the sample produced by the interaction of the pump beam with the sample.

WO 2021/084137

PCT/EP2020/080714

1

**OPTICAL SYSTEM AND METHOD**Technical Field

5 This invention relates generally to a method and apparatus for performing optical characterisation of particles such as up-converting nanoparticles.

Background to the Invention

10 Up-converting materials emit higher energy light from lower energy excitation as a consequence of sequential absorption of two or more photons. In particular, lanthanide-based up-converting nanoparticles (UCNPs) emit at several bands including visible light upon absorption of lower energy near-infrared (NIR) light. This absorption-emission process precludes background fluorescence in the detection band, while the NIR excitation reduces light scattering and attenuation and has an increased penetration depth in biological materials. This has led to significant interest in these materials for a range of biomedical applications such as bio-imaging, bio-sensing, and drug  
15 delivery where one can excite with NIR light and detect the luminescence at the up-converted band(s). A key challenge, particularly in deep tissue applications where low excitation power densities are required, is the relatively low efficiency of the up-converting process which means you don't get much light out (luminescence) for the light you put in. This efficiency is characterised by the quantum yield (QY),  $\phi$ , which is defined as the ratio of the number of photons emitted to the number of photons absorbed, which is typically in the range of a few percent for UCNPs.  
20

Increasing the QY of up-converting materials such as UCNPs is the subject of intense ongoing research. Also, the QY of the up-converting material must be accurately known or characterised in order to characterise other properties of the sample based on the measured luminescence, such as quantifying the concentration of particles. Accurate objective and standardised methods of measuring the QY are therefore essential. In addition, as up-conversion is a non-linear optical process, the non-linear power dependence of the up-conversion process and thus luminescence and QY should be taken into account in any quantitative analysis. For example, it is not sufficient measure the QY at a single  
25 excitation power, rather, accurate characterisation over a range of power densities is required.

Experimentally, measurements of QY typically involve laser excitation of the sample (typically  
30 a cuvette filled with a liquid containing the UCNPs) at the absorption band of the UCNPs, measuring the luminescence intensity at detector such as a spectrometer or avalanche photodiode (APD) and estimating the number of absorbed photons from the excitation power and absorbance of the UCNPs at the laser wavelength (which may be known or determined through absorption measurements). In practice, the measurement of QY is a complex procedure because there are various experimental factors  
35 that can effect or distort the measured QY value and which should be taken into account or compensated for to yield accurate QY measurements. These factors include, but are not limited to: transmission loss through the limited band width of optical filters used that introduce error to the luminescence signal; and contributions from particle scattering in absorption measurements that effect the determination of absorbance, and the inner filter effect of the sample that distort the estimated  
40 number of absorbed photons. In addition, recent work of M. Mousavi *et al.* in Phys. Chem. Chem. Phys. 19, 22016 (2017) has demonstrated the importance of considering the intensity distribution of laser

WO 2021/084137

PCT/EP2020/080714

2

beam in QY measurements of UCNPs and analysis, since a non-uniform beam profile means that UCNPs at different positions within the laser beam will experience different excitation power densities and thus yield different QY. Traditionally, integrating-sphere instruments have been used to measure absolute QY, as light emitted in all directions can be collected. An alternative approach is to use a fluorometer-based set-up in which a detector collects light emitted from a limited solid angle to measure a relative QY. This requires measurement of a reference sample (e.g. a dye) with a known QY in the same measurement set-up/geometry to calibrate the measured QY, assuming that the spatial distribution of the emission from the two samples is identical. The advantage with the fluorometer-based set-up is that the excitation beam profile can be better controlled and measured.

There is currently no complete system that can adequately characterise the QY or other optical properties of fluorophores, particularly those which exhibit a non-linear power density dependence such as UCNPs. There is a demand for a compact optical characterisation system that takes into account the non-linear optical properties of luminescent materials such as UCNPs and is capable of measuring luminescence and/or QY over a wide dynamic range of excitation power densities with a broad spectral range to cover the multiple emission bands of interest for different samples. There is also a need for standardised method or protocol for measuring QY to allow for direct comparisons between values for various samples developed by different research groups.

Aspects and embodiments of the present invention have been devised with the foregoing in mind.

#### Summary of the Invention

According to a first aspect of the invention, there is provided a method of optical characterisation of a sample. The method may be a method of characterising or measuring the quantum yield of a sample, or another property or optical property of a sample. The sample may be a liquid sample or a solid sample. The sample may be or comprise a liquid or solid scattering medium. The sample may comprise particles, such as luminescent particles, non-linear luminescent particles/material, fluorophores or upconverting nanoparticles. Where the sample is liquid, the particles may be dispersed in a liquid scattering medium such as a solvent. Where the sample is solid, the particles may be dispersed within a solid sample or scattering medium. The sample may be a biological sample and/or comprise biological media, e.g. biological tissue. The sample may be held in a sample cell or the sample may comprise the sample cell holding the sample. The method may comprise illuminating a sample with a pump beam having a first beam width, a first centre wavelength and a first excitation power density at a detection region within the sample. The pump beam may have a substantially speckle-free beam profile and/or a substantially smooth continuous intensity distribution at a detection region within the sample. The method may further comprise detecting light emitted from the detection region of the sample produced by the interaction of the pump beam with the first beam width with the sample. Detecting light emitted from the detection region of the sample produced by the interaction of the pump beam with the sample may comprise detecting/measuring the luminescence of the sample or particles within the sample.

The method may further comprise illuminating the sample with a pump beam having the (same) first centre wavelength, a second beam width and a second excitation power density at the detection

region. The method may further comprise detecting light emitted from the detection region of the sample produced by the interaction of the pump beam with the second beam width with the sample. The method may comprise detecting light emitted from the detection region of the sample produced by the interaction of the pump beam with the respective first and second beam width with the sample.

5 The method may comprise deriving (e.g. at each beam width and excitation power density) a quantum yield of particles within the sample based on the detected pump-induced emitted light by performing quantum yield analysis. The method may comprise deriving (e.g. at each beam width and excitation power density) an optical property of particles within the sample based on the detected pump-induced emitted light (luminescence). For example, the method may be used for a number of  
10 applications, including but not limited to: measuring emission/absorption rates/lifetimes of particles in the sample, flow cytometry measurements of particles within the sample, monitoring a polymerase chain reaction (PCR) in the sample, and optogenetics.

Varying the beam width at the detection region gives access to a wider dynamic range of excitation power densities for the luminescence and/or quantum yield (QY) measurement. Typically,  
15 the excitation power of a pump beam can only be varied by a certain amount, which, for a single fixed beam width, provides a single range of excitation power densities. By varying the beam width, a number of ranges of excitation power densities, which may at least partially overlap, can be provided by independently varying the excitation power at the first and second beam widths. This allows the luminescence/QY of the particles to be characterised over a wider dynamic range of excitation power  
20 densities in a single system/measurement, which is significant as the luminescence/QY is a quantity that can exhibit a non-linear dependence on the excitation power density of the pump beam, particularly in up-converting materials such as up-converting nanoparticles, or any non-linear luminescent material.

The detected emitted light may be that which is emitted along a detection optical path that intersects the pump beam within the sample/sample cell at the detection region. The method may  
25 further comprise filtering out (scattered) light at the first centre wavelength or scattered light produced by the interaction of the pump beam with the sample along the detection optical path.

The respective pump beam may be produced by a light source. The light source may be or comprise a laser. The method may further comprise shaping the pump beam (having the respective first and/or second beam width) to have a substantially speckle-free beam profile and/or a substantially  
30 smooth continuous profile or intensity distribution at the detection region. Shaping the pump beam (having the respective first and/or second beam width) to have a substantially speckle-free beam profile may comprise passing the respective pump beam through a single mode optical fiber; and/or using a single mode laser as a light source producing the respective pump beam; and/or spatially filtering the respective pump beam. The method may comprise illuminating the sample with a pump beam (having  
35 the respective first and/or second beam width) having a substantially speckle-free beam profile and/or a substantially smooth continuous profile.

Speckle in the pump beam means that the power density varies in a substantially random non-uniform and uncontrolled manner across the beam profile or width at the detection region. This makes it difficult to accurately quantify or quantitatively analyse the luminescence or QY, particularly where  
40 the sample is or comprises a non-linear luminescent material such as up-converting nanoparticles. The QY is defined as the ratio of the number of emitted photons to the number of absorbed photons. The

WO 2021/084137

PCT/EP2020/080714

4

detected emitted light is proportional to the number of emitted photons. Accurate determination of the number of absorbed photons requires accurate knowledge of the excitation power density. Speckle in the pump beam leads to uncertainty in the true excitation power density at the detection region and thus inaccuracy in the QY measurement. It is then difficult to compensate for such beam profile induced distortions to the measured luminescence and QY. Speckle, by its random nature also makes it difficult to compare otherwise like-for-like measurements on samples performed using different apparatuses. By using a substantially speckle-free pump beam and/or shaping the beam to have a substantially speckle-free and/or smooth profile, the sample is excited in a more quantifiable way, fewer compensations are needed and thereby more accurate analysis of the luminescence and measurements of the QY can be made. Further, a speckle-free and substantially smooth beam profile means that any beam profile-induced distortion to the luminescence/QY value can be more easily and accurately compensated, leading to more accurate analysis of the luminescence and measurements of the QY.

The pump beam (having the respective first and/or second beam width at the detection region) may further have a uniform intensity distribution at the detection region. The method may further comprise shaping the pump beam (having the respective first and/or second beam width) to have a substantially uniform intensity distribution or beam profile at the detection region. This may comprise using one or more lenses in an illumination optical path between a light source producing the respective pump beam and the sample. Using a uniform profile pump beam means that all particles in the sample across the detection region are excited with the same intensity. This further provides for accurate quantitative analysis of the luminescence signal and measurements of the QY, particularly in materials which exhibit non-linear luminescence.

The pump beam having the respective first and second beam width may be produced by the same light source or a different light source. Where the pump beam with the respective first and second beam width is produced by the same light source, the step of illuminating the sample with a pump beam having the first centre wavelength, a second beam width and a second excitation power density at the detection region may comprise: adjusting the pump beam to have a second beam width and a second excitation power density at the detection region, and illuminating the sample with the (adjusted) pump beam at the second beam width and second excitation power density.

Adjusting the pump beam to have a second beam width may comprise adjusting and/or changing a lens arrangement in an illumination optical path between a light source producing the pump beam and the sample cell. The lens arrangement may comprise one or more lenses configured to provide a collimated beam of adjustable width. Adjusting and/or changing the lens arrangement may comprise (selectively) moving at least one of the one or more lenses into or out of the illumination optical path; and/or (selectively) directing the pump beam so as to pass through or bypass at least one of the one or more lenses.

The lens arrangement may comprise a focusing lens and a collimating lens. The focusing lens and the collimating lens may have a different focal length. The lens arrangement may comprise, in order, a first collimating lens, a focusing lens and a second collimating lens. The focusing lens and the second collimating lens may have a different focal length. Adjusting and/or changing the lens arrangement may comprise moving the focusing lens and the second collimating lens into or out of the

illumination optical path; and/or directing the pump beam so as to pass through or bypass the focusing lens and the second collimating lens.

The method may further comprise: varying the excitation power density of the pump beam having the first beam width at the detection region, and illuminating the sample with the respective pump beam at a plurality of excitation power densities. The method may comprise: varying the excitation power density of the pump beam having the second beam width at the detection region, and illuminating the sample with the respective pump beam at a plurality of excitation power densities. The method may comprise detecting, at each excitation power density, emitted light from the detection region of the sample (e.g. along the first detection optical path).

Varying the excitation power density of the pump beam with the respective first and/or second beam width may comprise adjusting an optical power output of a light source producing the respective pump beam; and/or attenuating the respective pump beam. Attenuating the respective pump beam may comprise adding, removing, changing and/or adjusting one or more optical density filter elements to/from/in an illumination optical path between a light source producing the respective pump beam and the sample. The one or more optical density filter elements may attenuate the respective pump beam by a fixed or variable amount. The one or more optical density filter elements may be or comprise a neutral density filter.

Detecting pump-induced emitted light from the detection region of the sample may comprise measuring a luminescence of particles within the sample and/or measuring the intensity of the detected pump-induced emitted light. The luminescence may be proportional to the intensity of detected pump-induced emitted light.

Detecting pump-induced emitted light from the detection region of the sample may comprise detecting light emitted along a detection optical path. The detection optical path may be co-linear or non-co-linear with the illumination optical path or incident pump beam. The detection optical path may be in a reflection, transmission or side-emission (i.e. at an angle to the incident pump beam) geometry.

The method may further comprise measuring an emission spectrum of the detected pump-induced emitted light. The emission spectrum may be the emission spectrum of the particles within the sample. The detected pump-induced emitted light may be the emitted light detected along the first detection optical path, and/or emitted light along a second detection optical path that intersects the pump beam within the sample/sample cell at the detection region. The quantum yield analysis may comprise compensating the detected pump-induced emitted light, or the measured luminescence or intensity of the detected pump-induced emitted light, for a limited transmission bandwidth of one or more optical elements in a (e.g. the first) detection optical path based on the measured emission spectrum.

The pump beam may be substantially monochromatic. The method may further comprise illuminating the sample with a (separate) broadband light beam having a broad spectral content. The broadband light beam may be produced by a broadband light source. The method may comprise detecting the light transmitted through the sample to derive an absorption spectrum of the sample. The quantum yield may be derived based on the detected pump-induced emitted light and the derived absorption spectrum, optionally or preferably, the component of the derived absorption spectrum at the centre wavelength of the pump beam. Detecting light transmitted through the sample may comprise

WO 2021/084137

PCT/EP2020/080714

6

measuring a transmission spectrum of the sample. The method may further comprise illuminating an empty sample cell with the broadband light beam and detecting the light transmitted through the empty sample cell to measure a transmission spectrum of the empty sample cell. The method may comprise deriving an absorption spectrum of the sample based on the transmission spectrum of the sample and the empty sample cell. Where the sample comprises particles dispersed in a solvent, the method may comprise illuminating a reference solvent sample (e.g. held in a separate sample cell) with the broadband light beam and detecting the light transmitted through the reference solvent sample to measure a transmission spectrum of the reference solvent sample. The method may comprise deriving an absorption spectrum of the reference solvent sample based on the transmission spectrum of the reference solvent sample and the empty sample cell. The method may comprise deriving an absorption spectrum of the particles based on the absorption spectrum of the sample and empty sample cell and the reference solvent sample, e.g. subtracting the absorption spectrum of the reference solvent sample from the absorption spectrum of the sample.

The method may comprise illuminating the sample, the empty sample cell and/or the reference solvent sample with the broadband light beam and detecting the light transmitted therethrough substantially simultaneously. The method may comprise detecting the light transmitted through each of the sample, the empty sample cell and/or the reference solvent sample using a separate detector or the same detector. The method may comprise splitting the broadband light beam into multiple secondary broadband beams for illuminating the sample, reference solvent sample and/or the empty sample cell. Where the same detector is used for measuring the transmission spectrum of the sample and reference solvent sample, the method may comprise modulating at least one of the secondary broadband light beams at a frequency and deriving an absorption spectrum of the particle based on the modulated detector output.

Measuring samples and/or the empty sample cell and/or the reference solvent sample simultaneously speeds up the measurement sequence thereby reducing the chances of errors due to any changes in experimental conditions over time. By modulating one of the secondary broadband light beams and using the same detector, the detector output comprises transmission data for two or more samples which can be analysed to derive an absorption spectrum of particles in the sample faster quickly more efficiently than using separate detectors or swapping out samples in the same sample holder.

The quantum yield may be derived based on the detected pump-induced emitted light and the derived absorption spectrum, and optionally or preferably, the component of the derived absorption spectrum at the first centre wavelength of the pump beam. The quantum yield analysis may comprise compensating for or substantially removing scattering contributions in/from the derived absorption spectrum. Where the sample contains particles dispersed in a solvent, the quantum yield analysis may comprise compensating for or substantially removing contributions from the solvent in the derived absorption spectrum.

The method may further comprise imaging an intensity profile of the pump beam to determine the excitation power density and/or intensity distribution at the detection region. The quantum yield analysis may comprise compensating for a non-uniform intensity distribution at the detection region based on the measured or imaged beam profile and a rate equation describing the emission process in

WO 2021/084137

PCT/EP2020/080714

7

the sample, and/or a model describing the power density dependence of quantum yield. The model may be derived from a rate equation describing the emission process in the sample or particles within the sample.

5 The method may comprise illuminating the sample with a focused, collimated or diverging pump beam.

The method may further comprise replacing the sample (or sample cell holding the sample) with a reference sample (or reference sample cell holding a reference sample) having predetermined quantum yield characteristic and repeating any or all of the above method steps to derive, at each beam width and excitation power density, a quantum yield of particles within the reference sample. The method may comprise calibrating the derived quantum yield of particles within the sample using the derived quantum yield of particles in the reference sample and the predetermined quantum yield characteristics of the reference sample. The reference sample may be illuminated using a pump beam having a different centre wavelength.

15 According to a second aspect of the invention, there is provided a particle characterisation apparatus or system. The apparatus may be configured to perform the method of the first aspect. The apparatus may comprise a first light source configured to produce a first pump beam having a first centre wavelength for illuminating, along a first illumination optical path, a sample. The sample may be held in a sample cell. This may produce emitted light by the interaction of the first pump beam with the sample. The apparatus may further comprise a first detector for detecting pump-induced emitted light from a detection region of the sample. The first detector may detect light emitted along a first detection optical path that intersects the first illumination optical path at the detection region within the sample/sample cell. The apparatus may comprise a first optical (wavelength) filter element in the first detection optical path for attenuating light at the first centre wavelength.

25 The sample may be a substantially liquid sample or a substantially solid sample. The sample may be or comprise a liquid or solid scattering medium. The sample may comprise particles or luminescent particles, such as fluorophores or upconverting nanoparticles. The sample may comprise non-linear luminescent particles such as upconverting nanoparticles. Where the sample is liquid, the particles may be dispersed in a solvent. Where the sample is solid, the particles may be dispersed within the solid sample or scattering medium sample, e.g. the sample may be or comprise biological media such as tissue.

30 The first detection optical path may be arranged in a side emission (i.e. angled with respect to the incident pump beam), transmission or reflection geometry.

The apparatus may be used for a number of optical applications based on detection of light emitted/scattered from the sample, particular luminescence particles within the sample, including but not limited to: measuring quantum yield of particles in the sample, measuring emission/absorption rates/lifetimes of particles in the sample, flow cytometry measurements of particles within the sample, monitoring a polymerase chain reaction (PCR) in the sample, and optogenetics.

The apparatus may comprise a first lens arrangement in the first illumination optical path configured to adjust the first pump beam to have a first beam width or a second beam width at the detection region.

40 It will be appreciated the advantages set out with respect to the first aspect apply equally to the apparatus of the second aspect.

WO 2021/084137

PCT/EP2020/080714

8

The apparatus may be configured illuminate the sample with a focused, collimated or diverging pump beam. The apparatus may further comprise a first focusing lens in the first illumination optical path for focussing the first pump beam (to a point) within the sample/sample cell. The first light source may be configured to produce a first pump beam with a substantially speckle-free beam profile and/or a substantially smooth continuous intensity distribution at the detection region. The first light source may comprise a single mode fiber coupled to the output of a laser. Alternatively or additionally, the first light source may be or comprise a single mode laser.

The first detector may be configured to measure the luminescence intensity of the detected pump-induced emitted light. Additionally or alternatively, the first detector may be configured to measure the emission spectrum of the detected pump-induced emitted light. The first detector may be or comprise a spectrometer or a photodetector, such as photodiode or an avalanche photodiode.

The first lens arrangement may be or comprise one or more lenses configured to provide a collimated beam of adjustable width. The first lens arrangement may be or comprise one or more lenses configured to provide a collimated beam of adjustable width impinging on the first focussing lens. At least one of the one or more lenses may be moveable and/or removable to provide the collimated beam of adjustable width. Alternatively or additionally, the first lens arrangement may comprise a plurality of mirrors arranged to selectively direct the first pump beam so as to pass through or bypass at least one of the one or more lenses to provide the collimated beam of adjustable width.

The first lens arrangement may be or comprise a focusing lens and a collimating lens. The focusing lens and the collimating lens may have a different focal length. The lens arrangement may comprise, in order, a first collimating lens, a focusing lens and a second collimating lens. The focusing lens and the second collimating lens may have a different focal length. The focussing lens and the second collimating lens (or collimating lens) may be moveable into and out of the first illumination optical path to provide the collimated beam of adjustable width. Alternatively or additionally, the first lens arrangement may comprise a plurality of mirrors arranged to selectively direct the first pump beam so as to pass through or bypass the focussing lens and the second collimating lens to provide the collimated beam of adjustable width.

The first pump beam may be a single mode beam with a Gaussian beam profile. The apparatus may further comprise a first beam shaping arrangement in the illumination optical path configured to transform the first pump beam to have a substantially uniform spatial intensity distribution at the detection region. The first beam shaping arrangement may be or comprise one or more lenses, and optionally a diffraction element, to transform the beam profile using truncation, refraction and/or diffraction. The beam shaping arrangement may comprise an aperture for truncating the first pump beam. The beam shaping arrangement may comprise a pair of lenses arranged in a 4f configuration with respect to the aperture for compensating for diffraction of the beam resulting from the truncation at the aperture. The beam shaping arrangement may comprise one or more beam shaping lens configured to transform a substantially Gaussian input beam profile to a substantially uniform beam profile at the detection region.

The apparatus may further comprise a means for varying, at the first and/or second beam width, the excitation power or power density of the first pump beam at the detection region. The means for varying the excitation power density of the first/second pump beam at the detection region may

comprise an adjustable power controller of the first light source; and/or one or more optical filter elements in the first illumination optical path configured to attenuate the first/second pump beam by a fixed or variable amount.

5 The first lens arrangement and/or the means for varying, at the first and/or second beam width, the excitation power density of the first pump beam at the detection region may be configured to provide a dynamic range of excitation power densities at the detection region of up to  $10^4$ ,  $10^5$ ,  $10^6$ ,  $10^7$  or  $10^8$ .

10 The apparatus may further comprise a beam profiler in the first illumination optical path for measuring a two-dimensional spatial intensity distribution of the first pump beam at a location equivalent to the detection region. The beam profiler may be positioned between the first focusing lens and the sample/detection region. The beam profiler may be or comprise a beam-splitter that directs a percentage of the first pump beam towards a two-dimensional imaging detector.

15 The apparatus may further comprise a second light source for producing a second pump beam having a second centre wavelength for illuminating, along a second illumination optical path, a sample to thereby produce emitted light by the interaction of the second pump beam with the sample. The sample may be a reference sample (e.g. held in a reference sample cell). Alternatively, the first light source may be configured to produce the first pump beam and the second pump beam.

20 The second illumination optical path may join the first illumination optical path. The second illumination optical path may join the first illumination optical path before the first focussing lens (between the first light source and the first focusing lens) such that the first focussing lens focusses the second pump beam within the reference sample cell; or before the first lens arrangement (between the first light source and the first lens arrangement); or (where present) before the first single mode fiber (between the first light source and the first single mode fiber).

25 Alternatively, the second illumination optical path may join the first illumination optical path after the first focusing lens (in the direction of propagation of the pump beam), or between the first focusing lens and the sample. Where the beam profiler is present, the second illumination optical path may join the first illumination optical path between the first focusing lens and the beam profiler. In this case, the apparatus may further comprise a second focussing lens for focussing the second pump beam within the sample cell. The apparatus may further comprise a second lens arrangement in the second illumination optical path substantially identical to the first lens arrangement for adjusting the second pump beam to have a first beam width or a second beam width at the detection region. The second light source may be configured to produce a second pump beam with a substantially speckle-free beam profile. The second light source may comprise a single mode fiber coupled to the output of a laser. Alternatively or additionally, the second light source may be or comprise a single mode laser.

30  
35 The first detector may be configurable to measure an emission spectrum of pump-induced emitted light from the sample. Alternatively or additionally, the apparatus may comprise a second detector for detecting the emission spectrum of pump-induced emitted light from the sample. The second detector may be configured to detect the spectrum of light emitted along a second detection optical path. The second detection optical path may intersect or join the first illumination optical path  
40 at the detection region.

WO 2021/084137

PCT/EP2020/080714

10

The first and/or second light source may be or comprise a laser. The apparatus may further comprise a broadband light source for producing a broadband light beam having a broad spectral content for illuminating, along a third illumination optical path, the sample for measuring an transmission spectrum of the sample. The third illumination optical path may join the first or second illumination optical path. The apparatus may be configurable such that the light transmitted through the sample is detectable by the first or second detector. Alternatively, the apparatus may comprise a third detector for detecting light transmitted through the sample.

The apparatus may comprise a means to modulate the first and/or second pump beam and/or broadband light beam. The means may comprise one or more optical choppers.

The apparatus may be configured to measure the transmission spectra of multiple different samples simultaneously. The apparatus may be configured to split the broadband light beam into multiple secondary beams directed to the multiple samples. Light transmitted through the multiple samples may be detected by the same or different detectors. Where the same detector (e.g. the first, second or third detector) is used to measure the transmission of multiple samples, one of the secondary broadband light beams may be modulated. This may allow transmission spectra from multiple samples to be measured using the same detector output.

The apparatus may be configured to measure/detect pump-induced light emission from the sample in more than one direction, e.g. simultaneously. The apparatus may be configured to measure pump-induced light emitted from the sample in the forward direction (e.g. in the transmission geometry) with respect to the incident pump beam, in addition to detecting light emitted at an angle to the incident pump beam. The third detector may be configured for detecting pump-induced emitted light from a detection region of the sample in the forward direction. The third detector may detect light emitted along a third/transmission detection optical path that intersects the first illumination optical path at the detection region within the sample/sample cell. The third detector may be configured to measure the luminescence intensity of the detected pump-induced emitted light. The third detector may be or comprise a spectrometer or a photodetector, such as photodiode or an avalanche photodiode. The first or second detector may be arranged and/or used to detect emission from the sample at a first (non-zero) angle to the incident pump beam along the first or second detection optical path (e.g. the angle may be substantially 90 degrees or in the range between substantially 45 to 135 degrees), and the third detector may be arranged and/or used to detect emission from the sample at a second angle that is different to the first angle. The second angle may be approximately 0 degrees i.e. the forward direction or transmission geometry. Alternatively, the first or second detector may be arranged and/or used to detect the emission at both the first and second angles, e.g. simultaneously. In this case, the third detection optical path may join the first/second optical detection path. The apparatus may comprise a means to modulate the light emitted along the first/second and/or third optical detection path, so as to enable separation of the emission signals. The means to modulate the light may be configured to permit light from only one detection optical path to impinge on, or be detected by, the first/second detector at any one time. The means may comprise one or more optical choppers, e.g. positioned in the first/second and/or third detection optical path(s). Using the same detector for detecting multiple signals removes relative errors originating from any different detector sensitivity.

The apparatus may be configured to measure absorption of the pump beam and pump-induced emission from the sample simultaneously. The third detector may be arranged and/or used/configured to detect light transmitted through the sample along the third detection optical detection path, and the first/second detector may be arranged and/or used/configured to detect emission from the sample along the first/second detection optical path(s). Alternatively, the first or second detector may be arranged and/or used to detect the transmitted light and the light emitted from the sample at the first angle, e.g. simultaneously. This allows QY to be determined at the pump wavelength using the same detector 70E, avoiding relative errors in the absorption and emission measurements originating any difference or drift in detectors sensitivity.

In this case, the third detection optical path may join the first/second optical detection path. The third detection optical path may comprise an optical filter to attenuate light emitted from the sample in the forward direction. The optical filter may also attenuate transmitted pump light. The optical filter may comprise a band pass filter and/or a neutral density filter. The apparatus may comprise a means to modulate the light emitted along the first/second and/or third optical detection path, so as to enable separation of the transmission and emission signals. The means to modulate the light may be configured to permit light from only one detection optical path to impinge on, or be detected by, the first/second detector at any one time. The means may comprise one or more optical choppers, e.g. positioned in the first/second and/or third detection optical path(s).

The apparatus may comprise an integrating sphere for holding the sample. The integrating sphere may comprise an excitation port for receiving the first or second pump beam and one or more detection ports for coupling to the first and/or second detector. The integrating sphere may be configured to collect light emitted from the sample in all directions.

The apparatus may be a quantum yield measurement apparatus. The apparatus may be operable to perform a quantum yield measurement of particles within the sample based on an output of the first detector.

The apparatus may be connectable to a processing device for performing a quantum yield measurement of particles within the sample based on an output from the first detector. The apparatus may comprise a processing device for receiving an output signal from the first and/or second detector and/or beam profiler, and deriving a quantum yield of particles within the sample based on the output from the first and/or second detector and/or beam profiler.

The apparatus may be operable for use in a range of optical applications based on detection of light emitted from luminescent particles, including but not limited to: optogenetics, flow cytometry, monitoring a polymerase chain reaction (PCR) within the sample.

The apparatus may further be operable to perform a dynamic light scattering measurement of particles within the sample based an output of the first detector.

Features which are described in the context of separate aspects and embodiments of the invention may be used together and/or be interchangeable. Similarly, where features are, for brevity, described in the context of a single embodiment, these may also be provided separately or in any suitable sub-combination. Features described in connection with the apparatus may have corresponding features definable with respect to the method(s), and vice versa, and these embodiments are specifically envisaged.

Brief Description of Drawings

In order that the invention can be well understood, embodiments will now be discussed by way of example only with reference to the accompanying drawings, in which:

- 5 **Figure 1** shows a block diagram of an apparatus according to the invention;  
**Figure 2** shows an example layout of an apparatus according to the invention in a first configuration;  
**Figure 3** shows the apparatus of figure 2 in a second configuration;  
**Figure 4** shows another example layout of an apparatus according to the invention in a first configuration;  
10 **Figure 5** shows another example layout of an apparatus according to the invention in a first configuration;  
**Figure 6** illustrates a beam shaping operation;  
**Figure 7** shows an example an example beam shaping arrangement;  
**Figures 8a-8d** show, respectively, an absorbance spectrum, a luminescence versus absorbed power curve, a luminescence spectrum, and a speckle-free beam profile obtain using the apparatus of figure 2;  
15 **Figure 9a and 9b** shows example emission spectra of a sample and reference sample suffering transmission loss through a band pass filter;  
**Figures 10a and 10b** show a method of measuring quantum yield according to the invention;  
**Figures 11a-e** show experimentally determined quantum yield curves obtained using the apparatus and methods of the invention;  
20 **Figures 12a-12e** show experimentally determined quantum yield curves obtained under different experimental conditions;  
**Figure 13** shows another example layout of the apparatus for measuring multiple samples;  
**Figure 14** shows an energy level diagram for a rare earth up-converting material system;  
25 **Figures 15a and 15b** show, respectively, experimental measurements of rise and decay lifetimes of the system of figure 14;  
**Figure 16** shows another example layout of the apparatus for measuring luminescence in reflection geometry; and  
**Figure 17** shows another example layout of the apparatus for measuring luminescence in transmission geometry.  
30

It should be noted that the figures are diagrammatic and may not be drawn to scale. Relative dimensions and proportions of parts of these figures may have been shown exaggerated or reduced in size, for the sake of clarity and convenience in the drawings. The same reference signs are generally used to refer to corresponding or similar features in modified and/or different embodiments.

35

Detailed Description

- For most practical applications of luminescent particles such as up-converting nanoparticles (UCNPs), a sample comprising the luminescent particles is excited and the luminescence is measured and quantitatively analysed to determine or derive one or more characteristics of the sample. This typically requires accurate knowledge or characterisation of the QY of the particles, which is particularly challenging with non-linear particles such as UCNPs which requires both characterisation

over a wide dynamic range of excitation powers and careful consideration of the beam profile. The invention provides a solution to this, and as such the apparatus 100 is initially described below in the context of QY measurements. However, the invention is not limited to QY measurements, but is applicable generally to luminescence measurements of luminescent particles.

5 Figure 1 shows a generalised block diagram of an apparatus 100 for characterising/measuring the luminescence and/or quantum yield (QY) of particles, such as fluorophores and up-converting nanoparticles (UCNPs) dispersed within a sample. In particular, the apparatus 100 is configured for performing accurate measurements of luminescence and/or QY over a wide dynamic range of excitation power densities that can be obtained quickly, to minimise errors due to any changing experimental  
10 conditions with time. The apparatus 100 is particularly well suited for optical measurements on non-linear luminescent particles such as UCNPs which exhibit a non-linear dependence of the luminescence and QY on excitation power density, particularly at low excitation levels applicable for many biomedical applications.

The sample can be a liquid sample or liquid scattering medium with particles dispersed within  
15 the sample. This is typically the case when characterising QY of particles. However, it will be appreciated, that in certain applications, the sample can be a non-liquid or substantially solid sample or scattering medium with particles dispersed therein, e.g. biological tissue.

The apparatus 100 comprises one or more light sources 10 for producing one or more pump beams for illuminating, along an illumination optical path 101 (indicated by the solid arrow in figure  
20 1), a sample or a sample held in a sample cell 60 to thereby produce emitted light by the interaction of the pump beam with the sample. The or each light source 10 is a laser that emits substantially monochromatic light at a centre wavelength  $\lambda_{\text{pump}}$  appropriate for the sample being measured. Where there is more than one light source 10, one or more or each light source 10 may be used to illuminate the same sample, for example to excite different absorption bands of the sample, or different samples,  
25 e.g. with different types of particles dispersed therein. In the latter case, one of the different samples may be a reference sample, such as a dye, having known properties, such as a known QY value used to calibrate the QY measurement of the other sample(s), as explained in more detail below.

A focusing lens 50 is provided in the illumination optical path 101 for focussing the pump beam to a focal point within the sample. The sample cell 60 is positioned in the focal plane of the  
30 focusing lens 50 such that the focal point of the focusing lens 50 is substantially in the centre/middle of the sample cell 60. A detector 70E is provided for detecting light emitted from the sample (indicated by the dashed arrows in figure 1) along a detection optical path 102 that intersects the illumination optical path at a detection region 65 within the sample cell 60 that coincides with the focal point of the focusing lens 50. The detector 70E may be configured to output a signal proportional to the amount or  
35 intensity of emitted light falling on detector 70E (luminescence). For example the detector 70E may be or comprise a photodetector such as an avalanche photodiode (APD) or camera. Alternatively or additionally, the detector 70E may be configured to output a signal containing the emission spectrum of the light falling on the detector 70E. For example the detector may be or comprise a spectrometer. Alternatively, a separate detector for measuring the emission spectra of light emitted along a separate  
40 detection optical path can be provided (e.g. see figure 2). One or more optical filter elements BP, such as a band pass filter, are provided in the detection optical path 102 to attenuate any scattered pump

WO 2021/084137

PCT/EP2020/080714

14

beam light while transmitting the emitted light to the detector 70E. The detector 70E and detection optical path 102 may be arranged and configured to collect and detect light emitted from a limited solid angle defined by the numerical aperture of a collimating/collecting lens, as in a conventional fluorometer-type set up, in which case measurements of a reference sample with a known QY value can be used to calibrate the measured QY yield of the sample. Alternatively, the apparatus 100 may comprise an integrating sphere 90 in which the sample cell 60 can be placed for collecting and detecting light emitted in all directions (a  $4\pi$  solid angle) and measuring an absolute QY value of the sample, as is known in the art. In this case, the integrating sphere 90 comprises an illumination port for receiving the pump beam (e.g. at the intersection of the dotted circle and the solid arrow in figure 1) and one or more detection ports at a or various locations around the sphere 90 (e.g. at the intersection of the dotted circle and the dashed arrows in figure 1) for coupling the emitted light to the detector 70E.

The apparatus 100 also comprises a broadband light source 80 for producing a broadband light beam having a broad spectral content for illuminating, along a third illumination optical path 103, the sample to thereby produce emitted light by the interaction of the broadband light beam with the sample for measuring an absorption spectrum of the sample. Another detector 70T, which is a spectrometer, is provided for detecting the spectrum of light transmitted through the sample to derive an absorption spectrum from which the absorbance of the sample at the pump wavelength  $\mu(\lambda_{\text{pump}})$  can be determined.

In an embodiment, the or each light source 10 is configured to produce a substantially speckle-free and smooth beam profile. This is achieved by using a single mode laser, and/or by coupling the laser output to a single mode optical fiber. Both cases produce a speckle-free pump beam with an approximately Gaussian beam profile. Use of a speckle-free pump beam means that the beam profile varies in a predicable way allowing for the effects of beam-profile non-uniformity to be compensated or mitigated (see below) thereby allowing for more accurate QY measurements to be made, as will be described in more detail below.

The beam width or spot size produced by the focusing lens 50 is dependent on the center wavelength of the pump beam  $\lambda_{\text{pump}}$ , the focal length of the lens 50 and the width of the pump beam impinging on the focusing lens 50. The apparatus 100 further comprises a lens arrangement 20 in the illumination optical path 101 configured to adjust the beam width or spot size of the pump beam at the detection region 65 (whilst preserving the speckle-free beam profile). In an embodiment, the lens arrangement 20 comprises one or more lenses configured to provide a collimated beam of adjustable width impinging on the focussing lens 50, as will be described in more detail below with reference to figures 2-5.

In known QY measurement apparatuses, the excitation power density is varied over a certain limited range by attenuating the pump beam and/or adjusting the power output of the laser. By varying the beam width at the detection region, the pump beam power can be independently varied using known means at each beam width to extend the range of excitation power densities over which QY measurements can be made in the apparatus. Each beam width effectively generates a separate QY versus power density curve of set of QY data which can be combined to provide a QY curve with extended dynamic range of power densities. The different beam widths can be chosen such that the

separate QY curves at least partially overlap in power density to produce a substantially continuous QY curve.

The apparatus 100 further comprises a beam profiler 40 in the illumination optical path for imaging the profile of the pump beam at a location equivalent to the detection region 65. The output of the beam profiler 40 provides imaging data that can be used to determine the beam width and/or intensity profile/distribution of the pump beam at the detection region 65. Additionally, the imaging data may be used to compensate the QY value for the effects of non-uniformity in the intensity distribution at the detection region (as would be the case for a Gaussian beam profile), as will be described in more detail below.

Alternatively or additionally, the apparatus 100 may further comprise a beam shaping arrangement 30 in the illumination optical path 101 to transform a non-uniform beam profile of the pump beam, e.g. Gaussian, to a substantially uniform beam profile. Such beam shaping is commonly employed in laser machining applications, and can be achieved using several known techniques, e.g. involving truncation of the pump beam or re-distribution of the pump beam intensity (e.g. using diffraction or refraction). For example, the pump beam can be truncated using an aperture to leave only the central substantially or near uniform/flat part of the beam, or specifically designed (commercially available) beam shaping lenses can be used. The latter typically requires a speckle-free Gaussian input beam. The provision of a substantially speckle-free and substantially uniform beam profile minimises beam profile-induced distortions to the QY value and therefore leads to more accurate QY measurements.

The apparatus 100 will now be described in more detail with reference to figures 2-5. Figure 2 shows an example layout of the apparatus 100. The apparatus 100 comprises a first light source 10A for producing a first pump beam 110 with a first pump wavelength  $\lambda_{\text{pump1}}$  and a second light source 10B for producing a second pump beam 120 with a second pump wavelength  $\lambda_{\text{pump2}}$ . The first and second light sources 10A, 10B each comprise a single mode fibre coupled to the output of a diode laser (not shown) to produce a substantially speckle-free pump beam 110, 120. The lasers are driven by a power controller (not shown) for varying the current through the diode lasers and their output power. A first illumination optical path 101 receives the first pump beam 110 and comprises a focusing lens 50 (also labelled L4 in figure 2) that focuses the first pump beam 110 to a detection region 65 within a sample held within a sample cell 60. A second illumination optical path 101' receives the second pump beam 120 and comprises a focusing lens 50' (also labelled L4' in figure 2) that focuses the second pump beam 120 to the detection region 65. The sample cell 60 may be a standard cuvette held in a sample/cuvette holder (not shown), as is known in the art. The sample comprises particles, such as fluorophores or UCNPs, dispersed in a solvent.

The second illumination optical path 101' is essentially a replica of the first illumination optical path 101. In this example, the two focusing lens 50, 50' are substantially identical and have the same focal length. The second illumination optical path 101' joins the first illumination optical path 101 at a position after the focusing lens 50 (i.e. in the direction of propagation of the first pump beam 110) at a first moveable mirror FM1 (and via a mirror M1) which can be selectively moved into and out of the second illumination optical path 101' to selectively direct the second pump beam 120 to the

detection region 65. (N.B. mirror M1 can be omitted if the second light source 10B is arranged such that the second pump beam crosses the first illumination optical path 101.)

A first lens arrangement 20 is provided in the first illumination optical path 101 for providing a collimated beam of adjustable width impinging on the focusing lens L4. This varies the beam width at the detection region 65. The first lens arrangement 20 comprises, in order, a first collimating lens L1, a focusing lens L2 and a second collimating lens L3. The focusing lens L2 is arranged to focus the collimated first pump beam 110 to a point between lenses L2 and L3, and the collimating lens L3 is arranged to re-collimate the diverging pump beam, as shown. The focal length,  $f_2$ , of the lens L2 is different to the focal length,  $f_3$ , of lens L3 (in this case with  $f_3 < f_2$ ) resulting in a collimated first pump beam 110 exiting lens L3 which has a different width (in this example, narrower) to the collimated first pump beam 110 impinging on lens L2. For this purpose, lens L3 is positioned at a distance  $f_2+f_3$  from lens L2. The second illumination optical path 101' comprises a second lens arrangement 20' substantially identical to the first lens arrangement 20. The second lens arrangement 20' comprises lens L1', L2', L3' which are substantially identical to lenses L1-L3.

Two different beam widths at the detection region 65 can be achieved by either including or not including lenses L2 (L2') and L3 (L3') in the first (second) illumination optical path 101 (101'). Figure 2 shows the apparatus 100 in a first configuration where the first (second) illumination optical path 101 (101') includes lenses L2 and L3 (L2' and L3') to produce a first beam width W1 at the detection region 65. Figure 3 shows the same apparatus 100 in a second configuration where the first (second) illumination optical path 101 (101') does not include lenses L2 and L3 (L2' and L3') to produce a second beam width W2 at the detection region 65.

For a given pump power, varying the beam width between W1 and W2 provides a different power density at the detection region. The first and second illumination optical paths 101, 101' further comprise one or more optical density filters ND, ND' to attenuate the pump power by a fixed or variable amount and adjust the excitation power density at the detection region 65. The filters ND, ND' may be movable into and out of the first and second illumination optical path 101, 101' to selectively attenuate the first and second pump beam 110, 120. The optical density filters ND, ND' may be or comprise a neutral density filter with a fixed or variable (e.g. a filter wheel) optical density, or a set of neutral density filters with different optical densities. For each beam width W1, W2 and optical density filter setting, the output power of the diode lasers can then be varied over a certain range using the power controllers. The combination of QY measurements taken at different beam widths W1, W2, optical density filter settings and laser output powers provides access to wide dynamic range of power densities of up to  $10^4$ ,  $10^5$  or  $10^6$ .

A first detection optical path 102 is provided for measuring the pump-induced luminescence (emission) signal of the sample. The first detection optical path 102 receives light emitted from particles dispersed within the sample. The intersection of the first illumination optical path 101 and the first detection optical path 102 defines the detection region 65. The first detection optical path 102 comprises a collimating lens L5 for collecting light emitted from the sample along the first detection optical path 102 and a focusing lens L8 for focusing the collected emitted light onto a detector 70E. In this example, the detector 70E is an APD configured to output a detector signal proportional to the intensity of detected emitted light. A first optical wavelength filter BP1 is positioned in the first

detection optical path 102 to filter/attenuate any scattered pump light and transmit the emitted light from the sample. The first optical wavelength filter BP1 may be a band pass filter, a long pass filter, or short pass filter (or a combination of multiple optical wavelength filters), depending on the sample being measured and the emission spectrum. Optionally, a spatial filter arrangement comprising, in order, a focusing lens L6, an aperture or slit A1 and a collimating lens L7 may be positioned between lenses L5 and L8 to focus emitted light through the aperture A1 to suppress any light originating from volumes in the sample other than the detection region 65.

A pair of linear polarisers P1 and P2 may be used to make the detected emitted light substantially independent of any anisotropy in the sample. For this purpose, a first linear polariser P1 (P1') is positioned in the first (second) illumination optical path 101 (101') at a given orientation, e.g. to vertically polarise the first (second) pump beam 110 (120), and a second linear polariser P2 is positioned in the first detection optical path 102 oriented at a magic angle of 54.7 degrees with respect to the first polariser P1. The first polariser P1 is preferably positioned in an expanded portion of first (second) pump beam 110 (120) as shown in figures 2 to 5, to prevent any damage of the polariser P1 due to the power density of the first (second) pump beam 110 (120).

A beam profiler 40 comprising a beam splitter BS and an imaging detector or camera 40D is positioned in the first illumination optical path 101 for imaging the beam profile of the first or second pump beams 110, 120 at the detection region 65. The beam splitter BS is positioned after (in the direction of propagation of the first/second pump beam 110, 120) the focusing lenses 50 and 50' and directs a small fraction of the first or second pump beam 110, 120 towards to the imaging detector 40D, which is positioned at the focal point of the focusing lenses 50 and 50'. In an embodiment, the imaging detector 40D is a high resolution charge coupled device (CCD) camera that outputs imaging data containing a two-dimensional image of the intensity distribution in the beam.

A second detection optical path 102' is also provided for measuring the pump-induced luminescence (emission) spectrum of the sample. Similar to the first detection optical path 102, the second detection optical path comprises a collimating lens L9 for collecting light emitted from the sample along the second detection optical path 102' and a focusing lens L10 for focusing the collected emitted light onto a detector 70E1, but in this case, detector 70E1 comprises a spectrometer that outputs a detector signal containing the spectrum of detected light. A second optical wavelength filter BP2 is also positioned in the second detection optical path 102' to filter/attenuate any scattered pump light and transmit the emitted light from the sample.

The first and second detection optical paths 102, 102' are oriented at an angle of substantially 90 degrees to the direction of the first and second pump beam 110, 120 through the sample cell to reduce the amount of pump light reaching the detectors 70E, 70E1. However, since emission from the sample is typically isotropic, the detection geometry is not limited to the geometry shown. Other detection geometries may be used to measure QY, e.g. where the first and/or second detection optical path 102, 102 is arranged to detect forwards, and backwards, upwards or downwards emission. Further, the first and second detection optical paths 102, 102' need not be at the same angle.

Another detector 70T is provided in a transmission geometry for detecting light transmitted through the sample cell 60 to derive an absorbance of the sample at each pump wavelength  $\mu(\lambda_{\text{pump1}}$  or  $\lambda_{\text{pump2}}$ ). The detector 70T can also be used to measure the power of the first or second pump beam. For

this purpose, the detector 70T may be a photodetector or calibrated power meter configured to output a detector signal proportional to the intensity of the detected transmitted light.

Alternatively or additionally, the detector 70T may comprise a spectrometer for measuring the transmission spectrum of the sample to derive an absorption spectrum  $\mu(\lambda)$ . Alternatively, the detector 5 70T can be replaced with an optical fiber or fiber bundle to collect and couple in the transmitted light and send it to the detector 70E1. In this way, the absorbance of the sample at each pump wavelength can be determined in a single shot measurement. For this purpose, a broadband light source 80 (e.g. a white light source) is provided for producing a broadband light beam 130 having a broad spectral content for measuring the broadband transmission, absorption and/or scattering spectrum of the sample. 10 A third illumination optical path 103 receives the broadband light beam 103 and comprises a collimating lens L11 for collimating the output of the broadband source 80. The third illumination optical path 103 joins the first illumination optical path 101 at a position before (in the direction of propagation of the first pump beam 110) the focusing lens 50 at a second moveable mirror FM2 which can be selectively moved into and out of the third illumination optical path 101' to selectively direct 15 the broadband light beam 130 to the detection region 65. Alternatively, the third illumination optical path 103 may join the second illumination optical path 101' at a position before (in the direction of propagation of the second pump beam 120) the focusing lens 50' by suitably positioning the second moveable mirror FM2 (not shown). An iris (not shown) can be placed in the collimated beam 130 to control the beam width and power of the broadband light beam 130 at the detection region.

20 The apparatus 100 is connectable to a processing device (not shown), e.g. comprising a data acquisition (DAC) device and one or more processors, for receiving the various output signals from detectors 70E, 70T, 70E1, 40D, controlling the laser output power and deriving, at each power density, a QY value based on the received detector data, as will be described in more detail below.

In the illustrated examples, the output of the light sources 10A, 10B is divergent by virtue of 25 the single mode fiber, and the first collimating lens L1, L1' is arranged to collimate the diverging output of the light source 10A, 10B. However, it will be appreciated that, alternatively the collimating lens L1 (L1') may be part of a beam expanding arrangement in the first (second) illumination optical path 101 (101'). Further, where a single mode laser is used instead of a laser and single mode fiber combination as the light source 10A, 10B such that the output of the light source 10A, 10B is 30 collimated, the lens L1 may be omitted altogether.

Figure 4 shows another example layout of the apparatus 100 where the second illumination optical path 101' joins the first illumination optical path 101 at a position before the focusing lens 50 via mirrors M1 and FM1. In this case, focusing lens 50' is not required - focusing lens 50 is used to focus both the first and second pump beams 110, 120 to the detection region. For example, the focusing 35 lens 50 can be an achromatic lens with a focal length that is substantially the same for the first and second pump wavelengths  $\lambda_{\text{pump1}}$ ,  $\lambda_{\text{pump2}}$ . However, it will be appreciated that the apparatus 100 can instead be configured such that the second illumination optical path 101' joins the first illumination optical path 101 at a position before the first lens arrangement 10 by suitably positioning the first moveable mirror FM1, thus also omitting the second lens arrangement 10'. Alternatively, the outputs of 40 the lasers of the first and second light sources 10A, 10B may be coupled to the same single mode fiber using a suitable fiber combiner/coupler, as is known in the art.

In the example layout of figures 2 to 4, the lenses L2 and L3 (L2' and L3') are movable, such that they can be selectively moved into and out of the first (second) illumination optical path 101 (101'). Alternatively, figure 5 shows another example layout of the apparatus 100 where the first (second) pump beam 110 (120) is selectively directed through the lenses L2 and L3 (L2' and L3') via a combination of mirrors M2 and M3 (M2' and M3') and third and fourth movable mirrors FM3 and FM4 (FM3' and FM4') which can be selectively moved into and out of the first (second) illumination optical path 101 (101'). In figure 5 the broadband light source 80 and third illumination optical path 103 have been omitted for clarity. In this way, the first (second) illumination optical path 101 (101') is effectively altered to include or bypass the lenses L2 and L3 (L2' and L3'). It will be appreciated that when movable mirrors FM3 and FM4 (FM3' and FM4') are moved out of the first (second) illumination optical path 101 (101') the collimated first (second) pump beam 110 (120) continues through to the focusing lens 50 (50') with an unaltered width similar to figure 3.

It will be appreciated that movement of the moveable optical elements, including the lenses (L2, L3, L2', L3'), the moveable mirrors (FM1, FM2, FM3, FM4, FM1', FM2', FM3', FM4') and/or the movable optical density filters ND, ND', may be manually effected/adjusted or automatically adjusted (motorised) depending on the optics mounts used. Any optics mount known in the art can be used that allows the moveable lenses and mirrors to move or be moved between a position out of the respective illumination optical path 101, 101' and a predefined position in the respective illumination optical path 101, 101' without having to re-adjust any optical elements in the apparatus 100 once set up. For example, they may be mounted on flip mounts, pivotable mounts, magnetic mounts, multi-position mounts, translation stages or fast change drop-in mechanics, any of which can be manually operated or motorised and controlled via an appropriate controller. Where the moveable optical elements are motorised, their movement may be controlled by the processing device.

The apparatus 100 may further include a beam shaping arrangement 30 comprising one or more lenses in the first and second illumination optical path for transforming the near Gaussian beam profile of the (speckle-free) first and second pump beams 110, 120 to a substantially uniform beam profile. This function is shown schematically in figure 6. Figure 7 shows an example beam shaping arrangement 30 based on beam truncation. An expanded input pump beam 110a with a Gaussian intensity profile is truncated by an aperture A2 which selects only a suitably flat or near-flat portion of the input beam 110a (typically the central part of the input beam 110a). Truncation or aperturing typically leads to diffraction effects at the edge of the truncated beam. Fourier optics is used to compensate for or removed these diffraction artefacts using a 4f-type configuration. A focusing lens L12 is positioned a distance equal to its focal length  $f_{12}$  away from the aperture A2 and focuses the truncated beam to a focal point. This is equivalent to performing a Fourier transform on the diffraction pattern of the truncated beam. A collimating lens L13 positioned a focal length  $f_{13}$  away from the focal point then collimates the diverging beam. The output truncated beam 110b observed a focal length  $f_{13}$  away from lens 13 (in the plane of the dotted line), which would be the detection region 65 of the sample cell 60, is the reconstructed shape of the aperture A2 without diffraction artefacts. An aperture A3 placed in the focal plane of lens L12 may be used to spatially filter light at the edges of the focussed beam which contain the diffraction artefacts. The above beam shaping arrangement may be placed between the

focusing lens L4, 50. Alternatively, it can be used in the place of the focusing lens L4, 50. In this case, it will be appreciated that the sample is illuminated with collimated light of varying beam width.

In another example, a beam shaping lens may be used to transform the Gaussian profile of the first or second pump beam 110, 120 impinging on it to a substantially uniform or top-hat profile. In one example, the focusing lens 50 (50') can be replaced with a beam shaping lens.

The apparatus 100 shown in figures 2 to 5 is based on a conventional fluorometer design. As such, the first detection optical path 102 may receive/collect light from a limited range of angles, defined by the numerical aperture of the collimating lens L5. In this case, it is common to measure the QY of a reference sample with a known or predetermined QY value in the same apparatus 100 to calibrate the measured QY of the sample, as described in the experimental section below. Alternatively, in another embodiment, the apparatus 100 comprises an integrating sphere 90 (see figure 1) in which the sample cell 60 can be placed for detecting light emitted from a  $4\pi$  solid angle for measuring an absolute QY value, as is known in the art. In this case, the integrating sphere 90 comprises an illumination port for receiving the first or second pump beam 110, 120 and one or more detection ports at different locations around the sphere for coupling the emitted light to the detector 70E and/or 70E1 in the first and/or second detection optical paths 102, 102'.

Figure 13 shows an alternative layout of the apparatus 100 configured to measure the transmission spectrum of multiple samples simultaneously using the broadband light beam 130 (the first and second illumination optical paths 101, 101' and beam profiler 40 have been omitted for clarity). Here, a second beam splitter BS2 is used to direct a fraction of the broadband light beam 130 towards a second sample cell 60r. This can be used to hold a reference sample, e.g. containing only the solvent the particles in sample cell 60 are dispersed in. The second beam splitter BS2 effectively splits the broadband light beam 130 into two secondary broadband light beams 130a, 130b. The light transmitted through the second sample cell 60r is detected by the detector 70T, i.e. the same detector used to measure the transmitted light through sample cell 60. For example, the light transmitted through sample cell 60r can be sent/routed to the detector 70E via an optical fiber (not shown). An optical chopper CH is positioned in one of the secondary light beams 130a, 130b to modulate the respective secondary beam 130a, 130b at a frequency, in this case the light beam illuminating sample cell 60. The output of the detector 70T is therefore also modulated and contains the transmission spectrum for both sample cell 60 and second sample cell 60r which can be readily be extracted. Alternatively, the light transmitted through sample cell 60r can be detected by a separate detector (not shown). This layout may speed up the QY measurement sequence, as described in more detail below.

A chopper CH can also be used to modulate the first and/or second pump beams 110, 120 to study the temporal dynamics of the QY, e.g. in the time shortly after pump excitation. This may be achieved using a suitably fast APD detector 70E.

In addition to any of the embodiments described above, the apparatus 100 can further be configured to detect pump-induced light emission from the sample 60 in more than one direction simultaneously. With reference to figure 13, detector 70E can be used to detect emission from the sample along the first detection optical path 102 at an angle (in this example 90 degrees) to the incident pump beam 110, 120, and detector 70T can be used to detect emission from the sample in the forward direction or transmission geometry along a third/transmission detection optical path 102''. In this case,

the transmission detection optical path 102'' is essentially a replica of the first optical detection path 102 comprising the same optical elements such as lenses L5-L8 and filters BP1, P2 (not shown). It will be appreciated that the light exiting the sample along the transmission detection optical path 102'' includes a large pump signal and a relatively small forward emission signal. The pump signal can be filtered out using one or more optical filters BP1. Alternatively, the same detector, e.g. detector 70E or 70T, can be used to detect both the side emission and the forward emission (not shown). An optical chopper (not shown) is positioned in the transmission detection optical path 102'' and/or the first detection optical 102 to modulate the respective signal(s) such that only one signal (i.e. transmission or side emission) is detected by the detector 70T/70E at any one time. The two signals can then be temporally separated. In an example where the detector 70E is used to detect both side emission and transmission signals, the transmitted light can be directed to the detector 70E by one or more mirrors or beam splitter and/or an optical fiber. Preferably, the transmission detection optical path 102'' can join the first detection optical path 102 so as to use at least some of the same optical elements. Using the same detector 70T/70E for detecting both signals removes relative errors originating from any difference or drift in detector sensitivity.

Alternatively, the above described arrangement can be used to measure the absorption and emission signal simultaneously with the same detector, e.g. detector 70E. In this case, instead of filtering out the pump signal in the transmission detection optical path 102'', the forward emission signal is filtered out or attenuated (before joining the first detection optical path 102). Here, the transmission detection optical path 102'' joins the first detection optical path 102 (e.g. using a beam splitter) after the band pass filter BP1. Because the forward emission signal is small (e.g. by several orders of magnitude) compared to the transmitted pump signal, filtering the forward emission signal can be done using a neutral density filter to attenuate both the pump light and the emitted light to a level suitable for the detector 70E, making the already small emission signal negligible. In practice, this is to a level that is close to the level of light emitted along the second detection optical path 102. This allows QY to be determined at the pump wavelength using the same detector 70E, avoiding relative errors in the absorption and emission measurements originating from any difference or drift in detector sensitivity.

The lenses L1-L11 shown in the illustrated embodiments are refractive optical elements. It will be appreciated that, in principle, one or more of the lenses may be replaced with a reflective lenses, as is known in the art.

#### IA Quantum yield measurement

The proposed method of measuring the QY of a sample comprises illuminating a sample with the pump beam 110 having the first beam width W1 (and thus a first excitation power density) at the detection region 65, detecting the resulting light emitted from the detection region of the sample, illuminating the sample with the first pump beam having the second beam width W1 (and thus a second excitation power density) at the detection region, the detecting resulting light emitted from the detection region of the sample, and deriving a QY of particles within the sample based on the pump-induced emitted light detected at the first and second beam widths W1, W2 by performing quantum yield analysis. The measurements at the first and second beam widths W1, W2 are repeated at

a plurality of pump powers by attenuating the pump beam and/or controlling the output power of the laser to yield a set of QY values over a wide dynamic range of power densities.

5 An example QY measurement procedure for a sample cell holding a sample containing UCNPs dispersed in a solvent is described below with reference to figure 10a. The method applies equally to other fluorophores. In step S1, the broadband transmission spectrum of the sample, a reference solvent  
10 sample (held in a separate sample cell) and an empty sample cell is measured to determine the net absorption spectrum of the UCNPs. This involves illuminating the sample, reference solvent sample, and empty sample cell with the broadband light beam 130 and detecting the light transmitted therethrough. This can be measured detector 70T, or the transmitted light can be collected and  
15 sent/routed (e.g. via an optical fiber) light to detector 70E1. In both cases, the detector is a spectrometer. The above transmission measurements are repeated for a reference sample containing reference particles, such as a dye, dispersed a reference solvent (i.e. transmission measurements are performed for the reference sample and its reference solvent sample). QY measurements of the reference sample are used to calibrate the QY measurements of the sample.

15 In step S2, the pump-induced luminescence emission signal and spectrum of the UCNPs in the sample is measured over a wide dynamic range of excitation power densities. This involves illuminating the samples with the first pump beam 110 at each beam width W1 and W2 and detecting the luminescence signal and emission spectra at detectors 70E and 70E1 at various pump beam powers. In an example, the pump beam power is varied at each beam width by varying the output power of the  
20 laser source 10A and repeating the measurements with and without the optical density filter ND in place.

In step S3, the beam profile for each beam width and beam power combination is imaged in imaging detector 40D and recorded. This step may occur simultaneously with step S2. Figure 8d shows an example 2D profile of the first pump beam 110 imaged at detector 40D, demonstrating a  
25 substantially speckle-free and smooth Gaussian beam profile. In step S4, the pump beam power at each beam width and beam power combination is measured using a power meter at the position of detector 70T. In step S5, steps S2-S4 are repeated for the reference sample using the second pump beam 120.

Both luminescence emission and signal measurements can be done simultaneously, and in real time. This is significant since the emission spectrum of the particles such as UCNPs or the reference  
30 sample may change (slightly) over time.

This completes the measurement sequence for QY characterisation. The outputs of the measurement sequence are: (i) broadband transmission spectra of the sample, reference sample, reference solvents and empty sample cell; (ii) pump-induced emission spectra of the samples and reference sample at each beam width and pump power combination; (iii) pump-induced luminescence  
35 signals for the samples and reference sample at each beam width and beam power combination; (iv) beam profiles of the first and second pump beams 110, 120 at each beam width and beam power combination; and (v) beam power measurements at each beam width and beam power combination.

#### IB. Quantum yield analysis

The QY analysis procedure is described below with reference to figure 10b. The QY analysis takes all the measurement outputs of the measurement sequence as inputs and calculated various optical parameters to yield a QY curve compensated for possible distortions.

In step S6, the compensated (absolute) absorbance at the pump wavelength determined. This is used to calculate the number of absorbed photons. The total absorbance of a medium  $x$  being measured ( $A_x$ ) is related to transmission by Beer-Lambert's law as:

$$A_x(\lambda) = \ln(I_0(\lambda)/I(\lambda)) \quad (1)$$

where  $I(\lambda)$  and  $I_0(\lambda)$  are the spectra obtained from the sample cell holding the medium and the empty sample cell, respectively. The absorbance is calculated for the sample, reference sample and reference solvents. As the sample contains UCNPs in a solvent, the net absorbance of the UCNPs is obtained by subtracting the absorbance of the reference solvent sample. Figure 8a shows an example net absorbance spectrum obtained from a sample containing UCNPs (see curve labelled A). The measured absorbance spectrum also contain contributions from light scattering that should be removed to yield accurate QY values. This is demonstrated in figure 8a, in which the absorption spectrum exhibits a strong background signal, particularly as shorter wavelengths, due to light scattering from the UCNPs. Following well known scattering laws, this scattering contribution can be removed by fitting to the background with a polynomial of the form  $A_{sc}(\lambda) = a\left(\frac{\lambda}{\lambda_0}\right)^b$  and subtracting the resulting fit to yield the absolute absorbance spectrum of the UCNPs in the sample  $A_{abs}^{ucnp}(\lambda)$ . Here,  $a$  and  $b$  are fitting coefficients that relate to the density and size of the particles. The curve labelled B in figure 8a shows an example fit to the polynomial. This procedure is repeated for the reference sample to obtain the absolute absorbance spectrum of the reference dye,  $A_{abs}^{dye}(\lambda)$ . The absolute absorbance of the UCNPs and the reference dye at the respective pump wavelengths can then be determined.

In step S7, the emission spectrum is used to determine a correction factor to compensate the luminescence signal for any transmission loss due to the limited bandwidth of the optical wavelength filter(s) BP1. This is particularly important in samples or reference samples with relatively broad emission characteristics. Figure 8c shows an example emission spectrum of a sample containing UCNPs, which is centred on 800 nm. The effect of the transmission loss through filter BP1 is demonstrated in figures 9a and 9b which show the normalised emission spectrum of the reference dye and the sample compared to the filtered emission spectrum, which is the product of the normalised emission spectrum and the transmission spectrum of the filter BP1. Transmission correction factors,  $T_{UCNP}$ ,  $T_{Dye}$  for the sample and the reference sample can be determined by integrating emission and filtered emission spectra and taking the ratio of the resulting values.

In step S8, the QY of the sample and reference sample is determined using the compensated absorbance of the sample and reference sample at the pump wavelength and the transmission correction factors derived in steps S6 and S7. The experimental quantum yield  $\phi_{exp}(\rho)$  (not compensated with the reference dye QY) of the UCNPs of the sample at the various power densities is obtained by taking the ratio of luminescence signal of the UCNPs  $L_{ucnp}(\rho)$  (compensated for the transmission losses through the filter BP1) to the number of photons absorbed per unit length in the middle of the sample cell  $N_{obs,ucnp}(\rho)$  (determined using the compensated absorbance).

To compensate for the inner filter effects, the power at the middle of the sample cell 60,  $P_c$ , can be defined as:

$$P_c = P_x e^{\left(\frac{A_{eff}^x(\lambda_{pump})}{2}\right)} \quad (2)$$

5 where  $x$  refers to the medium being measured (e.g. the sample or the reference sample),  $P_x$  is the power of the pump beam after passing through the medium and  $A_{eff}^x(\lambda_{pump})$  is the total absorbance of the medium at the pump wavelength calculated in equation 1 (including contributions from the solvent and scattering). Figure 8b shows an example plot of the luminescence signal from a sample containing UCNPs as a function of the absorbed power at the middle of the sample cell ( $P_c A_{abs}^{ucnp}$ ).

10 The number of photons absorbed by the UCNPs in the sample at the middle of the sample cell 60 is defined as:

$$N_{abs,ucnp1} = A_{abs}^{ucnp}(\lambda_{pump1}) \frac{\lambda_{pump1} P_c}{hc} \Delta T \quad (3)$$

where  $hc/\lambda_{pump1}$  is the photon energy of the first pump beam 110 and  $\Delta T$  is the time period the measurement/exposure. The experimental QY of the sample is then obtained from:

$$15 \quad \phi_{exp,ucnp}(\rho) = \frac{I_{ucnp}(\rho) T_{ucnp}}{N_{abs,ucnp}} \quad (4)$$

Equivalent equations can be written for the experimental QY of the reference sample,  $\phi_{exp,dye}(\rho)$ . However, because the absolute QY of the reference sample is known and constant ( $\phi_{abs,dye}$ ), the QY values for the sample can be calibrated relative to the reference dye value to obtain the relative QY of the UCNPs in the sample according to:

$$20 \quad \phi_{rel,ucnp}(\rho) = \frac{\phi_{exp,ucnp}(\rho) \cdot \phi_{abs,dye}(\rho) n_{ss}^2}{\phi_{exp,dye}(\rho) n_{rs}^2} \quad (5)$$

where  $n_{ss}$  and  $n_{rs}$  are the refractive indices of the sample solvent and the reference sample solvent, respectively, accounting for the reflections losses of light passing into and out of the sample and reference sample.

Equation 5 is calculated for each beam width, optical density filter and beam power combination to obtain four sets of QY values, one for each beam width and optical density filter combination (in this case present or not present) which are combined to provide a high dynamic range QY curve.

In step S10, the relative QY values are compensated for the non-uniform beam profile using the imaging data obtained in step S3 to avoid underestimating the QY values. Figure 8d shows an example 2D profile of the first pump beam 110 imaged at detector 40D. The image data contains a 2D matrix of pixels, each pixel having a pixel value proportional to the intensity of the beam at that position (i.e. an image-based intensity matrix). The beam profile is a substantially speckle-free smooth Gaussian shape. Beam profile compensation is implemented by calculating the QY for each pixel in the beam profile using a rate equation describing the emission process in the sample. This process can use the image-based intensity matrix, or a Gaussian-profile-based intensity matrix derived from fitting to the image-based intensity matrix with a 2D Gaussian distribution function. In the below discussion only image-based compensation is discussed, as Gaussian-based compensation follows the similar method.

The image is analysed in terms of its intensity matrix,  $\Gamma$ , with total power density,  $\Pi$ , represented by  $\Pi(\rho)=P(\rho)/\text{Area}$ , where  $P(\rho)$  is the total laser power for a given power density, and Area is the beam profile area. A compensation matrix,  $\gamma$  was obtained by normalizing the intensity matrix  $\Gamma$  such that the total intensity summed over all pixels in the matrix is equal to 1. Each element  $k$  of  $\gamma$  is then represented by  $\gamma_k = \Gamma_k / (\sum_k \Gamma_k)$ , where  $\Gamma_k$  is an element of the intensity matrix  $\Gamma$ ,  $\gamma_k$  is an element of the normalised compensation matrix and  $\sum_k$  represent the sum over  $k$ . A  $\gamma_k$  image-based compensation matrix is created for each beam width and optical density filter combination for the samples and the reference sample to obtain relative quantum yield values for all 4 configurations, as described below.

Directly from rate equations, the quantum yield,  $\phi$ , for two-photon emission process at a certain power density,  $\rho$ , is given by:

$$\phi = \phi_b \frac{\rho / \rho_b}{(1 + \rho / \rho_b)} \quad (6)$$

where  $\phi_b$  and  $\rho_b$  are the quantum yield and power density at the balancing point. The balancing point is related to the saturation of the absorption-emission process. Because the power density varies across the beam profile, the total quantum yield,  $\Phi_T$ , is by definition given by,

$$\Phi_T = \frac{\sum_{k=0}^N n_{e,k} \frac{hc}{\lambda_e}}{\sum_{k=0}^N n_{a,k} \frac{hc}{\lambda_a}} \quad (7)$$

where,  $n_{e(a),k}$  is the total number of photons emitted (absorbed) by UCNPs along the region due to the  $k$ th-pixel, and  $\frac{hc}{\lambda_{e(a)}}$  is the energy of each photon emitted (absorbed). However, based on equation 3,  $n_{a,k} \frac{hc}{\lambda_a} = A_{abs}^{ucnp} (\lambda_{pump1}) P_{c,k} \Delta T$ , where  $P_{c,k}$  is the power at each pixel, and  $P_{c,k} = P_c \gamma_k$  where  $P_c$  is the total measured power (at the centre of the sample cell 60). Then,

$$n_{a,k} \frac{hc}{\lambda_a} = A_{abs}^{ucnp} (\lambda_{pump1}) P_c \gamma_k \Delta T. \quad (8)$$

From equation 6, the quantum yield due to a certain pixel region can be defined as,

$$\phi_k = \phi_b \frac{\rho_k / \rho_b}{(1 + \rho_k / \rho_b)} \quad (9)$$

where  $\rho_k = P_c \gamma_k / A_{px}$  and  $A_{px}$  is the pixel area. Noting also that, by definition, the QY at each pixel is  $\phi_k = \frac{n_{e,k} \frac{hc}{\lambda_e}}{n_{a,k} \frac{hc}{\lambda_a}}$  and substituting in equation 8 gives,

$$n_{e,k} \frac{hc}{\lambda_e} = \phi_k A_{abs}^{ucnp} (\lambda_{pump1}) P_c \gamma_k \Delta T \quad (10)$$

Substituting equations 8, 9 and 10 into equation 7 it can be shown that the total quantum yield is

$$\Phi_T = 2 \frac{P_c \phi_b}{A_{px}} \sum_k^N \frac{\gamma_k^2}{(P_c \gamma_k / A_{px} + \rho_b)} \quad (11)$$

Equation 11 can be calculated for each beam width, optical density filter and beam power combination using only  $\phi_b$  and  $\rho_b$  as fitting parameters which are valid for the whole data set.  $\Phi_T$  is minimized against the  $\phi_{rel,ucnp}$  value for each power density point.

Any presence of speckles in the beam profile makes it more difficult to compensate for the beam profile.

## 35 II. Experimental validation

WO 2021/084137

PCT/EP2020/080714

26

To experimentally validate the apparatus and proposed method, QY measurements of two UCNP samples were performed using a setup according to figure 2. Sample 1 was water-soluble NaYF<sub>4</sub>:Tm core UCNPs (UCNP1) and sample 2 was water-soluble NaYF<sub>4</sub>:Tm core shell UCNPs (UCNP2), both produced from Hangzhou Fluo Nanotech Co. Ltd at a concentration of 10 mg/ml. The samples were diluted in distilled water at 5 mg/ml, 2.5 mg/ml for concentration repeatability measurements. These UCNPs have an emission wavelength around 800 nm. A reference sample containing a reference dye was used to calibrate the UCNPs QY value. The reference dye was sourced from Dyomics (Dy- 781). The reference dye has an emission wavelength centred similar to UCNP (800 nm) and a factory tabulated quantum yield of 11.9 % when dissolved in ethanol. The reference dye was diluted in ethanol solvent to have absorption values similar to 10 mg/ml UCNP samples used for this study. Two dedicated cuvettes with water and ethanol solvents were prepared as blank references to obtain absorption values of pure UCNPs and dye. 2 ml of each sample were placed in a quartz cuvette (Thorlabs, CV10Q3500FS) and the sealed to avoid any evaporation of the ethanol and water solvents.

Specific details of the apparatus 100 used in the experimental tests are as follows. Light sources: 10A = temperature stabilised diode laser at  $\lambda_{\text{pump1}} = 976$  nm coupled to a single mode fiber (Thorlabs, BL976-PAG500); 10B = temperature stabilised diode laser at  $\lambda_{\text{pump2}} = 785$  nm coupled to a single mode fiber (Thorlabs, FPL785S-250); 80 = Ocean Optics HL-2000. Optical wavelength filters: BP1= band pass (Edmund Optics, FBH800) and short pass (Thorlabs, FES0900) for samples 1 and 2, and band pass (Edmund Optics, FBH800) and long pass (Thorlabs, LP02785RU) for reference sample; BP2 = short pass for samples 1 and 2 (Thorlabs, FES0900). Detectors: 70E = APD (Thorlabs, APD120A), 70E1 = spectrometer (Ocean Optics QE Pro). Optical density filter: ND= optical density 1 (10% transmission). Lenses: L1 (f1=30 mm); L2 (f2=30 mm); L3 (f3=6mm); L4 (f4=200mm); L5-L11 (f=30mm). This selection of lenses produces two different widths at the detection region 65 of W1=700 $\mu$ m when the lens arrangement 10, 10' is in the first and second illumination optical paths 101, 101' and W2=150  $\mu$ m when the lens arrangement 10, 10' is moved out of the first and second illumination optical paths 101, 101'. The first light source 10A is used to excite the UCNPs in samples 1 and 2, and the second light source 10B is used to excite the dye in the reference.

#### IIA. Measurement method

Broadband (350-1100 nm) transmission spectrum of samples 1 and 2, a cuvette filled with reference solvent (water), and an empty cuvette was measured to determine the net absorption spectrum of the UCNPs, as described in sections IA and IB. In this case, detector 70T was replaced with a fiber bundle (Thorlabs, BFL200HS02) which collected and sent the transmitted light to detector/spectrometer 70E1. The above transmission measurements were repeated for the reference sample, and a cuvette filled with reference solvent (ethanol).

The pump-induced luminescence emission signal and spectrum of the UCNPs in samples 1 and 2 is measured over a wide dynamic range of excitation power density. The luminescence measurements are taken at various laser currents (20mA-800mA, with a 4mA steps) with and without the optical density filter ND. Measurements with the first beam width W1 (700  $\mu$ m) correspond to a low density regime, while measurements with the second beam width W1 (150  $\mu$ m) correspond to a high density regime.

The beam profile for each beam width and beam power was imaged in imaging detector 40D and recorded. The pump beam power at each beam width and beam power combination was measured using a power meter at the position of detector 70T. These measurements were repeated for the reference sample using the second pump beam 120 at  $\lambda_{\text{pump}2} = 785 \text{ nm}$  (20mA-850mA, with a 4mA steps).

The absolute absorbance (removing scattering contributions) for samples 1 and 2 and the reference dye ( $A_{\text{abs}}^{\text{ucnp}1}(\lambda)$ ,  $A_{\text{abs}}^{\text{ucnp}2}(\lambda)$ ,  $A_{\text{abs}}^{\text{dye}}(\lambda)$ ) was determined as described above. Transmission correction factors,  $T_{\text{UCNP}1}$ ,  $T_{\text{UCNP}2}$ ,  $T_{\text{Dye}}$  for the samples and the reference sample were determined using the measured emission spectra and transmission of the filter BP1.

The relative QY for the samples was calculated using equation 5 for each beam width, optical density filter and beam power combination to obtain four sets of QY values, one for each beam width and optical density filter combination (in this case present or not present) which were combined to provide a high dynamic range QY curve. Figure 11a-11d show the relative QY versus average power density (calculated using the full-width at half maximum (FWHM) of the beam profile imaged in step S3) for the QY values obtained, respectively, with the first beam width W1 and without the filter ND, the first beam width W1 with the filter ND, the second beam width W2 without the filter ND, and the second beam width W2 without the filter ND. Figure 11e shows the resulting high dynamic QY curve combining all the data, in this case spanning a dynamic range of  $10^4$ .

Next, the relative QY values were compensated for the non-uniform beam profile, using the procedure described in section IB. The resulting beam profile compensated QY curve is shown in figure 11e by the open circles (open squares show the results for Gaussian-based compensation). As is evident, the assumption of a uniform beam profile, which is the case when only the beam width is used to estimate the power density, leads to an underestimation of the QY. The approach described above properly takes the non-uniform beam profile into account leading to more accurate QY measurements.

The apparatus 100 was also tested under various experimental conditions to ensure its robustness. The following four variables were considered a) sonication of the samples b) intraday stability c) inter-day reproducibility d) different sample concentrations. The results of these measurements are summarized in figure 12. The sonication time was tested to understand optimal sonication time for the samples and it's clear from figure 12a that sonication time between 5-15 minutes does not influence the measured QY of UCNP's significantly. Figure 12b indicates that the intra-day variations were found to be within 4% variation at high QY values. Inter-day reproducibility was found to have similar variations (see figure 12c). It is worth noting that in the absence of all measurements and compensations, we found the assessed QY values to vary by up to 100%. The different sample concentrations were attributed to the changes in the turbidity of the UCNP sample. Correct compensation for scattering in the transmission spectral measurements resulted in a remaining negligible variation in QY values as illustrated in figure 12d. In addition to the inter-sample variations, the absence of this compensation yielded on average a 60% underestimation in QY values. These tests emphasize the need for multimodal measurements and compensation for the optimal characterization of QY of UCNP's.

Although only the 800 nm emission line of the NaYF<sub>4</sub>:Tm UCNP's was consider in the above experimental results, it will be appreciated that detection of other emission lines in other samples can

be achieved easily, by changing the optical wavelength filters BPI in the detection optical paths 102, 102' and by selecting a suitable dye matching the emission wavelength of UCNPs. In this case, the first light source 10A used for exciting the UCNPs remains the same, while the second light source 10B used for exciting the reference dye should be chosen based on the measurement protocol used for the tabulated QY of the selected dye.

Notably, the equation 6 (derived from rate equations for a 2 photon transition) developed for the 800 nm emission line may no longer be valid for other emission lines, as these lines might involve a greater number of photon transitions. As such, in generally, a model describing an n-photon transmission suitable for the sample and measurement should be used.

The above validation example, transmission measurements on different samples and solvents were performed in sequence placed in the same position. In an alternatively layout, the third illumination optical path 103 may not join the first or second illumination optical paths 101, 101' but may instead comprise a separate sample holder for measuring the transmission spectrum of samples or reference sample (e.g. containing reference solvent) in a separate beam line, optionally concurrently with luminescence measurements. This may speed up the measurement sequence, thus reducing errors in the assessed optical properties and in the obtained QY associated with changes in experimental conditions with time.

Although the second illumination optical path 101' was used to measure a reference dye to calibrate the quantum yield of UCNPs, this calibration factor will remain constant, provided, the apparatus 100 is robustly built and well tested under different experimental conditions. Therefore, the need for a reference arm is not essential once the set-up is calibrated at each emission line.

The above results demonstrate that the apparatus 100 is well suited for stability and reproducibility with a variation of less than 4% under different experimental conditions. Further, the results show that the obtained quantum yields of UCNPs can vary by up to 100% and have an offset of 60% in the absence of the multi-modal corrections included in this proposed method. The system and methods described herein results can therefore act as a precursor for standardizing the measurements of quantum yield values.

### III. Further applications

As described above, the apparatus 100 may be used to characterise various optical parameters of particles within a sample including absorption and scattering, luminescence emission spectra and luminescence signal and QY. Although the above description has focused on measurements of QY, the principle of exciting non-linear luminescent particles such as UCNPs with a substantially speckle-free uniform pump beam profile to improve the accuracy and reliability of the sample characteristics derived from the luminescence can be applied to a number of other applications. It is especially important for accurate quantification of luminescence of non-linear materials in the low power regime where the non-linearity is strongest, as applies to biomedical applications (e.g. where the sample comprises biological tissue) where high light levels can damage/denature the protein or other components of the biological media.

By way of example only, speckle-free uniform pump beam profile is important to accurately determine the radiative lifetime of electronic states in the particles. Figure 14 shows an example

electronic transitions in  $\text{Tm}^{3+}$  ions resulting from multiphoton 975 nm absorption in  $\text{Yb}^{3+}$  ions in a rare earth  $\text{NaYF}_4:\text{Yb,Tm}$  UCNP system. The upconversion emission shown by the 800nm and 474nm lines occurs due to the existence of long lifetimes present on intermediate excited energy levels. Measuring the radiative lifetime of individual levels (especially the ones involved on the multi electronic transitions steps) is important for characterizing the material as well as for modelling and understanding the optical processes. As well as the radiative lifetime, the time to populate and depopulate the energy levels (referred to here as raising and decay time, respectively) is also important to determine. Because the whole process is driven by the number of photons that the material is exposed to (i.e. the power density of the excitation line), it is also expected that the raising and decay time also exhibit a power density dependence. Therefore, having a proper beam illumination profile is important to properly evaluate the intrinsic properties of nonlinear optical materials. As such, the apparatus 100 and method of the invention provides an important step forward in developing novel materials with optimal features (e.g. UCNPs with high emission quantum yield). As an example, consider the energy levels  $a$  and  $b$  in the  $\text{Yb}^{3+}$  ions shown on figure 14. The population decay from the excited state to ground state depends on the  $b$  energy level population ( $N_b$ ), spontaneous radiative lifetime ( $\tau_b$ ), energy migration to the environment ( $W_d N_d$ ), and the energy transfer processes to the  $\text{Tm}^{3+}$  ions  $i$  energy level (i.e. the population density of the  $i$  level, being  $i$  equals to 1 or 2). Thus, the decay time is represented by  $\tau = 1/R_b$ , with  $R_b$  given by the following equation:

$$R_b = \frac{1}{\tau_b} + \sum_i W_i N_i + W_d N_d \quad (12)$$

The population of the  $i$  levels are power density dependent and, thus, so are the raising and decay time. The same is valid to the energy levels in  $\text{Tm}^{3+}$  which are involved in the upconversion emission process. Figures 15a and 15b show example measurements of raising and decay time, respectively, for the energy level 2 responsible for the 800nm emission in  $\text{NaYF}_4:\text{Yb,Tm}$  UCNPs under 975nm laser excitation with a speckle-free uniform beam profile at different power densities (indicated by the laser currents) using the apparatus 100 arrangement shown in figure 2. As is evident, the  $\tau$  values for the population raising and decay are different since during the decay measurement the pump light is absent and mechanisms involved in the process lack the pumping up electrons due to energy transfer initially driven by laser light absorption in the  $\text{Yb}^{3+}$  ions.

As a further example, in general, non-linear luminescent particles such as UCNPs can be used as a substitute for traditional fluorescence probes where a narrow bandwidth emission, auto-fluorescence background free emission (providing high dynamic range detection) is important. In these applications, use of a speckle-free beam profile plays critical role in the accurate quantification of UNCP luminescence, in particular at low power density where the UNCP luminescence exhibits strong non-linear behaviour. Such luminescent probe-based applications include, but are not limited to optogenetics, real time polymerase chain reaction (PCR), and flow cytometer.

*Optogenetics:* When optogenetics is performed on superficial tissue layers or on the transparent deep tissue layers, the use of the apparatus 100 with a speckle-free uniform beam profile provides uniform stimulation across the region of interest, and is a key enabler to excite non-linear particles

WO 2021/084137

PCT/EP2020/080714

30

such as UCNPs in quantifiable way. In particular, there is a limitation on the power levels for biological tissues to avoid tissue damage.

*Deep tissue probing applications using non-linear luminescent particles as biomarkers:* Deep tissue imaging systems measure luminescence particles deep within the tissue. The number and concentration of particles can be quantified from the measured luminescence if their emission properties are well characterised. However, the intensity of light is greatly attenuated while propagating in highly scattering media such as human tissue. As such, the use of the apparatus 100 and methods of the invention to accurately characterise the QY of such particles over a wide dynamic power density range (covering that which the particles will experience at depth) will enable better understanding of luminescence signals from biomarkers present deep inside tissue and deep tissue images.

*Real time PCR monitoring:* State of the art real time PCR apparatuses use fluorescence probes to monitor the amplification of DNA by the polymerase process. The fluorescence probes can be substituted with UCNPs. UCNPs exhibit narrower emission than fluorescence probes and also no background emission in the detection band. The reduced background signal enables better identification of the cycle quantification (Cq) value which is critical to assess amount of target nuclei acid present in the sample. Meanwhile, the narrower emission width of UCNPs means that multiple emission lines can be distinguished and detected simultaneously (multiplexed). For example, different UCNPs (that emit at different wavelengths) can be used to bind to different DNA strands, allowing for real time monitoring of multiple genes in the sample. In this case the assessment of DNA amplification requires the determination of UCNP concentration bound to DNA, which can be derived from the luminescence with improved accuracy using the apparatus 100 with a speckle-free uniform beam profile. The apparatus 100 can be also used to more accurately determine the Cq value.

*Flow cytometry:* In a flow cytometer, UCNPs can be used as substitute for traditional fluorophores. As above described above, the narrow bandwidth of emission lines and low background emission can be used for multiplexing multiple signatures of cells simultaneously. The use of the apparatus 100 with a speckle-free uniform beam profile provides more accurate quantification of UCNP bound to the target cells.

It will be appreciated that different detection geometries may be required for different measurements, applications and/or samples. Figure 16 shows another example arrangement of the apparatus 100 where light emitted from the sample is detected in reflection geometry. This may be suitable for application where the sample comprises substantially solid scattering media, e.g. biological tissue. Here, a dichroic mirror BS-d reflects and directs the pump beam 110 (at the first centre wavelength) toward the detection region 65 of the sample. Pump-induced light emitted from UCNPs in the sample (at a shorter wavelength) along the detection optical path 102 is collected by lens L5 and transmitted through the dichroic mirror BS-d onto the detector 70E via a band pass filter BP1 and polariser P2 as described previously. Pump light reflected from the sample is filtered by the dichroic mirror BS-d.

Figure 17 shows another example arrangement of the apparatus 100 where light emitted from the sample is detected in transmission geometry. For example, this arrangement may be suitable for PCR monitoring and/or flow cytometry. Here a beam splitter BS reflects and directs a portion of the

direct the pump beam 110 (at the first centre wavelength) toward the detection region 65 of the sample, and pump-induced light emitted from UCNPs in the sample (at a shorter wavelength) along the detection optical path 102 in transmission geometry is collected by lens L5 and focused onto the detector 70E by lens L6 via a band pass filter BP1 and polariser P2 as described previously. The apparatus 100 of figures 16 and 17 may include any of the features described above with reference to figures 2-5 and 13.

In addition, the apparatus 100 can be used to perform dynamic light scattering (DLS) measurements to derive properties such as the particle size and distribution of the sample. In this case, the optical wavelength filter(s) BP1 in the first detection optical path 102 is removed to allow scattered pump light to reach the detector 70E (fast APD). The DLS measurement principle is well known. Brownian (random direction) motion of dispersed particles in the sample causes the pump light to scatter in all directions to a varying extent depending on the particle size and temperature. The scattered light thus varies over time and the autocorrelation function of the detector signal recorded over a period of time contains information on the particle size distribution in the sample which can be determined through the Stokes-Einstein equation using known methods. As such, the apparatus 100 may readily be configured to perform a DLS measurement based on the detector output.

From reading the present disclosure, other variations and modifications will be apparent to the skilled person. Such variations and modifications may involve equivalent and other features which are already known in the art, and which may be used instead of, or in addition to, features already described herein.

Although the appended claims are directed to particular combinations of features, it should be understood that the scope of the disclosure of the present invention also includes any novel feature or any novel combination of features disclosed herein either explicitly or implicitly or any generalisation thereof, whether or not it relates to the same invention as presently claimed in any claim and whether or not it mitigates any or all of the same technical problems as does the present invention.

Features which are described in the context of separate embodiments may also be provided in combination in a single embodiment. Conversely, various features which are, for brevity, described in the context of a single embodiment, may also be provided separately or in any suitable sub-combination.

For the sake of completeness it is also stated that the term "comprising" does not exclude other elements or steps, the term "a" or "an" does not exclude a plurality, and any reference signs in the claims shall not be construed as limiting the scope of the claims.

WO 2021/084137

PCT/EP2020/080714

32

## CLAIMS

1. A method of optical characterisation of a sample, comprising:  
illuminating a sample with a pump beam having a first centre wavelength, and a first beam  
5 width, a first excitation power density and a substantially speckle-free beam profile at a detection  
region within the sample; and  
detecting light emitted from the detection region of the sample produced by the interaction of  
the pump beam with the sample.
2. The method of claim 1, further comprising shaping the pump beam to have the substantially speckle-  
10 free beam profile and/or a substantially smooth continuous intensity distribution at the detection  
region.
3. The method of claim 2, wherein shaping the pump beam comprises: passing the pump beam through  
a single mode optical fiber; using a single mode laser as a light source producing the pump beam;  
and/or spatially filtering the pump beam.
- 15 4. The method of any preceding claim, wherein the pump beam further has a substantially uniform  
intensity distribution at the detection region; and/or the method further comprises: shaping the pump  
beam to have a substantially uniform intensity distribution at the detection region using one or more  
lenses in an illumination optical path between a light source producing the pump beam and the sample.
5. The method of any preceding claim, further comprising illuminating the sample with a pump beam  
20 having the first centre wavelength, and a second beam width, a second excitation power density and a  
substantially speckle-free beam profile at the detection region.
6. The method of claim 5, wherein the pump beam having the respective first and second beam width is  
produced by the same light source, and the step of illuminating the sample with a pump beam having  
the first centre wavelength, and a second beam width, a second excitation power density and a  
25 substantially speckle-free beam profile at the detection region comprises: adjusting the pump beam to  
have the second beam width and second excitation power density at the detection region.
7. The method of claim 6, wherein adjusting the pump beam to have the second beam width at the  
detection region comprises adjusting and/or changing a lens arrangement in an illumination optical path  
between a light source producing the pump beam and the sample; and/or optionally or preferably,  
30 wherein the lens arrangement comprises one or more lenses configured to provide a collimated  
beam of adjustable width; and adjusting and/or changing the lens arrangement comprises:  
moving at least one of the one or more lenses into or out of the illumination optical  
path; and/or  
directing the pump beam so as to pass through or bypass at least one of the one or more  
35 lenses.
8. The method of any of claims 5 to 7, further comprising shaping the pump beam having the second  
beam width at the detection region to have the substantially speckle-free beam and/or a substantially  
smooth continuous intensity distribution at the detection region.
9. The method of claim 8, wherein shaping the pump beam comprises: passing the pump beam through  
40 a single mode optical fiber; using a single mode laser as a light source producing the pump beam;  
and/or spatially filtering the pump beam.

WO 2021/084137

PCT/EP2020/080714

33

10. The method of any of claims 5 to 9, wherein the pump beam having the second beam width at the detection region further has a uniform intensity distribution at the detection region; and/or the method further comprises: shaping the pump beam having the second beam width at the detection region to have a substantially uniform intensity distribution at the detection region using one or more lenses in an illumination optical path between a light source producing the respective pump beam and the sample.
- 5
11. The method of any preceding claim, further comprising:
- varying the excitation power density of the pump beam having the first beam width at the detection region, and illuminating the sample with said pump beam at a plurality of excitation power densities; and
  - 10 detecting, at a plurality of excitation power densities, light emitted from the detection region of the sample produced by the interaction of the pump beam with the sample.
12. The method of any of claims 5 to 11, further comprising:
- 15 varying the excitation power density of the pump beam having the second beam width at the detection region, and illuminating the sample with said pump beam at a plurality of excitation power densities; and
  - detecting, at a plurality of excitation power densities, light emitted from the detection region of the sample produced by the interaction of the pump beam with the sample.
13. The method of claim 11 or 12, wherein varying the excitation power density of the respective pump beam comprises:
- 20 adjusting an optical power output of a light source producing the respective pump beam; and/or attenuating the respective pump beam.
14. The method of any preceding claim, further comprising:
- 25 measuring an emission spectrum of the detected pump-induced emitted light; and
  - compensating the detected pump-induced emitted light for a limited transmission bandwidth of one or more optical elements in a detection optical path based on the measured emission spectrum.
15. The method of any preceding claim, further comprising deriving one or more optical properties of particles within the sample based, at least in part, on the detected pump-induced emitted light.
16. The method of any preceding claim, further comprising deriving a quantum yield of particles within the sample based, at least in part, on the detected pump-induced emitted light by performing quantum yield analysis.
- 30
17. The method of claim 16, wherein the method further comprises:
- illuminating the sample with a broadband light beam having a broad spectral content; and
  - 35 detecting the light transmitted through the sample to derive an absorption spectrum of the sample, and
  - wherein the quantum yield is derived based on the detected pump-induced emitted light and the derived absorption spectrum, optionally or preferably, the component of the derived absorption spectrum at the centre wavelength of the pump beam.
18. The method of claim 17, wherein the quantum yield analysis comprises compensating for or substantially removing scattering contributions in/from the derived absorption spectrum.
- 40

WO 2021/084137

PCT/EP2020/080714

34

19. The method of any of claims 16 to 18, further comprising imaging an intensity profile of the pump beam to determine the excitation power density and/or beam profile or intensity distribution at the detection region; and, optionally or preferably, wherein the quantum yield analysis comprises compensating for a non-uniform intensity distribution of the respective pump beam at the detection region based on the measured or imaged beam profile and a model describing a power density dependence of quantum yield, optionally or preferably, wherein the model is derived from a rate equation describing the emission process in the sample.
20. The method of any of claims 16 to 19, further comprising:
- replacing the sample with a reference sample having a predetermined quantum yield characteristic;
  - repeating the method steps of any of claims 16 to 19 to derive, at each beam width and excitation power density, a quantum yield of particles within the reference sample; and
  - calibrating the derived quantum yield of particles within the sample using the derived quantum yield of particles in the reference sample and the predetermined quantum yield characteristics of the reference sample; and
  - optionally or preferably, wherein the reference sample is illuminated using a pump beam having a different centre wavelength.
21. A particle characterisation apparatus, comprising:
- a first light source configured to produce a first pump beam having a first centre wavelength and a substantially speckle-free beam profile for illuminating, along a first illumination optical path, a sample to thereby produce emitted light by the interaction of the first pump beam with the sample;
  - a first detector for detecting pump-induced emitted light from a detection region within the sample along a first detection optical path; and
  - a first optical filter element in the first detection optical path for attenuating light at the first centre wavelength.
22. The apparatus of claim 21, wherein the first light source comprises a single mode fiber coupled to the output of a laser, and/or wherein the first light source comprises a single mode laser, so as to produce a first pump beam with a substantially speckle-free beam profile and/or a substantially smooth continuous intensity distribution at the detection region.
23. The apparatus of claim 21 or 22, further comprising a first beam shaping arrangement in the illumination optical path configured to transform the first pump beam to have a substantially uniform spatial intensity distribution at the detection region; and optionally or preferably,
- wherein the first beam shaping arrangement comprises one or more lenses, and optionally a diffraction element, to transform the beam profile using truncation, refraction and/or diffraction.
24. The apparatus of any of claims 21 to 23, comprising a first lens arrangement in the first illumination optical path configured to adjust the first pump beam to have a first beam width or a second beam width at the detection region.
25. The apparatus of claim 24, wherein the first lens arrangement comprises one or more lenses configured to provide a collimated beam of adjustable width; and, optionally or preferably:
- wherein at least one of the one or more lenses is moveable and/or removable to provide the collimated beam of adjustable width; and/or

wherein the first lens arrangement comprises a plurality of mirrors arranged to selectively direct the first pump beam so as to pass through or bypass at least one of the one or more lenses to provide the collimated beam of adjustable width.

26. The apparatus of claim 25, wherein the first lens arrangement comprises a focusing lens and collimating lens, and wherein:

the focussing lens and the collimating lens are moveable into and out of the first illumination optical path to provide the collimated beam of adjustable width; and/or

the first lens arrangement comprises a plurality of mirrors arranged to selectively direct the first pump beam so as to pass through or bypass the focussing lens and the collimating lens to provide the collimated beam of adjustable width.

27. The apparatus of any of claims 21 to 26, further comprising a means for varying the excitation power of the pump beam at the detection region; and, optionally or preferably, wherein the means for varying the excitation power of the first pump beam at the detection regions comprises:

an adjustable power controller of the first light source; and/or

one or more optical filter elements in the first illumination optical path.

28. The apparatus of claim 27 when dependent from any of claims 24 to 26, wherein the means for varying the excitation power density of the first pump beam at the detection region and the first lens arrangement are configured to provide a dynamic range of excitation power densities at the detection region of up to  $10^4$ ,  $10^5$ ,  $10^6$ ,  $10^7$  or  $10^8$ .

29. The apparatus of any of claims 21 to 28, further comprising a beam profiler in the first illumination optical path for measuring a two-dimensional spatial intensity distribution of the first pump beam at a location equivalent to the detection region; and, optionally or preferably,

wherein the beam profiler comprises a beam-splitter that directs a percentage of the first pump beam towards a two-dimensional imaging detector.

30. The apparatus of any of claims 21 to 29, further comprising a second light source for producing a second pump beam having a second centre wavelength and a substantially speckle-free beam profile for illuminating, along a second illumination optical path, a reference sample to thereby produce emitted light by the interaction of the second pump beam with the reference sample; and, optionally or preferably, wherein the second illumination optical path joins the first illumination optical path.

31. The apparatus of claim 30, wherein the apparatus further comprises:

a second lens arrangement in the second illumination optical path substantially identical to the first lens arrangement for adjusting the second pump beam to have a first beam width or a second beam width at the detection region; and optionally or preferably,

wherein the second light source comprises a single mode fiber coupled to the output of a laser, and/or wherein the second light source is a single mode laser, so as to produce a second pump beam with a substantially speckle-free beam profile and/or a substantially smooth continuous intensity distribution at the detection region.

32. The apparatus of any of claims 21 to 31, wherein the first light source comprises a laser, and the apparatus further comprises a broadband light source for producing a broadband light beam having a broad spectral content for illuminating, along a third illumination optical path, the sample for measuring an absorption spectrum of the sample; and optionally or preferably, wherein:

WO 2021/084137

PCT/EP2020/080714

36

the third illumination optical path joins the first illumination optical path;  
the first detector is configurable to measure the absorption spectrum; and/or  
the apparatus comprises a second detector for detecting light transmitted through the sample for measuring the absorption spectrum.

- 5 33. The apparatus of any of claims 21 to 32, wherein the apparatus comprises an integrating sphere for holding the sample, the integrating sphere comprising an excitation port for receiving the first pump beam and one or more detection ports for coupling to the first detector.
34. The apparatus of any of claims 21 to 32, wherein the apparatus is operable to perform a quantum yield measurement of particles within the sample based, at least in part, on an output of the first  
10 detector.
35. The apparatus of claims 34, further comprising a processing device for deriving, at each excitation power density and beam width, a quantum yield measurement of particles within the sample based, at least in part, on an output from the first detector
- 15 36. The apparatus of any of claims 21 to 35, wherein the apparatus is operable to perform a dynamic light scattering measurement of particles within the sample based on an output of the first detector.
37. The apparatus of any of claims 21 to 36, wherein the apparatus is operable to perform flow cytometry measurements of particles within the sample based on an output of the first detector.
38. The apparatus of any of claims 21 to 37, wherein the apparatus is operable for use in monitoring a polymerase chain reaction in the sample based on an output of the first detector.
- 20 39. The apparatus of any of claims 21 to 38, wherein the apparatus is operable for detecting light emitted from particles within a liquid or solid sample.



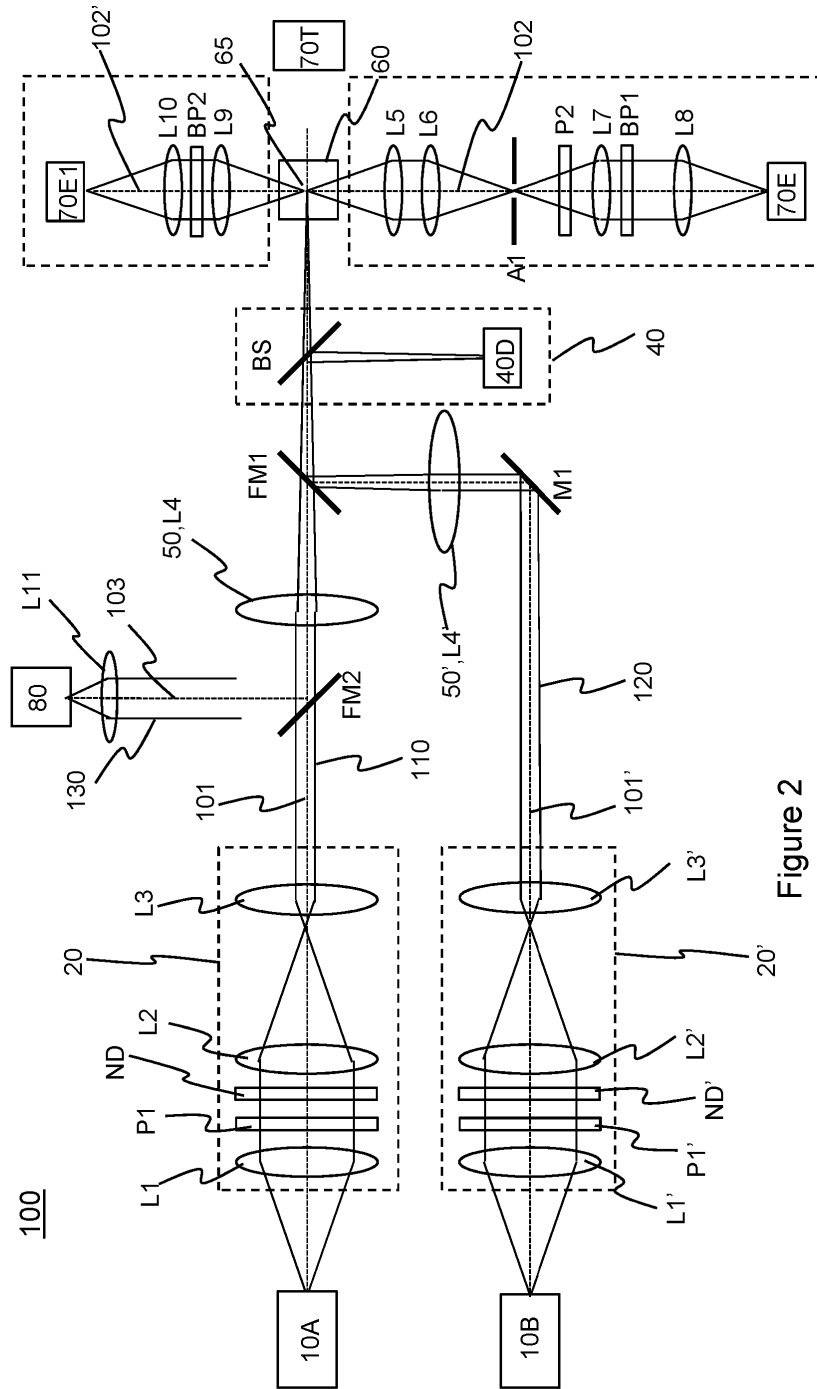


Figure 2

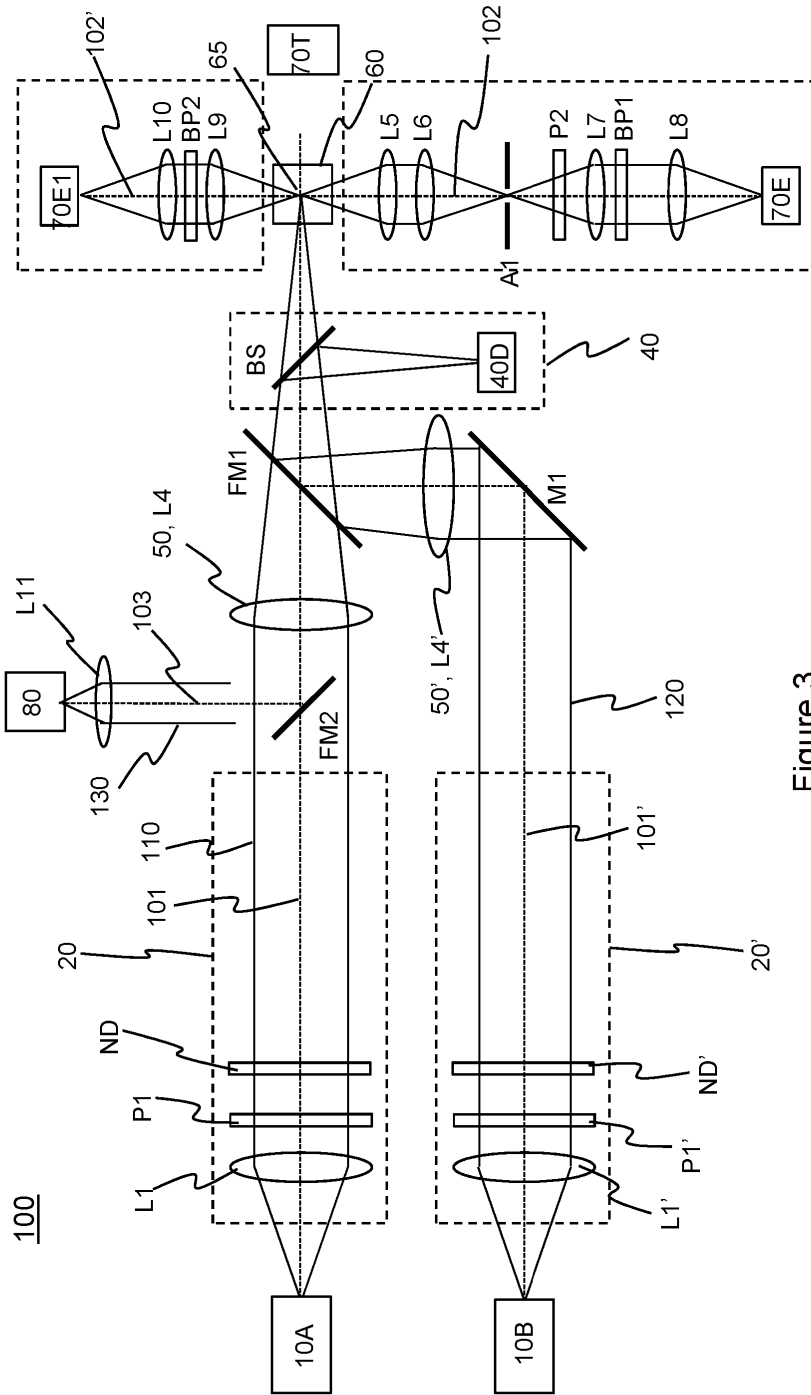


Figure 3

SUBSTITUTE SHEET (RULE 26)

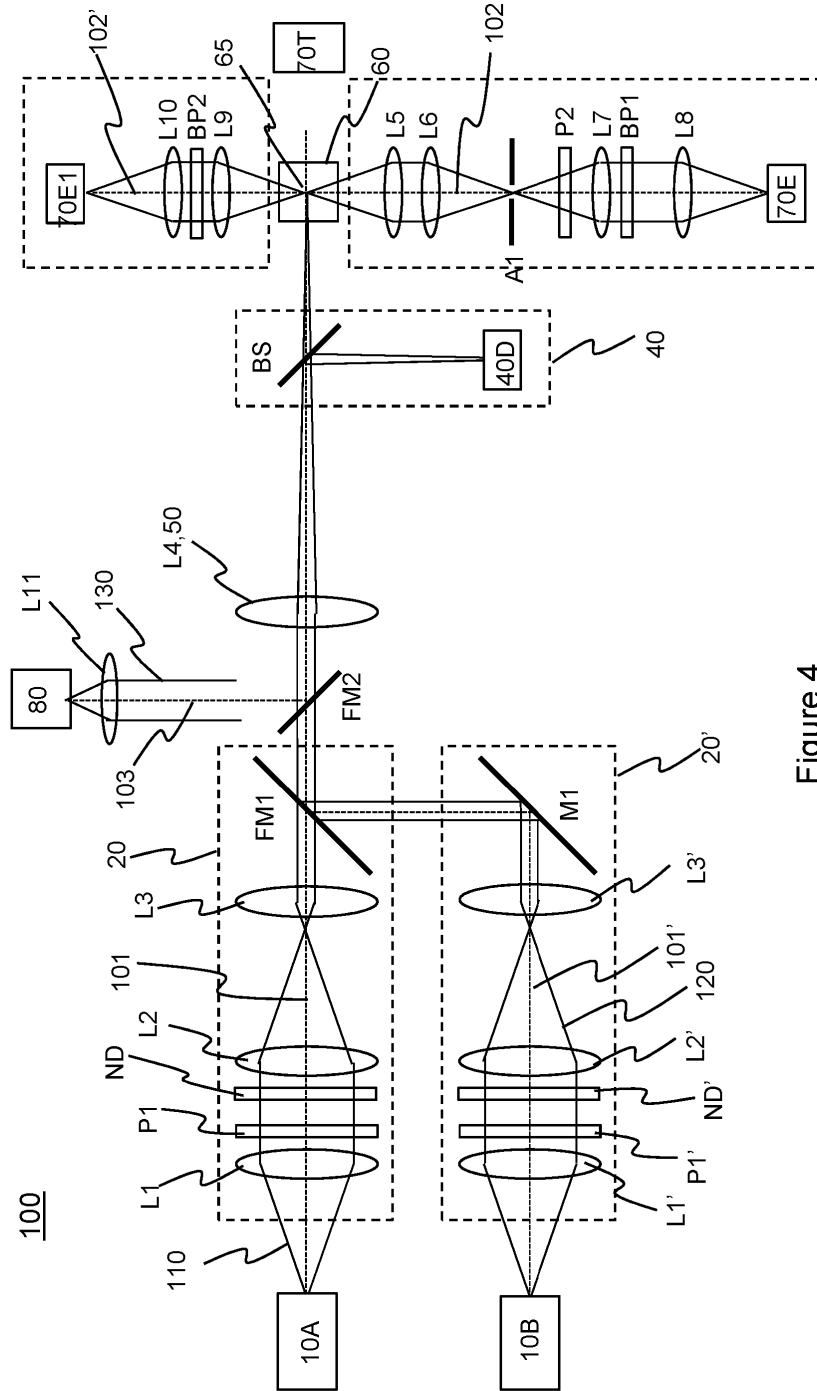


Figure 4



WO 2021/084137

PCT/EP2020/080714

6/15

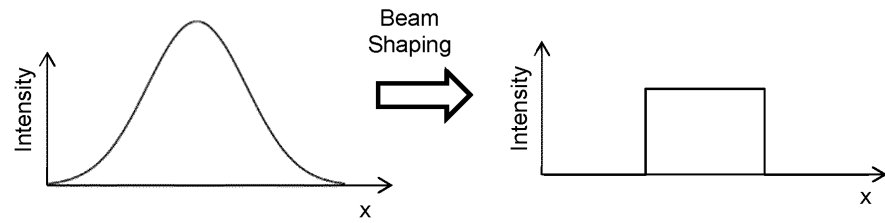


Figure 6

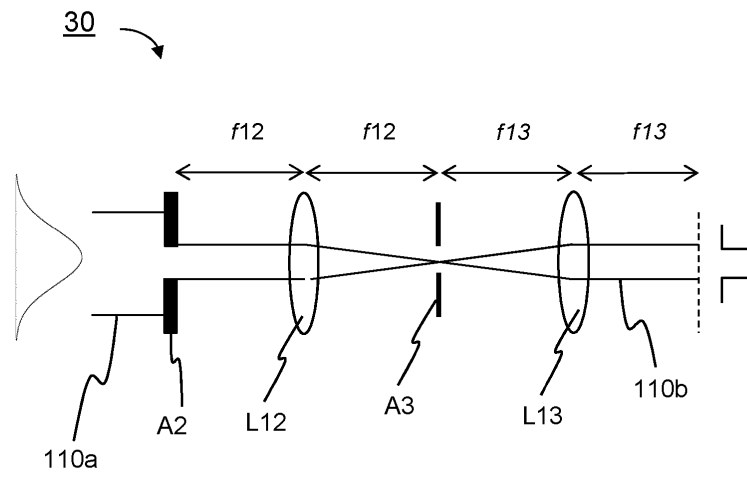


Figure 7

SUBSTITUTE SHEET (RULE 26)

WO 2021/084137

PCT/EP2020/080714

7/15

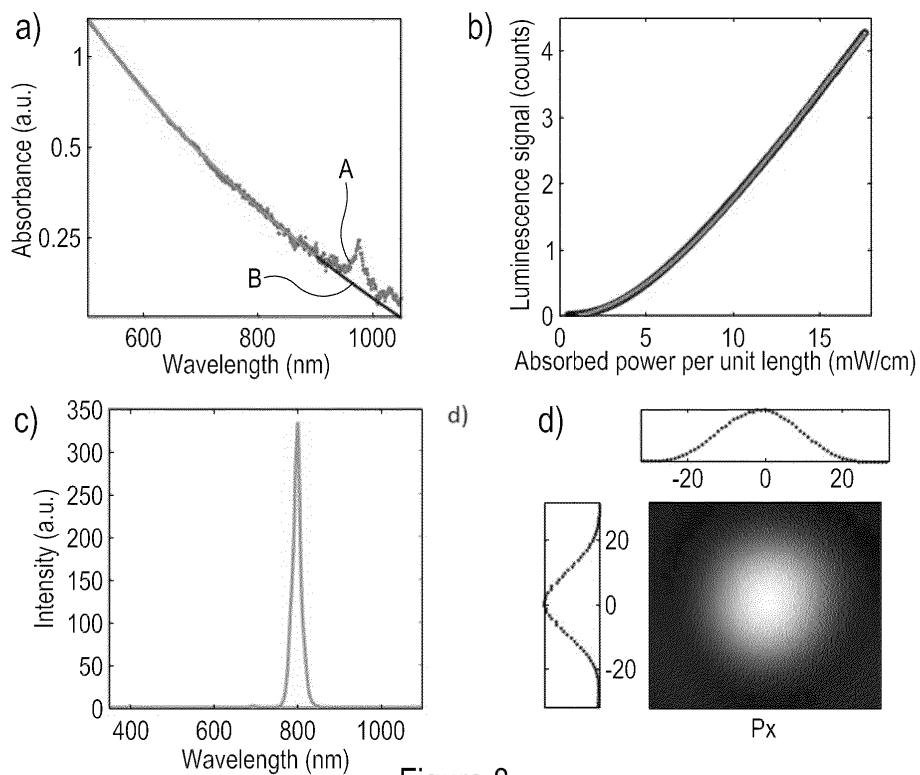


Figure 8

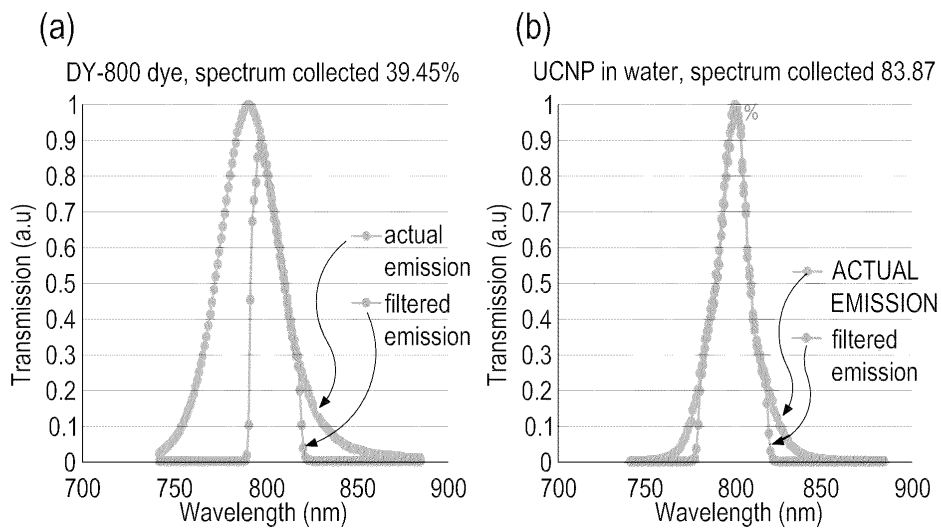
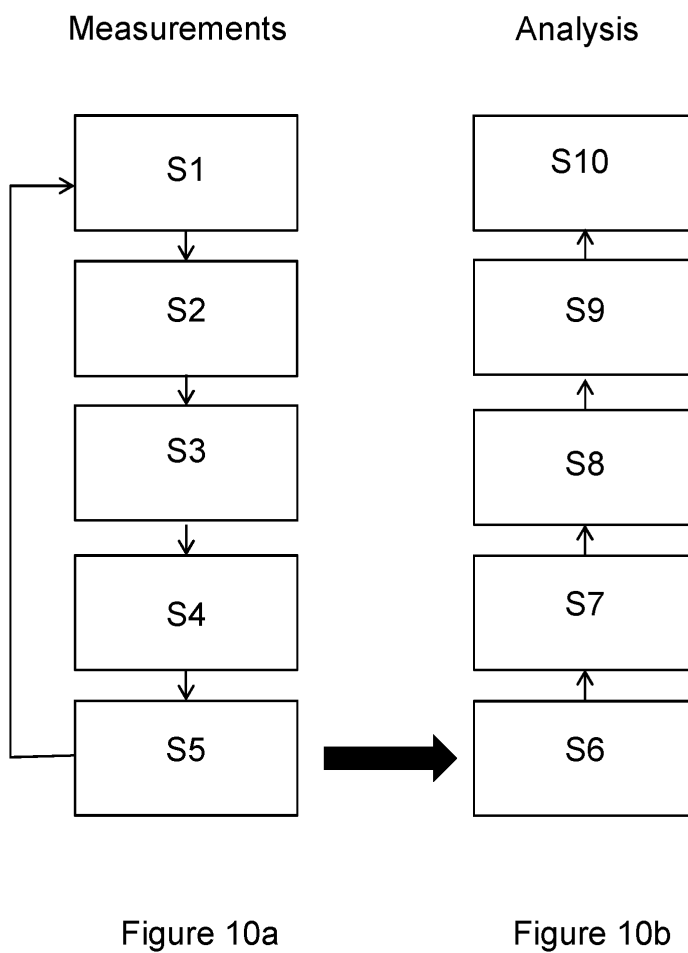


Figure 9

SUBSTITUTE SHEET (RULE 26)



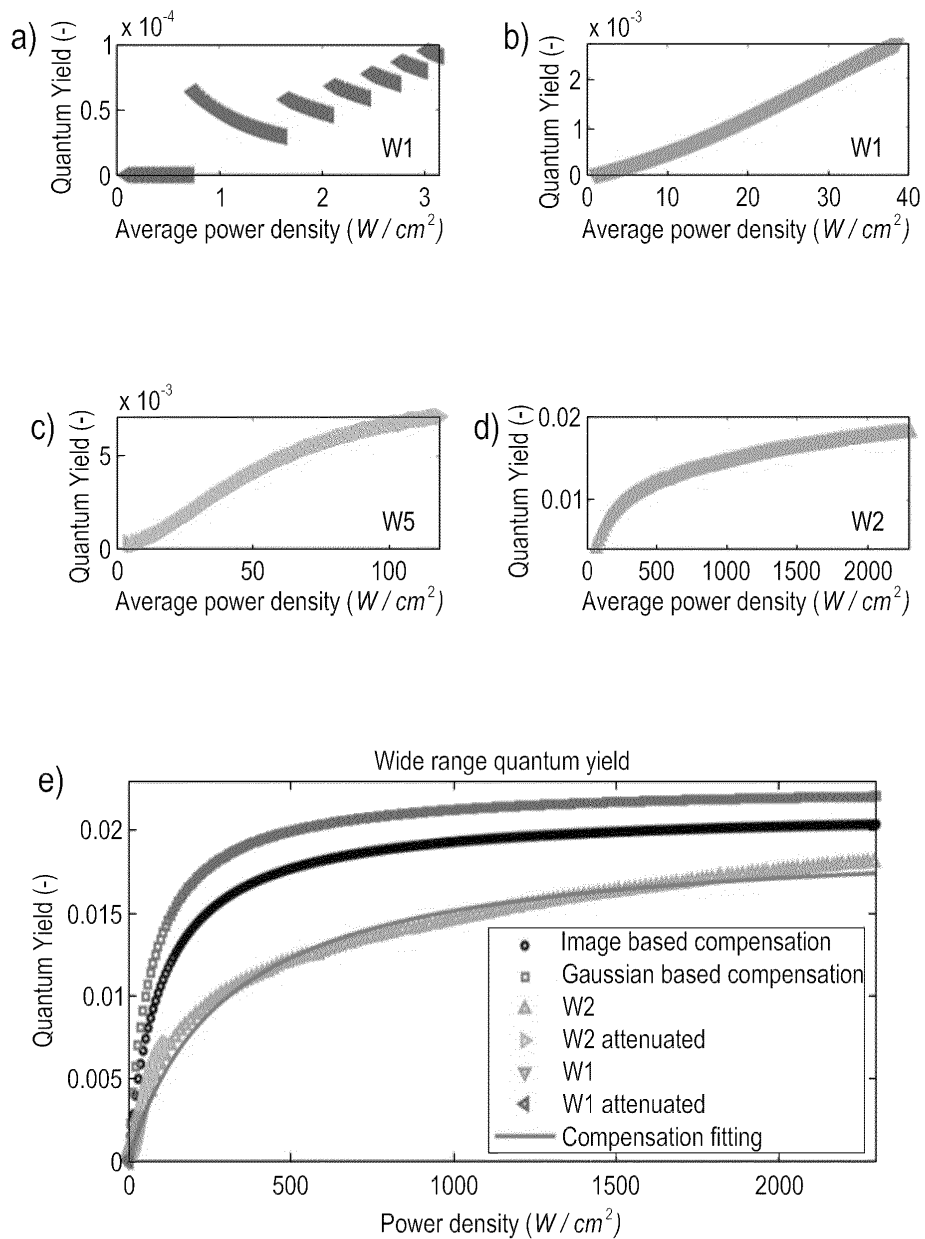


Figure 11

SUBSTITUTE SHEET (RULE 26)

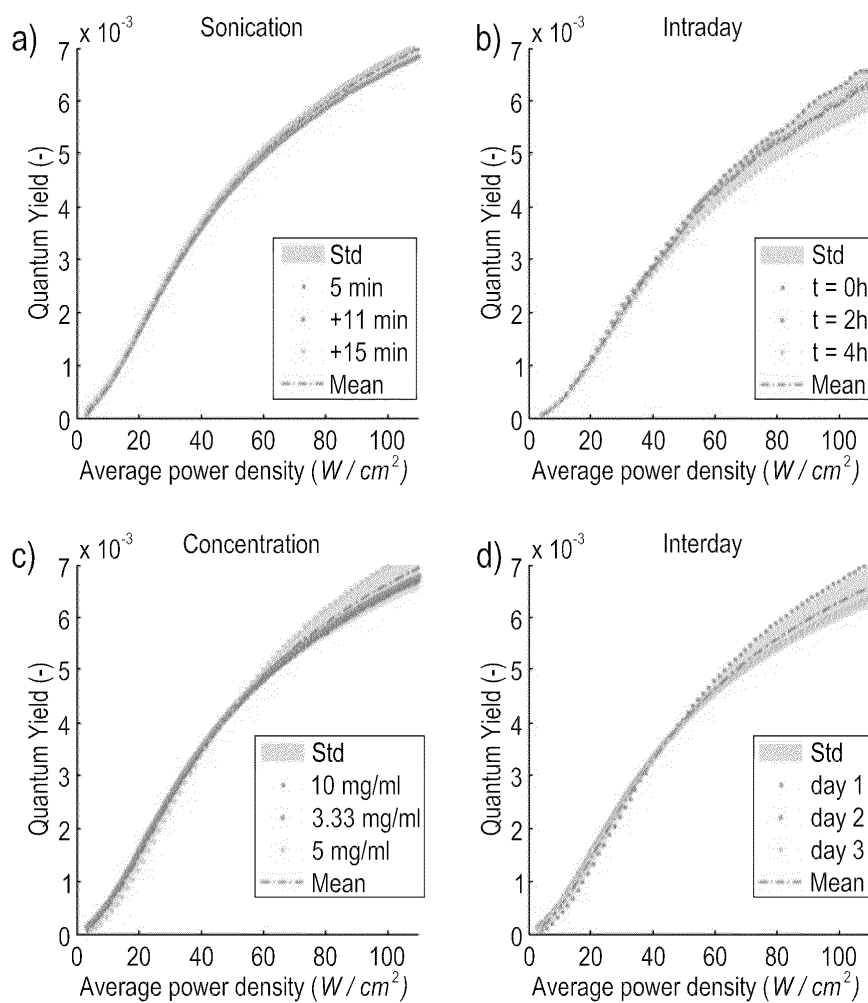


Figure 12

SUBSTITUTE SHEET (RULE 26)

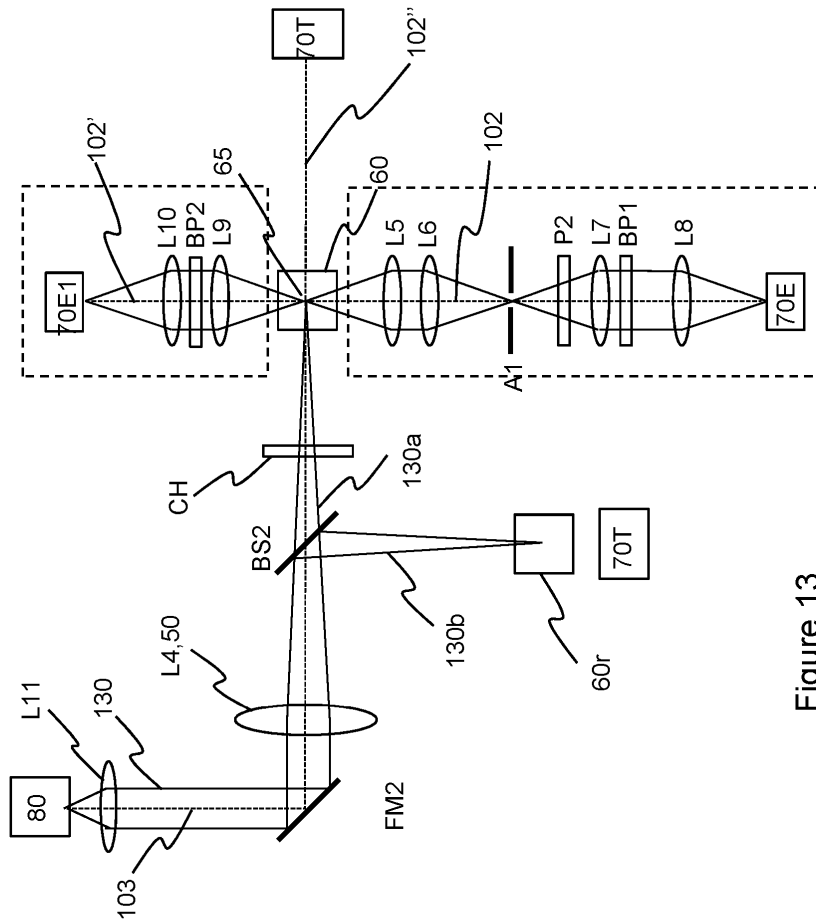


Figure 13

100

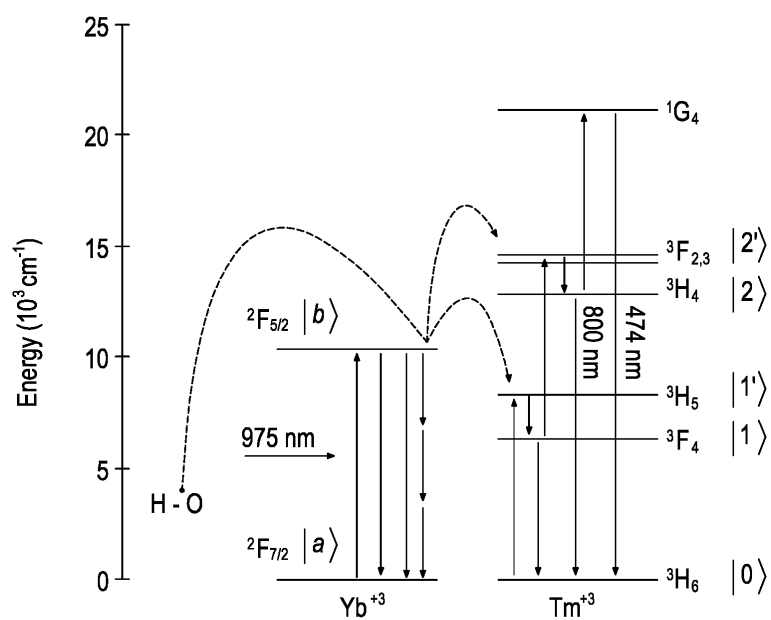


Figure 14

SUBSTITUTE SHEET (RULE 26)

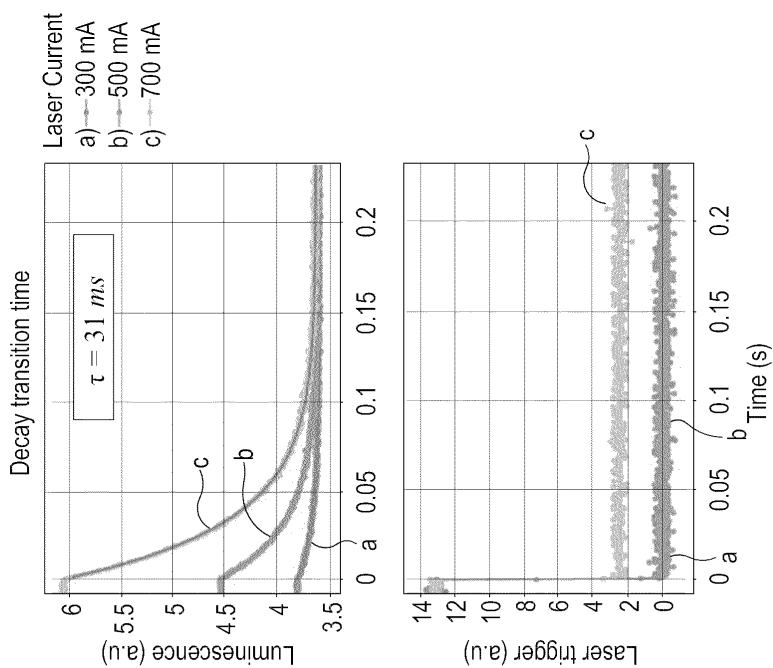


Figure 15b

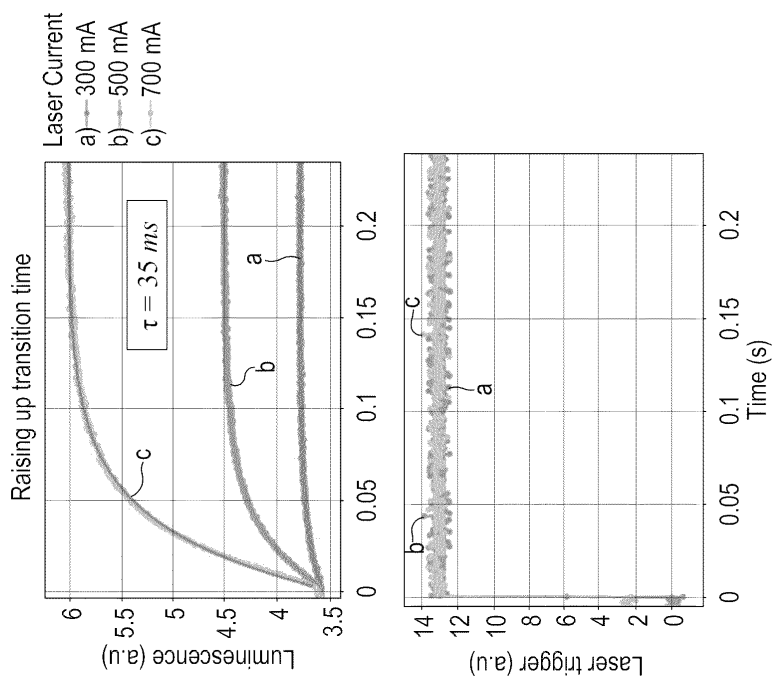


Figure 15a

SUBSTITUTE SHEET (RULE 26)

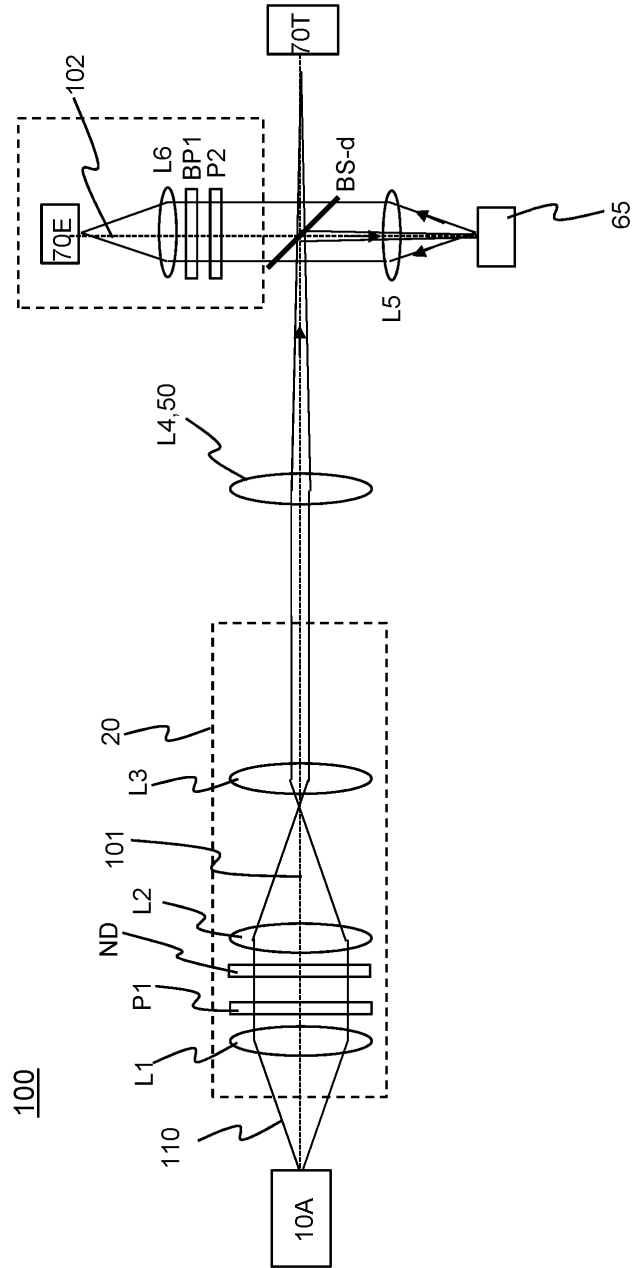


Figure 16

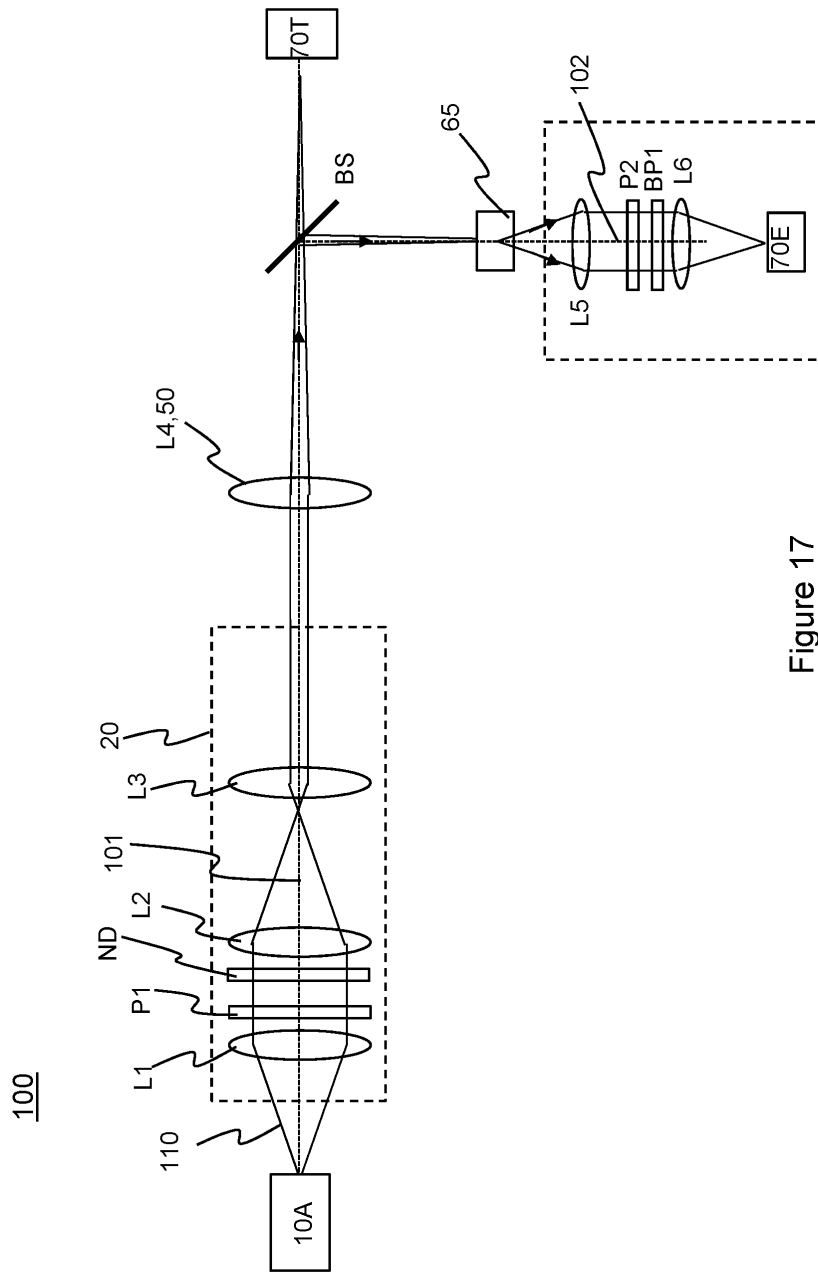


Figure 17

SUBSTITUTE SHEET (RULE 26)

INTERNATIONAL SEARCH REPORT

International application No  
PCT/EP2020/080714

<b>A. CLASSIFICATION OF SUBJECT MATTER</b> INV. G01N15/02 G01N15/14 G01N21/64 G02B27/09 G02B27/48 G01N15/00 G01N15/10 ADD. According to International Patent Classification (IPC) or to both national classification and IPC		
<b>B. FIELDS SEARCHED</b> Minimum documentation searched (classification system followed by classification symbols) G01N G02B Documentation searched other than minimum documentation to the extent that such documents are included in the fields searched Electronic data base consulted during the international search (name of data base and, where practicable, search terms used) EPO-Internal, WPI Data		
<b>C. DOCUMENTS CONSIDERED TO BE RELEVANT</b>		
Category*	Citation of document, with indication, where appropriate, of the relevant passages	Relevant to claim No.
X	US 2019/324281 A1 (DIEBOLD ERIC D [US] ET AL) 24 October 2019 (2019-10-24)	1-29, 32-39
Y	paragraphs [0011], [0014], [0019], [0034], [0037], [0038], [0041], [0061], [0062], [0065], [0068], [0079], [0087], [0132]; figures 1B,2 -----	30,31
X	US 2017/322133 A1 (TRAINER MICHAEL [US]) 9 November 2017 (2017-11-09)	1-29, 32-39
Y	paragraphs [0085], [0091], [0109], [0114], [0562]; figure 73 -----	30,31
X	US 2019/025212 A1 (EVANS KENNETH MICHAEL [US]) 24 January 2019 (2019-01-24)	1-29, 32-39
Y	paragraphs [0061], [0062], [0065], [0067], [0080] - [0082]; figures 1,2 paragraph [0145] - paragraph [0150]; figures 26-28 -----	30,31
-/--		
<input checked="" type="checkbox"/> Further documents are listed in the continuation of Box C. <input checked="" type="checkbox"/> See patent family annex.		
* Special categories of cited documents : "A" document defining the general state of the art which is not considered to be of particular relevance "E" earlier application or patent but published on or after the international filing date "L" document which may throw doubts on priority claim(s) or which is cited to establish the publication date of another citation or other special reason (as specified) "O" document referring to an oral disclosure, use, exhibition or other means "P" document published prior to the international filing date but later than the priority date claimed "T" later document published after the international filing date or priority date and not in conflict with the application but cited to understand the principle or theory underlying the invention "X" document of particular relevance; the claimed invention cannot be considered novel or cannot be considered to involve an inventive step when the document is taken alone "Y" document of particular relevance; the claimed invention cannot be considered to involve an inventive step when the document is combined with one or more other such documents, such combination being obvious to a person skilled in the art "&" document member of the same patent family		
Date of the actual completion of the international search		Date of mailing of the international search report
4 February 2021		17/02/2021
Name and mailing address of the ISA/ European Patent Office, P.B. 5818 Patentlaan 2 NL - 2280 HV Rijswijk Tel. (+31-70) 340-2040, Fax: (+31-70) 340-3016		Authorized officer  Eidmann, Gunnar

2

## INTERNATIONAL SEARCH REPORT

International application No PCT/EP2020/080714
---

C(Continuation). DOCUMENTS CONSIDERED TO BE RELEVANT		
Category*	Citation of document, with indication, where appropriate, of the relevant passages	Relevant to claim No.
Y	US 2002/158212 A1 (FRENCH TODD E [US] ET AL) 31 October 2002 (2002-10-31) paragraphs [0089], [0116], [0121], [0129]	30,31
A	----- BALABHADRA S ET AL: "A cost-effective quantum yield measurement setup for upconverting nanoparticles", JOURNAL OF LUMINESCENCE, ELSEVIER BV NORTH-HOLLAND, NL, vol. 189, 24 March 2017 (2017-03-24), pages 64-70, XP085069569, ISSN: 0022-2313, DOI: 10.1016/J.JLUMIN.2017.03.054 abstract	33
A	----- Anonymous: "Köhlersche Beleuchtung", LEXIKON DER PHYSIK, 1 January 1998 (1998-01-01), pages 1-2, XP055771894, Heidelberg Retrieved from the Internet: URL:https://www.spektrum.de/lexikon/physik/koeblersche-beleuchtung/8146 [retrieved on 2021-02-03] section "Köhlersche Beleuchtung"; figure 1 -----	1,21

**INTERNATIONAL SEARCH REPORT**

Information on patent family members

International application No  
PCT/EP2020/080714

Patent document cited in search report	Publication date	Patent family member(s)	Publication date
US 2019324281 A1	24-10-2019	AU 2019257598 A1 CN 112119547 A EP 3785338 A1 US 2019324281 A1 WO 2019209548 A1	27-08-2020 22-12-2020 03-03-2021 24-10-2019 31-10-2019
US 2017322133 A1	09-11-2017	NONE	
US 2019025212 A1	24-01-2019	AR 112611 A1 AU 2018302191 A1 BR 112020000896 A2 CA 3068874 A1 CN 110945343 A EP 3655754 A1 US 2019025212 A1 WO 2019018609 A1	20-11-2019 06-02-2020 21-07-2020 24-01-2019 31-03-2020 27-05-2020 24-01-2019 24-01-2019
US 2002158212 A1	31-10-2002	NONE	

Form PCT/ISA/210 (patent family annex) (April 2005)